University of California
Santa Barbara

In-Depth Understanding of Loss Mechanisms in High Performing Polymer:Non-fullerene Acceptor Bulk-Heterojunction Organic Solar Cells

A dissertation submitted in partial satisfaction of the
requirements for the degree
Doctor of Philosophy
in
Chemistry

by

Akchheta Karki

Committee in charge:

Professor Thuc-Quyen Nguyen, Chair

Professor Michael Chabinyc

Professor Martin Moskovits

Professor Mattanjah de Vries

September 2020

The dissertation of Akchheta Karki is approved.

_____

Professor Mattanjah de Vries

_____

Professor Martin Moskovits

_____

Professor Michael Chabinyc

_____

Professor Thuc-Quyen Nguyen, Committee Chair

June 2020

In-Depth Understanding of Loss Mechanisms in High Performing Polymer:Non-fullerene Acceptor Bulk-Heterojunction Organic Solar Cells

ACKNOWLEDGEMENTS

The content of this dissertation is a culmination of vastly collaborative efforts with wonderful professors, mentors, friends, and colleagues — I would like to express my deepest gratitude to them.

First and foremost, to my advisor, Professor Thuc-Quyen Nguyen, for her invaluable guidance and direction, which provided me with many opportunities to learn and grow. Quyen has constantly pushed me to ask critical scientific questions that have helped shape the way I think, question, and write. I will forever be indebted to her for all that I have learned over the course of the past 5 years.

To my committee members, Professors Michael Chabinyc, Martin Moskovits, and Mattanjah de Vries, for being a part of my committee, and for so willingly providing their valuable scientific feedback and advice.

To my mentors, Dr. Sam Collins and Dr. Niva Ran, for their high standards that kept me at my toes.

To Dr. Gert-Jan Wetzelaer, for his insightful feedback and helpful contributions for my first manuscript, which helped shape the way I thought about my future work.

To Dr. Joachim Vollbrecht, for his constant support, significant contributions, and helpful brain-storming sessions.

To Dr. Manju Gollapalli, for his eagerness and passion to share his immense knowledge on NMR spectroscopy.

To Dr. Alex Gillett, for his insightful ideas and suggestions, which have truly expanded my understanding and helped me get a more comprehensive view of my research.

To Dr. Alexander Mikhailovsky, for help with optical measurements and for his willingness to troubleshoot numerous problems that came up in lab.

To Max Schrock, for being so diligent and organized, so as to have become a highly efficient expert in photo-conductive AFM measurements in such a short amount of time.

To the rest of the amazing and supportive past and present co-workers from the Nguyen group: Dr. Viktor Brus, Dr. Seo-Jin Ko, Dr. Hung Phan, Dr. Tung Nguyen, Dr. Mike Heiber, Dr. Brett Yurash, Dr. Yuanyuan Hu, Dr. Michael Hughes, Alex Lill, David Cao, Ben Luginbuhl, Jianfei Huang, Zhifang Du, Nora Schopp, Alana Dixon, Sangcheol Yoon, Katie Rosenthal, Hiba Wakidi, Sangmin Chae, Ik Chatsirisupachai, and Tam Panoy: whom have all been excellent companions, friends, and colleagues.

To Professors Richard Friend, Paul Blom, Brad Chmelka, Harald Ade, Gui Bazan, and Franz Schauer, for their generous support and fruitful collaborations.

To the people in various other groups whom have actively contributed to productive collaborations: Dr. Martin Seifrid, Dr. Phillip Selter, Dr. Jaewon Lee, Dr. Vojtech Nádaždy, Dr. Steven S. Xiao, Dr. Yali Yang, and Zhengxing Peng, for their significant contributions.

To Tarnuma, for her warm friendship, food, and laughter.

To my family, for their support, encouragement, and love.

To Suraj, for his endless patience, humor, and love.

This dissertation was financially supported by the Holbrook foundation fellowship, Schlumberger foundation fellowship, and the Department of the Navy, Office of Naval Research Award No. N00014-14-1-0580.

Curriculum Vitae
of
Akchheta Karki

Education

2020	Doctor of Philosophy (PhD) in Materials Chemistry, University of California, Santa Barbara, California 93106 USA
2015	Bachelor of Arts (BA) in Chemistry and Mathematics (double major), *Summa cum laude*, Mount Holyoke College, South Hadley, Massachusetts, 01075 USA

Publications

2020	Gillett, A.G.; Privitera, A.; Dilmurat, R.; **Karki, A**.; Qian, D.; Pershin, A.; Londi, G.; Myers, W. K.; Lee, J.; Yuan, J; Ko, S-J.; Reide, M. K.; Gao, F; Bazan, G. C.; Nguyen, T.-Q.; Beljonne, D.; Friend, R.H.; The Role of Charge Recombination to Spin-Triplet Excitons in Non-fullerene Acceptor Organic Solar Cells, **2020**, *submitted*.
2020	**Karki, A.**; Vollbrecht, J.; Gillett, A. G.; Xiao, S. S.; Yali, Y; Peng, Z.; Schopp, N.; Dixon, A. L.; Schrock, M.; Reddy, G. N. M.; Ade H.; Friend, R. H.; Nguyen, T.-Q., The Role of Bulk and Interfacial Morphology in Charge Generation, Recombination, and Extraction in Non-Fullerene Acceptor Organic Solar Cells, **2020**, *in prep.*
2020	**Karki, A.**; Vollbrecht, J.; Gillett, A. G.; Selter, P.; Lee, J.; Peng, Z.; Nádaždy, V.; Schopp, N.; Dixon, A. L.; Schrock, M.; Schauer F.; Ade H.; Chmelka, B. F.; Bazan, G. C.; Friend, R. H.; Nguyen, T.-Q. Unifying Charge Generation, Recombination, and Extraction in Polymer:Non-fullerene Acceptor Bulk-Heterojuction Organic solar cells with low energetic offsets, *Advanced Energy Materials* 2020, *accepted (in-press)*.
2020	Jiang, Z.; Wang, F; Fukuda, K; **Karki, A.**; Huang, W.; Yu, K.; Yokota, T; Tajima, K; Nguyen, T.-Q.; Someya, T. Highly efficient organic photovoltaics with enhanced stability through the formation of doping-induced stable interfaces, PNAS 2020.
2019	**Karki, A.;** Vollbrecht, J.; Dixon, A. L.; Schopp, N.; Schrock, M.; Reddy, G. N. M.; Nguyen, T.-Q. Understanding the High Performance of over 15% Efficiency in Single-Junction Bulk Heterojunction Organic Solar Cells, *Advanced Materials* **2019**, 1903868.

2019 Vollbrecht, J.; Brus, V. V.; Ko, S.-J.; Lee, J.; **Karki, A**.; Cao, D. X.; Cho, K.; Bazan, G. C.; Nguyen, T.-Q. Quantifying the Nongeminate Recombination Dynamics in Nonfullerene Bulk Heterojunction Organic Solar Cells. *Advanced Energy Materials* **2019**, 9, 1901438.

2019 Lee, J.; Ko, S.-J.; Lee, H.; Huang, J.; Zhu, Z.; Seifrid, M.; Vollbrecht, J.; Brus, V. V.; **Karki, A.**; Luginbuhl, B. R. Side-Chain Engineering of Nonfullerene Acceptors for Near-Infrared Organic Photodetectors and Photovoltaics (Vol 4, Pg 1401, 2019). *ACS ENERGY LETTERS* **2019**, *4* (7), 1732–1732.

2019 Rosenthal, K. D.; Hughes, M. P.; Luginbuhl, B. R.; Ran, N. A.; **Karki, A.**; Ko, S.-J.; Hu, H.; Wang, M.; Ade, H.; Nguyen, T.-Q. Quantifying and Understanding Voltage Losses Due to Nonradiative Recombination in Bulk Heterojunction Organic Solar Cells with Low Energetic Offsets. *Advanced Energy Materials* **2019**, *9* (27), 1901077.

2019 **Karki, A.**; Wetzelaer, G.-J. A. H.; Reddy, G. N. M.; Nádaždy, V.; Seifrid, M.; Schauer, F.; Bazan, G. C.; Chmelka, B. F.; Blom, P. W. M.; Nguyen, T.-Q. Unifying Energetic Disorder from Charge Transport and Band Bending in Organic Semiconductors. *Advanced Functional Materials* **2019**, *29* (20), 1901109.

2018 Huang, J.; **Karki, A.**; Brus, V. V.; Hu, Y.; Phan, H.; Lill, A. T.; Wang, M.; Bazan, G. C.; Nguyen, T. Solution□Processed Ion□Free Organic Ratchets with Asymmetric Contacts. *Advanced Materials* **2018**, *30* (46), 1804794.

2018 Lee, J.; Ko, S.; Seifrid, M.; Lee, H.; McDowell, C.; Luginbuhl, B. R.; **Karki, A.**; Cho, K.; Nguyen, T.; Bazan, G. C. Design of Nonfullerene Acceptors with Near□Infrared Light Absorption Capabilities. *Advanced Energy Materials* **2018**, *8* (26), 1801209.

2018 Lee, J.; Ko, S.; Seifrid, M.; Lee, H.; Luginbuhl, B. R.; **Karki, A.**; Ford, M.; Rosenthal, K.; Cho, K.; Nguyen, T. Bandgap Narrowing in Non□Fullerene Acceptors: Single Atom Substitution Leads to High Optoelectronic Response Beyond 1000 Nm. *Advanced Energy Materials* **2018**, *8* (24), 1801212.

2018 Xu, X.; Fukuda, K.; **Karki, A.**; Park, S.; Kimura, H.; Jinno, H.; Watanabe, N.; Yamamoto, S.; Shimomura, S.; Kitazawa, D.; et al. Thermally Stable, Highly Efficient, Ultraflexible Organic Photovoltaics. *PNAS* **2018**, 201801187.

2018 Hu, Y.; Rengert, Z. D.; McDowell, C.; Ford, M. J.; Wang, M.; **Karki, A.**; Lill, A. T.; Bazan, G. C.; Nguyen, T.-Q. Doping Polymer Semiconductors by Organic Salts: Toward High-Performance Solution-Processed Organic Field-Effect Transistors. *ACS Nano* **2018**, *12* (4), 3938–3946.

2018	Ran, N. A.; Love, J. A.; Heiber, M. C.; Jiao, X.; Hughes, M. P.; **Karki, A.**; Wang, M.; Brus, V. V.; Wang, H.; Neher, D.; Bazan, G. C.; Nguyen, T.-Q. Charge Generation and Recombination in an Organic Solar Cell with Low Energetic Offsets. *Advanced Energy Materials* **2018**, *8* (5), 1701073.
2016	**Karki, A.**; Nguyen, L.; Sharma, B.; Yan, Y.; Chen, W. Unusual Morphologies of Poly(Vinyl Alcohol) Thin Films Adsorbed on Poly(Dimethylsiloxane) Substrates. *Langmuir* **2016**, *32* (13), 3191–3198.

Presentations

2020	**Karki, A.**; Vollbrecht, J.; Gillett, A. G.; Selter, P.; Lee, J.; Peng, Z.; Nádaždy, V.; Schopp, N.; Dixon, A. L.; Schrock, M.; Schauer F.; Ade H.; Chmelka, B. F.; Bazan, G. C.; Friend, R. H.; Nguyen, T.-Q. *Center for polymers and organic solids (CPOS) annual symposium*, Santa Barbara, CA, USA, **2020**.
2019	**Karki, A.**; Wetzelaer, G.-J. A. H.; Reddy, G. N. M.; Nádaždy, V.; Seifrid, M.; Schauer, F.; Bazan, G. C.; Chmelka, B. F.; Blom, P. W. M.; Nguyen, T.-Q. *Center for polymers and organic solids (CPOS) annual symposium*, Santa Barbara, CA, USA, **2019**.
2018	**Karki, A.**; Wetzelaer, G.-J. A. H.; Reddy, G. N. M.; Nádaždy, V.; Seifrid, M.; Schauer, F.; Bazan, G. C.; Chmelka, B. F.; Blom, P. W. M.; Nguyen, T.-Q. *Schlumberger foundation Annual Research Conference*, Boston, MA, USA, **2018**.
2018	**Karki, A.**; Wetzelaer, G.-J. A. H.; Reddy, G. N. M.; Nádaždy, V.; Seifrid, M.; Schauer, F.; Bazan, G. C.; Chmelka, B. F.; Blom, P. W. M.; Nguyen, T.-Q. *Gordon Research Conference*, Barja, Italy, **2018**.
2017	Ran, N. A.; Love, J. A.; Heiber, M. C.; Jiao, X.; Hughes, M. P.; **Karki, A.**; Wang, M.; Brus, V. V.; Wang, H.; Neher, D.; Bazan, G. C.; Nguyen, T.-Q. *Annual CAOP Meeting*, Atlanta, GA, USA, **2017**.

Awards and Honors

2016-2020	Schlumberger foundation fellowship
2015-2016	Holbrook Foundation Fellowship
2015	Elected to the phi beta kappa
2015	Summa cum laude in chemistry for the writing of an exceptional thesis and maintaining a GPA above 3.75
2014	Louisa Stone Stevenson Prize for excellence in chemistry

ABSTRACT
In-Depth Understanding of Loss Mechanisms in High Performing Polymer:Non-fullerene Acceptor Bulk-Heterojunction Organic Solar Cells

by

Akchheta Karki

Even though significant breakthroughs with unprecedented power conversion efficiencies (*PCE*s) approaching 18% have been achieved for polymer:non-fullerene acceptor (NFA) organic solar cells (OSCs) recently, not many studies in the literature have focused on acquiring a comprehensive understanding of the underlying mechanisms governing these novel systems. The common knowledge in the OSC community is that to achieve high performances, there needs to be a minimization of the voltage losses due to charge generation, recombination, and energetic disorder, as well as an optimal control of the bulk heterojunction morphology for beneficial charge transport and extraction. In practice, it is extremely challenging to obtain such parameters simultaneously and even more complex to delineate device photophysics in polymer:NFA blends comprehensively. Furthermore, tracing origins of the differences in device photophysics to the subtle differences in energetics and morphology can be particularly complicated. This dissertation encompasses four studies that unify approaches to understand the complicated device photophysics of organic semiconductor devices. Firstly, a systematic study of a series of polymer:NFA blends is conducted to unify and correlate the cumulative effects of i) voltage losses ii) charge generation efficiencies, iii) non-geminate recombination and extraction dynamics, and iv) nuanced morphological differences with device performances. Most importantly, a deconvolution of the major loss processes in polymer:NFA blends and their connections to the complex BHJ morphology and energetics are established. Secondly, the device

photophysics in the high performing PM6:Y6 blend system is investigated. This blend system is found to exhibit low voltage losses coupled with moderate non-geminate recombination and exceptional extraction that can explain its high efficiencies of over 15%. Thirdly, a study is conducted to understand the role of morphology in the key operating processes of high performing polymer:NFA organic solar cells. Varying polymer molecular weight fractions is used as a tool to exert fine control over the interfacial and bulk morphology. This study provides an avenue to understand two fundamental and complex questions that are relevant to the OSC community: i) the role of the nature of the D:A BHJ interface on charge generation and recombination processes, and ii) the factors affecting charge extraction and transport in OSCs. The results from this work provide recommendations on the significant bulk and interfacial morphological features that are critical in optimizing charge generation, recombination, and extraction processes to give high performances, expediting the pathway to the commercialization of OSCs in the near future. Lastly, the DOS distribution widths of two structurally unique organic semiconducting polymers are characterized by using a combination of techniques that have not be explored together. These include, temperature-dependent current density-voltage (*J-V*) measurements, Kelvin probe measurement (KP) of band bending, and energy-resolved electrochemical impedance spectroscopy (ER-EIS). A quantitative correlation between energetic disorder from band□bending measurements and charge transport is established, providing direct experimental evidence that charge□carrier mobility in disordered materials is compromised due to the relaxation of carriers into the tail states of the DOS. Distinction and quantification of locally ordered and disordered regions of thin films at an atomic level was achieved using solid□state NMR spectroscopy.

TABLE OF CONTENTS

Curriculum Vitae..... vi
Abstract..... ix

Chapter 1. Introduction 1
1.1. Background and Motivation..... 1
1.2. Working Mechanisms of Bulk Heterojunction Organic Solar Cells..... 4
1.3. Contributions to Voltage losses..... 7
1.4. Energetic Disorder in Organic Semiconductors..... 8
1.5. Working Principles of Commonly Used Techniques and Models..... 11
1.6. Summary of Chapters..... 19

Chapter 2. Unifying Charge Generation, Recombination, and Extraction in Low-offset Non-fullerene Acceptor Organic Solar Cells 23
2.1. Introduction..... 23
2.2. Results and Discussions..... 25
2.3. Conclusions..... 54
2.4. Experimental Section..... 57

Chapter 3. Understanding the High Performance of over 15% Efficiency in Single-Junction Bulk Heterojunction Organic Solar Cells 65
3.1. Introduction..... 65
3.2. Results and Discussions..... 66
3.3. Conclusions..... 82
3.4. Experimental Section..... 83

Chapter 4. The Role of Bulk and Interfacial Morphology in Charge Generation, Recombination, and Extraction in Non-Fullerene Acceptor Organic Solar Cells 88
4.1. Introduction..... 88
4.2. Results and Discussions..... 89
4.3. Conclusions..... 113
4.4. Experimental Section..... 113

Chapter 5. Unifying Energetic Disorder from Charge Transport and Band Bending in Organic Semiconductors 121
5.1. Introduction..... 121
5.2. Results and Discussions..... 123
5.3. Conclusions..... 141
5.4. Experimental Section..... 141

Appendices..... 145
References..... 230

Chapter 1

Introduction

1.1 Background and Motivation

In 2019, renewable sources of energy consumption in the US accounted for only 11% of the total energy consumption with fossil fuels like petroleum (36%) and natural gas (31%) leading as suppliers of energy.[1] In addition to the obvious downside of fossil fuels that they are limited in capacity, they also produce large amounts of carbon dioxide, which is the largest contributor to greenhouse gas emissions.[2] Greenhouse gas emissions have a heating effect on the atmosphere which leads to global warming.[3] The National Climate Assessment released a report stating that "Earth's climate is now changing faster than at any point in the history of modern civilization, primarily as a result of human activities."[4] Unfortunately, Earth's fast changing climate has already manifested as increasing numbers of devastating wildfires, storms, flooding, and droughts in recent years across the world. Therefore, there is a dire need for the development of renewable energy technologies that can aid in abating greenhouse gas emissions. Amidst the many different sources of renewable energies such as biomass, wind, hydroelectric, and geothermal, the work included in this thesis primarily focuses on harvesting solar energy.

While the most commercially used solar panels for harvesting solar energy are made from silicon due to their high efficiency, they have some drawbacks to them which limit their applicability such as needing to be processed under high temperatures and pressures and requiring sturdy structures for support. In contrast, solar cells made from organic

semiconductors, which are organically synthesized molecules with conjugated backbones, allow for electron delocalization along the π orbitals. The semiconducting properties of these conjugated molecules arise from their ability to form bonding or antibonding interactions with adjacent p-orbitals of the same sign. **Figure 1.1** shows an example of how the conjugated benzene structure forms these bonding and antibonding orbitals based on the molecular orbital theory that give rise to the highest occupied molecular orbital (HOMO) and lowest unoccupied molecular orbital (LUMO) levels giving these conjugated systems their semi-conducting properties.

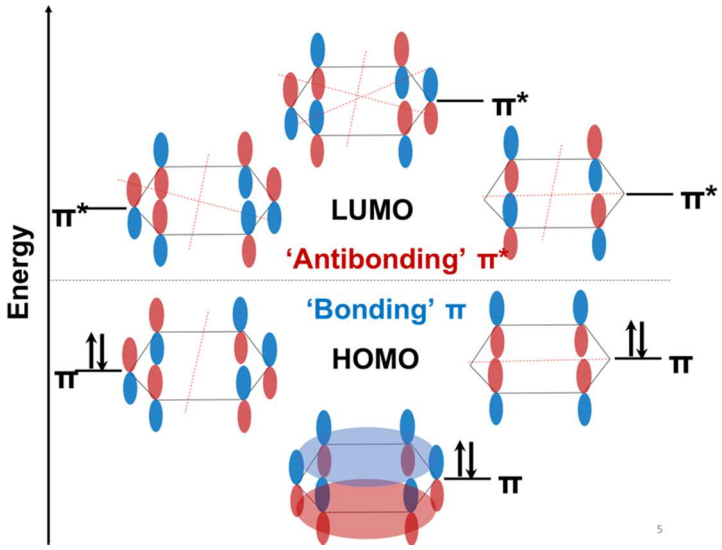

Figure 1.1. The bonding and antibonding p-orbitals of a benzene ring.

Since these organic molecules are made via synthetic methods, they can be made from abundant source materials, be solution processable, and have tunable absorption properties. Consequences of these properties are that in contrast to silicon solar cells, organic solar cells can be printed via roll-to-roll deposition technology which can massively reduce the cost of production. Furthermore, they can be deposited onto lightweight and flexible substrates so that they can be applied to curves surfaces such as the body of a car. Their tunable absorption means that they can be made semi-transparent for harvesting electricity by incorporating them

as windows of buildings or roofs of greenhouses so that they can achieve net-zero operations.[5,6] More recently, there has also been a remarkable development and interest in integrating organic solar cells that employ low intensity diffuse lights inside buildings to generate electricity and power Internet of things (IoT) devices.[7] These novel applications of organic solar cells shown in **Figure 1.2**a have grown just over the last decade due to the increase in the power conversion efficiencies (*PCE*s) to over 17%[8,9] in recent years as a result of the development of a new class of non-fullerene acceptors (**Figure 1.2**b), and there is enormous potential for a lot more development to push the limits of innovation even further with increasing efficiencies.

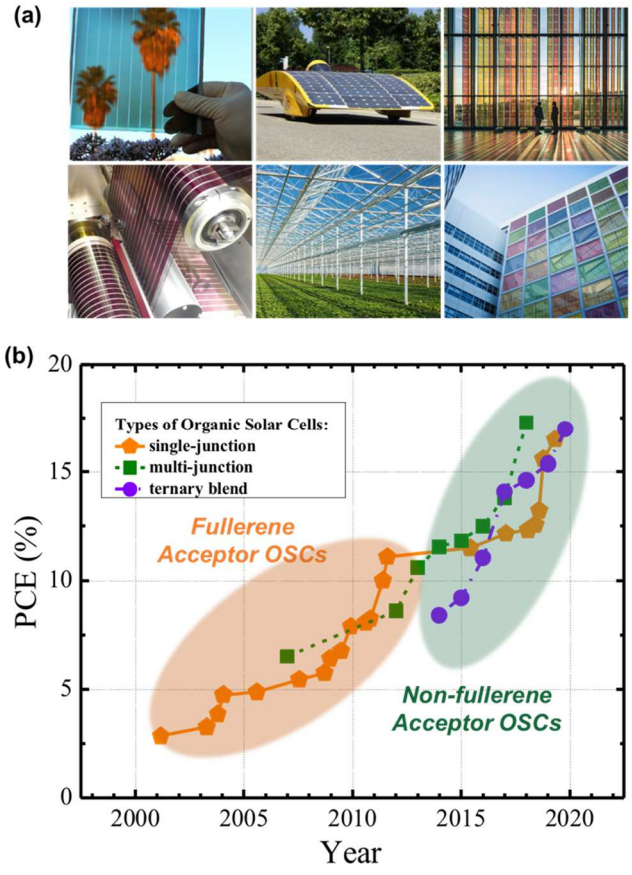

Figure 1.2. (a) Novel applications of organic solar cells which have grown over the last few years. (images sources: © *minicel73/Stock.adobe.com*, swisstechconventioncenter/solaronix, infinitypv.com, dutchscenery/istockphoto, imec.be/bipv)(b) Growth in power conversion efficiencies (*PCE*s) of organic solar cells over the past 20 years.

1.2 Working Mechanisms of Bulk Heterojunction Organic Solar Cells

In this section, the basic working mechanisms in bulk heterojunction (BHJ) organic solar cells (OSCs) will be discussed. A BHJ OSC comprises of a mixture of electron donor (D) and electron acceptor (A) material. Therefore, a D:A OSC will have many D:A interfaces. An example of a D:A interface is shown in **Figure 1.3** and the interface is, in fact, where all the important photophysical processes happen. The working mechanism of an organic solar cell starting with photon absorption and ending with charge extraction at the electrodes is full of potential loss pathways for the photogenerated charges. The goal throughout my thesis was to accurately characterize and quantify these loss pathways. To be able to quantify and understand these loss mechanisms, it is important to first have a clear and full picture of the working mechanisms.

When we shine light on an OSC, the photon is absorbed by the donor and acceptor components in the blend to create excitons, which is a bound electron hole pair. The exciton will then diffuse to the D:A interface and form a charge transfer (CT) state, i.e. a bound electron-hole pair at the D:A interface. The CT state can dissociate at the interface such that charges move away from each other. In an ideal case, the charges will form free electron and holes, which then get extracted at the respective electrodes. However, things are never ideal, so in competition with the extraction process is a process called recombination where instead of the charges getting extracted at the respective electrodes, they recombine with each other, i.e. they come together and cancel each other out. There are two known types of recombination pathways. The first one is called geminate recombination where charges that are from the same exciton end up cancelling each other out. The second one is called non-geminate

recombination which is a more dominant recombination process in high performing OSCs. In non-geminate recombination, charges that have separated at the D:A interface find other oppositely charge carries or traps to recombine with. Hence, non-geminate recombination losses are further characterized into two types: trap-assisted recombination and bimolecular recombination. These two types of non-geminate recombination processes can be distinguished by their dependence on the charge carrier density, n. In the case of bimolecular recombination, since you have two charge carriers recombining with each other, the rate of recombination will be proportional to n^2. Conversely, in the case of trap-assisted recombination, the rate of recombination will be proportional to n since only one charge carrier is involved in this process. It is worth noting that the non-geminate recombination process is in competition with the charge extraction process. It has been shown that if the charge extraction time (τ_{ex}) is faster than or comparable to the recombination time (τ_{rec}), then charge recombination can be further reduced to improve the device efficiencies, and so understanding the interplay between these two processes is also quite important to understand the power conversion efficiencies.

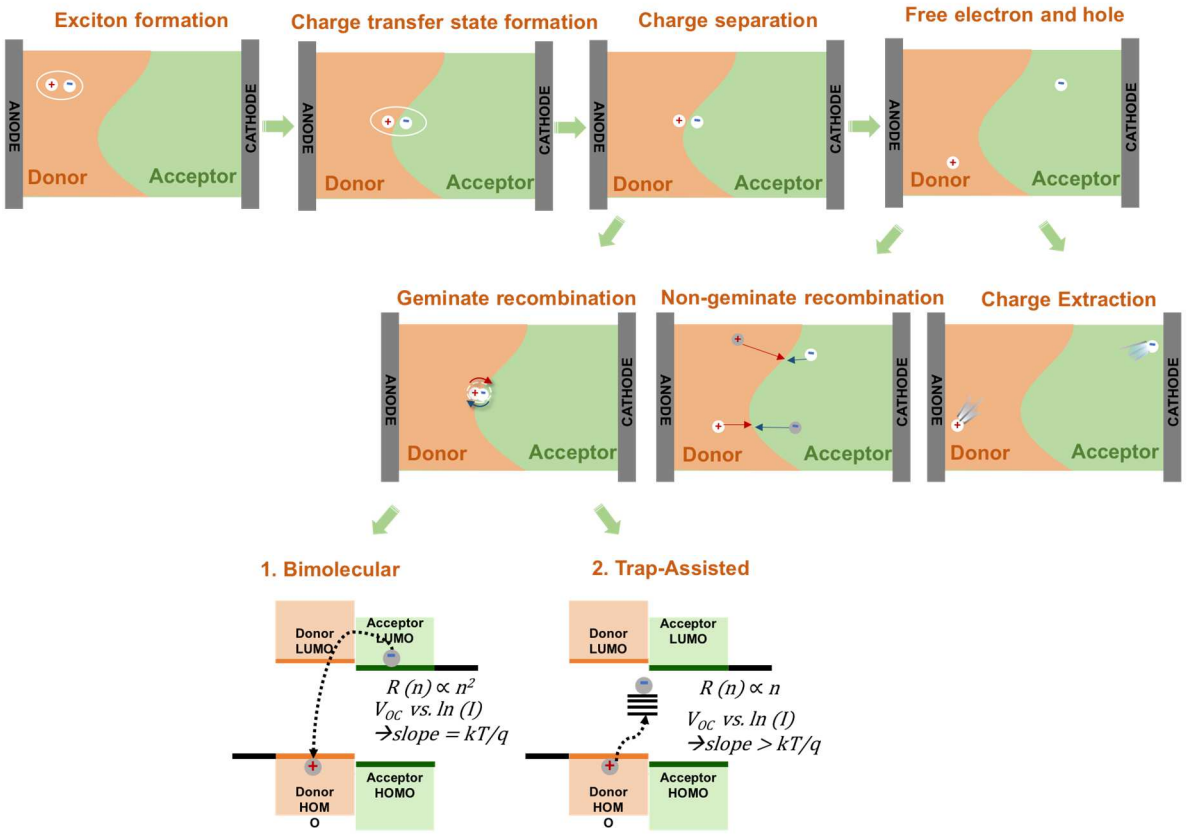

Figure 1.3. A schematic showing the different loss processes of organic solar cells including exciton formation, geminate recombination, charge transfer state formation, charge separation, free electron and hole formation, non-geminate recombination (bimolecular and trap-assisted), and charge extraction.

To determine the power conversion efficiencies of OSCs, the current density vs. voltage curve (*J-V*) is measured. (**Figure 1.4**) This is done by illuminating the OSC with white light containing a filter that simulates the emission spectrum of the sun (100 mW cm^{-2} AM 1.5). Under illumination, a range of voltages is applied to the solar cell and the resulting current is recorded as the *J-V* curve. We are specifically interested in three main points of the *J-V* curve. First, is the open-circuit voltage (V_{OC}), which is the applied voltage where there is no driving force to extract charges, and therefore, all the generated charge carriers recombine resulting in no net current. Second, is the short-circuit current (J_{SC}) where even though there is no applied voltage, there is an internal field that assists in charge separation and extraction and

finally, the fill-factor (*FF*) which is a parameter that describes the ratio between the actual power (P_{max}) in devices and the ideal maximum power (P_{ideal}) given by the product of the *FF* and V_{OC}. The power conversion efficiency is obtained from the following equation:

$$PCE = \frac{P_{MAX}}{P_{IN}} = \frac{V_{OC}\ J_{SC}\ FF}{P_{IN}} \tag{2}$$

and is used as a standard measure for determining how efficient OSCs are.

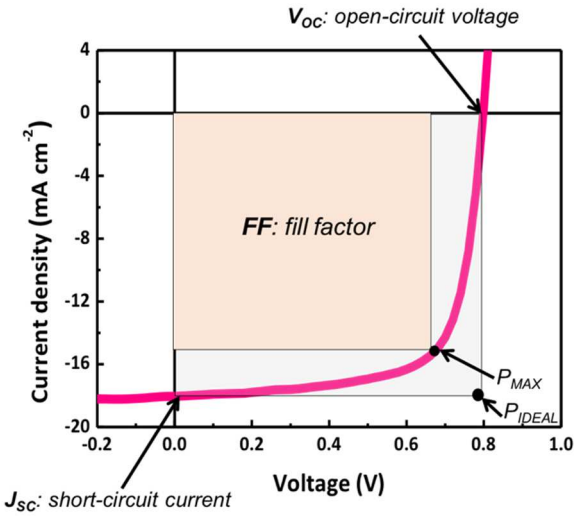

Figure 1.4. *J-V* curve of an organic solar cell showing the parameters (J_{SC}, V_{OC}, *FF*) required to obtain the *PCE*.

1.3 Contributions to Voltage losses

In this section, the origins of the V_{OC} losses will be discussed. **Figure 1.5**a show the energy potential well diagram following an absorption event, where an electron gets excited from the ground state to the singlet exciton energy (S_1) state. This is equivalent to the process of exciton generation described in the earlier section. Following this, the exciton formed at the donor or acceptor phase migrates to the D:A interface where the hole or electron transfer events can occur. In this case, we refer to the energetic offset as the difference between the S_1 and *CT* state (**Figure 1.5**b). There are additional losses from the CT state which are classified into radiative and non-radiative recombination losses (**Figure 1.5**c). All of these processes

together end up dictating the V_{OC} losses in organic solar cells and give rise to this commonly shown voltage loss diagram in **Figure 1.5**d.

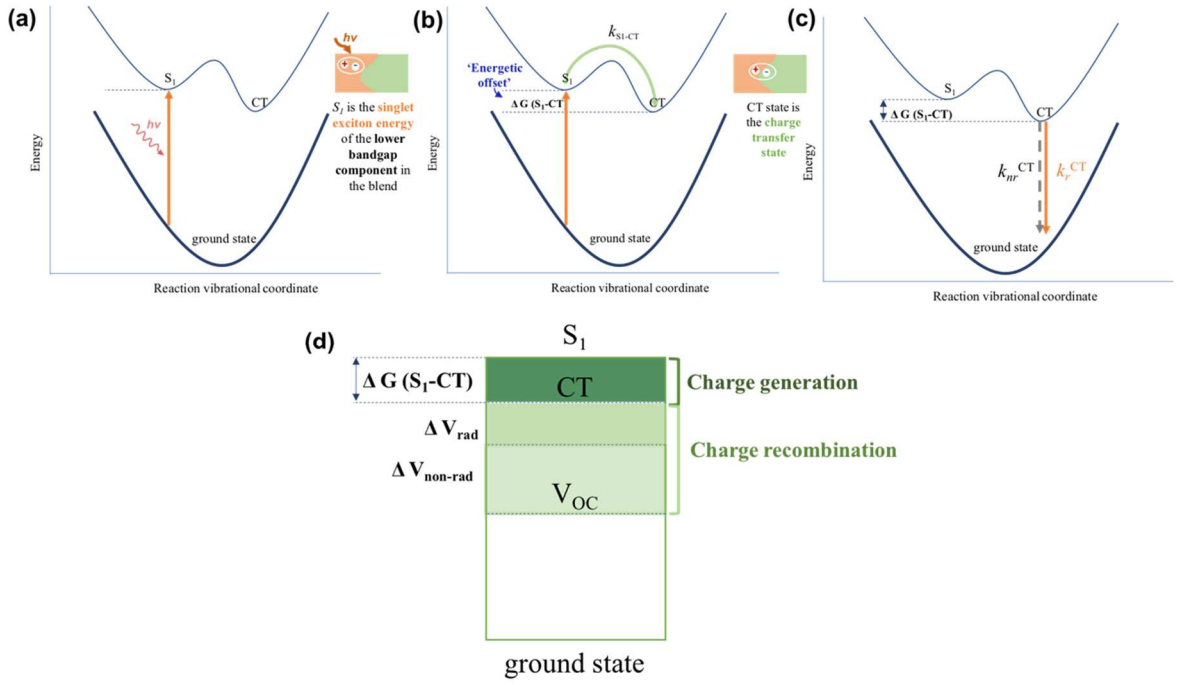

Figure 1.5. Energy potential well diagrams for systems with low S_1-CT offsets showing losses from S_1 to V_{OC}.

1.4 Energetic Disorder in Organic Semiconductors

The final chapter of my thesis covers the study of energetic disorder in organic semiconductors. In order to begin to understand energetic disorder, we must first start with an understanding of the density of states (DOS) and its origins. **Figure 1.6**a shows the DOS distribution of three classes of materials: i) ordered semiconductor such as crystalline silicon, ii) amorphous semiconductor such as amorphous silicon, and iii) disordered semiconductor such as polymers. In ordered systems such as crystalline silicon, there are clearly defined conduction and valence band edges. In polymer organic semiconductor systems, however, there exists a more morphologically diverse film. This is due to the different types of intra and

inter-molecular interactions, rotation and kinking of polymer chains, and conformational diversity. This morphological diversity brings about an energetic variation of states, and so even though we commonly draw out the HOMO and LUMO levels as these bands for convenience, they really consist of different states that are distributed in energy, manifesting as the extension of localized states into the bandgap. These states are more commonly described by a Gaussian distribution and is known as the DOS distribution. Gaussian distributions have a characteristic width (σ), which is the standard deviation of this curve and more commonly referred to as the disorder parameter. **Figure 1.6**b shows a picture of the density of states, where each of the grey lines represent states where charge carriers may potentially reside. These states are denser towards the middle and sparser towards the edges. If we now consider the motion of a charge carrier generated at an arbitrary site within the DOS distribution, it hops from one site to the next, and ultimately relaxes towards the tail of the distribution. Initially, energetically downhill hops dominate the path, but ultimately a balanced equilibrium between downhill and thermally activated uphill jumps will be established and a mean-quasi equilibrium energy (ε_∞) will be attained. Charge carriers in a broad DOS distribution tend to migrate to an equilibrium energy proportional to its width (σ). A consequence of this is that when the width is broad, the equilibrium energy resides much lower in the tail states where the number of states is sparser. Since it is more difficult for charges to hop near the tail ends of the distribution (due to the low number of states) the charge carrier mobility as well as the activation energy is compromised in systems with a broad DOS distribution.

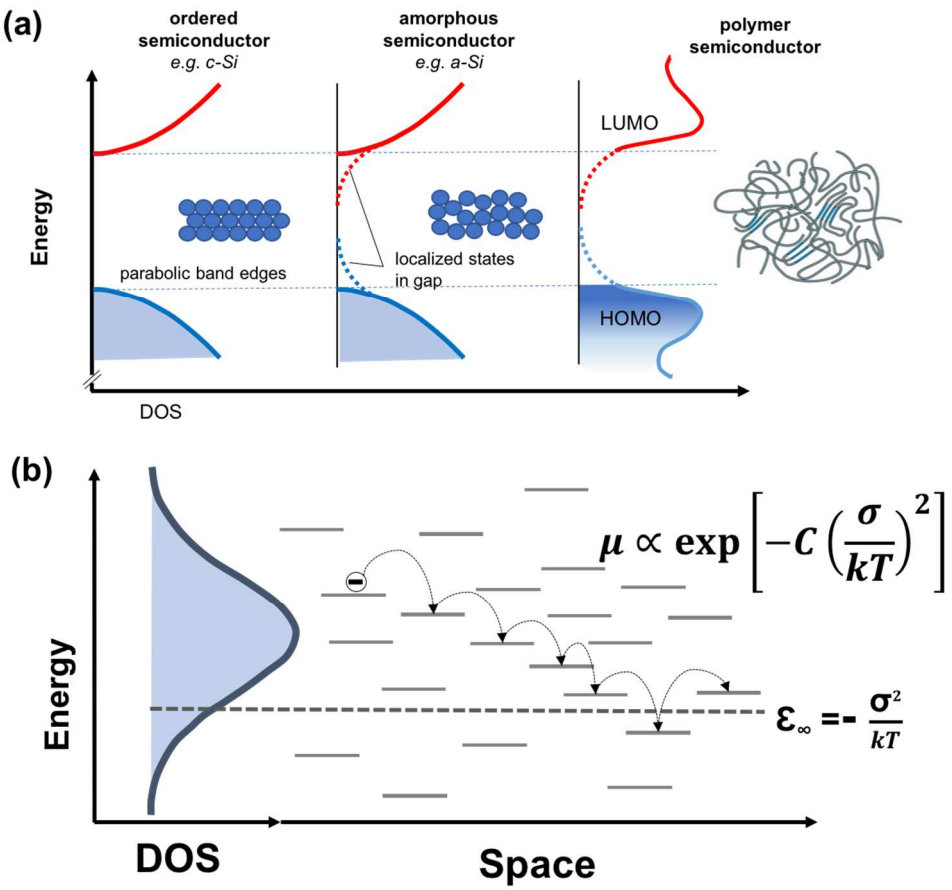

Figure 1.6. (a) The DOS distributions of three classes of materials: i) ordered semiconductor such as crystalline silicon, ii) amorphous semiconductor such as amorphous silicon, and iii) disordered semiconductor such as polymers. (b) A picture of the DOS distribution and the pathway for charge carriers to hop.

1.5 Working Principles of Commonly Used Techniques and Models

1.5.1. Measuring Non-Radiative Recombination losses with External Quantum Efficiency of Electroluminescence (EQE_{EL})

The non-radiative recombination losses in OSCs can be measured experimentally by determining its radiative efficiency which is known as the external quantum efficiency of its electroluminescence (EQE_{EL}). The EQE_{EL} is defined as the ratio of the photons emitted from the device recorded by measuring the photodiode current (I_0) divided by the electrons injected into the device (I_{device}).

$$EQE_{EL} = \frac{I_0}{I_{device}} \tag{1}$$

where I_0 is a corrected photodiode current obtained by dividing the actual emission of the photodiode (I_{PD}) by the wavelength of the emission spectra of the device, $i(\lambda)$, and the sensitivity of the photodiode, $s(\lambda)$:

$$\frac{I_{PD}}{\int_{\lambda_1}^{\lambda_2} i(\lambda)s(\lambda)d\lambda} = I_0 \tag{2}$$

Figure 1.7 shows the measurement set-up for EQE_{EL}. A bias range corresponding to the relevant working voltages of an organic solar cell device (generally ranging from -1 to 2 V) is applied to a device and the resulting luminescent output is measured using an appropriate silicon or germanium photodiode depending on the wavelength of interest for the emission. The non-radiative recombination losses (ΔV_{nonrad}) is found from the equation below and was first derived in this work[10]:

$$\Delta V_{nonrad}(T) = -\frac{kT}{q} ln(EQE_{EL}) \tag{3}$$

A way to understand the basis of this derivation is by thinking about what would happen when the ratio of the emitted photons divided by the electron injected into the device are equal. In such a case, all of the emission would be radiative, the EQE_{EL} ratio would be equal to 1, and the losses due to non-radiative recombination would be 0.

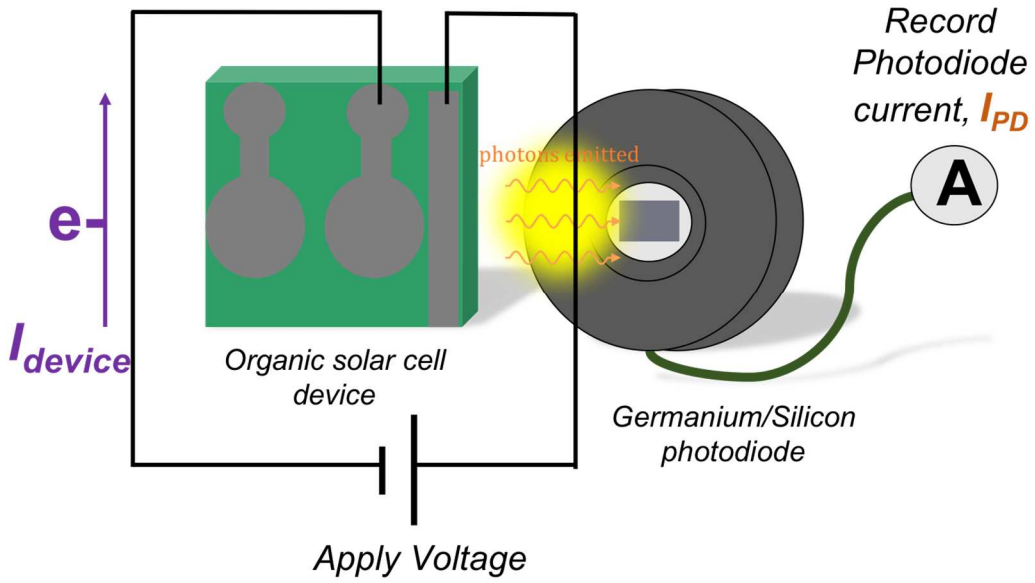

Figure 1.7. The measurement set-up for measuring the external quantum efficiency of luminescence (EQE_{EL}).

1.5.2. Measuring Charge Generation Efficiency with Ultrafast pump-probe spectroscopy

Figure 1.8 shows a schematic of an ultrafast transient absorption pump-probe set-up. Ultrafast transient absorption spectroscopy is used to probe the steps starting from exciton formation at the donor or acceptor phase to charge separation at the D:A interface. Ultrafast transient absorption spectroscopy allows us to look into the absorption properties of species that exist in the excited state after photoexcitation by using a pump laser of the appropriate wavelength to excite the sample. Since the excited states are typically short-lived and transient, this technique is used to acquire temporal properties. In order to get species from the ground state to the excited state, an optical pulse is used to first "pump" the sample. As

shown in **Figure 1.8**, there is a delay line in the set-up which is a line that a second "probe" pulse goes through. It is the job of the "probe" to then monitor the spectral characteristics of the species in the excited state before they decay back down. Since the "probe" pulse goes through the delay line, it comes to the sample after a short duration of time when the species have reached an excited state and is able to take spectral snapshots of what the excited states are doing, i.e., how they are decaying back down to the ground state. By increasing the delay time by moving the delay line, you are delaying the time difference between the "pump" and "probe" pulses to map out the temporal characteristics of the excited state species and how they decay over time. The bottom graph in **Figure 1.8** shows what it means to delay the "probe" in order to record the sample response over time.

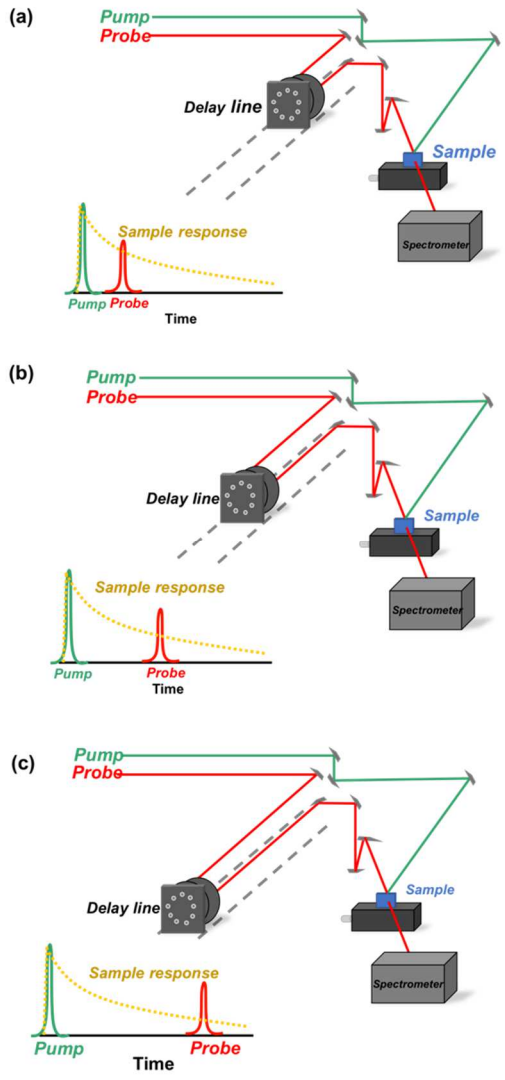

Figure 1.8. A schematic showing the ultra-fast transient absorption pump-probe technique. The sequence of schematic (a-c) illustrates how the delay line can be used to acquire the sample response of excited species over time.

1.5.3. Photoconductive Atomic Force Microscopy

Figure 1.9a shows the photoconductive atomic force microscope (pc-AFM) set-up. The set-up consists of a 300 W Xenon light source that passes through an inverted optical microscope which is used to focus the incident light onto the transparent side of an OSC. The AFM itself is operated in contact mode such that a conductive tip can simultaneously provide nanoscale morphology and photocurrent image of a film. In contact mode operation, the tip scans the

sample while being in close contact with the surface such that the force on the tip is repulsive. The force that is required for operation in contact mode is set by pushing the cantilever against a sample surface with a piezo electric material. In contact mode AFM, the cantilever deflection is measured and adjusted to a desired value by a DC feedback amplifier that can apply a voltage to the piezo to raise or lower the sample relative to cantilever. In a pc-AFM set-up, the conductive tip acts like the top electrode such that while scanning the active layer of the device, you are essentially creating a "nano-scale solar cell device." **Figure 1.9**b and **Figure 1.9** shows the way this technique works. As we know, a BHJ OSC blend really comprises of small phase separated donor or acceptor regions. What this means is that when we zoom into a specific region in the blend, we really have separate donor- or acceptor-rich regions which are not visible by naked eye or in most cases, even optical microscopes. When we shine light on the transparent OSC bottom contact, since the conductive tip acts as the top electrode, the tip collects holes from where there are donor phases present and electrons from where there are acceptor phases present. In such a way, from the magnitude of the photocurrent recorded, we can distinguish between the hole and electron containing regions (i.e. the donor or acceptor regions) in a BHJ blend film.

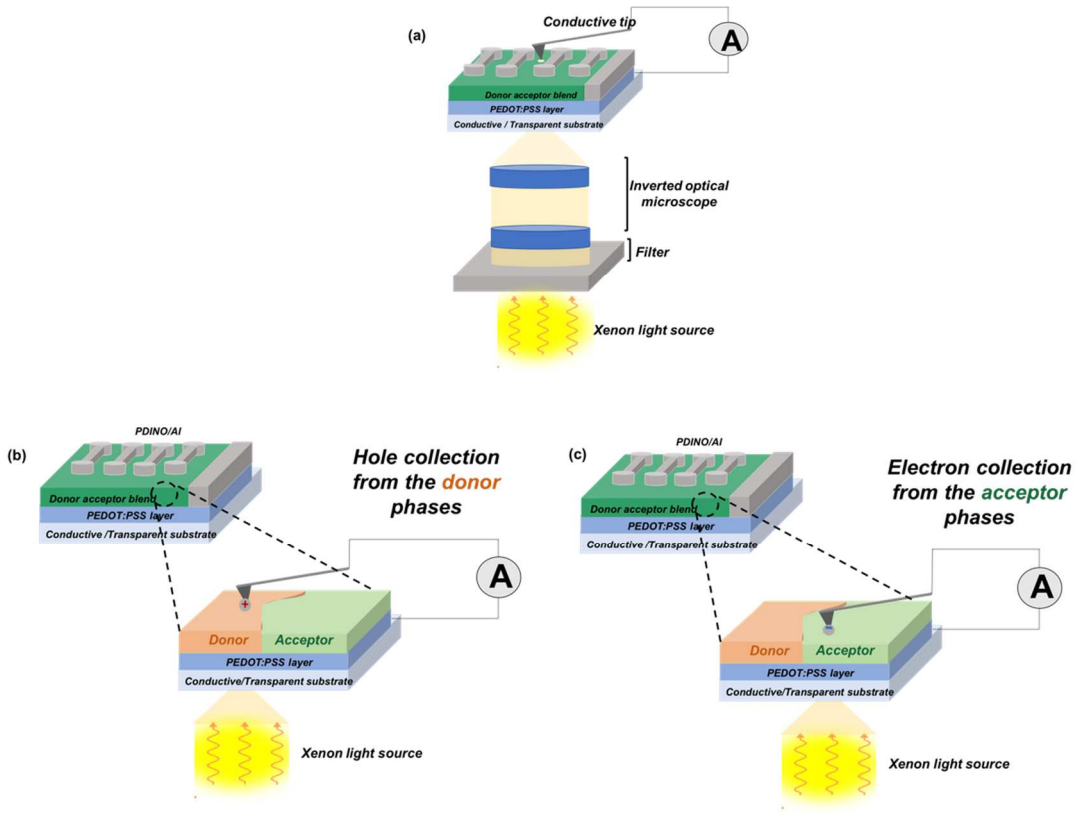

Figure 1.9. (a) The photoconductive atomic force microscope (pc-AFM) set-up. (b) hole collection from the donor phase and (c) electron collection from the acceptor phase.

Figure 1.10 shows an example for the simultaneous mapping of the topography and the hole and electron photocurrent images of a BHJ blend. It can be seen that when the light source is turned off, the features that are seen due to photocurrent generation are absent. Interestingly in this blend system, we can correlate the round features in the topography image to the regions of low hole photocurrents and high electron photocurrents suggesting that the rounded features correspond to acceptor (electron-rich) phases.

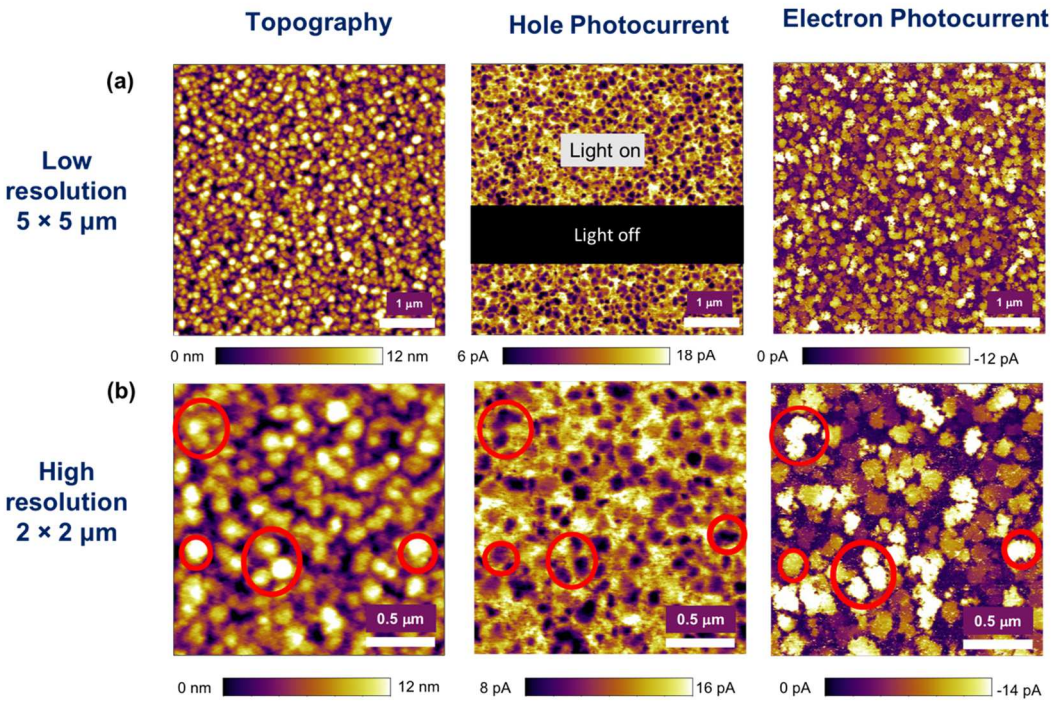

Figure 1.10. (a) 5 × 5 µm and (b) 2 × 2 µm sized images of topography and the corresponding hole and electron photocurrents. Red circles show regions corresponding to the round features which seem to be coming from the acceptor phase.

1.5.4. The Kelvin Probe Technique for Measuring the Work function

Figure 1.11a shows a schematic of the kelvin probe (KP) technique used to measure the work function or the fermi energy at the surface of semiconductor samples. The technique is a capacitive, non-contact measurement that consists of a steel tip of 2 mm diameter and a sample stage with a grounding probe. **Figure 1.11**b shows a complete schematic of how the kelvin probe setup works. The left most schematic depicts the energy levels of the tip and sample surface before a measurement when they are separated by a certain distance (d) and electrically disconnected. In such a case, the vacuum levels are aligned but the fermi energy levels of the tip and sample are different. The middle schematic shows what happens when you electrically connect the tip and the sample and bring the tip closer to the sample. In such

a case, we can expect the fermi levels of the tip and the sample to align through electron current flow and the system to reach an equilibrium state. The tip and the sample surface will now be charged and an apparent contact potential difference (V_{CPD}) will be formed. In this case, the fermi levels of the tip and sample are aligned but the vacuum levels are no longer aligned, and as a result, a V_{CPD} between the tip and the sample will form. The right most schematic now shows how the work function values are recorded. In this case, the KP applies a backing potential that has a magnitude of the V_{CPD} in order to eliminate the surface charges upon applying an external bias. The amount of applied external bias that nullifies the electrical force due to the V_{CPD} is equal to the work function difference between the tip and the sample. The work function of the tip is calibrated using a freshly cleaved highly ordered pyrolytic graphite (HOPG) sample and the work function of the sample can be found from adding the work function of tip to the V_{CPD}.

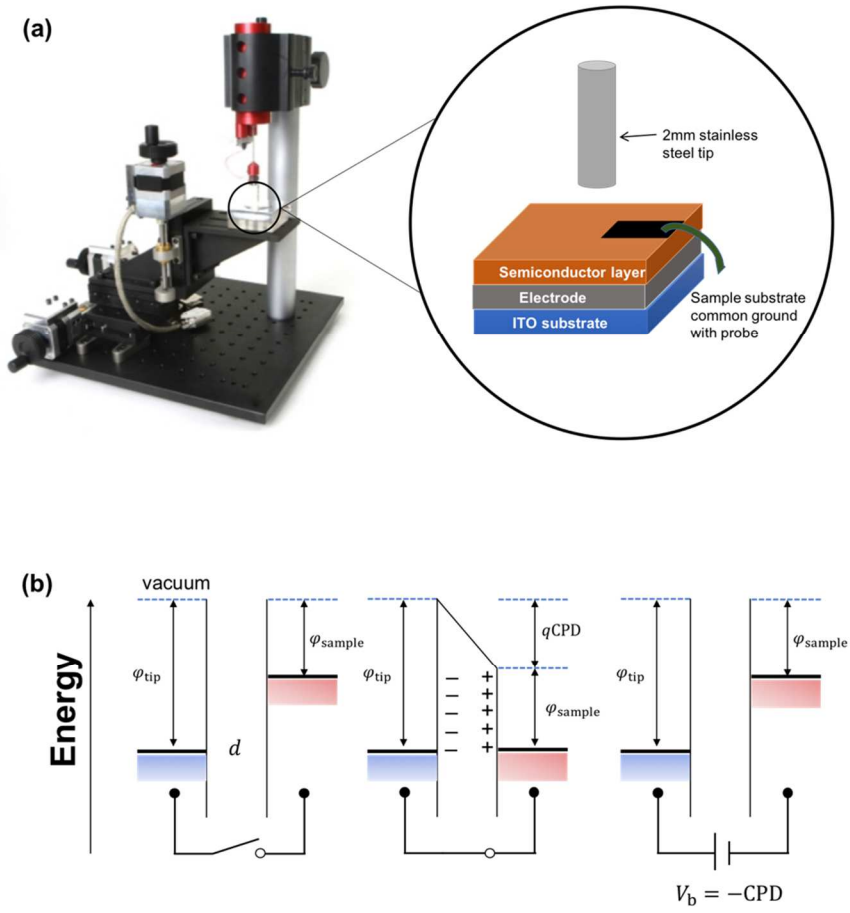

Figure 1.11. (a) A schematic of the Kelvin Probe set-up and (b) working principles.

1.6 Summary of Chapters

Chapter 2

Even though significant breakthroughs with over 17% power conversion efficiencies (*PCE*s) in polymer:non-fullerene acceptor (NFA) bulk heterojunction organic solar cells (OSCs) have been achieved, not many studies have focused on acquiring a comprehensive understanding of the underlying mechanisms governing these systems. This is because it can be challenging to delineate device photophysics in polymer:NFA blends comprehensively, and even more

complicated to trace the origins of the differences in device photophysics to the subtle differences in energetics and morphology. Here, a systematic study of a series of polymer:NFA blends was conducted to unify and correlate the cumulative effects of i) voltage losses ii) charge generation efficiencies, iii) non-geminate recombination and extraction dynamics, and iv) nuanced morphological differences with device performances. Most importantly, a deconvolution of the major loss processes in polymer:NFA blends and their connections to the complex BHJ morphology and energetics were established. An extension to advanced morphological techniques, such as solid-state NMR (for atomic level insights on the local ordering and donor:acceptor π-π interactions) and resonant soft x-ray scattering (for donor and acceptor interfacial area and domain spacings), provided detailed insights on how efficient charge generation, transport, and extraction processes can outweigh increased voltage losses to yield high *PCE*s.

Chapter 3

The highly efficient single-junction bulk-heterojunction (BHJ) PM6:Y6 system can achieve high open circuit voltages (V_{OC}) while maintaining exceptional fill-factor (*FF*) and short-circuit current (J_{SC}) values. With a low energetic offset, the blend system was found to exhibit radiative and non-radiative recombination losses that are among the lower reported values in the literature. Recombination and extraction dynamic studies revealed that the device shows moderate non-geminate recombination coupled with exceptional extraction throughout the relevant operating conditions. Several surface and bulk characterization techniques were employed to understand the degree of mixing, phase separation, long-range ordering, as well as donor:acceptor (D:A) inter- and intramolecular interactions at an atomic-level resolution.

This was achieved using photo-conductive atomic force microscopy (pc-AFM), grazing incidence wide angle x-ray scattering (GIWAXS), and solid state ^{19}F Magic-Angle Spinning (MAS) NMR spectroscopy. The synergy of multifaceted characterization and device physics was used to uncover key insights, for the first time, on the structure-property relationships of this high performing BHJ blend. Complementary morphological and structural information obtained from these techniques revealed that the high performance of over 15% efficiency in this blend can be correlated to a beneficial morphology that allows high J_{SC} and *FF* to be retained despite the low energetic offset.

Chapter 4

Some fundamental questions in the organic solar cell (OSC) community are related to the role of bulk and interfacial morphology on key processes such as charge generation, recombination, and extraction that dictate power conversion efficiencies (PCEs). The challenges with answering these questions arise due to the difficulty in accurately controlling, as well as comprehensively characterizing the morphology in bulk-heterojunction (BHJ) OSC blends. In this work, varying the molecular weight fractions of the donor polymer was used as a tool to exert control over the interfacial and bulk morphology in high performing PM6:Y6 OSCs. A drop in PCEs from ~15% to ~5% was observed when the concentration of low molecular weight fractions (LMWFs) of the PM6 polymer was increased from 1% to 52%. The drop in PCEs was found to be due to the lowering of J_{SC} and *FF* values as a result of compromised charge generation efficiencies, increased bulk trap densities, reduced charge transport, and inefficient charge extraction. The origins for the high device performance in the 1% LMWF blend could be rationalized by the favorable bulk and interfacial morphological

features, resolved from four techniques at sub-nanometer to sub-micrometer length scales. First, the long-range ordering and optimal phase separating of the donor:acceptor (D:A) regions led to superior charge transport and extraction. Second, the closer D:A interactions, smaller D and A domains, and increased D:A interfacial area facilitated ultrafast electron and hole transfer at the D:A interface.

Chapter 5

Characterizing the density of states (DOS) width accurately is critical in understanding the charge-transport properties of organic semiconducting materials as broader DOS distributions lead to an inferior transport. From a morphological standpoint, the relative densities of ordered and disordered regions are known to affect charge transport properties in films; however, a comparison between molecular structures showing quantifiable ordered and disordered regions at an atomic-level and its impact on DOS widths and charge transport properties has yet to be made. In this work, for the first time, the DOS distribution widths of two model conjugated polymer systems are characterized using three different techniques. A quantitative correlation between energetic disorder from band bending measurements and charge transport is established, providing direct experimental evidence that charge carrier mobility in disordered materials is compromised due to the relaxation of carriers into the tail states of the DOS. Distinction and quantification of ordered and disordered regions of thin films at an atomic-level was achieved using solid-state NMR spectroscopy. An ability to compare solid-state films morphologies of organic semiconducting polymers to energetic disorder, and in turn charge transport, can provide useful guidelines for applications of organic conjugated polymers in pertinent devices.

Chapter 2

Unifying Charge Generation, Recombination, and Extraction in Low-offset Non-fullerene Acceptor Organic Solar Cells

2.1. Introduction

A significant leap in record-breaking power conversion efficiencies (*PCE*s) of single-junction bulk-heterojunction (BHJ) organic solar cells (OSCs) to over 17%[11] has recently been achieved. This can be credited to the rapid developments of new non-fullerene acceptors (NFAs) paired with suitable high performing polymer donors. While these breakthroughs are encouraging, it remains crucial to attain a deeper and more comprehensive understanding of the underlying mechanisms governing these novel and high performing polymer:NFA systems. Several recent studies have attributed the high performances of NFA-based solar cells to an improvement in the open-circuit voltage (V_{OC}) without significantly diminishing the charge generation efficiency.[12–14] Particularly, in polymer:NFA systems, high V_{OC} values have been achieved with efficient charge generation regardless of a very small energetic driving force for exciton dissociation ($\Delta G_{S1\text{-}CT}$), where $\Delta G_{S1\text{-}CT}$ is defined as the energy difference between the charge-transfer (CT) state and singlet-exciton (S_1) state of the lower bandgap component in the blend. While blend systems with low energetic offsets are sought for achieving high V_{OC} values, such blends commonly suffer from modest short-circuit current (J_{SC}) and fill-factor (*FF*) values, which can limit the *PCE*.[15–18] This compromise between V_{OC}, J_{SC}, and *FF* has been observed in numerous recently reported systems, and was more

commonly found in polymer:fullerene blends.[15–19] However, of late, some reported high performing polymer:NFA blends have managed to optimally balance this tradeoff and achieve *PCEs* ranging from 10-17%.[8,9,11,15,20–22] Therefore, attaining a deeper understanding of the charge generation dynamics in conjunction with a study of the voltage losses in blends with low energetic offsets has become crucial. Besides an understanding of the aforementioned processes, non-geminate recombination and charge extraction dynamics are the other important parameters needed to understand the delicate interplay between V_{OC}, *FF*, and J_{SC}. Non-geminate recombination has been shown to be the dominant loss process in most high performing non-fullerene acceptor BHJ OSCs.[14,23–27] As a consequence, reducing non-geminate recombination would give rise to an overall improved device performance. Non-geminate recombination occurs when free electrons and holes originating from different excitons meet and recombine. In competition with the non-geminate recombination process is charge extraction. It has been shown that if the charge extraction time (τ_{ex}) is faster than or comparable to the recombination time (τ_{rec}), then charge recombination can be curtailed, and *FF* and J_{SC} values can be improved.[16,28,29] Concomitant with all these processes is the morphology of the BHJ blend that warrants an in-depth investigation due to its direct impact on the charge generation, recombination, and extraction processes.[16,20,28] The morphological insights obtained in most studies in the literature are often restricted to atomic force microscopy (AFM) or grazing incidence wide angle x-ray scattering (GIWAXS) analyses. However these techniques provide limited information on more nuanced structural features, such as how donor (D) and acceptor (A) molecules pack in polymer:NFA BHJ blends. Here, morphological investigations that include solid-state NMR (for insights on D:A interactions and local atomic-level ordering)[30] and resonant-soft x-ray scattering (RSoXs) (for the D:A

interfacial area and domain spacings)[31] provide a more detailed picture of the connections between device photophysics and morphology.

In this work, we begin by systematically varying the S_1-CT offsets for a series of polymer:NFA blend systems by fluorinating the IOTIC-based NFAs. For the first time, the cumulative effect is investigated of systematically tuning the S_1-CT offset for a series of polymer:NFA systems on the i) voltage losses, ii) charge generation efficiencies, iii) non-geminate recombination and extraction dynamics, and iv) D:A interfacial area, short-range atomic-level (nm to sub-nm) ordering and interactions. We posit that low energetic offset polymer:NFA systems with low voltage losses are key in attaining high *PCE*s – but not without a caveat. The drawbacks brought forth by low energetic offset systems can only be circumvented with a comprehensive understanding of the charge generation, recombination, and extraction dynamics, as well as a further deconvolution of the role of the nuanced differences in the BHJ morphology in these specific processes. Hence, from this systematic work, we uncover the genuine effects of changing the energetic offsets on the tradeoffs between V_{OC}, *FF*, and J_{SC} of the studied blend systems.

2.2. Results and Discussions

2.2.1. Chemical Structures and Energy Levels of Donor and Acceptors

Figure 2.1 shows the energy levels and chemical structures of the polymer donor and NFAs used in this study. The PTB7-Th donor polymer was used in conjunction with a series of IOTIC-based acceptors. The consecutive additions of two fluorine atoms on the IOTIC-based acceptors (2- and 4- fluorine atoms) causes the highest occupied molecular orbital (HOMO) of the acceptors to be deeper leading to larger energetic offsets. For a consistent comparison of the three blends, conventional devices with a PEDOT:PSS layer as the bottom

contact and evaporated barium capped with aluminum electrodes as the top contact were used.

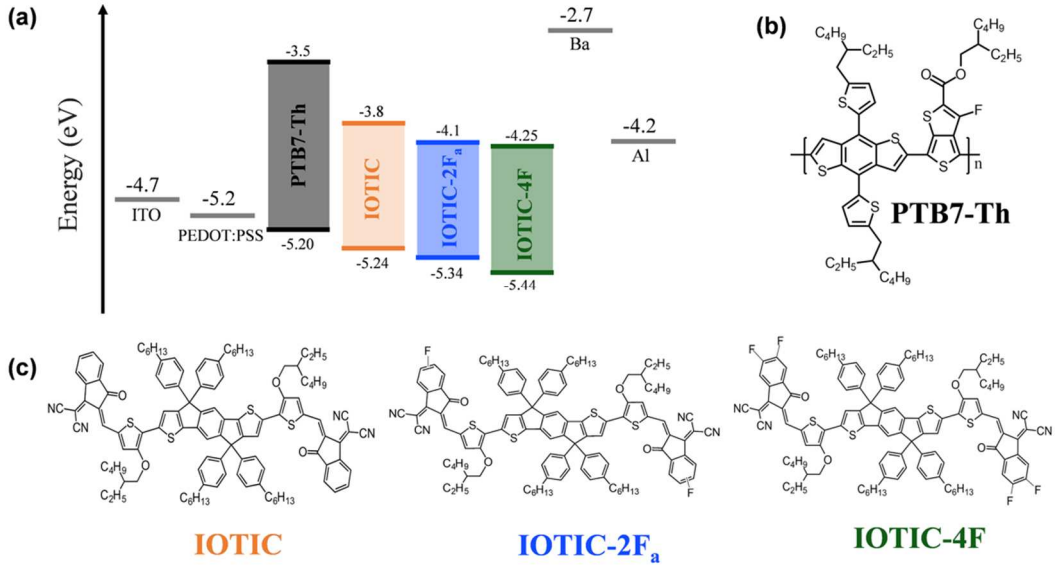

Figure 2.1. (a) Energy levels of materials used obtained by cyclic voltammetry and chemical structures of (b) PTB7-Th donor and (c) IOTIC, IOTIC-2F$_a$, and IOTIC-4F NFAs.

2.2.2. Photovoltaic Performance

Figure 2.2a shows the *J-V* curves at 1 sun illumination (100 mWcm^{-2}, AM 1.5) of the three optimized blend systems. The average *PCE* values from 30 devices for each blend system are included in Table A1. The three representative *J-V* curves show that with a decrease in the energetic offsets (i.e., from PTB7-Th:IOTIC-4F to PTB7-Th:IOTIC), there is an increase in the V_{OC} values from 0.72 V to 0.88 V and a concomitant decrease in the J_{SC} values from 20.5 mA/cm^2 to 10.7 mA/cm^2 of the devices. Decent *FF* values above 60% are retained in all three systems, with the PTB7-Th:IOTIC-4F blend system exhibiting the highest *FF* of 68%. Integrated J_{SC} values from external quantum efficiency (EQE) spectra of all three blend systems are within 4% of the average J_{SC} values measured via the *J-V* characteristics of the devices at 1 sun illumination (Table A1). A combined simulation and experimental approach[32] was used to obtain the internal quantum efficiencies (IQEs) for all three blend

systems. The IQE is defined as the ratio of the number of charge carriers extracted from the device to the number of photons absorbed in the active layer. Therefore, IQE measurements provide useful information about the electrical properties of a device that EQE measurements alone cannot.[32] Here, differences in the IQEs of the three blends suggest decreased charge generation efficiency and extraction upon going from the PTB7-Th:IOTIC-4F to the PTB7-Th:IOTIC blend system (Figure 2.2b).

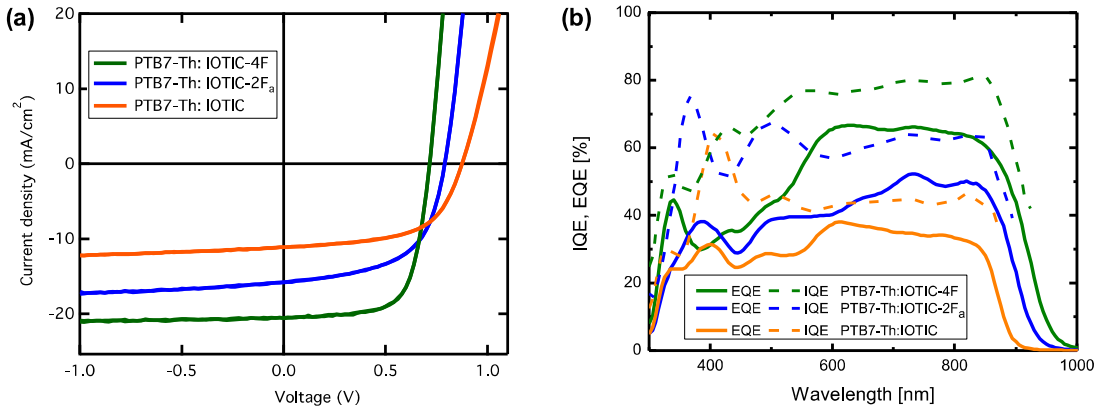

Figure 2.2. (a) *J-V* curves at 1 sun illumination (100 mWcm^{-2}, AM 1.5) and (b) EQE and IQE spectra of the three blend films.

To ensure that all three blend systems were pertinent for a systematic comparative study, the solar cells were first tested under varying light intensities (I) to qualitatively determine the dominant type of non-geminate recombination mechanism by measuring the light intensity dependence of the V_{OC} (Figure A1).[33,34] The light intensities were decreased by neutral density filters and the V_{OC} vs. ln(I) plots exhibited a slope of $s \approx 1\ kT/q$ for all three blends, where k is the Boltzmann constant, T is the absolute temperature, and q is the elementary charge. To ensure that the effect of leakage current did not contribute to (increase) the slopes of the V_{OC} vs. ln(I) plots[35], the dark *J-V* curves at different light intensities were plotted and analyzed (Figure A2). The V_{OC} vs. ln(I) plots were further measured at temperatures ranging from 200 K to 300 K. Remarkably, all three blend systems showed $s \approx 1\ kT/q$ at all temperatures in the

range of 200-300 K, suggesting dominant bimolecular recombination mechanism processes (Figure A3). Evaluating the temperature dependence behavior of V_{OC} vs. ln(I) plots is often neglected in the literature, however, its importance has been highlighted by Koster *et al*.[33] for confirming the dominant recombination loss processes. Such a confirmation is especially important for a comparison of the three blend systems chosen for this systematic study, as variations in the dominant recombination mechanisms; for example, the presence of trap assisted recombination could lead to an inconsistent comparison of the three blend systems.

2.2.3. Quantifying Voltage Losses

To quantify the voltage losses that limit the V_{OC} in the three blends, we evaluate the energy loss, E_{loss} as:

$$E_{loss} = S_1 - qV_{OC}, \quad (1)$$

where, S_1 is the singlet exciton energy of the lower bandgap component in the blend and q is the elementary charge. For a precise measurement of the singlet exciton energy of the lower bandgap components in the blends, we use the optical method described by Vandewal *et al.*[36] (Figure A4). The S_1 states of the three blend systems are also shown in the energy loss diagram depicted in **Figure 2.3**. To obtain the S_1, the intersection points of the emission spectra (from electroluminescence measurements, EL) and absorption spectra (from photovoltaic EQE measurements, EQE_{PV}) of the lower bandgap components in the blends (NFAs: IOTIC, IOTIC-2F_a, IOTIC-4F) were determined. From this analysis, it was found that upon fluorination, the IOTIC-based NFAs show a decrease in the S_1 from 1.44 eV (IOTIC) to 1.36 eV (IOTIC-2F_a) to 1.34 eV (IOTIC-4F).

Losses limiting the V_{OC} can be further divided into two parts: losses due to charge transfer as defined by the difference between the S_1 and the energy of the CT state (E_{CT}), and losses

due to recombination and energetic disorder defined by the differences in E_{CT} and V_{OC}. Commonly, to identify the CT state in a blend, the EQE_{PV} is measured, and the CT state is identified as the absorption feature visible at energies lower than the bandgap of either the donor or the acceptor. The E_{CT} is then determined by fitting an expression derived from Marcus theory (Equation S1) to the tail of the blend EQE_{PV} spectrum.[37] However, the CT state is not always pronounced in the low-energy tail of the EQE_{PV} spectra, especially in blends where the energetic offsets between the donor and acceptor are low (i.e., low HOMO-HOMO or LUMO-LUMO offsets)[15,18,21,38] , and so it can be difficult to distinguish the energy of the CT state from the donor or acceptor singlet state. It is possible, however, to significantly reduce the degrees of freedom in the fitting by 1) performing a simultaneous fit to both the EQE_{PV} (Equation S1) and the EL (Equation S2) spectra[13,19,20,39–41] using equations derived from Marcus theory, as was first demonstrated by Vandewal *et al*.[37] and 2) calculating the EQE_{PV} down to values on the order of 10^{-7} using sensitively measured EL data and the reciprocity relationship shown in Equation S3.[10] In all three blend systems, the added sensitivity of up to four orders of magnitude with the calculated EQE_{PV} data (Equation S3) from the reciprocity relationship allows for a better deconvolution of the Gaussian-shaped CT absorption which was previously absent from the sharp absorption tail of the measured EQE_{PV} data (Figure A5). From such an analysis, the E_{CT} values in the three blend films were estimated to be 1.390 eV, 1.295 eV, and 1.260 eV for PTB7-Th:IOTIC, PTB7-Th:IOTIC-$2F_a$, and PTB7-Th:IOTIC-4F, respectively. It is worth noting that despite the reduction in degrees of freedom in the Marcus fitting, the E_{CT} values obtained here serve only as an estimate, due to the significant uncertainty that arises in separating the CT state emission and the singlet exciton emission in low energetic offset systems. Therefore, we report the CT energy in this

blend – as has been done in some recently reported papers[19,20,41,42]– with a caveat that the obtained E_{CT} value is an estimate only.

Nevertheless, due to the uncertainty in the absolute values of the obtained CT energies, we adopt the temperature-dependent V_{OC} method as a second technique to further corroborate the trends of the measured E_{CT} values at room temperature of the three blend systems (Figure A6). It has been shown that the extrapolation of temperature-dependent V_{OC} conducted at different light intensities to 0 K corresponds to the E_{CT} value at 0 K.[37] Since the E_{CT} values exhibit some temperature dependence, the values at 0 K will be lower than the values measured at room temperature.[37,43,44] The similar variation in the E_{CT} values between the three blend systems of ~130 meV at both room temperature and 0 K can be used to verify – if not the absolute values – at least the trends in the E_{CT} values measured at room temperature (Table S2).[44] From such an analysis, a rough estimate of the energetic offsets ($\Delta G_{S1\text{-}CT}$) in these systems can now be determined. The PTB7-Th:IOTIC, PTB7-Th:IOTIC-2F_a, and PTB7-Th:IOTIC-4F blends exhibit energetic offsets of approximately ~0.050 eV, ~0.065 eV, and ~0.080 eV, respectively.

Next, losses due to recombination, which can be divided into radiative (ΔV_{rad}) and non-radiative losses ($\Delta V_{non\text{-}rad}$) are quantified (Equation S4). As derived from a detailed balance analysis, about 0.200-0.250 eV of radiative recombination is needed to establish thermodynamic equilibrium.[45] On the other hand, it has been shown that a large part of recombination losses occur non-radiatively, spanning a range of 0.210-0.550 eV.[46,47] In recent years, there have been numerous reported studies showing correlations between non-radiative recombination losses and carbon-carbon bond vibrations,[46] molecular orientation at the donor-acceptor interface,[39,48] energetic driving force,[13,15,19] and E_{CT} values.[46]

From the equations described in the SI (Section 5), losses due to radiative recombination in the PTB7-Th:IOTIC, PTB7-Th:IOTIC-2F_a, and PTB7-Th:IOTIC-4F blend systems are calculated to be 0.227 ± 0.003 eV, 0.212 ± 0.003 eV, and 0.203 ± 0.003 eV, respectively. Inserting the experimentally measured EQE_{EL} (Figure A7) into Equation S6, the losses due to non-radiative recombination in the PTB7-Th:IOTIC, PTB7-Th:IOTIC-2F_a, and PTB7-Th:IOTIC-4F blend systems are determined to be 0.284 ± 0.003 eV, 0.300 ± 0.003 eV, and 0.330 ± 0.003 eV, respectively. The measured non-radiative recombination values are further confirmed by the calculated non-radiative recombination, using the procedures described in the SI. The breakdown of the voltage losses from S_1 to V_{OC} comprising of losses from charge transfer and charge recombination in the three blend systems are summarized in Table S3 and shown schematically in Figure 3.

In this study, increased non-radiative recombination losses are observed with a concomitant decrease in the radiative recombination losses as the energetic offsets in the blend systems are increased (from PTB7-Th:IOTIC to PTB7-Th:IOTIC-4F). The suppression of non-radiative recombination losses with decreased energetic offset has been observed in several previously reported studies.[13,15,19,46] This observation can be explained by the idea that a decreased overlap of the vibrational wave function of the CT and ground state leads to the suppression of the non-radiative recombination pathway.[46] Additionally, the recent paper by Qian *et al*.[15] suggests that in low energetic offset systems, hybridization of the CT state with the highly emissive S_1 state will increase the radiative ability of the CT state through the intensity borrowing mechanism.[49,50] From the modelling of excitonic and CT states, it was found that if the radiative relaxation channel can be made efficient in this way, the non-radiative voltage losses should decrease.[15] The three blend systems reported here provide a

suitable platform, by systematically varying the S_1-CT offset, to experimentally measure such a tradeoff between the radiative and non-radiative recombination losses. To further corroborate that the S_1 states of the acceptors are in fact relatively more emissive than the blends, we measured the EQE_{EL} of the acceptor only devices, (Figure A8), confirming the consistently lower non-radiative recombination values in the acceptor only devices by approximately 0.03 eV [IOTIC ($\Delta V_{non\text{-}rad}$) = 0.250 ± 0.003 eV; IOTIC-2F$_a$ ($\Delta V_{non\text{-}rad}$) = 0.270 ± 0.003 eV; IOTIC-4F ($\Delta V_{non\text{-}rad}$) = 0.300 ± 0.003 eV], compared to that of the blends.

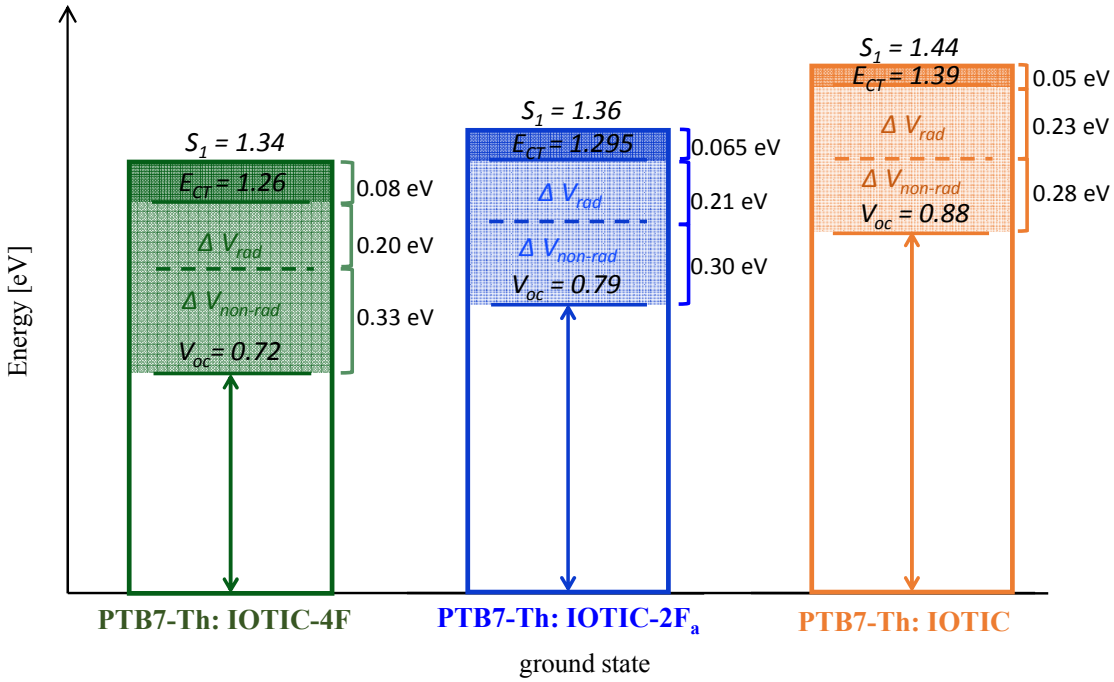

Figure 2.3. Energy loss diagrams of the three studied blend systems from S_1 to V_{OC}.

Moreover, to rule out differences in energetic disorder between the blends as a major contributor to the voltage losses, the density of states (DOS) spectra of the three blends were measured by using Energy-Resolved Electrochemical Impedance Spectroscopy (ER-EIS).[51–53] (Details about the ER-EIS technique and measurements are described in the Appendix A). Figure A9 shows the DOS spectra of the three studied blend systems obtained from ER-EIS,

which exhibit no distinct differences suggesting that the energetic disorder in the three blend systems are comparable. Additionally, as a further confirmation of the similarities in the exponential tail states disorder in the three blend systems, the Urbach energies (E_U) from the tail states of highly sensitive EQE spectra of $E_U \approx 25$ meV were determined (details in the Appendix A, Figure A10). An Urbach energy approaching a thermal energy of $E_U \approx kT$ may suggest that the contribution to the voltage losses in the systems from energetic disorder is minimal.[17,44,53–55] It is worth noting that the Urbach energy measurements may lead to some uncertainty in disordered materials[56] and cannot be directly comparable to the ER-EIS method, which gives disorder contributions coming from the HOMO and LUMO DOS distributions separately. Nevertheless, from these analyses, the possible effects of differences in the DOS distributions of the three studied blend systems on the charge generation, recombination, and extraction dynamics can be excluded.

2.2.4. Probing the Charge Generation Dynamics

To investigate the effect of decreasing energetic offsets on the charge generation dynamics of the three blend systems, ultrafast (100 fs – 2 ns) transient absorption (TA) spectroscopy were performed. Initially, we conducted TA in both the visible (500 – 950 nm) and NIR (1050-1300 nm) spectral regions on films of the NFA blended with a non-interacting polymer, polystyrene (PS), to determine the spectral features and exciton lifetimes associated with the acceptor materials. These blend films were fabricated by using an identical polymer weight fraction and deposition conditions to the optimized PTB7-Th:NFA blend in an attempt to best replicate the morphological properties of the active layer used in the actual device.[15] All IOTIC derivatives exhibit a ground state bleach (GSB) feature that closely matches the absorption spectra of the material, with two distinct vibronic peaks visible (Figure A11 a-f).

Additionally, the photo-induced absorption (PIA) band of the first singlet excited state is centered at around 1200 nm in all of the derivatives (Figures A12 a-f). The lifetime of the excited state is relatively short, owing to the narrow band gaps of the acceptors and the effect of the energy gap law on the rate of the non-radiative transitions.[57] For IOTIC, the half-life ($t_{1/2}$) of the singlet excited state is 45 ps, for IOTIC-2F$_a$, $t_{1/2}$ = 30 ps and for IOTIC-4F, $t_{1/2}$ = 35 ps (Figure A11 a-f).

Next, we examine the visible region TA of the PTB7-Th:NFA blends by selectively exciting the NFA component of these films below the bandgap of PTB7-Th to probe solely the hole transfer process. In the PTB7-Th:IOTIC-4F film, excited at 925 nm with a fluence of 0.51 μJ cm^{-2} (Figure A13a,b), we initially observe only the IOTIC-4F GSB at 300 – 400 fs. After 1 ps, the IOTIC-4F GSB begins to decrease in intensity rapidly and a new positive feature spanning 600 – 750 nm forms. As the spectral position and vibronic features closely match those of PTB7-Th, it is assigned to the GSB of the polymer, consistent with the bleaching of the PTB7-Th ground state transition by the hole transfer process. Interestingly, as the hole transfer progresses, the IOTIC-4F GSB continues to fall rapidly, and there is only a muted growth of the PTB7-Th GSB. This could be caused by one of two things: rapid recombination leading to excited state population loss, or a new PIA band forming under the GSB regions that has the effect of decreasing the apparent GSB intensity. As the blend demonstrates good IQE, we can rule out the former, as this would result in significantly reduced levels of photocurrent generation and a consequently low IQE. Therefore, we assign this PIA underneath the GSB region as belonging to the electron located on IOTIC-4F, as the PIA of the hole on PTB7-Th has widely been reported to lie at around 1150 nm.[15,58–60] Additionally, we note the presence of electro-absorption (EA) features at the band edge of the

donor and acceptor, consistent with the separation of charges in OPV blends.[61] Turning to the PTB7-Th:IOTIC-2F$_a$ blend (Figure A13c,d), excited at 900 nm with a fluence of 0.87 μJ cm^{-2}, we observe very similar photophysics to the PTB7-Th:IOTIC-4F blend with a relatively slow hole transfer taking place. However, the PTB7-Th:IOTIC blend, excited at 860 nm with a fluence of 0.50 μJ cm^{-2} (Figure A13e,f), exhibits markedly different behavior. In this case, there is no obvious formation of the PTB7-Th GSB until timescales of 300 – 400 ps, as can be seen in the normalized TA spectra (Figure A14a). By this point, the GSB features have a much weaker intensity than in the other two blends, implying the presence of a much smaller population of holes due to a higher proportion of exciton decay prior to charge transfer.

To gain a better understanding of the hole transfer timescales in the blends, the TA spectra were deconvoluted using a Genetic Algorithm (GA). In all blends, we observe an initial "pre-charge transfer" spectral species, consisting of the NFA GSB only, and a final "post-charge transfer" species, comprised of both the donor and acceptor GSBs and EA features. The IOTIC-4F and IOTIC-2F$_a$ blends can be readily deconvoluted into these two distinct species (Figure A14b,c and S14d,e), with their relative contributions to the overall TA spectra at each time point providing insight into the kinetics of the hole transfer process. Comparing these fitted kinetics, we can immediately see that this process is faster for the PTB7-Th:IOTIC-4F blend, with hole transfer completed by 50 ps, compared to 160 ps for the PTB7-Th:IOTIC-2F$_a$ blend (**Figure 2.4**a). This can be readily explained by the slightly larger driving energy for the hole transfer from the NFA to the donor in this blend. However, it was not possible to satisfactorily deconvolute the TA spectra of the PTB7-Th:IOTIC blend, likely due to the significant spectral overlap of the donor and acceptor GSBs. Nevertheless, we expect the hole transfer in this blend to be the slowest of the three NFA systems as it possesses the smallest

energy offset, consistent with the trend observed between IOTIC-4F and IOTIC-2F_a and the significantly lower remaining GSB intensity.

To confirm our hypothesis that there are significantly fewer charges present in the PTB7-Th:IOTIC blend after selective NFA excitation, we turn to the NIR region where we can directly observe the PIA of the holes on PTB7-Th. All films were excited with a pump wavelength of 800 nm for selective NFA excitation and care was taken to use an extremely low fluence to avoid any non-linear recombination processes (PTB7-Th:IOTIC-4F = 0.13 μJ cm^{-2}, PTB7-Th:IOTIC-2F_a = 0.18 μJ cm^{-2} and PTB7-Th:IOTIC = 0.17 μJ cm^{-2}) (Figure A15a-f). For all blends, the initial density of excited states (n_0) created on the NFA were roughly equal, ~3–4x10^{16} cm^{-3}, a value which is highly comparable to the charge carrier densities in these devices operating under 1-sun illumination, as determined via impedance spectroscopy in the following section. Consequently, these measurements are representative of realistic device operating conditions. In all blends, the singlet PIA at 1200 nm decreases in intensity over similar timescales to the hole transfer process previously observed, leaving behind a long-lived PIA at 1175 nm that belongs to the holes on PTB7-Th. By comparing the relative intensities of the hole PIA at 1.5 – 1.8 ns, a timescale where all hole transfer and exciton decay is completed, with only the PIA of the PTB7-Th holes remaining, we can gain insights into the relative charge generation efficiencies of the blends (**Figure 2.4**b). We note that the strongest PIA, and therefore the most holes, are found in the PTB7-Th:IOTIC-4F blend, followed by PTB7-Th:IOTIC-2F_a and finally PTB7-Th:IOTIC. This can be rationalized by considering the interplay between exciton decay and hole transfer in the blends: as hole transfer slows with decreasing driving force, it begins to compete with exciton decay. Thus, these processes are finely balanced in low offset NFA OPVs, where even small changes to the

rate of one can result in a drastic change in the overall charge generation efficiency.

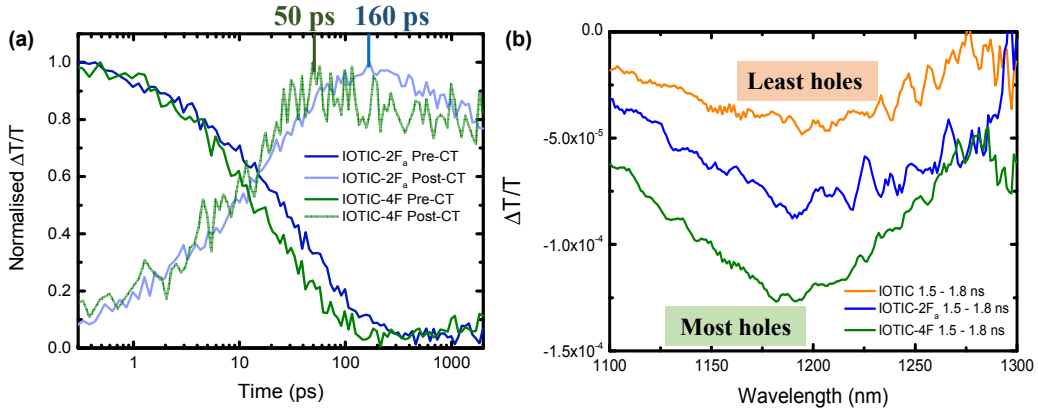

Figure 2.4. (a) Comparison of the hole transfer kinetics for PTB7-Th:IOTIC-2F$_a$ and PTB7-Th:IOTIC-4F blends. (b) PIA of the remaining holes on PTB7-Th after hole transfer and exciton decay is completed to gain insight into the relative charge generation efficiencies of the three blend systems.

Additionally, we have also investigated the photophysics of the blend when exciting primarily PTB7-Th with a pump wavelength of 600 nm, a wavelength where there is relatively little absorption by the IOTIC derivatives, but still a quite strong absorption by PTB7-Th. In the visible region, TA of both the PTB7-Th:IOTIC-4F and PTB7-Th:IOTIC-2F$_a$ blends (Figure A16a-d), the donor and acceptor GSBs are present from the earliest times of 100 fs. This is likely due to some unavoidable direct excitation of the NFA, though the intensity of the NFA GSB suggests other ultrafast processes that lead to bleaching of the NFA ground state have already occurred. However, it is interesting that the PTB7-Th GSB swiftly falls over the first 5 ps (a timescale largely free from hole transfer), whilst the NFA GSB grows in. Following this, the NFA GSB drops rapidly from 5 ps onwards, whilst there is a slight growth of the PTB7-Th GSB, consistent with the previously observed timescales of hole transfer. We expect the NFA GSB to drop rapidly when NFA molecules become anionic, due to the presence of the electron PIA under its GSB, as observed when the NFA is selectively excited.

However, the growth of this feature over timescales where one might expect electron transfer to occur is a surprise. It suggests that rather than solely electron transfer occurring from PTB7-Th to the NFA, a significant amount of energy transfer is occurring too. This population transfer from donor to acceptor would explain the rise of the NFA GSB and fall of the PTB7-Th GSB on ultrafast timescales. The presence of Förster Resonance Energy Transfer (FRET) is not surprising, given the significant overlap of the PTB7-Th emission spectrum[15] with the NFA high oscillator strength absorption and has previously been observed in other NFA systems.[62] In the IOTIC blend (Figure A16e,f), it appears that a significant amount of FRET also occurs, but due to the relative inefficiency of the hole transfer process, the GSB of both the donor and acceptor continue to fall rapidly after FRET. The presence of FRET in these blends serves to underline the importance of the balance between the NFA exciton decay and hole transfer rates, as the majority of the charge generation appears to proceed through the lower gap NFA, regardless of on which component the exciton was initially generated. Thus, the trend of decreasing J_{SC} with decreasing offset between the devices can at least partly be explained by differences in hole transfer rates, controlled by the small changes in driving energy.

2.2.5. Understanding the Non-Geminate Recombination and Charge Extraction Dynamics

To gain further insights on the timescales of the loss processes of the three blend systems, we measured the non-geminate recombination and extraction dynamics. As a guideline, in any OSC device, the goal is to minimize the charge extraction time, while maximizing the charge carrier lifetime, as this leads to a reduction of non-geminate charge recombination.[16,28,29] To begin this analysis, as a first step, the photocurrent density (J_{ph}) of the devices were calculated:

$$J_{ph} = J_{light} - J_{dark}, \quad (2)$$

where J_{light} is the current density under illumination and J_{dark} is the current density in the dark (Figure A17a). The differences in V_{OC} of the studied blend systems have to be taken into account, which is why the photocurrent density is plotted against the effective voltage (V_0-V_{cor}; where V_0 is the voltage at which $J_{ph} = 0$). Furthermore, the corrected voltage V_{cor} can be obtained by subtracting the voltage losses over the series resistance:

$$V_{cor} = V_{app} - J \cdot R_{series}, \quad (3)$$

where J is the current density, and R_{series} is the series resistance which is assumed to be equal to the saturated differential resistance at forward biases (i.e., $\partial V_{app}/\partial J$ = constant).[20] When comparing the photocurrents J_{ph} of the three blend systems, a clear trend can be observed, where the values for J_{ph} increase with increasing number of fluorine atoms in the NFA. In addition, it is possible to estimate the probability of charge collection (P_C) by the ratio between the saturated photocurrent density $J_{ph,sat}$ and the values for J_{ph} at different biases[63]:

$$P_C = \frac{J_{ph}}{J_{ph,sat}}. \quad (4)$$

As can be seen in Figure A17b, the P_C retains comparatively high values for the PTB7-Th:IOTIC-4F blend, while a steeper reduction of P_C can be observed for the other two NFAs at forward biases. In particular, this observation suggests that the PTB7-Th:IOTIC-4F devices exhibit advantageous charge collection, while the PTB7-Th:IOTIC-2F$_a$ and PTB7-Th:IOTIC devices are both afflicted by inferior charge collection.

As was previously established, all three blend systems exhibited behaviors consistent with $s \approx 1\ kT/q$ at temperatures down to 200 K, indicating dominant bimolecular recombination processes in the three blends. Nevertheless, an advanced recombination analysis is still needed for a quantitative confirmation of the dominant loss processes.[64] This can be done based on a

quantitative analysis that utilizes capacitance spectroscopy.[65–67] The capacitance of the BHJ obtained *via* this measurement technique can be used to determine the charge carrier density (n) and the effective mobility (μ_{eff}) of the studied solar cells under operating conditions (Figure A17c,d).[28,68] The details for the procedures used to determine the charge carrier densities and effective mobilities under operating conditions are described in Appendix A (Figure A18). The measured charge carrier densities for these blend systems are in a range of $n = 10^{16}$ - 10^{17} cm^{-3}, with the PTB7-Th:IOTIC-4F blend exhibiting the highest values ($n = 1.2 \cdot 10^{17}$ cm^{-3}) compared to the PTB7-Th:IOTIC-2F$_a$ ($n = 5.6 \cdot 10^{16}$ cm^{-3}) and PTB7-Th:IOTIC ($n = 5.8 \cdot 10^{16}$ cm^{-3}) blends under open-circuit conditions (Figure A17c). Under reverse bias, the highest carrier density was measured for the PTB7-Th:IOTIC blend ($n = 4.5 \cdot 10^{16}$ cm^{-3}), which is only slightly lower than the values at open-circuit conditions. This observation could be a sign for inefficient charge extraction, as there should be a significant reduction in the carrier density at reverse biases. In contrast, the PTB7-Th:IOTIC-4F blend shows the lowest carrier density at reverse bias ($n = 2.2 \cdot 10^{16}$ cm^{-3}), indicating comparatively good extraction, which was also underscored by its high values for the P_C. Moreover, a clear trend can be seen for the effective mobilities, with the PTB7-Th:IOTIC-4F devices having the highest values ($\mu_{eff} = (2.7 – 6.1) \cdot 10^{-5}$ cm^{2}V^{-1}s^{-1}), followed by the PTB7-Th:IOTIC-2F$_a$ ($\mu_{eff} = (1.4 – 5.1) \cdot 10^{-5}$ cm^{2}V^{-1}s^{-1}), and the PTB7-Th:IOTIC having the smallest effective mobilities ($\mu_{eff} = (0.7 – 5.5) \cdot 10^{-5}$ cm^{2}V^{-1}s^{-1}).

Next, a full quantitative analysis approach for the determination of the non-geminate recombination dynamics was adopted to obtain the bimolecular recombination coefficients (k_{bm}) for the three blend systems (Figure A19; detailed procedure described in Appendix A). From this analysis, it was found that all three blend systems show, across the entire voltage

range, similar k_{bm} values ranging from $(0.18 - 2.20) \cdot 10^{-12}$ cm^3/s. As the bimolecular recombination coefficients between the blends are quite similar, this alone cannot explain the performance differences in the three blend systems. Therefore, the extraction of charge carriers has to also be quantified to obtain a comprehensive understanding of the recombination dynamics in the studied devices. To this end, the effective extraction time (τ_{ex}) was calculated. For this analysis, it was assumed that a charge carrier traverses, on average, half of the active layer thickness, until it reaches one of the electrodes and that the active layer can be treated as an effective medium.[29] The following relationship can be derived based on these assumptions:

$$\tau_{ex} = \frac{qLn}{J}, \tag{5}$$

where L is the active layer thickness, q is the elementary charge, n is the charge carrier density, and J is the current density obtained from the J-V curves.[20] A direct comparison of the extraction time (τ_{ex}) and the charge carrier lifetime (τ_{rec}) can be made by rearranging Equation S16 and then be used to assess and understand the relative contributions of the competing non-geminate recombination and extraction processes, as shown in Figure A20.[20] In particular, it turns out that the PTB7-Th:IOTIC blend has a significantly slower τ_{ex} = 8.5 – 107 µs over the voltage range examined, compared to the other two blends: PTB7-Th:IOTIC-2F$_a$ (τ_{ex} = 2.3 – 54.9 µs) and PTB7-Th:IOTIC-4F (τ_{ex} = 1.6 – 33.2 µs). Ultimately, the voltage-dependent competition factors, which is defined as the ratio between the recombination and extraction times ($\theta = \tau_{ex}/\tau_{rec}$) serves as a metric for understanding the superior *FF* and J_{SC} values of the PTB7-Th:IOTIC-4F-based devices (**Figure 2.5**). The PTB7-Th:IOTIC and PTB7-Th:IOTIC-2F$_a$ devices show similar competition factors ($\theta = 0.003 - 10$) over the voltage range investigate, whereas the PTB7-Th:IOTIC-4F devices show significantly smaller competition

factors (θ = 0.0006 – 2) (Figure 2.5). Generally, smaller competition factors have been shown to correlate to higher *FF* and J_{SC} values.[28,29] As a point of comparison, in our recently published work[20] on the PM6:Y6 BHJ OSCs with over 15% *PCE*s, we calculated very low θ values ranging from 0.0002 to 0.56 over the relevant voltage range, due to exceptionally fast charge extraction compared to non-geminate recombination in the blend. Therefore, the low voltage-dependent competition factor in the PTB7-Th:IOTIC-4F devices can be explained by a favorable combination of fast extraction and long charge carrier lifetimes, which is absent in the PTB7-Th:IOTIC and PTB7-Th:IOTIC-2F_a blends.

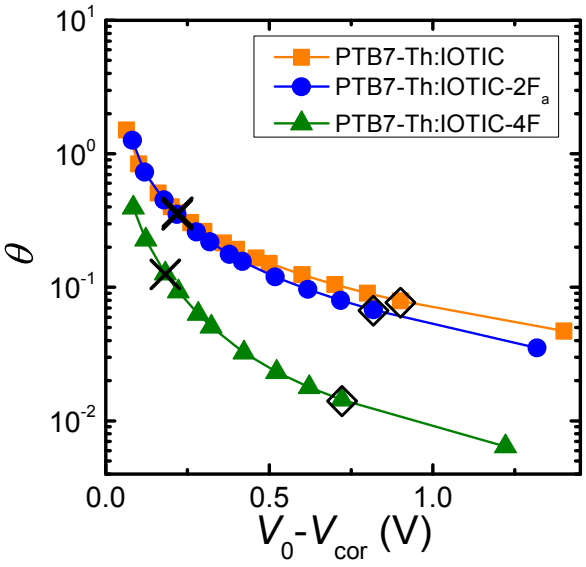

Figure 2.5. Voltage-dependent competition factor (θ), the ratio between the extraction and recombination times, of the three blend systems. Relevant operating conditions such as maximum power (crosses) and short-circuit (open diamond symbols) conditions are highlighted.

2.2.6. Morphological Insights to Understand Device Photophysics

The photophysical phenomena of OSCs are directly linked to its complicated BHJ morphology, which has been shown to influence the charge generation, recombination, and

extraction processes.[16,20,39,69–72] By analyzing BHJ morphologies over different length scales (from μm to sub-nm) it is possible to evaluate the roles of different structural features on the device photophysics of the blend systems. To begin, photoconductive atomic force microscopy (pc-AFM) was used to determine the height and photocurrent features at the surface of the active layers. To do this, an electrically conductive Pt/Cr tip was used to scan the surface of the active layers of the tested solar cell devices under white light illumination. During the pc-AFM scan, a white light source was focused on the area of scanning, which enabled the photo-responsive features in the blend film to be spatially mapped. A comparison of the photocurrent images normalized to the device with the highest photocurrent (PTB7-Th:IOTIC-4F) across multiple biases (Figure A21) confirmed that the highest photocurrents are obtained for the PTB7-Th:IOTIC-4F blend, followed by the PTB7-Th:IOTIC-2F_a and PTB7-Th:IOTIC blends. This trend of nanoscale photocurrents is in agreement with what was observed in the J_{SC} of the tested devices (Figure 2.2) and can be seen in the photocurrent scale readings shown in Figure A22. However, we were unable to resolve any significant differences in the sizes of the photo-conductive domains of the three blend films with high resolution (1 x 1 μm) pc-AFM (Figure A23).

Next, we probe the molecular orientation and long-range ordering in the films using GIWAXS. Analyses of GIWAXS (Figures A24 and A25) on the three blend films mostly showed face-on orientation with significant isotropic scattering making it difficult to unambiguously characterize differences in the blend films (details of GIWAXS analyses are included in Appendix A). It must be further highlighted here that, while techniques such as pc-AFM and GIWAXS provide useful insights, interpretations of the overall BHJ morphology using just these techniques can be limiting because they can either only be used to access the

surface of the BHJ blend, in the case of pc-AFM, or only the ordered regions of the BHJ film, in the case of GIWAXS. Therefore, we turn to advanced tools, such as RSoXS and solid-state NMR techniques for insights on more nuanced morphological traits, such as the nature of the domain purity and sizes, and the local ordering and interactions of the donor and acceptor species in the blend systems.

The RSoXS technique uses soft X-rays, which are well suited for studying organic blends comprising of carbon or nitrogen atoms, and is commonly used to probe the domain sizes and the donor and acceptor domain purity in BHJ blends.[73,74] Figure A26 shows the Lorentz corrected and circularly averaged RSoXS profiles of the three studied blend films. Table A5 summarizes the parameters extracted from fitting the RSoXS profiles. The profiles of the PTB7-Th:IOTIC-4F and PTB7-Th:IOTIC-2F_a blends were fitted with two lognormal peaks, whereas the profile of the PTB7-Th:IOTIC blend was fitted with a single lognormal peak, which suggests that there is a multilength scale morphology in the two former and not in the latter case. Comparing the long-period corresponding to the low-*q* peak in the three blends shows that the PTB7-Th:IOTIC blend has a higher long period of around 97 nm while the PTB7-Th:IOTIC-2F_a and PTB7-Th:IOTIC-4F blends show smaller and similar long periods of 67 and 68 nm, respectively. Additionally, for the PTB7-Th:IOTIC-2F_a and PTB7-Th:IOTIC-4F blends, the fitting identified the presence of smaller domains (reflected by the high q-peaks), which was negligible in the case of the PTB7-Th:IOTIC blend. The root-mean-square (RMS) composition variation (which is monotonically related to the domain purity) of the three blend systems were determined by obtaining the integrated scattering intensities (ISI). A higher value for the RMS composition variation indicates larger average purity of domains in the blends. Interestingly, it was found that the domain purity was highest for the

PTB7-Th:IOTIC blend, followed by the PTB7-Th:IOTIC-2F$_a$ and PTB7-Th:IOTIC-4F blends. A high average purity in the blends has been shown to be related to a smaller D:A interfacial area, due to the reduced distributed acceptor molecules in the polymer-rich phase.[16,41,74,75] Therefore, an increase in the relative volume fraction of small domains and a decrease in the domain purity, from the PTB7-Th:IOTIC to the PTB7-Th:IOTIC-4F blend, suggests that increased charge generation efficiencies may also be partly attributed to an increase in the D:A interfacial area. This implies that in the studied polymer:NFA blends, charge generation efficiencies may not only be dictated by the increased S_1-CT energetic offsets, but also further influenced by the amount of D:A interfacial area in the BHJ morphology.

To understand the origins of the differences in charge transport and extraction, solid-state NMR was used to probe differences in the local ordering and D:A interactions of the two blend systems showing the biggest differences in charge transport and extraction timescales. These were the PTB7-Th:IOTIC blend, which was afflicted by the slowest charge extraction (τ_{ex} = 8.5 – 107 μs) and transport (μ_{eff} = (0.7 – 5.5) · 10^{-5} $cm^2V^{-1}s^{-1}$) and the PTB7-Th:IOTIC-4F blend, which exhibited the fastest charge extraction (τ_{ex} = 1.6 – 33.2 μs) and transport (μ_{eff} = (2.7 – 6.1) · 10^{-5} $cm^2V^{-1}s^{-1}$). Solid-state NMR is sensitive to the local environments of nuclear spins, making it particularly useful to investigate both ordered and disordered materials on a molecular level, which is generally not possible with X-ray diffraction methods. However, characterizing heterogeneous materials containing multiple ordered and disordered domains poses additional challenges, as the NMR signals from the different domains tend to interfere and overlap, resulting in broad spectra that are challenging to resolve and analyze. In the case of polymers, statistical distributions of the local environments of otherwise

chemically equivalent nuclei (e.g., ^{1}H atoms in polymer backbones that experience variations in local π-π packing) are often manifested as broad chemical shift distributions (compare **Figure 2.6**a). Similarly, the abundance of near-equivalent species results in large distributions of overlapping signals (e.g., a large number of CH_2 groups in the aliphatic region). A third contribution arises from the anisotropic bulk magnetic susceptibility (ABMS), which is the tendency of a sample to become magnetized in the presence of an external magnetic field. While magic angle spinning (MAS) reduces the influence of the ABMS significantly, it cannot completely remove it, and a small contribution to the observed chemical shift often remains, leading to additional broadening of the resonance.[76–79] Combined, these effects result in signals with broad, Gaussian line shapes, an effect that is often called "inhomogeneous broadening".

In addition to the statistical broadening, strong anisotropic spin-spin interactions in the solid -state lead to reduced coherence lifetimes and thereby increased natural linewidth (exponential broadening, Lorentzian line shapes, also referred to as "homogeneous broadening"). The strength of the anisotropic interactions and thus the extent of lifetime broadening is related to the abundance of the nuclei in question, with ^{1}H being affected most due to its ubiquity in organic materials and almost 100% natural abundance.

By combining careful data processing and analysis with information gained from powerful two-dimensional (2D), dipolar-mediated correlation NMR spectroscopy techniques, valuable information on the local order and disorder in the polymer:NFA blends can be obtained. Figure 6b,c show schematic diagrams of the molecular structures and ^{1}H MAS NMR spectra of PTB7-Th, IOTIC, IOTIC-4F, and their respective blends acquired at 800 MHz (18.8 T) at 28.490 kHz MAS and ambient conditions. Two groups of ^{1}H signals can be

discerned, corresponding to signals in the region from 5.5 ppm to 8.0 ppm from aromatic ^{1}H atoms, and signals in the range of 0 ppm to 3.5 ppm from aliphatic sidechains. The aliphatic protons nearest to the linker groups can be discerned as small, broad peaks in the range of 3 - 5 ppm. In general, the ^{1}H MAS NMR spectra are characterized by broad signals with Gaussian-Lorentzian line shapes, indicating a significant distribution of the chemical shifts (Gaussian component), in addition to the broadening caused by the rapid signal decay (Lorentzian component), due to the strong anisotropic spin-spin interactions. The effect of overlapping chemical shifts is exemplified by the aliphatic peak in PTB7-Th, which is a superposition of numerous Lorentzian lines with slightly different chemical shifts arising from the more than 50 aliphatic ^{1}H atoms of each monomer. By contrast, the broadening in the aromatic region of the ^{1}H MAS NMR spectrum of PTB7-Th, which has only three inequivalent ^{1}H sites on the backbone, is caused by the variation of the chemical shift due to local disorder. The broad component of the aromatic region is assigned to the two protons of the thiophene side group, whereas the narrower signal is assigned to the benzodithiophene unit. The broad line of the former is most likely due to conformational disorder, leading to a Gaussian distribution of chemical shifts.

With the exception of pure PTB7-Th, with its three inequivalent aromatic proton sites per monomer, the aromatic region between 6 ppm and 8 ppm shows few resolved features due to the signal overlap of the numerous aromatic proton sites, though a small, broad shoulder around 6.3 ppm is discernable in the case of the PTB7-Th:IOTIC-4F blend. This signal is not present in either PTB7-Th or IOTIC-4F, indicating that the displaced signal is a result of the blending. Furthermore, a similar shift is not observed for the blend with IOTIC. Displacements of the aromatic ^{1}H signals to lower ppm values in conjugated polymers is usually a sign of

increased ring-current effects caused by neighboring aromatic systems and is commonly associated with strong π-π interactions.[30,80–82] Therefore, the presence of this new signal at 6.3 ppm hints at increased π-packing in the PTB7-Th:IOTIC-4F blend, though whether this occurs in the polymer, the NFA, or at the interface between the two is not discernible, based on the 1D ^{1}H MAS spectra alone. Interestingly, the ^{1}H MAS spectrum of the PTB7-Th:IOTIC-4F blend exhibits overall narrower signals with better resolution, especially in the aliphatic range between 0 ppm and 4 ppm.

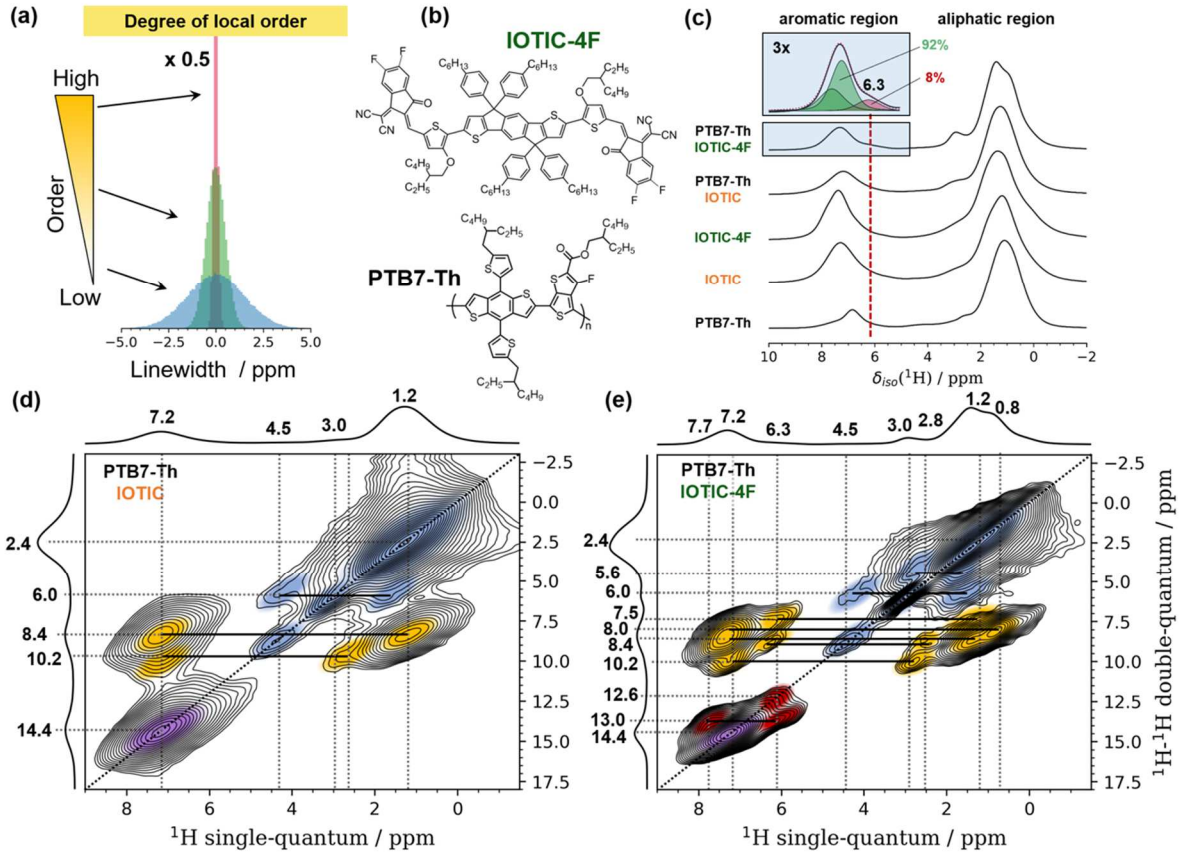

Figure 2.6. (a) Schematic representation of how local order and disorder are manifested in ^{1}H NMR line shapes. (b) Molecular structure of PTB7-Th and IOTIC-4F, (c)1D ^{1}H MAS NMR spectra of PTB7-Th, IOTIC, IOTIC-4F, and their respective blends acquired at 18.8 T (800 MHz for ^{1}H) and 28.490 kHz MAS, using a Hahn-Echo to remove the background signal of the probe head. (d,e) 2D ^{1}H-^{1}H Double-Quantum/Single-Quantum (DQ-SQ) correlation

spectra of (d) PTB7-Th:IOTIC and (e) PTB7-Th:IOTIC-4F acquired using back-to-back DQ-excitation over two rotor periods. Note the difference in linewidths in the 2D spectra. Violet contour-levels indicate intensity correlations between aromatic-aromatic protons, yellow aromatic-aliphatic protons, and blue aliphatic-aliphatic protons. Red contour-levels correspond to intensity correlations between aromatic-aromatic protons associated with the signal at 6.3 ppm. Correlated signals involving these moieties are connected by black bars.

The aggregation of PTB7-Th, IOTIC, and IOTIC-4F molecules and their interactions in blends can be further assessed by determining their intermolecular proximities, as evidenced by dipole-dipole-coupled species. Powerful 2D ^{1}H-^{1}H double-quantum single-quantum correlation analyses (Figure 2.6d,e) probe the combined chemical shifts of spin-pairs (double quantum coherences) that are correlated via 'through-space' dipolar interactions to the chemical shifts of the respective types of spins (single quantum coherences). These allow correlated signals from pairs of dipole-dipole coupled ^{1}H nuclei to be resolved and identified in a 2D frequency map, which is typically presented as 2D contour-plot spectrum.[83–86] The excitation efficiency for the double-quantum coherences is directly related to the dipolar coupling strength, which in turn is proportional to the inverse cube of the separation distance, as well as to the DQ-excitation time measured in rotational periods, making this experiment particularly sensitive to ^{1}H pairs in close spatial proximity (up to 5 Å). In addition, since the chemical shift in the double-quantum dimension (vertical axis) is the sum of the single quantum chemical shifts (horizontal axis), the experiments allow for spin pairs formed by equivalent ('self-correlated' signals, observed along the double diagonal) or inequivalent ('cross-correlated' signals, observed as two peaks with the same double-quantum frequency but with different single-quantum frequencies) to be resolved. Similar to the ^{1}H MAS NMR spectra, the DQ-SQ spectrum of PTB7-Th:IOTIC shows mostly broad signals with few discernible features, while the spectrum of PTB7-Th:IOTIC-4F exhibits better resolution, especially in the aromatic region. Both of the spectra show intense self-correlation signals in

the aliphatic range of $\delta(^1H)^{SQ}$ = 0 - 3 ppm and $\delta(^1H)^{DQ}$ = 0 - 6 ppm, the aromatic range $\delta(^1H)^{SQ}$ = 6 - 8 ppm and $\delta(^1H)^{DQ}$ = 12 - 16 ppm, as well as cross-correlations between the two regions. The aforementioned signal at around $\delta(^1H)^{SQ}$ = 6.3 ppm is readily observed as cross-correlated to both an aromatic signal at ca. $\delta(^1H)^{SQ}$ = 7.7 ppm and to signals in the aliphatic region. The two cross-correlated signals are observable after just a single rotor period of DQ-excitation, indicating a spatial proximity of 4 Å or less. A weak self-correlated signal at $\delta(^1H)^{SQ}$ = 6.3 ppm and $\delta(^1H)^{DQ}$ = 12.6 ppm becomes apparent at longer recoupling times of two and more clearly after four rotor periods of DQ-excitation (data shown in Apendix A). Information on the signal at $\delta(^1H)^{SQ}$ = 7.7 ppm is obfuscated by the overlapping signals in the aromatic region. Overall, the new signal observed at 6.3 ppm is more clearly resolved in the 2D DQ-SQ NMR and data for the blend PTB7-Th:IOTIC-4F shows much better resolution compared to PTB7-Th:IOTIC.

In principle, this can be attributed to two effects, either an increase in local order and thereby a reduction of the width of the chemical shift distribution (less inhomogeneous broadening), or the presence of increased motional averaging leading to longer signal lifetime and narrower lines (less homogeneous broadening).[83,87–89] To distinguish between the two cases, we performed ^1H-^{13}C DIPSHIFT experiments on both blends.[90–92] The objective of the experiment was to quantify the degree of motional averaging by measuring the apparent strength of the ^1H-^{13}C dipolar couplings of CH or CH_2 moieties and comparing these to theoretical values.[91,93] Details of the experiment are provided in the Supporting Information; data obtained for both blends show no significant differences in the extents of motional averaging between the two. Thus, the narrower ^1H NMR signals in the PTB7-Th:IOTIC-4F blend are most likely the result of decreased inhomogeneous broadening, indicating a higher

extent of atomic-level order in PTB7-Th:IOTIC-4F, compared to PTB7-Th:IOTIC.

The presence of a single, relatively isolated fluorine moiety in the polymer backbone of PTB7-Th offers the potential to probe the molecular-level environment of the donor polymer backbone through ^{19}F MAS NMR. In a similar fashion, the fluorine atom of the acceptor material IOTIC-4F enables the molecular-level environment of the NFA also to be established. 1D ^{19}F MAS NMR spectra of PTB7-Th, IOTIC-4F, and the two blends PTB7-Th:IOTIC-4F and PTB7-Th:IOTIC were acquired and are shown in **Figure 2.7**a. The spectrum of PTB7-Th shows a broad, predominantly Gaussian signal at -111 ppm with a full-width-at-half-maximum, FWHM of $\Delta\delta(^{19}F)$ = 6.2 ppm. Furthermore, apart from a reduction in the intensity of this signal due to the dilution, the signal appears unchanged in the two blends. The large ^{19}F width and Gaussian line shape associated with the fluorine atoms in PTB7-Th are indicative of a significant degree of local disorder of the polymer backbone, though whether this is related to conformational or π-packing disorder is unclear. ABMS effects might also contribute to the linewidth, though those reported in literature are usually smaller (below 2 ppm in diamagnetic samples, often 1 ppm or less).[77,78] The effect of the bulk magnetic susceptibility is expected to affect all of the signals equally, leading to similar broadening of the ^{1}H, ^{19}F and ^{13}C signals in a given domain when measured in units relative to the Larmor frequency (ppm).

Compared to the broad ^{19}F signal associated with the polymer backbone, the ^{19}F signals from the fluorine moieties in IOTIC-4F are much narrower ($\Delta\delta(^{19}F)$ = 1.5 ppm - 2 ppm, FWHM), though several overlapping signals are observed for neat IOTIC-4F as well as in the blend. Differences in the isotropic ^{19}F chemical shift are most likely linked to polymorphism of the IOTIC-4F in the two blends, or the presence of commingled crystalline and amorphous

fractions. The much narrower, more Lorentzian-shaped ^{19}F lines of IOTIC-4F indicate a higher degree of local order in the NFA part of the PTB7-Th:IOTIC-4F blend. 2D ^{19}F-^{19}F double-quantum single-quantum 2D correlation and ^{19}F-^{1}H heteronuclear-correlation NMR spectra (Figure 7b,c) provide the resolution necessary to distinguish the overlapping signals. These reveal a number of correlated signals (indicated by Roman numerals in Figure 2.7), with signal labels I, II, and III being observed in the case of neat IOTIC-4F, and a new set of signals IV dominating the 2D ^{19}F-^{19}F NMR spectrum of the blend. These groups of signals in the 2D 19F-19F data correspond to different pairs of fluorine atoms in individual IOTIC-4F molecules, which in turn are in different molecular environments (i.e., different polymorphs or commingled fractions). The observation of a new group (IV) indicates the blending with PTB7-Th leads to significant changes in the molecular level environment of the NFA.

Further, 2D ^{19}F-^{1}H heteronuclear correlation spectra in Figure 2.7c show correlated intensity between the ^{19}F signal at -126 ppm associated with group IV, and the ^{1}H signal at 6.3 ppm, indicating that the increased π-π interactions previously associated with this ^{1}H signal are occurring either in the NFA or at the polymer:NFA interface. Therefore, solid-state NMR analyses indicate that the superior charge transport and extraction properties in the PTB7-Th:IOTIC-4F blend can be explained by the increased atomic-level local ordering and π-π interactions in present in the blend.

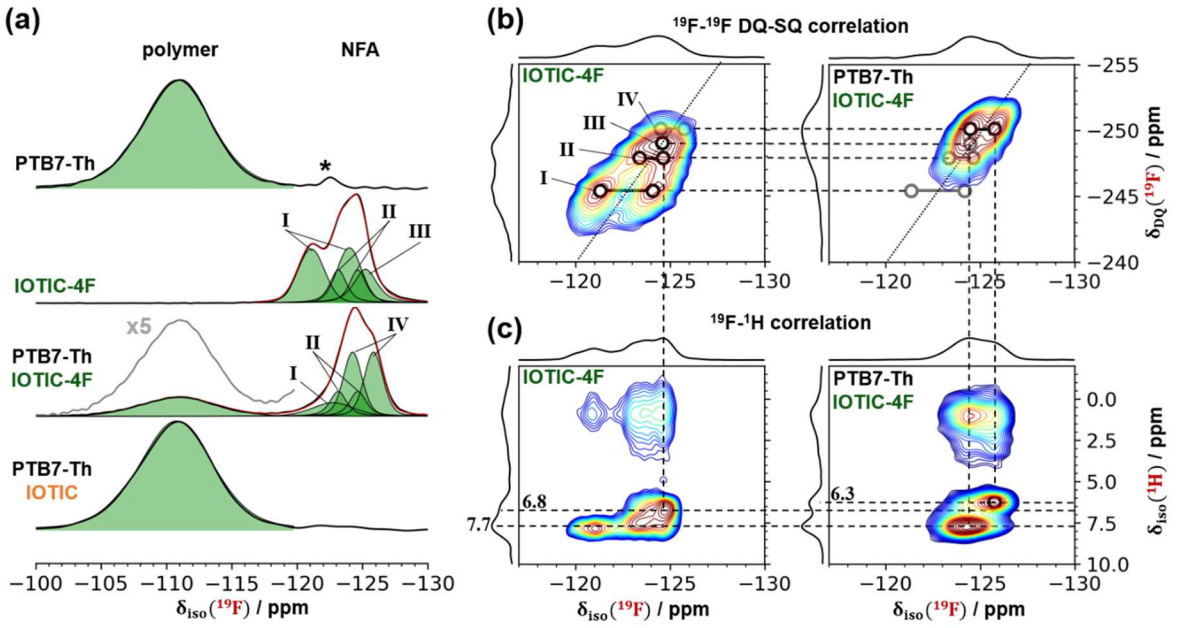

Figure 2.7. (a) 1D ^{19}F MAS NMR spectra of PTB7-Th, IOTIC-4F, PTB7-Th:IOTIC-4F, and PTB7-Th:IOTIC, acquired at 9.4 T and 25.0 kHz MAS. Deconvoluted signals are shown in green; the asterisk marks a small PTFE impurity. The Roman numerals denote ^{19}F signals from dipole-dipole-coupled moieties, as determined from (b) 2D ^{19}F-^{19}F double-quantum single-quantum (DQ-SQ) correlation spectra. (c) 2D ^{19}F-^{1}H heteronuclear correlation spectra of the pure NFA IOTIC-4F and its blend with PTB7-Th. Only the shift ranges corresponding to the NFA are shown.

2.2.7. Impact of Charge Generation, Recombination, Extraction, and Voltage Losses on the Device Performance

For the polymer:NFA systems examined here, the use of NFAs with identical chemical structures except for different fluorine substitutions resulted in different energetic offsets and device morphologies, which affected their respective device performances. The objective of this study was to determine the impact of changing both energetic offsets and morphology on the device performance. First, to see the effect of changing energetic offsets on the device parameters, transient absorption spectroscopy and in-depth voltage loss studies were performed. Transient absorption spectroscopy was used to understand the charge generation dynamics, where it was found that hole transfer slows with decreasing energetic driving force,

which can lower the J_{SC} generated from the devices. A systematic study achieved by first affirming that bimolecular recombination is the dominant pathway in all blend systems helped identify and accurately compare origins of the radiative and non-radiative recombination losses. More specifically, we found that the increase in the V_{OC} was due to a decrease in the non-radiative recombination losses as energetic offsets were decreased as a result of the intensity borrowing mechanism and the design rules formulated in a previous study.[15] Second, an in-depth study of the thin-film morphology (i.e., D:A interfacial area, local ordering, and π-π interactions) in the blend systems obtained from RSoXS and solid-state NMR spectroscopy analyses led us to understand why the highest performing devices exhibit the most superior *FF* and J_{SC} values. Specifically, we found that increased D:A interfacial area obtained from RSoXS measurements in the blends can be correlated to increased charge generation efficiencies, which further contributed to higher J_{SC} values. Additionally, increased local ordering and π-π interactions, characterized by solid-state NMR spectroscopy in the PTB7-Th:IOTIC-4F blend, led to the fastest charge transport and the best competition factors ($\tau_{ex} << \tau_{rec}$) resulting in the highest *FF* and J_{SC} values.

2.3. Conclusions

In summary, this work builds upon recent novel findings on the device photophysics of polymer:NFA blends by adding some new and detailed insights to understand the multi-faceted components that lead to efficient OSC devices. Specifically, a deconvolution of the different loss processes in polymer:NFA blends and the connections to nuanced BHJ morphology and energetics were established. The following primary conclusions from this work can be added to the recent body of literature regarding the advantages offered by polymer:NFA systems:

i. We were able experimentally measure a tradeoff between the radiative and non-radiative recombination losses by systematically varying the S_1-CT offsets, by fluorinating a series of NFAs, for the first time. For a systematic comparison of the total voltage losses between the three systems, we established that all three blend systems showed dominant bimolecular recombination loss processes at temperatures down to 200 K, and that losses due to energetic disorder were comparable and minimal in all three systems. Overall, it was possible to accurately unravel the different contributions to the voltage losses in the three blend systems as well as to understand one of the reasons for a concomitant increase in J_{SC} with decreasing V_{OC}.

ii. Insights into the relative charge generation efficiencies of the three blends showed that as hole transfer slows with decreasing energetic driving force, it begins to compete with exciton decay. Furthermore, the presence of FRET in these blends underlines the importance of the balance between the NFA exciton decay and hole transfer rates, as the majority of the charge generation appears to proceed through the lower gap NFA, regardless of on which component the exciton was initially generated. Therefore, it was found that these processes are finely balanced in low energetic offset polymer:NFA blends, where small changes to hole transfer rates can notably deteriorate the charge generation efficiencies and ultimately the current generated from the devices.

iii. In polymer:NFA blends, aside from the quantification of the voltage losses and charge generation efficiencies, an understanding of the non-geminate charge recombination and extraction dynamics, along with a detailed picture of BHJ morphology is further

warranted for an overall understanding of the different components required to achieve high *PCE*s. Specifically, the competition between non-geminate recombination and extraction dynamics in the three blend systems were shown to correlate with the *FF* and J_{SC} values. Superior *FF* and J_{SC} values in the PTB7-Th:IOTIC-4F blend were found to be due to a favorable combination of slow recombination and fast extraction dynamics leading to smaller competition factors. Beyond the commonly reported GIWAXS and AFM analyses, which provide limited interpretations of the complex BHJ morphology, solid-state NMR and RSoXS were used to understand the D:A interactions, atomic-level local ordering, nature and types of domains, as well as the domain purity. RSoXS data on the relative volume fractions of the small domains in the blend and root-mean-square composition variation suggest that an increased D:A interfacial area with increasing energetic offsets (from PTB7-Th:IOTIC to PTB7-Th:IOTIC-4F blend systems) may further aid in the charge generation efficiencies of the studied polymer:NFA blend systems. Solid-state NMR provides detailed atomic-level insights on the nature and origins of the increased local ordering and π-π interactions in the NFA or at the polymer:NFA interface, which explain the superior charge transport and extraction in the PTB7-Th:IOTIC-4F devices. These advanced characterization techniques enable identifying and understanding molecular-level origins of OSC properties, and the roles they play in highly efficient polymer:NFA OSC.

Ultimately, the enhanced J_{SC} and *FF* values in the highest performing blend system (PTB7-Th:IOTIC-4F), as a result of a beneficial atomic-level local ordering (which affects charge transport and extraction) and a favorable S_1-CT offset and D:A interfacial area (which affects

charge generation), were found to outweigh the increased voltage losses, to yield the highest *PCE*s. Comprehensive studies of this nature, which focus on ascertaining the fundamental mechanisms and processes by which high power conversion efficiencies are achieved, can increase the likelihood of achieving even higher efficiencies, bringing us a step closer to the commercialization of OSCs in the near future.

2.4. Experimental Section

Materials: PTB7-Th (number-average molecular weight (Mn) =106 kDa, PDI =2.0) was purchased from 1-material Inc. IOTIC, IOTIC-2F$_a$, and IOTIC-4F were synthesized as reported in the previous literature.[94–96] Note that the change in the name of the IOTIC-2F compound (as reported in the previous literature[94]) to IOTIC-2F$_a$ is due to the difference in isomeric ratios between this batch and the previously reported batch.

Device Fabrication: Indium tin oxide (ITO) patterned glass substrates were cleaned by scrubbing with soapy water, followed by sonication in soapy water, deionized (DI) water, acetone, and isopropanol for 20 minutes each. The substrates were dried using compressed nitrogen and placed in an oven overnight at 100 °C. The ITO substrates were treated with UV-ozone for 15 minutes and a layer of poly(3,4-ethylenedioxythiophene): poly(styrenesulfonate) (PEDOT:PSS, Clevios P VP Al 8043) was spin-coated at 3000 rpm for 40 s onto the ITO substrates. The substrates were then annealed in air at 150 °C for 20 minutes. 21 mg/mL active layer blend solutions were prepared with a D:A ratio of 1:1.5 in chlorobenzene with 1% v/v 1,8-Diiodooctane (DIO). The active layers were spin-cast inside a nitrogen glovebox at spin-speeds of 800-2000 rpm. The substrates were then pumped down under vacuum (< 10^{-7} torr), and a 5 nm thick Barium interlayer followed by a 100 nm thick Aluminum electrode was

deposited on top of the active layer by thermal evaporation. Devices of neat materials (PTB7-Th or IOTIC-derivatives) were prepared using similar solid concentrations as that in the blend solution.

Device Testing: Photovoltaic characteristic measurements were carried out inside the glove box using a high-quality optical fiber to guide the light from the solar simulator equipped with a Keithley 2635A source measurement unit. *J-V* curves were measured under AM 1.5G illumination at 100 mW cm^{-2} for devices with an electrode area of 0.22 cm^2.

External quantum efficiency (EQE_{PV}) measurements: External quantum efficiency (EQE) for all solar cells was measured using a 75 W Xe light source, monochromator, optical chopper (138 Hz), and a lock-in amplifier. Power-density calibration of the EQE characteristics was achieved using a calibrated silicon photodiode from Newport. For the sub-bandgap EQE, higher sensitivity settings were used with a longer time delay between measurement points.

Internal quantum efficiency (IQE) measurements: The total reflectance of the solar cell devices with the configuration: glass/ITO/PEDOT:PSS/Active layer/Ba/Al were measured with an integrating sphere to obtain the total absorption, which was corrected for the parasitic absorption simulated with the transfer matrix model.[97] The active layer optical properties were measured with transmittance and reflectance measurements using an integrating sphere. The optical properties of the other layers were determined from ellipsometry with a Woolam M-2000DI Variable Angle Spectroscopic Ellipsometer, with reflectance and transmission measurements, or taken from the literature.[98,99] The IQE spectra of the devices were calculated by subtracting the parasitic absorption from the total device absorption to obtain the active layer absorption and dividing the EQE spectra by the corresponding fraction of active layer absorption. As described in the literature report,[32] since the experimentally measured total

absorption is highly accurate, errors in the resulting active layer absorption are only as small as the errors in the parasitic absorptions.

Electroluminescence and EQE_{EL} Measurements: EL measurements were performed using two setups depending on the wavelength range of interest. For measurements under 1050 nm, a home-made EL spectrometer was used. The EL emission from a sample driven by a Keithley source-measure unit (model 2602A) was collected by a lens system and focused on the entrance slit of a spectrograph (Acton Research SP-500) equipped with a Si charge-coupled detector (Princeton Instruments Pixis:400). The spectra collected by the detector were corrected for the instrument response function. The correction factors were determined by measuring the spectrum of a black body-like light source (Ocean Optics LS-1). For EL measurements in the range 900 - 1700 nm, we utilized a Photon Technology International (PTI) Quantamaster fluorimeter equipped with an Edinburgh Instruments EI-L Ge detector. The excitation monochromator of the fluorimeter was not used, and the EL emission was generated by driving the devices by a Keithley 2602 source-measure unit. An optical chopper (Thorlabs MC2000) was placed in front of the emission monochromator to make use of the fluorimeter's lock-in amplifier-based detection system. The PTI Felix fluorimeter software was used for the data collection and correction of the instrumental artifacts. The efficiency of electroluminescence was obtained by applying a bias from -1 to 2V with a dual-channel Keithley 2602 to the solar cell and placing a silicon or germanium photodiode directly in front of it to collect the emission as a function of applied bias. The current running through the device and the photodiode were simultaneously measured.

Transient Absorption (TA) spectroscopy: TA was performed on either one of two experimental setups. For "visible" region TA (500 – 950 nm), a Yb amplifier (PHAROS, Light Conversion), operating at 38 kHz and generating 200 fs pulses centered at 1030 nm with an output of 14.5 W was used. The pump pulse was provided by a TOPAS optical parametric amplifier. The probe is provided by a WL supercontinuum generated in a YAG crystal. After passing through the sample, the probe is imaged using a Si photodiode array (Stresing S11490). This setup provided additional flexibility by allowing for broadband spectrum acquisition in one measurement for improved consistency, as well good signal to noise (s/n) in the 750 – 850 nm region, which is difficult to obtain on the other setups due to large fluctuations in the WL seed around the 800 nm fundamental. The near infrared (NIR) TA was performed on a setup was powered using a commercially available Ti:sapphire amplifier (Spectra Physics Solstice Ace). The amplifier operates at 1 kHz and generates 100 fs pulses centered at 800 nm with an output of 7 W. For these measurements, a small fraction of the 800 nm fundamental was used as the pump. The probe was provided by a broadband NIR NOPA. To complement the NIR probe wavelengths available, the probe pulses are collected with an InGaAs dual-line array detector (Hamamatsu G11608-512DA), driven and read out by a custom-built board from Stresing Entwicklungsbüro. The probe beam was split into two identical beams by a 50/50 beamsplitter. This allowed for the use of a second reference beam which also passes through the sample but does not interact with the pump. The role of the reference was to correct for any shot-to-shot fluctuations in the probe that would otherwise greatly increase the structured noise in our experiments. Through this arrangement, very small signals with a $\frac{\Delta T}{T} < 10^{-5}$ could be measured.

Capacitance spectroscopy: Capacitance spectroscopy measurements were performed with an impedance analyzer Solartron 1260A in the dark and under 1 sun AM1.5 illumination inside a nitrogen-filled glovebox. The amplitude of the AC signal was 40 mV to ensure a negligible impact on the measured impedance.

Energy-resolved Electrochemical Impedance spectroscopy: Electrochemical microcells were formed on ITO substrates with deposited BHJ blend thin films. Thin films were spin cast with the same spin-speed and conditions as the optimized devices to avoid any morphological changes. The solution of 0.1 M TBAPF6 in anhydrous acetonitrile was used as the supporting electrolyte. The dissociation of this electrolyte in the inert atmosphere occurred at an overpotential of 63.5 V. The active polymer electrode area was 12 mm^2. The potential of the working electrode with respect to the reference Ag/AgCl electrode was controlled via a potentiostat. Pt wire was used as the counter electrode. The potential recorded with respect to the reference Ag/AgCl electrode was recalculated to the local vacuum level assuming the Ag/AgCl energy vs. vacuum value of 4.66 eV. An Impedance/ gain-phase analyzer, Solartron analytical, model 1260 (Ametek, Berwyn, USA), was used. The AC harmonic voltage signal frequency was 0.5Hz, its amplitude was 100mV, and the sweep rate of the DC voltage ramp was 10 mV/s. Bode and Cole-Cole diagrams in the frequency range of 0.01–1 MHz were used as a preliminary ER-EIS method adjustment. The sensitive nature of the experimental method requires the experiment to be conducted in an inert atmosphere, yielding reproducible measured DOS spectra.

Photo-conductive atomic force microscopy (pc-AFM): Photoconductive atomic force microscopy (pc-AFM) measurements were done with an Asylum Research MFP-3D microscope sitting atop an inverted optical microscopy (Olympus, IX71). All measurements

were conducted under inert atmosphere. A white light source with a power of 30 W cm^{-2} was used to generate photocurrent morphology which was recorded by an internal preamplifier (Asylum Research ORCA head model). Electrically conductive Chromium/Platinum-coated silicon probes with a spring constant of 0.2 N m^{-1} and resonant frequency of 13 kHz (Budget Sensors) were used. A light spot with 160 μm diameter was focused on the active layer of the device through an inverted optical microscope (Olympus), and the conductive tip was positioned at the center of the light spot.

Grazing incidence wide angle X-ray Scattering (GIWAXS): This measurement was performed at the Advanced Light Source at Lawrence Berkeley National Lab on the 7.3.3 beamline. The sample was scanned for 40 seconds at an incidence angle of 0.12° and a photon energy of 10 keV (λ = 1.24 Å), while under a helium environment to minimize beam damage and reduce air scattering. The width of the incident X-ray beam is about 1 mm, and silver behenate was used to calibrate the lengths in the reciprocal space. A 2D detector (PILATUS 2 M from Dectris) with a sample-to-detector distance of 276.9 mm was used to collect the images. The Nika software package for Igor (by Wavemetrics) and the Igor script WAXStools were used to process the image.

Resonant-Soft X-ray Scattering (R-SoXs): R-SoXS was performed at the beamline 11.0.1.2[100] Advanced Light Source (ALS), Lawrence Berkeley National Laboratory. Samples for R-SoXS measurements were prepared on a PSS modified ITO substrates under the same conditions as those used for device fabrication, and then transferred by floating in water to a 1.5 × 1.5 mm^2, 100 nm thick Si3N4 membrane supported by a 5 × 5 mm, 200 mm thick Si frame (Norcada Inc.). R-SoXS was performed in a transmission geometry with linearly polarized photons under high vacuum (1×10^{-7} torr) and a cooled (-45 °C) CCD (Princeton PI-

MTE) was used to capture the soft X-ray scattering 2D maps and PS300 was used for geometry calibration.

Solid-State NMR: Neat and blend films for solid-state NMR analyses were scratched off from glass substrates with spin-coated films. ^{1}H MAS and ^{1}H-^{1}H DQ-SQ correlation NMR spectra were acquired on a Bruker AVANCE III spectrometer operating at 18.8 T / 800 MHz, using a Bruker 2.5 mm Double Resonance probe. The chemical shift and RF fields were calibrated on a sample of Adamantane (1.8 ppm, 100 kHz nutation frequency[101,102]), the Magic Angle was calibrated using $NaNO_3$, all experiments were acquired using a Hahn-Echo sequence to remove the proton background of the probe. For DQ excitation the Back-to-Back (BaBa) scheme[103,104] with XY16 phase cycling[105] was used, spinning at 28.490 kHz MAS. Relaxation delays were determined using the saturation recovery experiment and delays between 2 and 4 seconds were employed. The number of scans was 16 for the 1D spectra and 64 for the two-dimensional spectra to facilitate complete phase cycling to remove all background signals. A z-filter delay of 20 rotor periods was used before acquisition to remove spurious magnetization. The acquisition in the indirect dimension was rotor-synchronized, 64 data points were recorded using the States-TPPI method. ^{19}F Hahn-Echo, Spin-Lock and ^{19}F{^{1}H} CP/MAS and HETCOR experiments were recorded on a Bruker AVANCE III spectrometer operating at 9.4 T (376.5 MHz / 400 MHz) using a Bruker 2.5mm H/F/X triple resonance Probe, spinning at 25.0 kHz. The chemical shift and RF fields were calibrated on a sample of Adamantane (1.8 ppm, 100 kHz nutation frequency) and PTFE tape (-122 ppm, 83.3 kHz and 100 KHz), the Magic Angle was calibrated using $NaNO_3$, CP contact times were varied between 0.2 and 2 ms. Relaxation delays were determined using the saturation recovery method, between 64 and 256 scans were used for the 1D and 2D spectra. The indirect

dimension was sampled in 80 μs steps, over 96 data points using the States-TPPI method. For the Spin-Lock experiments a nutation frequency of 100 kHz was used, data processing and analysis was done in Python; the code for the programs used can be provided by the authors upon request. $^{13}C\{^{1}H\}$ CP/MAS spectra were acquired on a AVANCE III spectrometer operating at 11.7 T (125.8 MHz / 500 MHz), the chemical shift and RF fields were calibrated on a sample of Adamantane (29.5 ppm (lower ppm signal), 50 kHz ^{13}C nutation frequency, 62.5 kHz ^{1}H nutation frequency), the Magic Angle was calibrated using $NaNO_3$. Relaxation delays were measured using the saturation recovery method, between 1.5 and 4 seconds were used, depending on the duty cycle of the hardware. A spinning speed of 10 kHz was used to avoid the overlap of signals and spinning sidebands, ramped amplitude cross-polarization employing a 80-100% ramp on the ^{13}C channel was used. The bandwidth of the ramp was checked using Adamantane at various offsets, for the final spectra the carrier was placed at 100 ppm. For the $^{13}C\{^{1}H\}$ DIPSHIFT experiments the modified pulse sequence of Ivanir-Dabora et al. was used, with a MAS frequency of 10 kHz.[106] For data analysis, the approach described by Hackel et al. was implemented in Python; the code for the programs used can be provided by the authors upon request.[107]

Chapter 3

Understanding the High Performance of over 15% Efficiency in Single-Junction Bulk Heterojunction Organic Solar Cells

3.1. Introduction

Polymer:non-fullerene acceptor (NFA) based single-junction organic solar cells (OSCs) have recently attained record-breaking power conversion efficiencies (*PCE*s) of over 16%.[8] Numerous recently reported studies attribute the high performance of polymer:NFA-based OSCs to an improvement in the open-circuit voltage (V_{OC}) without significantly impeding the charge generation efficiency.[13,108,109] Such improvements in the V_{OC} can be credited to a rise in the number of systems with relatively low energetic offsets ($\Delta G_{S1\text{-}CT}$), which is defined as the energy difference between the charge transfer (CT) state and the singlet exciton state (S_1) of the lower bandgap component in the blend.[15,16,108] While blend systems with low energetic offsets are sought for achieving high open-circuit-voltages, such blends commonly suffer from modest short-circuit current (J_{SC}) and fill-factor (*FF*) values, which can limit the *PCE*.[15–19,110]

In this study, the recently reported high performing blend system, PM6:Y6, was examined to obtain an in-depth understanding of the voltage losses, as well as the charge recombination and extraction dynamics. Remarkably, the PM6:Y6 blend is simultaneously able to achieve high V_{OC} (0.825V) with exceptional *FF* (74%) and J_{SC} (25.2 mA/cm^2) values, which is likely linked to a favorable morphology. Therefore, to gain detailed insights into the morphology of the blend, three different morphology characterization techniques were used in combination to visualize the photoconductive donor and acceptor phase-separated regions on the surface

of the blend film, characterize the ordering in the bulk of the blend film, and probe the D:A inter- and intramolecular interactions. This work provides key insights on the device physics and detailed morphology of the highly efficient single-junction OSC blend, while unravelling the underlying mechanisms for achieving *PCEs* of over 15 %.

3.2. Results and discussions

The chemical structures of the donor and acceptor materials, along with the energy levels and device structure of the PM6:Y6 blend system are shown in **Figure 3.1**. Devices with PEDOT:PSS as the bottom electrode and solution processed PDINO layer capped with evaporated Aluminum electrodes were optimized as reported in the previous work.[111] The *J-V* characteristics of a device at 1 sun illumination (100 mW cm^{-2} AM 1.5) is shown in **Figure B1**. The average *PCE* in **Table B1** was obtained from testing 20 devices, and the best performing device exhibited a *PCE* of up to 15.35%. To understand what makes this blend system achieve over 15% *PCE*, we examine the individual components that make up the *PCE* (V_{OC}, *FF,* and J_{sc}) in detail.

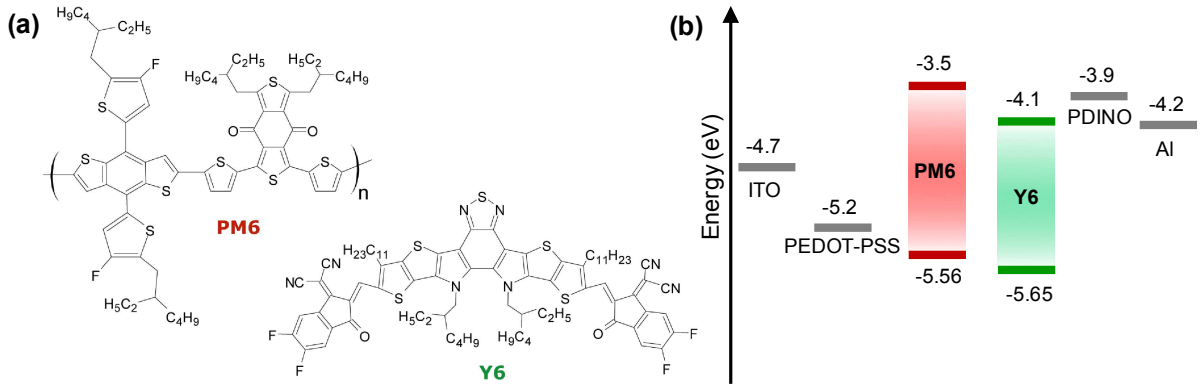

Figure 3.1. (a) Chemical structures of PM6 and Y6, and (b) Energy levels of PM6 and Y6 based on CV measurements and device structure used.

To understand the high V_{OC}, we begin by delving deeper into understanding the voltage losses in this blend. For evaluating the losses limiting the V_{OC} in this blend, we evaluate the energy loss, E_{loss} as:

$$E_{loss} = S_1 - qV_{OC}, \quad (1)$$

where, S_1 is the singlet exciton energy of the lower bandgap component in the blend and q is the elementary charge. A recently published paper by Vandewal el. al.[36] dissuades the use of ill-defined absorption onsets or HOMO and LUMO energies as reference points for evaluating voltage losses. Therefore, we adopt the optical method described in the paper[36] for a precise measurement of the singlet exciton energy. To obtain the S_1, the intersection point of the emission spectra (from electroluminescence (EL) measurements) and absorption spectra (from photovoltaic external quantum efficiency (EQE_{PV}) measurements) of the lower band-gap component in the blend (acceptor, Y6) is obtained (**Figure B2)**. The S_1 obtained from this method was found to be 1.36 eV.

Losses limiting the V_{OC} can be further divided into two parts: losses due to charge transfer as defined by the difference between the S_1 and the energy of the CT state (E_{CT}), and losses due to recombination defined by the difference in E_{CT} and V_{OC}. Commonly, to identify the CT state in a blend, the EQE_{PV} is measured, and the CT state is identified as the absorption feature visible at energies lower than the bandgap of either the donor or acceptor. The E_{CT} is then determined by fitting an expression derived from Marcus theory (**Equation S1**) to the tail of the blend EQE_{PV} spectrum.[17,37] However, the CT state is not always pronounced in the low-energy tail of the EQE_{PV} spectra, especially in blends where the energetic offsets between the donor and acceptor are low (i.e., low HOMO-HOMO or LUMO-LUMO offsets)[15,18,38,108], and so it can be difficult to distinguish the energy of the CT state from the donor or acceptor singlet

state. It is possible, however, to significantly reduce the degrees of freedom in the fitting by 1) performing a simultaneous fit to both the EQE_{PV} (**Equation S1**) and the electroluminescence (EL) (**Equation S2**) spectra[13,19,39,40,112] using equations derived from Marcus theory, as was first demonstrated by Vandewal *et. al.*[37] and 2) calculating the EQE_{PV} down to 10^{-7} using sensitively measured EL data and the relationship shown in **Equation B3**.[10] The added sensitivity of four orders of magnitude in the measurements allows for the deconvolution of the Gaussian-shaped CT absorption which was previously absent from the sharp absorption tail of the measured EQE data. In fact, a recently published paper[112] has shown that this method significantly lowers errors in the fitting parameters (E_{CT}, λ, f) in low energetic offset systems. Using this analysis, the E_{CT} in the PM6:Y6 blend was determined to be 1.31 ± 0.003 eV (**Figure 3.2**) further confirming the low offset in this system with a difference between S_1 and E_{CT} of only ~ 0.05 eV. It is worth noting, however, that despite the reduction in degrees of freedom in the Marcus fitting, the E_{CT} value obtained here serves only as an estimate due to the significant uncertainty that arises in separating the CT state emission and the singlet exciton emission in low energetic offset systems.

Next, losses due to recombination (E_{CT} to V_{OC}), which can be divided into radiative (ΔV_{rad}) and non-radiative losses ($\Delta V_{non\text{-}rad}$) are quantified using **Equation S4**. As derived from a detailed balance analysis, about 200-250 meV of radiative recombination is needed to establish thermodynamic equilibrium.[17] The radiative recombination can be calculated based on the Marcus fitting parameters f, λ, and E_{CT} as shown in **Equation S5**. Non-radiative recombination losses, on the other hand, constitute a larger part of the recombination losses, spanning a range of 210-550 meV.[46,47] In recent years, an increasing number of non-radiative recombination loss-related studies have led us to understand the nature and origin of this

recombination in more detail, with studies showing that this recombination can be attributed to carbon-carbon bond vibrations[46], molecular orientation at the donor-acceptor interface[39,48], energetic driving force[13,15,19], and E_{CT} values[46].

Using the fit parameters obtained from **Equations S2** and **S3**, we can now calculate the losses due to radiative recombination in the PM6:Y6 blend system from **Equation S5** to be 0.199 ± 3 eV. From EQE_{EL} measurements of 12 devices, losses due to non-radiative recombination are measured to be 0.286 ± 3 eV ($EQE_{EL} \approx 1.3\times10^{-5}$). This value is confirmed from the calculated non-radiative recombination measurements obtained from plugging in **Equation S5** into **Equation S4** and is summarized in **Table B2**.

The breakdown of the losses from S_1 to V_{OC} is shown schematically in an energy loss diagram in **Figure 3.2**. Notably, the total voltage loss due to recombination ($E_{CT} - V_{OC}$) is ~ 0.485 eV and is among one of the lower recombination-related loss values reported in the literature.[15,16,46,108,112]

Furthermore, the suppression of non-radiative recombination losses with a decreased energetic offset has been observed in several recently reported studies.[13,15,19,46] This observation has been explained by the idea that a decreased overlap of the vibrational wave function of the CT and ground state leads to the suppression of the non-radiative recombination pathway.[46] In addition, the recent *Nat. Mater*. paper by Qian et. al.[15] suggests that in low energetic offset systems, hybridization of the CT state with the highly emissive S_1 state will increase the radiative ability of the CT state through the intense borrowing mechanism.[49,50] In such a case, an efficient transition from the CT state back to the S_1 state can be possible, which opens up an additional radiative relaxation pathway through the highly emissive S_1 state. From the modelling of excitonic and CT states, it was found that if the

radiative relaxation channel from the highly emissive S_1 state can be made efficient in this way, the non-radiative voltage losses via the CT state should synchronously decrease.[15] To further confirm that the S_1 state (Y6) is in fact highly emissive, we measured the EQE_{EL} of the Y6 only devices (Appendix B, **Figure B2**f), confirming the lower non-radiative recombination ($\Delta V_{non\text{-}rad} = 0.242 \pm 5$ eV) in the acceptor only device compared to that of the blend ($\Delta V_{non\text{-}rad} = 0.286 \pm 3$ eV eV).

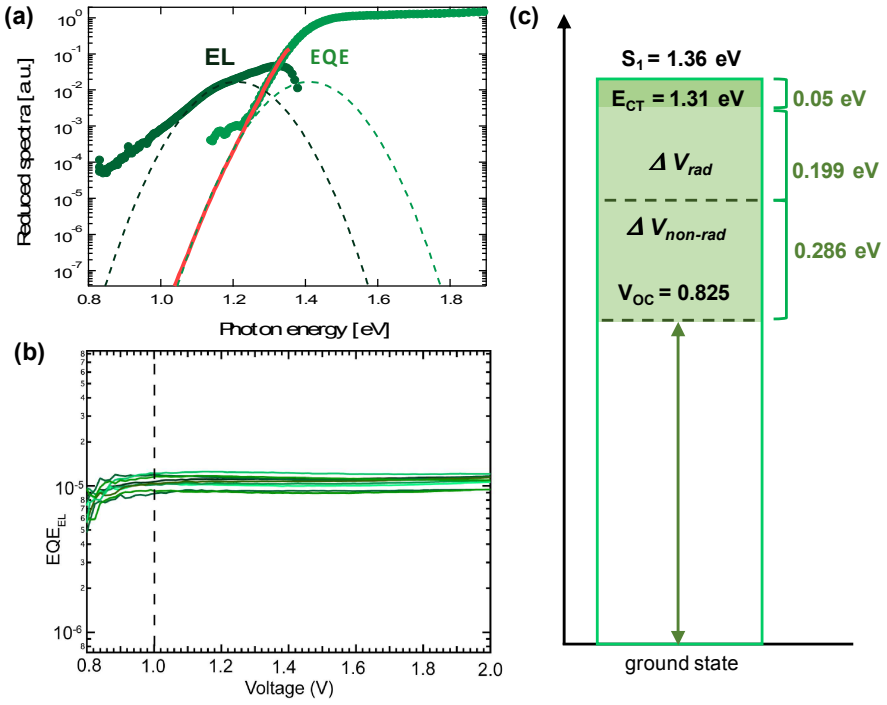

Figure 3.2. (a) Simultaneous fitting of the reduced EQE_{PV} and EL spectra; reciprocity relationship between EQE_{PV} and EL from **Equation S3** was used to calculate the EQE_{PV} down to 10^{-7} shown by the red solid line, the fitting parameters used were: $\lambda = 0.10$ eV, $E_{CT} = 1.31$ eV, $f = 3.0 \times 10^{-3}$ eV^2. (b) Measured EQE_{EL} vs. applied bias for 12 devices, where the EQE_{EL} values were extracted from the voltage at which the injected current is equal to the J_{SC} of the devices under 1 sun illumination (shown approximately by the black dotted line) and $\Delta V_{non\text{-}rad}$ was calculated from **Equation S6** after obtaining the measured EQE_{EL}. (c) Schematic representation of the breakdown of voltage losses from S_1 to V_{OC}.

In addition to the low voltage losses that help to maximize the V_{OC}, the blend system also exhibits high J_{SC} and *FF* values, which are crucial for the remarkable *PCE* of 15.35% in the best performing device – such a combination of low voltage losses with high J_{SC} and *FF* is uncommon in the literature. To gain further insight into this, the recombination and extraction dynamics in the blend were measured and analyzed. It has been shown that if the charge extraction time is faster than or compatible to the recombination time, charge recombination can be reduced.[16,28,29] The photocurrent density (J_{ph}) of the device is calculated using the following equation:

$$J_{ph} = J_{light} - J_{dark}, \quad (2)$$

where J_{light} is the current density measured under illumination and J_{dark} is the current density measured in the dark. The photocurrent density is plotted against the effective voltage $V_{eff} = V_0 - V_{cor}$ (Supporting Information, **Figure B3a,b**), where V_0 is the voltage at which $J_{ph} = 0$ ($V_0 = 0.842$ V). The corrected voltage V_{cor} can be obtained by taking into account the voltage losses over the series resistance:

$$V_{cor} = V_{app} - J \cdot R_{series}, \quad (3)$$

where V_{cor} is the corrected voltage, J is the current density, and R_{series} is the series resistance which is equal to the saturated differential resistance at forward bias (i. e. $\partial V_{app}/\partial J = \text{const.}$).[65,115] Relatively high photocurrents were achieved for the PM6:Y6 BHJ and the value of J_{ph} remains high even at comparatively low effective voltages ($V_{eff} = 0.1$ V). Subsequently, the probability of charge collection P_C can be estimated by analyzing the ratio between the saturated photocurrent density $J_{ph,sat}$ and the values for J_{ph} at different biases[63]:

$$P_C = \frac{J_{ph}}{J_{ph,sat}}. \quad (4)$$

Figure 3.3a shows that the collection probability P_C retains very high values under short-circuit ($P_{C,SC}$ = 97.7 %, blue circle), and maximum power conditions ($P_{C,MP}$ = 91.8 %, red cross), followed by a considerable drop once the voltage approaches open-circuit conditions ($P_{C,OC}$ = 7.03 %), which is indicative of an exceptional charge extraction and at the same time, moderate charge carrier recombination losses. In the next step, the PM6:Y6 solar cells were tested under varying light intensities I by measuring light intensity dependent short-circuit current density and open-circuit voltage in order to qualitatively determine the dominant type of non-geminate recombination (**Figure B4**). The light intensities were decreased by neutral density filters. The relationship between the J_{SC} and I ($J_{SC} \propto I^{\alpha}$) has been used to calculate the exponent of $\alpha = 0.92 \pm 0.02$. Since the devices show exceptional charge extraction under short-circuit conditions ($P_{C,SC}$ = 97.7 %), it can be hypothesized that the influence of bimolecular recombination on the J_{SC} is limited and it has to be further noted that deviations in the exponent ($\alpha < 1$) can also be caused by space charge effects.[116,117] Overall, these considerations constrain the predictive abilities of this type of measurement on the recombination dynamics. To better understand the recombination processes, the relationship between the V_{OC} and the light intensity I was also determined.[34] The V_{OC}-ln(I)-plot exhibits a slope of s = 1.02 ± 0.03 kT/q, where k is the Boltzmann constant, T is the absolute temperature (T = 300 K), and q is the elementary charge. In order to rule out the effect of leakage on the slope of the V_{OC}-ln(I)-plot, the J-V curves at different light intensities were plotted and analyzed (**Figure B4c,d)**. This result indicates that bimolecular recombination is the dominant recombination mechanism. However, other types of recombination such as bulk ($s > 1$ kT/q) and surface trap-assisted ($s < 1$ kT/q) recombination should also be taken into account as loss mechanisms, most notably because the opposite influence of surface and bulk trap-assisted

recombination on the slope s could cause slopes of $s \approx 1\ kT/q$, which could be falsely attributed to pure bimolecular recombination.[64] Therefore, a more in-depth analysis based on capacitance spectroscopy was carried out to obtain quantitative results.[65,66,118]

The capacitance of the PM6:Y6 BHJ, C_b, was used to determine the charge carrier density n and the effective mobility μ_{eff} of the studied solar cell under any operating conditions (**Figures B8 and B10;** a detailed description of obtaining the effective mobility is provided in the SI).[28,68] Under forward bias conditions, a carrier density of $n > 10^{17}$ cm^{-3} was observed, placing the n in this system at the upper end of high performing NFA blends.[119] Additionally, the effective mobility ($\mu_{eff} \approx 1 \times 10^{-4}$ cm^{2}V^{-1}s^{-1}) determined using the procedure described in the SI is comparable to other high performing NFA as well as fullerene blend systems.[28] Furthermore, it is assumed that the recombination current density ($J_{rec} = J_{ph,sat} - J_{ph}$) is a superposition of the three aforementioned recombination mechanisms:

$$J_{rec} = J_{bm} + J_{t,b} + J_{t,s} = qL\left(\frac{n}{\tau_{bm}} + \frac{n}{\tau_{t,b}} + \frac{n}{\tau_{t,s}}\right) = qL\left(k_{bm}n^2 + k_{t,b}n + k_{t,s}(V_{OC})\right). \quad (5)$$

Here L is the active layer thickness, τ is the charge carrier lifetime, and k is the recombination coefficient of the three different recombination mechanisms (bm: bimolecular; t,b: bulk trap-assisted; t,s: surface trap-assisted). It was possible to obtain the recombination coefficients by reconstructing the recombination current density obtained using the *J-V* characteristics from the charge carrier density n and the effective mobility μ_{eff} (**Figure B6**). The carrier density, effective mobility, voltage, and dielectric constants were used as input parameters, while the reduction factor (ξ), bulk-trap density ($N_{t,b}$) , and surface-trap density ($N_{t,s}$) were the fitting parameters. Based on these results, it can be confirmed that bimolecular recombination is the dominant non-geminate recombination mechanism, while bulk trap-assisted recombination is negligible, and surface trap-assisted recombination has only a very limited contribution at high

forward biases.[120] Overall, the dependence of bimolecular recombination on the applied bias and the charge carrier density is less pronounced and the values for the respective coefficients are relatively small (k_{bm} = 3.0 – 5.8 × 10^{-13} cm^3/s) in comparison to other high performing NFAs and up to one order of magnitude lower than that for high performing fullerene solar cells.[28,121,122] In addition, open-circuit voltage decay (OCVD) measurements (also referred to as transient photovoltage decay) were conducted as a second technique to analyze and confirm the recombination dynamics, since other approaches relying on the electron and hole mobility determined via SCLC are not viable due to the questionable mobility values (**Figure B8**).[123,124] This technique yields a higher value for the bimolecular recombination coefficient when compared to the results obtained from the capacitance spectroscopy analysis ($k_{bm,OCVD}$ = (4.54 ± 0.15) · 10^{-12} cm^3/s vs. $k_{bm,CS}$ = 3.0 – 5.8 · 10^{-13} cm^3/s). However, such a trend (i.e. $k_{bm,OCVD} > k_{bm,CS}$) between these two types of measurement techniques has been observed and reported in previous studies for fullerene and NFA solar cells.[28,118] Nonetheless, the extraction of charge carriers has to also be quantified to obtain a comprehensive understanding of the processes in the studied devices.

To gain quantitative insights into the charge carrier extraction dynamics, the effective extraction time, τ_{ex}, was determined under the assumption that a charge carrier needs to traverse, on average, half of the PM6:Y6 active layer thickness until it reaches one of the electrodes. Furthermore, the active layer is treated as an effective medium[29] and the following relationship was used:

$$\tau_{ex} = \frac{qLn}{J}, \quad (6)$$

where L is the active layer thickness, q is the elementary charge, n is the charge carrier density, and J is the current density obtained from the *J-V* curves (detailed derivation is given in the

Supporting Information Equations S21-S23). The effective extraction time τ_{ex} can then be directly compared to the effective charge carrier lifetime τ_{rec}, which can be accessed by re-arranging **Equation 5** (**Figure 3.3b**).[118] Interestingly, extraction is at least two orders of magnitude faster than recombination over most of the operating conditions. Only at high forward biases, approaching V_{OC}, do the effective extraction and charge carrier lifetimes converge. This observation correlates well with the high photocurrents J_{ph} and collection probabilities P_C retained under forward bias, as displayed in **Figure 3.3a**. In addition, the voltage dependent competition factor θ was calculated by taking the ratio of the effective extraction and recombination times ($\theta = \tau_{ex}/\tau_{rec}$) (**Figure 3.3c**).[29] A smaller competition factor has been shown to correlate to higher FF.[28,29] In essence, the collection probability P_C and the quantitative analysis based on capacitance spectroscopy show that the PM6:Y6 BHJ device exhibits exceptional extraction coupled with moderate bimolecular recombination losses, which is the basis for the high *FF* and J_{SC} observed. While the detailed analyses of extraction and recombination processes in PM6:Y6 provide sufficient evidence on the bulk electronic characteristics, much of these favorable charge carrier properties are expected to originate from the BHJ morphology. To confirm this, we carried out detailed morphological and structural characterization of PM6:Y6 blends at different length scales.

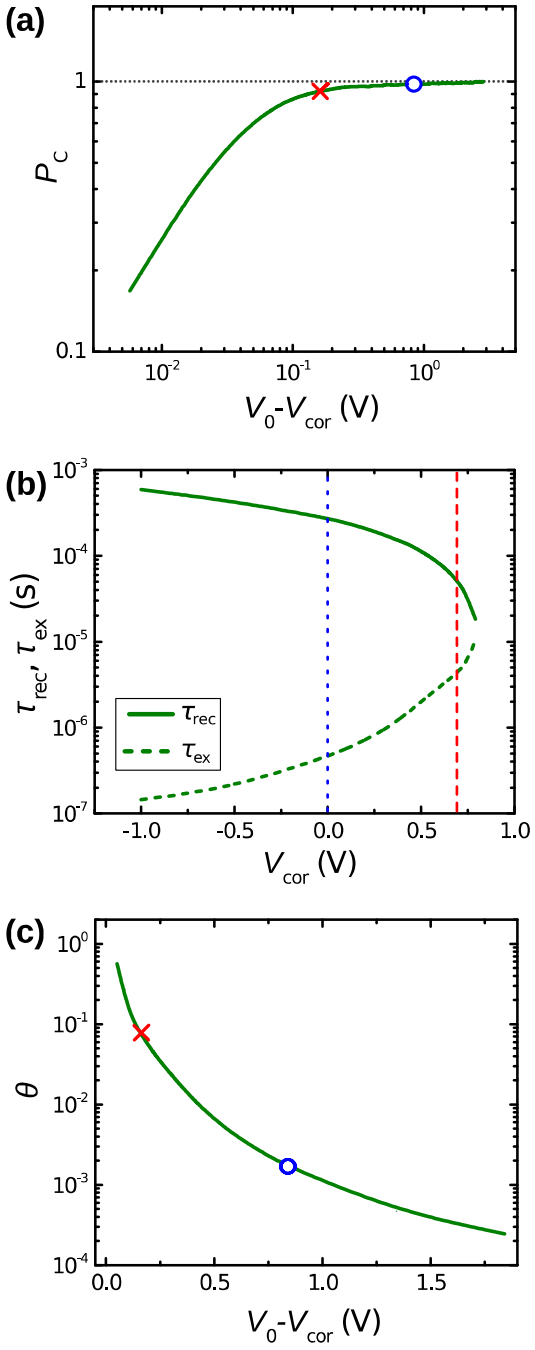

Figure 3.3. (a) Collection probability P_C, (b) charge carrier lifetime τ_{rec} and extraction time τ_{ex}, as well as (c) voltage dependent competition factor θ of the investigated solar cells. Short-circuit (blue circle) and maximum power (red cross) conditions are highlighted by the blue and red dotted vertical lines in (b), respectively.

The BHJ morphology has significant consequences on the device performance.[16,125–127] To gain detailed insights into the morphology of the PM6:Y6 blend at different length scales, three different techniques were used: photo-conductive atomic force microscopy (pc-AFM, sub-μm to μm) for visualizing the photoconductive hole and electron rich domains on the film surface, Grazing-Incidence Wide-Angle X-ray Scattering (GIWAXS) for probing the long-range structural order (ca. 100's nm) in the bulk of the blend film, and one and two dimensional (1D, 2D) solid-state-NMR for elucidating the D:A inter- and intramolecular interactions at sub-nm to nm distances. In a pc-AFM measurement, an electrically conductive Platinum-Chromium coated tip was used to scan the surface of photoactive layers using a white light source, which allows to map out the photo-responsive features in the PM6:Y6 blend films. The topography images (**Figure B9a,b**) show features amounting to small root-mean-square (RMS) roughness values (~ 0.8 nm) and the photocurrent image (**Figure B9c,d**) reveals small phase separated domain sizes (ranging from 20-30 nm) of hole (PM6) and electron rich (Y6) regions on the film surface in comparison to other reported blends.[16,126–130] Such a small degree of phase separation can explain the efficient charge separation and moderate recombination in the blend.[34,70,125,131–133] Next, in order to characterize the ordered regions in the PM6:Y6 blend film, we investigated the GIWAXS of the blend film **(**Supporting Information, **Figure B10)**. As was also previously reported for this blend[111], the GIWAXS pattern of PM6:Y6 showed that the blend displays face-on orientation which can be beneficial for charge transport in the direction normal to the substrate surface.[134,135] A detailed discussion of the GIWAXS analyses in the blend can be found in the SI.

Several theoretical and experimental studies have suggested that the nature of the D:A interactions can affect the rates of charge transfer and recombination[48,69,72], electronic

coupling[39], charge generation[39,69], and charge delocalization[136] — all of which can in turn influence the loss mechanisms in an OSC. While the correlation between the D:A interactions in a blend and bulk optoelectronic properties can be highly useful to understand the device performance, it is rarely studied for polymer:NFA-based BHJs. Here, solid-state ^{19}F MAS NMR spectroscopy has been employed to obtain atomic-level insights about the inter- and intramolecular interactions of the PM6:Y6 BHJ films. Solid-state NMR spectroscopy provides information on local structures and intermolecular interactions at sub-nm to nm distances, which could be related to both ordered and disordered regions of OPV blends. The isotropic chemical shifts and dipole-dipole couplings are sensitive to inter- and intramolecular interactions and relative orientations of donor and acceptor molecules in the BHJ morphologies. These interactions can be used, in particular, to measure internuclear distances in the absence of long-range structural order by measuring and analyzing heteronuclear dipolar couplings in heterogeneous soft matter materials.[51–53] For example, quantitative insights into the ordered and disordered regions in organic semiconductors and interfacial contacts in BHJs have been previously attained by solid-state NMR analyses in conjunction with X-ray scattering measurements and DFT calculations. [80,133,138–140]

The 1D and 2D ^{19}F MAS NMR spectra of PM6, Y6, and the PM6:Y6 blend were analyzed and compared in order to understand the changes in the local environments of ^{19}F sites in PM6 and Y6 upon BHJ formation. The intrinsic high sensitivity due to 100% natural abundance and large chemical shift range associated with ^{19}F MAS NMR enabled the local environments of ^{19}F sites in PM6 and Y6 to be distinguished and assigned (**Figure 4.4**). The ^{19}F signal at -131 ppm (**Figure 4a**) was attributed to local environments of ^{19}F sites in fluorinated thiophene groups of PM6 backbone moieties. In contrast, the ^{19}F MAS NMR spectrum of Y6 exhibited

different distributions of signals that are only partially resolved in the range between -115 ppm and -130 ppm (**Figure 4.4b**). These distributions of ^{19}F chemical shifts and signal intensities were attributed to the ^{19}F sites in different Y6 backbone structures, which is consistent with the presence of distinct structural orders that co-exist in the Y6 material as previously characterized by Yuan et. al. using GIWAXS measurements and analysis.[111] To confirm this analysis, 2D $^{19}F\{^{19}F\}$ spin-diffusion (SD) experiments[141] were carried out in order to identify and distinguish whether or not these ^{19}F pairs are spatially proximate to each other at sub-nm to nm distances (**Figure B11**). In a 2D $^{19}F\{^{19}F\}$ spin-diffusion experiment, the ^{19}F magnetization is allowed to exchange between different ^{19}F sites of spatially close ^{19}F nuclei for a given mixing period, which leads to self- and cross-correlation intensities. The self-correlation intensities at the diagonal of the 2D $^{19}F\{^{19}F\}$ correlation spectrum of Y6 acquired using shorter mixing period of 100 ms (**Figure B11**) indicate that this mixing time is not adequate enough for the magnetization exchange to occur between different ^{19}F sites. At a relatively longer mixing time of 1 s (**Figure B11b**), the cross-correlation intensities are observed between ^{19}F signals at -120 and -124 ppm confirming the exchange of magnetization between different ^{19}F sites in Y6 backbone moieties. These cross-correlation intensities at very long mixing times (> 500 ms) were expected to originate from weak ^{19}F-^{19}F dipole-dipole interactions. This further confirms the spectral assignments of signals at -120 and -124 ppm to ^{19}F sites in different endgroups of Y6 rather than two ^{19}F sites in *ortho* position to each other within the same endgroup. Otherwise strong cross-correlation intensities at much shorter mixing times due to efficient magnetization exchange between ^{19}F sites that are close to each other would be observed. To further corroborate this analysis, the ^{19}F chemical shifts of neat PM6 and Y6 moieties were compared with analogous chemical shifts in the PM6:Y6 blends

(**Figure 4.4c**). Interestingly, the ^{19}F signals of Y6 at -120 ppm displaced towards a lower frequency and at -124 ppm displaced towards a slightly higher frequency that leads to a relatively narrow distribution of signal intensities centered at -123 ppm. This indicates the improved structural order of Y6 molecules accompanied by subtle differences in the local environments of ^{19}F sites in the fluorinated endgroups of Y6 moieties in the PM6:Y6 blend. By comparison, the ^{19}F chemical shift of fluorinated thiophene groups in the PM6 polymer remains at -131 ppm, which reveals the retained organization of the thiophene endgroups in the PM6 polymer upon blend formation with Y6. In addition, the 2D $^{19}F\{^{19}F\}$ correlation spectra of PM6:Y6 (**Figure B11c,d**) exhibited self-correlation intensities exclusively along the diagonal for the spectra recorded using short and long mixing times (100 ms, 1 s) confirming that there is no magnetization exchange between ^{19}F sites in PM6 and Y6. This rules out, at least in part, the likelihood of Y6 backbone moieties in between the π–π stacked PM6 polymer chains and confirms the lack of close contact between the acceptor moieties on the Y6 and the PM6 backbones.

From a combined investigation of the morphology using the aforementioned three different techniques, we can deduce important insights about the structural arrangement of the PM6:Y6 blend. Firstly, the phase separation of donor and acceptor regions at smaller length scales, as revealed by pc-AFM, results in moderate recombination and efficient charge separation. Secondly, GIWAXS measurements show that the blend displays good π-π stacking, which has been shown to be beneficial for charge transport.[134,135]. Although X-ray scattering and pc-AFM techniques are capable of unveiling such structural details at μm to 10-nm length scales, these methods do not have sufficient spatial resolution to identify atomic-level information. To this end, thirdly, solid-state ^{19}F MAS NMR analyses provide

information about atomically resolved inter- and intramolecular D:A interactions. The main finding from ss-NMR is that there is no close contact between the acceptor moieties on the Y6 and the PM6 backbones. This was confirmed from the 2-D spin diffusion correlation studies, where there is clear evidence that the spins of the F atoms in the donor and acceptor do not mix with each other within a 1 nm distance. This alludes to a well-defined D:A interface. Several previously reported studies have shown that an enhanced intermixing of the donor and acceptor in a blend can be detrimental to the device performance by increasing charge recombination.[16,66,70] Therefore, the moderate recombination rates in this blend can be explained by the beneficial phase separation between the polymer and NFA, as visualized on a micron-scale by pc-AFM, and confirmed on a sub-nm to nm scale by ss-NMR. The exceptional extraction observed in the devices can be attributed to two things. First, in the neat Y6, two different packing motifs were resolved with the 1D ^{19}F ss-NMR. In the blend, only the signal from one of these two motifs dominates, which indicates a more uniform and structured packing of the Y6 molecules in the blend. Second, the 1D ^{19}F ss-NMR results indicate that the PM6 packing remains unaffected with the addition of Y6 confirming that the order of the PM6 observed in the neat film is also retained in the blend. It is worth noting that the π-π stacking peaks of PM6 and Y6 obtained from GIWAXS, as reported in the previous literature,[111] are broad and quite close to each other to definitively distinguish if the π-π stacking peak observed in the blend is coming from PM6 or Y6. In this regard, the ss-NMR observations which are sensitive to short range structures and interactions are more insightful. Ultimately, the simultaneous retention of organized PM6 and Y6 domains in the blend likely gives rise to the exceptional extraction in the devices due to the unencumbered pathways for sweeping out charge carriers via multiple unhindered charge transport pathways.

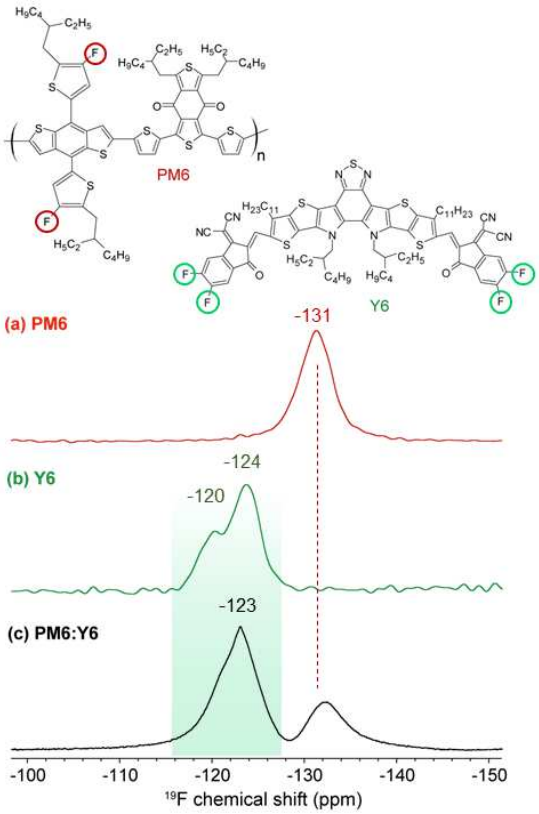

Figure 4.4. Solid-state ^{19}F MAS NMR spectra of (a) PM6, (b) Y6 and (c) PM6:Y6 blend acquired at 60 kHz and at room temperature. The distributions of ^{19}F chemical shifts in Y6 centered at -120 and -124 ppm were attributed to the distribution of different ^{19}F sites in different Y6 backbone structures. A narrow distribution of chemical shifts centered at -123 ppm in the PM6:Y6 blend indicates the changes in the Y6 backbone structures upon mixing with the PM6 polymer.

3.3. Conclusion

To summarize, the low energetic offset PM6:Y6 blend system was found to exhibit radiative and non-radiative recombination losses that are among the lower reported values in the literature (~0.485 eV). This work shows that *PCE*s of over 15% require low voltage losses, coupled with moderate non-geminate recombination and exceptionally good charge extraction ($\tau_{rec} >> \tau_{ex}$) throughout most of the relevant operating conditions of the device. An ability for the blend to retain high *FF* and J_{SC} values despite of a low energetic offset is shown to be due to a beneficial morphology as suggested by pc-AFM, GIWAXS, as well as solid-state ^{19}F

MAS NMR and 2D $^{19}F\{^{19}F\}$ correlation analyses. The moderate recombination rates in this blend can be explained by the beneficial phase separation between the polymer and NFA, as visualized on a micron-scale by pc-AFM and confirmed on a nm to sub-nm scale by ss-NMR. The exceptional extraction in the blend can be attributed to the unencumbered pathways for sweeping out charge carriers via organized PM6 and Y6 domains in the blend. These insights from atomically resolved measurements provide explanations for the moderate recombination and exceptional extraction in the studied devices with *PCE*s of over 15%.

3.4. Experimental Section

Materials: PM6 (number-average molecular weight (Mn) =106 kDa, PDI =2.4), Y6, and perylene diimide amino N-oxide (PDINO) were purchased from 1-material Inc.

Fabrication of devices: Indium tin oxide (ITO) patterned glass substrates were cleaned by scrubbing with soapy water, followed by sonication in soapy water, deionized (DI) water, acetone, and isopropanol for 20 minutes each. The substrates were dried using compressed nitrogen and placed in an oven overnight at 100 °C. The ITO substrates were treated with UV-ozone for 15 minutes and a layer of poly(3,4-ethylenedioxythiophene): poly(styrenesulfonate) (PEDOT:PSS, Clevios P VP Al 8043) was spin-coated at 3000 rpm for 40 s onto the ITO substrates. The substrates were then annealed in air at 150 ^{0}C for 20 minutes. 18 mg/mL of PM6:Y6 blend solutions were prepared with a D:A ratio of 1:1.2 in chloroform with 0.5% v/v 1-chloronaphthanene (CN). The active layers were spin-cast inside a nitrogen glovebox at 4000 rpm and annealed inside the glovebox at 110 ^{0}C for 10 minutes. The substrates were left to cool for 5 minutes and 1 mg/mL PDINO solution dissolved in methanol was spin-coated on top of the active layer. The substrates were then pumped down under vacuum (< 10^{-6} torr), and a 100 nm thick Aluminum electrode was deposited on top of the active layer by thermal

evaporation. Devices of neat materials (PM6 or Y6) were prepared using similar solid concentrations as that in the blend solution. Symmetric hole only diodes were fabricated with the following configuration: ITO/PEDOT:PSS/Active layer/MoOx/Ag. Electron only diodes were fabricated with the following configuration: ITO/ZnO/Activate layer/PDINO/Al.

Testing devices: Photovoltaic characteristic measurements were carried out inside the glove box using a high-quality optical fiber to guide the light from the solar simulator equipped with a Keithley 2635A source measurement unit. *J-V* curves were measured under AM 1.5G illumination at 100 mW cm^{-2} using an aperture of area 9.4 mm^2. Dark J-V curves were tested for analysis of SCLC measurements of hole and electron only diodes. Symmetric hole-only diodes and asymmetric electron-only diodes with low leakage currents were used for analysis.

EQE_{PV} measurements: External quantum efficiency (EQE) for all solar cells was measured using a 75 W Xe light source, monochromator, optical chopper (138 Hz), and a lock-in amplifier. Power-density calibration of the EQE characteristics was achieved using a calibrated silicon photodiode from Newport. For the sub-bandgap EQE, higher sensitivity settings were used with a longer time delay between measurement points.

Electroluminescence and EQE_{EL} Measurements: EL measurements were performed using two setups depending on the wavelength range of interest. For measurements under 1050 nm, a home-made EL spectrometer was used. The EL emission from a sample driven by a Keithley source-measure unit (model 2602A) was collected by a lens system and focused on the entrance slit of a spectrograph (Acton Research SP-500) equipped with a Si charge-coupled detector (Princeton Instruments Pixis:400). The spectra collected by the detector were corrected for the instrument response function. The correction factors were determined by measuring the spectrum of a black body-like light source (Ocean Optics LS-1). For EL

measurements in the range 900 - 1700 nm, we utilized Photon Technology International (PTI) Quantamaster fluorimeter equipped with Edinburgh Instruments EI-L Ge detector. The excitation monochromator of the fluorimeter was not used and the EL emission was generated by driving the devices by Keithley 2602 source-measure unit. An optical chopper (Thorlabs MC2000) was placed in front of the emission monochromator to make use of the fluorimeter's lock-in amplifier-based detection system. PTI Felix fluorimeter software was used for the data collection and correction of the instrumental artifacts. The efficiency of electroluminescence was obtained by applying a bias from -1 to 2V with a dual-channel Keithley 2602 to the solar cell and placing a germanium photodiode directly in front of it to collect the emission as a function of applied bias. The current running through the device and the photodiode were simultaneously measured.

Capacitance spectroscopy: Capacitance spectroscopy measurements were performed with an impedance analyzer Solartron 1260A in the dark and under 1 sun AM1.5 illumination inside a nitrogen-filled glovebox. The amplitude of the AC signal was 40 mV to ensure a negligible impact on the measured impedance.

V_{OC}-decay: The V_{OC}-decay measurements were performed with devices placed in a cryostat in vacuum. The devices were illuminated by a fast switching light source (white LED) and once the illumination was turned off, the decay of the V_{OC} was monitored with the help of an oscilloscope connected *via* a high impedance buffer to ensure the necessary sub-microsecond time resolution of the measurements under open-circuit conditions. Due to the high impedance buffer, it can be assumed that the decay of the V_{OC} over time is only due to recombination taking place within the tested solar cells under high level of excitations. The intensity of the

white LED was set to a value of 100 mW/cm^2. The measurement setup was grounded to reduce noise.

Photo-conductive atomic force microscopy (pc-AFM): Photoconductive atomic force microscopy (pc-AFM) measurements were done with an Asylum Research MFP-3D microscope sitting atop an inverted optical microscopy (Olympus, IX71). All measurements were conducted under inert atmosphere. A white light source with a power of 30 W cm^{-2} was used to generate photocurrent morphology which was recorded by an internal preamplifier (Asylum Research ORCA head model). Electrically conductive Chromium/Platinum-coated silicon probes with a spring constant of 0.2 N m^{-1} and resonant frequency of 13 kHz (Budget Sensors) were used. A light spot with 160 μm diameter was focused on the active layer of the device through an inverted optical microscope (Olympus), and the conductive tip was positioned at the center of the light spot.

GIWAXS measurements. This measurement was performed at the Advanced Light Source at Lawrence Berkeley National Lab on the 7.3.3 beamline. The sample was scanned for 40 seconds at an incidence angle of 0.12° and a photon energy of 10 keV (λ = 1.24 Å), while under a helium environment to minimize beam damage and reduce air scattering. The width of the incident X-ray beam is about 1 mm, and silver behenate was used to calibrate the lengths in the reciprocal space. A 2D detector (PILATUS 2 M from Dectris) with a sample-to-detector distance of 276.9 mm was used to collect the images. The Nika software package for Igor (by Wavemetrics) and the Igor script WAXStools were used to process the image.[1]

Solid-state NMR spectroscopy. For solid-state NMR, thin films were prepared by spincoating the PM6, Y6, and PM6:Y6 blends on glass substrates. These thin films ware scraped off the substrates and approximately 3 mg of powdered thin films was transferred into 1.3 mm

zirconia rotors with a Vespel® cap. All solid-state MAS NMR spectra were acquired on a 21.1 T Bruker AVANCE NEO NMR spectrometer equipped with 1.3 mm H-X probehead and Bruker variable temperature (VT) control unit to regulate probe temperature. One-dimensional ^{19}F MAS NMR spectra of PM6, Y6 and PM6:Y6 were acquired under 60 kHz MAS conditions using 128 co-added transitions using a T_1 relaxation delay of 20 seconds, corresponding to a total experimental time of 45 minutes each. The ^{19}F chemical shifts of fluorinated aromatic end groups are consistent with the analogous chemical shifts reported in the literature.[142] The coexistence of distinct different structural orders[143] in Y6 molecules, and inter- and intramolecular interactions between Y6 and PM6 moieties in the PM6:Y6 blends were established using 2D ^{19}F MAS NMR spectroscopy. 2D $^{19}F\{^{19}F\}$ spin diffusion experiments of Y6 and PM6:Y6 were acquired using 100 ms, 500 ms and 1 s mixing times to probe short and long-range ^{19}F-^{19}F proximities, respectively. 2D spectra were acquired using 128 t_1 increments, each with 8 co-added transients, with a rotor-synchronized t_1 increment of 16.66 μs, corresponding to an overall experimental time of 6 h each. Solid-state ^{19}F chemical shifts of PM6, Y6 and PM6:Y6 materials were calibrated to ^{19}F chemical shifts of neat $CFCl_3$ (^{19}F, 0 ppm) as an external reference.

Chapter 4

The Role of Bulk and Interfacial Morphology in Charge Generation, Recombination, and Extraction in Non-Fullerene Acceptor Organic Solar Cells

4.1. Introduction

With polymer:non-fullerene acceptor (NFA) bulk-heterojunction (BHJ) organic solar cells (OSCs) reaching unprecedented power conversion efficiencies (PCEs) of over 18%[144], it has become essential to get an in-depth understanding of the role of bulk and interfacial morphology in the key processes determining their PCEs. However, precisely controlling and characterizing the bulk and interfacial morphology remains challenging. In this work, varying the molecular weight (M_w) fractions of donor polymer was used as a tool to exert fine control over the interfacial and bulk morphology in the high performing PM6:Y6[111] BHJ OSCs. Although a few studies[75,145,146] have previously shown that the M_w of polymers can significantly affect device performances in NFA-based OSCs, its effect on interfacial and bulk morphologies, and subsequently, the key processes ranging from charge generation to extraction remain largely unexplored.

In this work, we were able to precisely control the atomic level D:A interactions of two PM6:Y6 BHJ blend systems by varying the amount of low M_w fractions (LMWFs) of the PM6 polymer. One- (1D) and two-dimensional (2D) solid-state NMR (ssNMR) spectroscopy was used to identify and accurately characterize D:A inter- and intra-molecular interactions. Furthermore, ssNMR results were corroborated by morphological characterization using grazing incidence wide angle scattering (GIWAXS), photo-conductive AFM (pc-AFM), and

resonant soft x-ray scattering (RSoXS) techniques. Therefore, the characterization of morphology at different length scales (sub-nanometer to sub-micrometer) enabled a comprehensive understanding of the bulk and interfacial morphology. Subsequently, the role of such morphological differences on the processes dictating device performances could be established. Thus, this study provides an understanding of two fundamental and complex questions that are highly relevant to the OSC community: i) the role of the nature of the D:A BHJ interface on charge generation and recombination processes, and ii) the morphological factors affecting charge extraction and transport in BHJ OSCs.

4.2. Results and Discussions

4.2.2. Chemical Structures, Energy Levels, and Device Configuration

Figure 4.1 shows the energy levels, device configuration, chemical structures, and the schematic representations of four different PM6 polymer batches that were tested for this study. The PM6 donor polymer batches comprised of high and low number average molecular weight (M_n) fractions, as depicted in the green and red illustrations in **Figure 4.1**c. The schematic pathway to the synthesis of the PM6 donor polymers and the extraction procedures for obtaining the different batches of polymers are described in Appendix C (Figure C1-C3). From gel permeation chromatography (GPC) (Table C1), it was found that the different PM6 batches contain high and low M_w fractions of M_n = 40 kDa and M_n = 2.5 kDa, respectively. It should be noted that the LMWFs with a M_n = 2.5 kDa consists of about 4 PM6 monomers, whereas the HMWFs with a M_n = 40 kDa consists of about 64 PM6 monomers. The batches vary in the ratio of low and high molecular weight fractions (HMWFs) present, and are referred to as 1%, 7%, 9%, and 52% LMWF PM6 donor polymers as shown in **Figure 4.1**c.

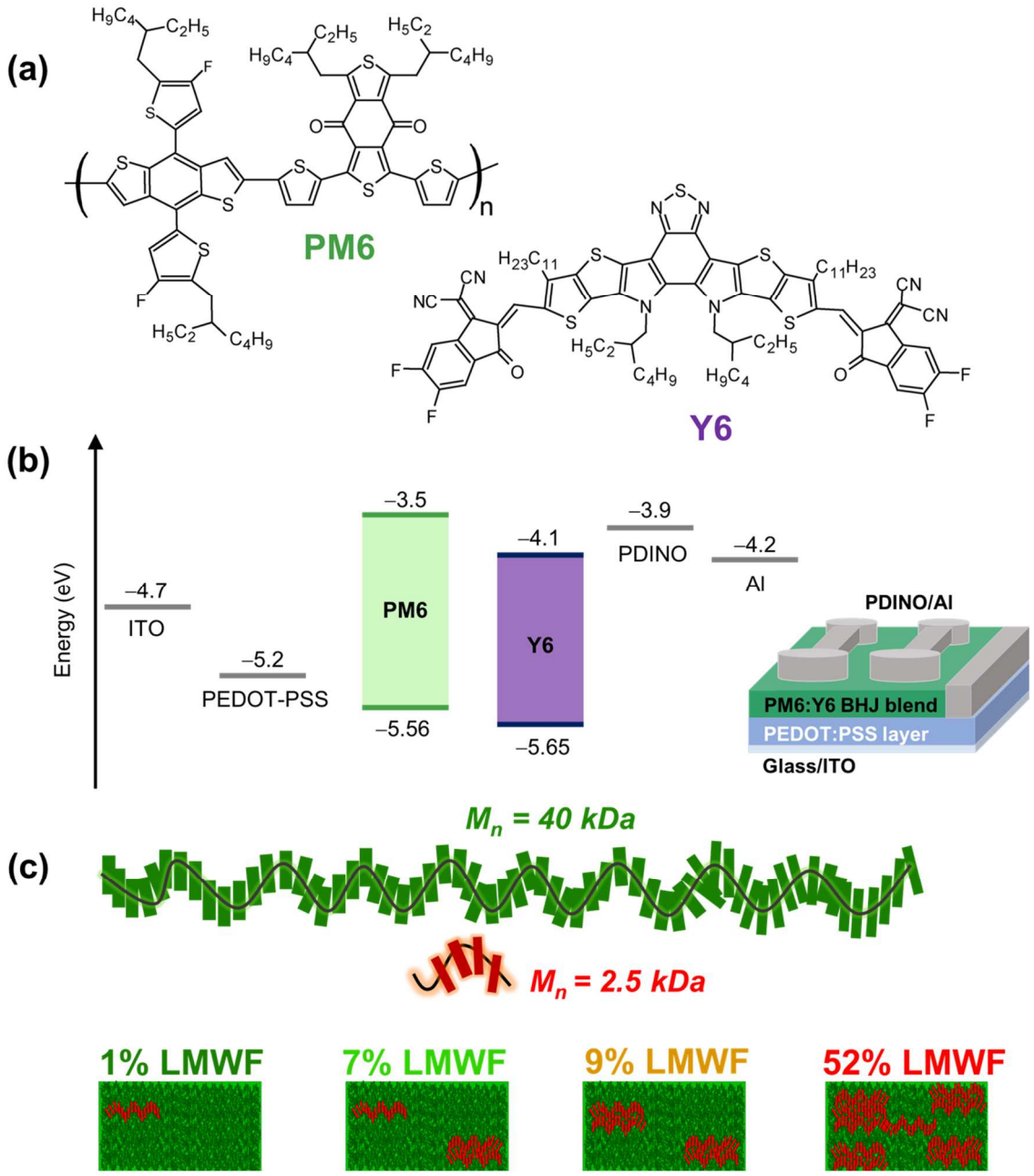

Figure 4.1. (a) Chemical structures of PM6 and Y6. (b) Energy levels of PM6, Y6, and hole and electron transport layers as well as the device architecture used. (c) Schematic representation of the different LMWFs (1%, 7%, 9%, and 52%) in the PM6 polymer batches used.

4.2.3. Solar Cell Characteristics

We begin this study by testing the four different batches of PM6 donor polymers containing 1%, 7%, 9%, and 52% LMWFs with the Y6 NFA. To ensure a systematic comparison between the four batches, the device configuration, D:A blend ratios, processing solvents, and

annealing conditions for the devices across the different PM6 batches were kept the same. As depicted in the box plots in **Figure 4.2**a, the PCE decreases with increasing LMWFs (1%, 7%, 9%, and 52%) of the PM6 polymer in the blends from about 15% to 5% (Table S2). To further investigate why the PCE drops with increasing LMWFs, we examine the *J-V* curves of the different LMWF blends in further detail. **Figure 4.2**b shows the *J-V* curves at 1 sun illumination (100 mW cm^{-2} AM 1.5) of the four different blend systems. Since the 7% and 9% LMWF blends do not show large differences in the PCEs, an in-depth study was conducted to understand the reasons behind the PCE differences in the 1% and 52% LMWF blend systems. The large drop in PCEs from 15% to 5% in the 1% and 52% LMWF blends was found to be dictated by a reduction in the *FF* and J_{SC} values. The small differences in the V_{OC} values can be explained by the decrease in the S_1-CT offset in the 52% LMWF blend (Figure C4). **Figure 4.2**c shows the external quantum efficiency (EQE) spectra of the 1% and 52% LMWF blends. Furthermore, the integrated J_{SC} values were found to be within 4% of the average J_{SC} values measured via the *J-V* characteristics. A combined simulation and experimental approach[32] was used to obtain the internal quantum efficiencies (IQEs) for the 1% and 52% LMWF blend systems. The difference in IQEs in going from the 1% LMWF to the 52% LMWF blend systems confirms the decreased charge generation and extraction efficiencies.

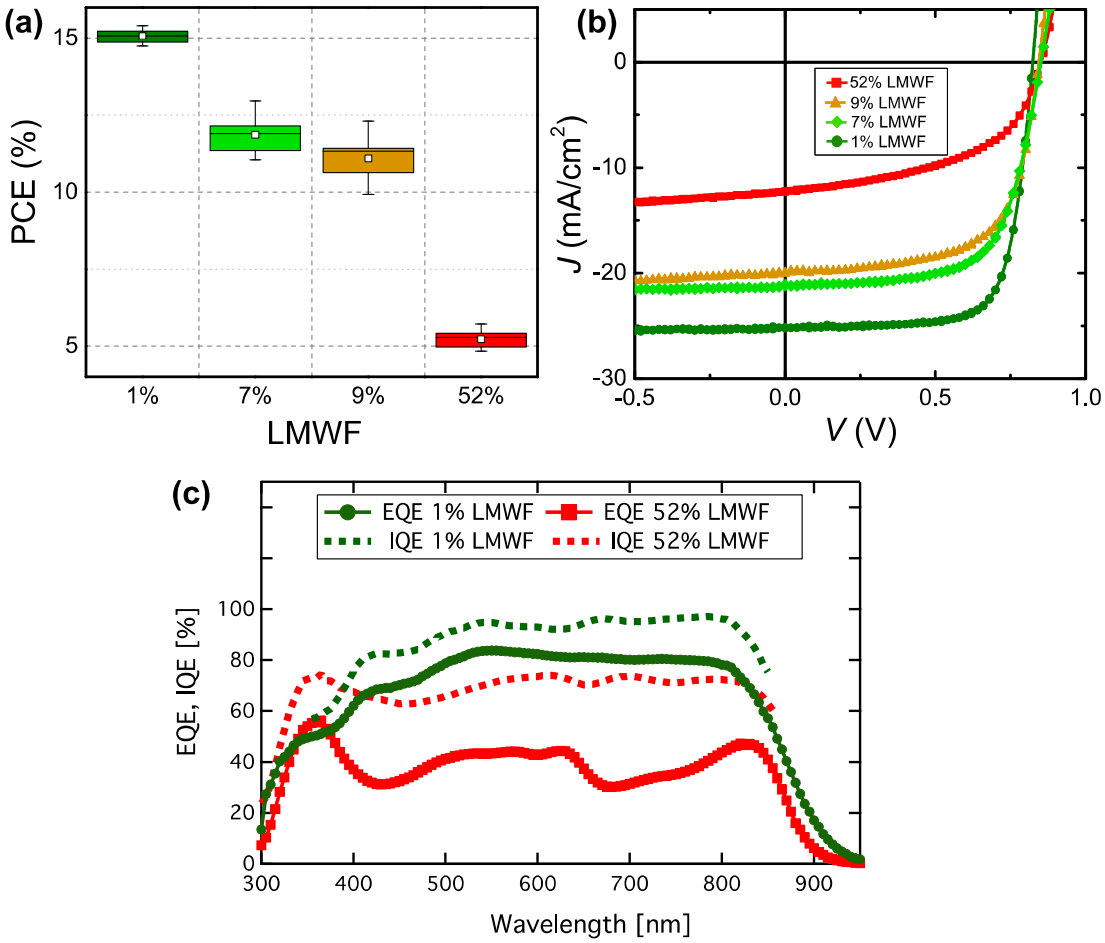

Figure 4.2. (a) Box plots showing PCE averages for the 1%, 7%, 9%, and 52% LMWF PM6:Y6 blends. (b) *J*-*V* curves of the 1%, 7%, 9%, and 52% LMWF PM6:Y6 blends and (c) EQE and IQE spectra of the 1% LMWF and 52% LMWF PM6:Y6 blends.

4.2.4. Morphological Characterization

Next, we establish the interfacial and bulk morphological differences in the 1% and 52% LMWF PM6:Y6 blend systems. Differences in OSC device performances have been shown to be largely affected by the BHJ morphology.[20,39,53,125,144,147,148] Therefore, by characterizing the bulk and interfacial morphology in the two blend systems, we can identify the effects of these differences on the processes ranging from charge generation to extraction that dictate device performances.[16,20,39,125,126,149,150] To obtain a comprehensive picture of the BHJ

morphology in the two PM6:Y6 blends from sub-nanometer to sub-micrometer length scales, four techniques as depicted in **Figure 4.3**, were used.

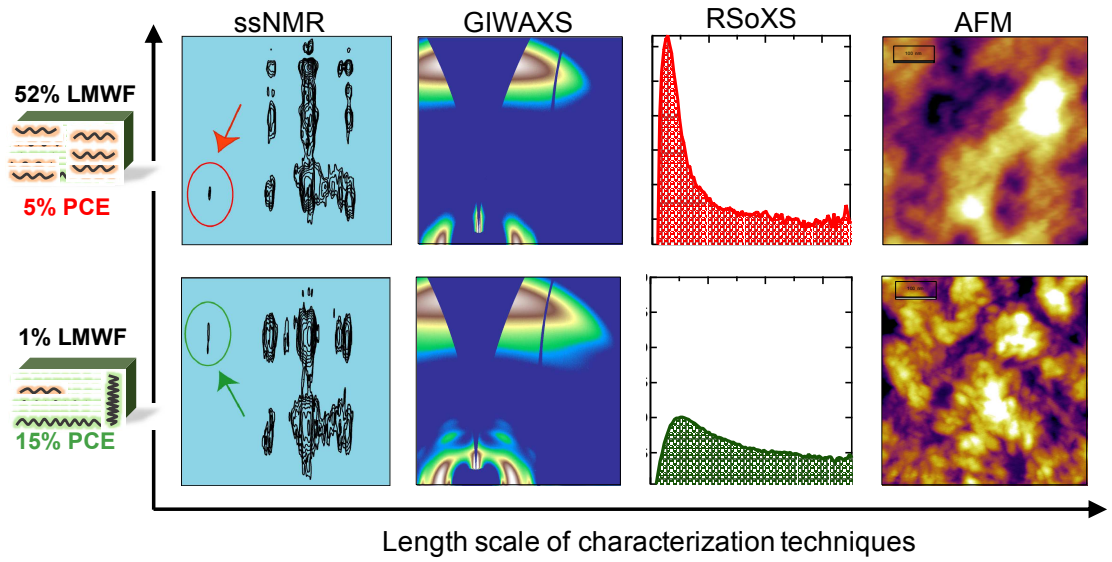

Figure 4.3. Four techniques ranging from sub-nm to sub-µm length scales used for the characterization of 52% LMWF and 1% LMWF PM6:Y6 blends. Detailed analyses of the measurement techniques are given in the Supporting Information (Figure C5-C12).

First, photo-conductive atomic force microscopy (pc-AFM) was used to visualize the domain sizes and the hole and electron rich domains on the BHJ blend film surfaces at sub-micrometer length scales. Figure C5a,b shows the topography images of the 1% and 52% LMWF blends. The high resolution 500 × 500 nm sized images show identifiable differences in the domains of the two blend films. The 1% LMWF blend exhibits smaller and more defined, grain-like features amounting to small root-mean-square (RMS) roughness values of ~0.9 nm. The 52% LMWF blend displays larger and less defined features with higher roughness values of ~1.7 nm. The consequence of these differences is shown in the pc-AFM images in Figure C5c. In a pc-AFM measurement, an electrically conductive platinum-chromium coated tip is used to scan the surface of the photoactive layers of the devices under white light illumination such that features of high and low photocurrents in the two blend

films corresponding to hole or electron rich regions can be spatially mapped. The comparison of the pc-AFM images under white light illumination elucidate two advantages in the nanoscale morphology of the 1% LMWF blend films: an increase in the nanoscale photocurrent; consistent with the higher J_{SC} values of the tested devices, and a continuous interpenetrating network of electron and hole rich domains suggesting finely phase-separated donor and acceptor networks throughout the film surface.

Second, grazing incidence wide-angle X-ray scattering (GIWAXS) was used to probe differences in the long-range structural order (ca. hundreds of nanometers). Figure C6 shows the GIWAXS spectra of the two blend films which reveal that both have a primarily face-on orientation. The GIWAXS 1D line cuts corresponding to the in-plane (q_{xy}) and out-of-plane (q_z) scattered intensities are also shown in Figure C6, and the corresponding d-spacing, π–π and lamellae stacking distances are listed in Table S3. It was found that while the peaks corresponding to both PM6 and Y6 could be resolved in the 1% LMWF blend, the scattering peak in the 52% LMWF blend corresponding to Y6 could not be resolved. In addition, it was found that the 1% LMWF blend contained additional lamellar scattering peaks from Y6 at 0.22 q_{xy} (*d*: 2.85 nm, *Lc*: 26.30 nm) and 0.43 q_{xy} (*d*: 1.46 nm, *Lc*: 5.91 nm), which is absent in the 52% LMWF blend. Furthermore, the 1% LMWF blend was generally found to have longer crystalline coherence lengths (L_C). Therefore, we can conclude that the 1% LMWF blend exhibits a superior long-range ordering compared to the 52% LMWF blend.

Third, resonant soft X-ray scattering (RSoXS) was used to obtain information on the domain purity and the domain spacings. Figure C7 shows the Lorentz corrected and circularly averaged RSoXS profiles of the blend films, and the fitting parameters are shown in Table C4. Domain sizes of ~126 nm for the 52% LMWF blend and ~56 nm for the 1% LMWF blend

were extracted from the RSoXS profiles, which were consistent with the differences in domain sizes obtained from the pc-AFM measurements. Variations in the domain sizes between the two LMWF blends can be explained by considering the impact of the polymer viscosity on the film formation; blends containing more low M_w PM6 chains are less viscous and as a result have more time to undergo liquid-liquid transition, which delays the liquid-solid transitions to form larger domains.[75] The root-mean-square (RMS) composition variation (which is monotonically related to the domain purity) of the 1% and 52% LMWF blends were determined by obtaining the integrated scattering intensities. A higher value for the RMS composition variation indicates larger average purity of domains in the blends. In comparison to the 1% LMWF blend, it was found that the RMS composition variation was higher for the 52% LMWF blend. A high average purity has been shown to be related to a smaller D:A interfacial area due to the reduced distribution of acceptor molecules in the polymer-rich phase.[16,41,74,75] Therefore, the RSoXS data suggests that the 1% LMWF blend has an increased D:A interfacial area. This observation is consistent with the nanoscale phase separation visualized from pc-AFM where more continuously phase separated D:A interfaces can be observed in the 1% LMWF blend.

The morphological techniques discussed so far reveal differences in the long-range macroscopic features of the 1% and 52% LMWF PM6:Y6 blends. However, several theoretical and experimental studies have suggested that the nature of the D:A interactions can affect the rates of charge transfer and recombination,[48,69,72] electronic coupling,[39,151] charge generation,[39,69] and charge delocalization[136]. In this study, insights into short-range structures and D:A interactions of the 1% LMWF and 52% LMWF PM6:Y6 blends were obtained by employing multi-nuclear 1D and 2D solid-state NMR spectroscopy techniques.

Solid-state NMR (ssNMR) spectroscopy is a short-range technique that allows local structures and interactions in heterogeneous polymers and blends to be measured and distinguished at a sub-nanometer to nanometer resolution.[20,81,82,133,140,152–154] For example, ^{1}H, ^{13}C, and ^{19}F chemical shifts and line-shapes are sensitive to local bonding environments, non-covalent interactions, and molecular conformations in π-conjugated materials.[20,80,84,155] In such materials, information on molecularly proximate and dipole-dipole coupled ^{1}H-^{1}H and ^{1}H-X pairs (X=^{13}C, ^{15}N and ^{19}F etc.) at sub-nano to nanometer distances can be obtained by analyses of powerful 2D correlation NMR spectra. In addition, *in situ* and *ex situ* NMR techniques have been employed to understand the phases transitions, crystallization, melting and solid-to-solution transformations or vice-versa.[139,143,156,157] Furthermore, combined X-ray scattering, ssNMR spectroscopy, and computational modeling approaches have shown enormous potential to elucidate the structures of π–conjugated systems[82,84] and packing interactions in polymer:fullerene BHJ blends.[133] Such multi-technique approaches are seldom applied to study BHJ blends with non-fullerene acceptors due to the presence of structurally identical donor and acceptor moieties that lead to intrinsically complex compositions which are difficult to deconvolute. However, in this case, by combining careful data processing and analysis with information gained from powerful 1D and 2D NMR spectroscopy techniques, valuable information on the nature of the D:A inter- and intra-molecular interactions in the 1% and 52% LMWF blends could be obtained.

In this study, we examined different ^{1}H, ^{13}C and ^{19}F sites in the 1% and 52% LMWF PM6 donor polymers and Y6 acceptor molecules and their respective blends. Although ^{1}H ssNMR spectra benefit from intrinsically high sensitivity, severely overlapped spectra of PM6:Y6 blends hinder the identification of signals corresponding to distinct aliphatic and aromatic ^{1}H

sites (Figure C8). 1D and 2D ^{19}F ssNMR techniques have been employed to characterize the local ^{19}F sites in PM6 donor and Y6 acceptors moieties (Figure C9). Detailed insights into through-space proximities between ^{1}H and ^{13}C nuclei at sub-nm to nm distances can be obtained by analyzing and comparing 2D ^{13}C-^{1}H heteronuclear correlation (HETCOR) NMR spectra of neat molecules and BHJ blends (**Figure 4.4** and Figure C10-C12). In particular, 2D ^{1}H-^{13}C HETCOR NMR experiments facilitates spectral simplification by distributing the ^{1}H and ^{13}C signals into two frequency dimensions, which allow distinct 2D ^{13}C-^{1}H correlation intensities to be resolved. The homonuclear decoupling was applied during the acquisition of vertical indirect ^{1}H dimension using a DUBMO pulse sequence.[158,159] The 2D ^{13}C-^{1}H correlation intensities present in the 1% and 52% BHJ blends can be compared to the analogous signals in the 2D ^{13}C-^{1}H correlation spectra of neat PM6 and Y6 materials to obtain valuable information on the nature of the D:A inter- and intra-molecular interactions, as discussed below.

Figure 4.4 shows the 2D ^{13}C-^{1}H HETCOR NMR spectra of the 1% and 52% LMWF PM6:Y6 blends together with the 1D ^{13}C{^{1}H} CP-MAS spectra of neat Y6, PM6, and the PM6:Y6 blends (**Figure 4.4a,c**). Aliphatic and aromatic ^{1}H and ^{13}C signals associated with PM6 and Y6 molecules are shown in colored circles depicted in their schematic structures. Analogous 2D ^{13}C-^{1}H HETCOR NMR spectra of neat Y6 material and different batches of PM6 polymers were analyzed and compared (Figure C11-C12). In the 2D ^{13}C-^{1}H spectra of the 1% LMWF (high performing) PM6:Y6 blend shown in **Figure 4.4**b, correlation signals between ^{13}C (13, 15 ppm) and ^{1}H (1.5 ppm) and between ^{13}C (25-35 ppm) and ^{1}H (1.7-2.5) originate from –CH_3 and –CH_2 groups of alkyl side chains, respectively. Of particular interest is the 2D correlation signal between ^{13}C (13 and 15 ppm) and aromatic ^{1}H signals (6-7.5 ppm)

depicted in the green color box, which indicates the close intermolecular proximities between PM6 and Y6 molecules. By comparison, in both PM6 and Y6 molecules, the C-H moieties in the aromatic core are relatively far from the terminal methyl groups in aliphatic chains and the intramolecular C-H dipolar interactions are less likely to contribute to such 2D correlation peaks. This can be verified by the 2D HETCOR NMR spectra of neat Y6 and PM6 compounds shown in Figure C11-C12, which exhibited no such correlation peaks between aliphatic and aromatic C-H moieties. In addition, 2D correlation signals between aromatic ^{13}C (120-150 ppm) and aliphatic ^{1}H (1-2.5 ppm) in **Figure 4.4**b are expected to originate from both inter- and intra-molecular through space proximities between PM6 and Y6 molecules in BHJ blends. However, these signals are partially overlapped and convoluted to be accurately distinguished and identified, which hinders the ability to extract information about the intermolecular interactions between PM6 and Y6 molecules. Nevertheless, well-resolved 2D correlation intensity between the carbonyl groups of Y6 (^{13}C, 186 ppm, purple dot) and aliphatic ^{1}H signals of PM6 (1.2-1.5 ppm) depicted in the green oval (**Figure 4.4**b) indicates the close spatial proximity between the Y6 aromatic groups and PM6 sidechains. In contrast, no such 2D correlations between ^{1}H (1.2 -1.5 ppm) and ^{13}C signals (186 ppm - purple dot in Y6, and 178 ppm - ivory dot in PM6) were detected in the 2D HETCOR NMR spectra of the neat Y6 and PM6 compounds (Figure C11-C12). These results indicate the close (< 1 nm) intermolecular proximity between PM6 and Y6 molecules in the 1% LMWF PM6:Y6 blend.

Next, to probe the D:A interactions in the 52% LMWF (low performing) PM6:Y6 blend, we analyzed and compared the 1D $^{13}C\{^{1}H\}$ CP-MAS and 2D ^{13}C-^{1}H HETCOR spectra of neat compounds and the BHJ blend (**Figure 4.4**c,d). Although the 2D correlation signals between ^{13}C (12, 15 ppm) and ^{1}H (1.7 ppm) and between ^{13}C (24-35 ppm) and ^{1}H (2.2-2.5 ppm) sites

originating from $–CH_3$ and $–CH_2$ groups of alkyl side chains are observed, no such 2D correlation intensities associated with the intermolecular interactions between PM6 and Y6 molecules are detected in the low performing blend (dashed rectangle). Unlike in the 1% LMWF blend, the 2D correlation intensity associated with carbonyl groups of Y6 (^{13}C, 186 ppm) and aliphatic ^{1}H signals (1.2-1.5 ppm) of PM6 shown in the green oval (**Figure 4.4**b) was not detected in the 2D ^{13}C-^{1}H correlation spectrum of the 52% LMWF blend (**Figure 4.4**d). Instead, a correlation intensity between ^{13}C signals of carbonyl groups and aromatic ^{1}H signals (~7 ppm) of Y6 aromatic groups (depicted within the red oval) was observed, which is expected to arise from the intramolecular ^{13}C-^{1}H proximity within Y6 molecules as shown in the 2D ^{13}C-^{1}H correlation spectrum of neat Y6 (Figure C12b). The absence of 2D ^{13}C-^{1}H correlation peaks corresponding to the D:A intermolecular interactions in the 52% LMWF blend suggests the lack of close D:A interactions, unlike those found in the 1% LMWF blend.

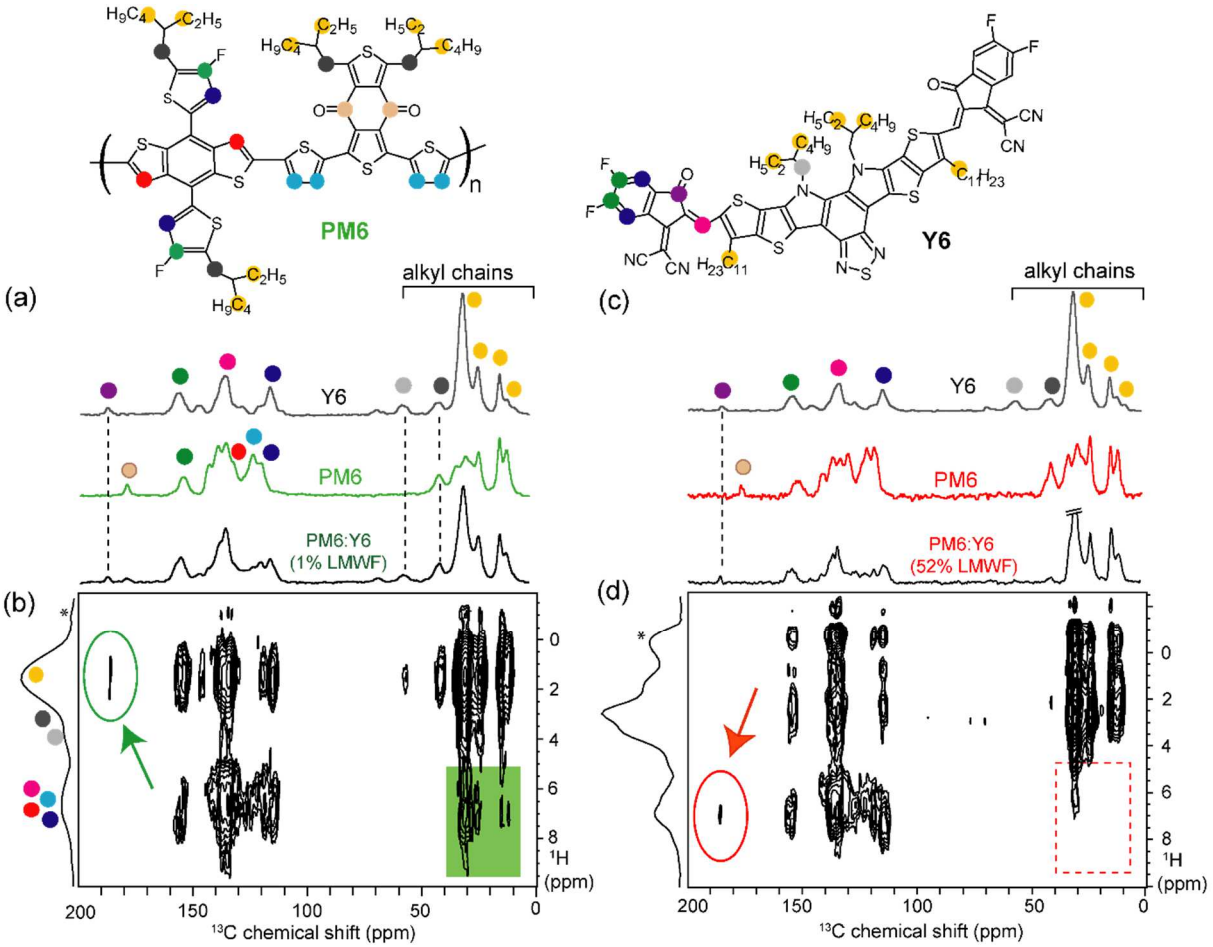

Figure 4.4 Comparison of 1D $^{13}C\{^{1}H\}$ CP-MAS spectra of Y6, PM6 and PM6:Y6 blends with (a) PM6:Y6 (1% LMWF), (b) PM6:Y6 (52% LMWF) and 2D ^{13}C-^{1}H heteronuclear correlation NMR spectra of (c) PM6:Y6 (1% LMWF), (d) PM6:Y6 (52% LMWF) acquired at 9.4 T (12.5 kHz MAS) with 4 ms of CP contact time. *denotes the carrier frequency of ^{1}H homonuclear decoupling.

To summarize the morphological findings, systematic analyses using the four characterization techniques (from sub-nanometer to sub-micrometer length scales) revealed bulk and interfacial morphological differences in the 1% and 52% LMWF PM6:Y6 blends. Notably, analyses of 2D ^{13}C-^{1}H HETCOR spectra revealed intermolecular ^{13}C-^{1}H proximities between PM6 and Y6 molecules in the 1% LMWF blend, which were absent in the 52% LMWF blend. Although these results imply different intermolecular packing arrangements in PM6:Y6 blends with different LMWFs of the PM6 donor polymers, development of complete

three-dimensional packing models of such intrinsically complex blends using ssNMR results alone is less straightforward and is beyond the scope of this work. Nevertheless, ssNMR results were found to successfully resolve crucial differences in the D:A interactions between the two blends. Additionally, from a combination of the four morphological techniques, we established that the high-performing (1% LMWF) BHJ blend has better long range ordering, a more continuous and optimal D:A phase separation, larger D:A interfacial area, and closer D:A interactions. We will now investigate the impact of these bulk and interfacial morphological differences on the charge transfer dynamics at the D:A interface, as well as the non-geminate recombination and extraction dynamics of the 1% and 52% LMWF PM6:Y6 blends.

4.2.5. Charge Generation Dynamics

The use of transient absorption (TA) spectroscopy allows us to fully-characterize the charge generation processes in the two different LMWF PM6:Y6 blends. Thus, a detailed understanding of the effect of BHJ morphology on the charge generation dynamics can be obtained. For the simplest picture, we begin by selectively exciting Y6 in the blends with an 800 nm pump pulse to induce hole transfer to PM6. Importantly, great care was taken to ensure that identical excitation densities were used across all TA measurements for both blends (n_0 ~$1x10^{17}$ cm^{-3}; highly comparable to the carrier densities measured in the following section under operating conditions), allowing for a direct comparison of the resulting photophysics. The TA spectra and kinetics of the 1% LMWF blend after excitation with a low fluence of 0.45 $\mu J/cm^2$ are shown in **Figure 4.5**a,b. At 0.2 ps, we observe the presence of a positive feature between 700 – 900 nm and a narrow photo-induced absorption (PIA) at 920 nm. By

referencing the TA of a polystyrene:Y6 1:1.2 film (Figure C13), we attribute the positive feature to the ground state bleach (GSB) of Y6 and the PIA to the Y6 singlet exciton (S_1). Additionally, the PM6 GSB is also visible between 530 – 650 nm (Figure C14). The presence of the polymer GSB, despite selective excitation of Y6 below the band gap of PM6, suggests that some hole transfer from Y6 occurs on ultrafast (<0.2 ps) timescales. As time progresses, the PM6 GSB continues to rise and peaks after ~100 ps, confirming hole transfer is completed by this time. Additionally, new negative bands form between 700 – 800 nm and at the edge of the probe range around 950 nm. Through comparison to a PM6:$PC_{60}BM$ film (Figure C15), we confirm that the 950 nm band is due to the absorption of holes on PM6. Interestingly, we can associate the band between 700 – 800 nm to an electro-absorption (EA) feature of PM6 (Figure C15): the EA represents the Stark-shift of the PM6 absorption spectrum by the electric field of the separating charges.[61,160–162] Thus, the presence of a strong EA signal is consistent with the efficient free charge generation in the 1% LMWF blend.

For comparison, we have also excited the 52% LMWF blend at 800 nm with a low fluence of 0.50 μJ/cm^2, with the resulting TA spectra and kinetics displayed in **Figure 4.5**c,d. At 0.2 ps, we again observe the Y6 GSB. However, in clear contrast to the 1% LMWF blend, the PM6 GSB is not visible at this time. In fact, the PM6 GSB does not noticeably form until 10 ps (Figure C16): thereafter a particularly muted growth ensues. The peak PM6 GSB intensity occurs at 200 ps, suggesting hole transfer is complete, after which time it begins to rapidly decay again. Additionally, the Y6 GSB, which remains at a relatively constant intensity in the 1% LMWF blend, also significantly decreases over time of the experiment. Given the slow hole transfer process in this blend, it is likely that the fall in Y6 GSB intensity is due to the decay of un-dissociated Y6 S_1 back to the ground state. By 2 ns, the weak intensity of the

remaining spectral features, including the PM6 EA and hole PIA, in the 52% LMWF blend confirms that fewer of the initially-generated excitons are successfully converted to free charges (Figure C17); this is fully consistent with the lower performance observed in this blend.

Next, we preferentially excite PM6 at 580 nm to track the electron transfer process from PM6 to Y6. However, as there is still some absorption by Y6 at 580 nm, a small fraction of the NFA will also unavoidably be excited. Beginning with the 1% LMWF blend (Figure C18a,b), pumped with a low fluence of 0.67 μJ/cm^2, the PM6 and Y6 GSB are both present at 0.2 ps. After this time, the spectral evolution closely resembles that of the blend after selective excitation of Y6 at 800 nm, when only hole transfer can take place. The lack of early-time spectral evolution implies that the electron transfer process is completed on ultrafast timescales. To confirm this, we have also performed TA on the near-infrared (NIR) region from 1250 – 1600 nm, where the S_1 PIAs of PM6 and Y6 reside (Figure C18c). Here, we observe rapid quenching of the PM6 S_1 PIA at 1250 nm by 1 ps. Thus, the electron transfer process from PM6 to Y6 also appears to be extremely efficient, in-line with the excellent performance obtained in the 1% LMWF device. In the 52% LMWF blend, excited at 580 nm with a fluence of 0.95 μJ/cm^2, the resulting behavior is markedly different (Figure C19a,b). After peaking initially at 0.2 ps, the PM6 GSB actually decreases in intensity over the first 10 ps. Taking a kinetic trace between 675 – 725 nm, which corresponds to the vibronic shoulder of the Y6 GSB, we notice this region actually increases in intensity over the same timescales. Further, in the NIR region, there is actually some increase in the intensity of the Y6 S_1 PIA as the PM6 S_1 PIA is quenched (Figure C7c). Taken together, it is clear that a significant proportion of the PM6 S_1, estimated to be 30% from the decrease of the PM6 GSB by 10 ps,

undergo Förster resonance energy transfer (FRET) from PM6 to Y6 in the 52% LMWF blend. We note that FRET is not detectable in the 1% LMWF blend, where the rapid charge transfer out-competes any FRET processes. Following FRET in the 52% LMWF blend, the PM6 GSB regains intensity from 10 ps onwards and the PM6 EA feature begins to form; this is consistent with the timescales and dynamics of the hole transfer process from Y6 to PM6.

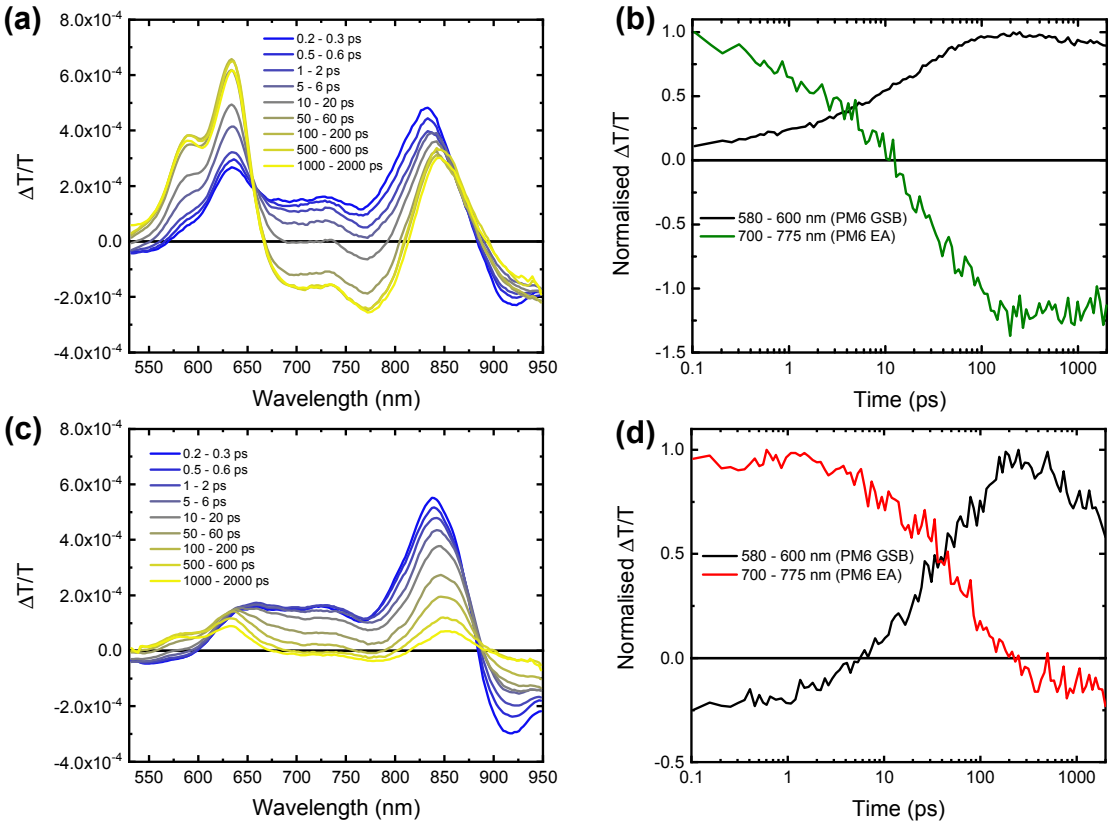

Figure 4.5. Visible region TA spectra and fitted kinetics of the PM6:Y6 (a,b) 1% LMWF blend (pump: 800 nm and fluence: 0.45 μJ cm^{-2}) and (c,d) 52% LMWF blend (pump: 800 nm and fluence: 0.50 μJ cm^{-2}).

Having now characterized the contrasting charge transfer dynamics of the two blends, we are well-positioned to rationalize the experimental behavior against the known morphological features. The key observation is that both electron and hole transfer processes are faster and more efficient in the 1% LMWF blend, which contributes to the improved PCE. Beginning

with the electron transfer process, the fact that FRET can out-compete electron transfer in the 52% LMWF blend suggests that the charge transfer process is compromised. As the 52% LMWF blend has larger D and A domains, as well as a smaller D:A interfacial area, this means PM6 excitons are likely to be generated further from the D:A interface. Whilst charge transfer is a short range process, typically taking place between adjacent D and A molecules[163], FRET can occur over comparatively long-ranges (~5 nm).[164] Thus, FRET can compete with charge transfer if it becomes significantly diffusion-limited. In a blend where hole transfer from A to D is equally as efficient as electron transfer, FRET is unlikely to significantly harm the charge generation efficiency, though it may be considered a marker for a non-ideal morphology. However, when the hole transfer process becomes inefficient, FRET channels excitons onto the component with a lower charge transfer efficiency. This then compounds the problem of an inefficient hole transfer process, as it now becomes responsible for dissociating an even larger fraction of the excitons. We note this is the case in the 52% LMWF blend.

Particularly interesting is the effect of morphology on the hole transfer process in the blends. Whilst there is also likely an aspect of diffusion limitation on the hole transfer rates, as discussed previously, the situation is somewhat more complex. The critical observation is the presence of some ultrafast (<0.2 ps) hole transfer taking place in the 1% LMWF blend, with this component entirely absent in the 52% LMWF blend. If diffusion was the sole factor limiting the hole transfer rate, we would expect to see a smaller, but finite, amount of ultrafast hole transfer. This is because a proportion of Y6 excitons would still be generated in close proximity to the D:A interface, regardless of the BHJ morphology. To rationalize this, we consider more deeply the nature of D:A interactions at the interface. As we have demonstrated, the 1% LMWF fraction blend exhibits closer D:A interactions. According to Marcus theory,

the rate of charge transfer process depends on, amongst other factors, the square of the D:A electronic coupling (H_{AB}).[151] As H_{AB} is approximately proportional to the overlap of the HOMO of D and the LUMO of A,[151] it plays a critical role in determining the charge transfer rate. It is then reasonable to assume that closer D:A interactions result in greater HOMO-LUMO overlap, increasing H_{AB} and therefore the charge transfer rate in the 1% LMWF blend. As hole transfer is typically slow (tens of ps) in low offset NFA systems,[165–167] it is in fine-balance with the rate of NFA exciton decay. Therefore, any unnecessary decrease in the hole transfer rate can have severe consequences for the charge transfer efficiency. The slower charge transfer is also compounded with the increasing exciton diffusion limitations in the 52% LMWF blend, resulting in the lower hole transfer efficiencies observed. Thus, we consider that close D:A interactions and moderate domain sizes, on the order of ~50 nm, are key to maximizing the efficiency of charge photogeneration in NFA OSC blends.

4.2.6. Non-Geminate Recombination and Extraction Dynamics

We measured the non-geminate recombination and extraction dynamics to gain further insights into the timescales of the loss processes of the 1% and 52% LMWF PM6:Y6 blends. Naturally, the goal is to minimize the charge extraction time, while maximizing the charge carrier lifetime, as this leads to a reduction of the losses caused by non-geminate recombination.[20,67,168] The first step of this analysis will be the calculation of the photocurrent density J_{ph}: $J_{ph} = J_{light} - J_{dark}$, (1)

where J_{light} is the current density under illumination and J_{dark} is the current density in the dark (**Figure 4.6**a). The photocurrent density J_{ph} is plotted against the effective voltage (V_0-V_{cor}; where

V_0 is the voltage at which $J_{ph} = 0$), since there are differences in V_{OC} for the two studied batches. In addition, the corrected voltage V_{cor} can be obtained by subtracting the voltage losses over the series resistance:

$$V_{cor} = V_{app} - J \cdot R_{series}, \quad (2)$$

where J is the current density, and R_{series} is the series resistance which is assumed to be equal to the saturated differential resistance at forward biases (i.e. $\partial V_{app}/\partial J$ = constant).[115] The devices employing the PM6 with the small LMWF of 1% exhibit significantly higher photocurrents over the entire investigated voltage range than their counterparts with the higher LMWF of 52% (**Figure 4.6**a). Furthermore, it is possible to estimate the probability of charge collection (P_C) by the ratio between the saturated photocurrent density $J_{ph,sat}$ and the values for J_{ph} at different biases:[20]

$$P_C = \frac{J_{ph}}{J_{ph,sat}}. \quad (3)$$

As can be seen in **Figure 4.6**b, the P_C retains comparatively high values close to unity for the high performing solar cells (LMWF = 1%), while a steep reduction of P_C can be observed for the solar cells with high ratios of the LMWF (52%). In particular, this suggests advantageous charge collection for the devices employing the donor polymer with insignificant amounts of the LMWF, while devices with the higher concentrations (LMWF = 52 %) are afflicted by inferior charge collection.

Additionally, *J*-*V*-curves at varying light intensities were measured to qualitatively inspect the non-geminate recombination mechanisms (Figure C20). Specifically which type of non-geminate recombination mechanism dominates can be determined by the relationship between the V_{OC} and the light intensity I:[34]

$$V_{OC} \propto \frac{kT}{q} ln(I), \quad (4)$$

where k is the Boltzmann constant, T is the absolute temperature ($T = 300$ K), and q is the elementary charge.[33] The V_{OC} vs. ln(I) plots exhibit a slope of $S = 1\ kT/q$ for solar cells in the case of ideal, pure bimolecular recombination. However, the presence of bulk or surface traps can cause monomolecular recombination that lead to deviations of the slope (bulk traps: $S > 1\ kT/q$; surface traps: $S < 1\ kT/q$).[64,67,169] The V_{OC} vs. ln(I) plots exhibit good linearity over the investigated light intensities and the solar cells with LMWF = 52% yielded slopes of $S \approx 1.15\ kT/q$, while the high performing batch exhibits values of $S \approx 1\ kT/q$. The presence of some traps in the solar cells with high concentrations of LMWF can therefore be assumed.

Nevertheless, a quantitative confirmation of the dominant loss processes requires a more advanced recombination analysis.[65] Hence, a quantitative analysis based on capacitance spectroscopy was employed.[65–67,170] This measurement technique yields the capacitance of the BHJ, which can be used to calculate important parameters such as the charge carrier density (n) and the effective mobility (μ_{eff}) of the studied solar cells under operating conditions (Figure C21).[28,68] A detailed description of the procedures to determine the charge carrier densities and effective mobilities under operating conditions are described in Appendix C. The measured charge carrier densities for the two different batches are in a range of $n = 10^{15}$ - 10^{17} cm^{-3}, with the high performing devices (LMWF = 1%) exhibiting the highest variation ($n = 9.0 \cdot 10^{14}$ to $8.5 \cdot 10^{16}$ cm^{-3}) compared to the low performing devices (LMWF = 52 %; $n = 3.5 \cdot 10^{16}$ to $1.7 \cdot 10^{17}$ cm^{-3}), which show comparatively high charge carrier densities at reverse bias (Figure C22a). This observation is interpreted as a sign of inefficient charge extraction, since there should be ideally a significant reduction in the carrier density at reverse biases.[168] This is also consistent with the low values for the P_C that have been determined for the low performing devices (LMWF = 52 %). Furthermore, a clear trend can

be seen for the effective mobilities, where the high performing devices exhibit mobilities more than one order of magnitude higher than their low performing counter parts (LMWF = 1%: $\mu_{eff} = [4.4 - 34.0] \cdot 10^{-5}$ cm^{2}V^{-1}s^{-1}; LMWF = 52%: $\mu_{eff} = [3.9 - 6.0] \cdot 10^{-6}$ cm^{2}V^{-1}s^{-1}; Figure C22b)

To obtain a quantitative understanding of the non-geminate recombination mechanisms it is assumed that the overall measured recombination current density ($J_{rec} = J_{ph,sat} - J_{ph}$) is a superposition of the three aforementioned recombination mechanisms that contribute a certain part to the total recombination current density J_{rec}:

$$J_{rec} = J_{bm} + J_{t,b} + J_{t,s} = qL\left(\frac{n}{\tau_{bm}} + \frac{n}{\tau_{t,b}} + \frac{n}{\tau_{t,s}}\right) = qL\left(k_{bm}n^2 + k_{t,b}n + k_{t,s}n\right), \quad (5)$$

where q is the elementary charge, L is the active layer thickness, τ is the charge carrier lifetime, n is the charge carrier density, and k is the recombination coefficient of the three different recombination mechanisms (bm: bimolecular; t,b: bulk trap-assisted; t,s: surface trap-assisted). By reconstructing the recombination current density J_{rec} obtained from the *J-V*-curves with the charge carrier density (n) and the effective mobility (μ_{eff}), which is explained in the Section 9.4 of the SI, it is possible to quantify the recombination coefficients (k) (Figure C22c).[20,67] This quantitative analysis showed that the solar cells – across the relevant voltages – have a similar range for the bimolecular recombination coefficient (LMWF = 1%: $k_{bm} = 3.1 \cdot 10^{-13}$ cm^3/s; LMWF = 52%: $k_{bm} = 1.9 \cdot 10^{-13}$ cm^3/s) (Table S5). Therefore, the difference in performance between the studied devices must result from the contribution of trap-assisted recombination in the bulk for the low performing devices. This is exemplified by the contrast in the bulk trap density (LMWF = 1 %: $N_{t,b} < 10^{10}$ cm^{-3}; LMWF = 52 %: $N_{t,b} = 3.13 \cdot 10^{15}$ cm^{-3}), whereas the role of surface trap-assisted recombination is in both cases less significant (LMWF = 1%: $N_{t,s} = 2.72 \cdot 10^{10}$ cm^{-2};

LMWF = 52%: $N_{t,s} = 8.56 \cdot 10^{11}$ cm^{-2}; Figure C22c). It is possible to calculate the charge carrier lifetime τ_{rec} by rearranging equation (5), since the carrier density n and the relevant recombination coefficients (k_{bm}, $k_{t,b}$, $k_{t,s}$) are now known (Figure 4.6c). The charge carrier lifetime τ_{rec} of the high performing devices is significantly longer than their low performing counterparts, specifically under short-circuit conditions and under reverse bias (LMWF = 1%: τ_{rec} = [15 – 3631]µs; LMWF = 52%: τ_{rec} = [25 – 71]µs).

Finally, the extraction of charge carriers has to be quantified as well to obtain a comprehensive understanding of the non-geminate recombination dynamics in the studied devices. To this end, the effective extraction time (τ_{ex}) was calculated, utilizing a previously-employed approach.[20] It is assumed that a charge carrier needs to traverse, on average, half of the active layer thickness, until it reaches one of the electrodes and that the active layer can be treated as an effective medium. The following relationship can be derived based on these assumptions:

$$\tau_{ex} = \frac{qLn}{J}, \tag{6}$$

where L is the active layer thickness, q is the elementary charge, n is the charge carrier density, and J is the current density obtained from the *J-V* curves. The direct comparison of the extraction time (τ_{ex}) and the charge carrier lifetime (τ_{rec}) can then be used for a comprehensive understanding of the competing non-geminate recombination and extraction processes as shown in Fig. 6c. In particular, it turns out that the high performing devices have a significantly faster extraction time over the studied voltage range, compared to the low performing solar cells (LMWF = 1%: τ_{ex} = [0.05 – 8.43] µs; LMWF = 52%: τ_{ex} = [3.18 – 57.60] µs). Once the extraction and non-geminate recombination dynamics are known over the relevant voltage range, it is possible to calculate the voltage dependent competition factor,

which is defined as the ratio between the extraction and non-geminate recombination times ($\theta = \tau_{ex}/\tau_{rec}$). The competition factor was introduced by Bartesaghi *et al*. as a figure of merit that encompasses the aforementioned interplay between extraction and non-geminate recombination dynamics into a single, dimensionless number. Generally, smaller competition factors have been shown to correlate to higher *FF* and J_{SC} values.[28,29] As can be seen in Fig. 6d, the competition factor (θ) of the high performing devices employing the PM6 batch with insignificant amounts of the LMWF (1%) is at least between one and two orders of magnitude smaller over the entirety of the relevant voltage range than their respective counterparts using the PM6 batch with high values of the LMWF (52%). This stark contrast in θ between the investigated devices was caused by differences in extraction and non-geminate recombination times. Overall, the results obtained for the extraction and non-geminate recombination dynamics are consistent. The low performing devices (LMWF = 52%) exhibit significantly more trap-assisted recombination in the bulk, reduced effective mobilities, and compromised charge extraction leading to the reduction in the J_{SC} and *FF* values. The presence of trap-assisted recombination in the 52% LMWF blend can be understood by the high concentration of the LMWFs, which consist of small packets of PM6 dimers, and are likely acting as trap states for charge carriers. More importantly, the compromised long-range ordering and suboptimal phase separated D:A regions in the 52% LMWF blend is the reason for its inferior charge transport and extraction.[20] In summary, better long range ordering, reduction in the LMWF, and optimally phase separated D:A regions are crucial for efficient charge transport and extraction in NFA OSC blends.

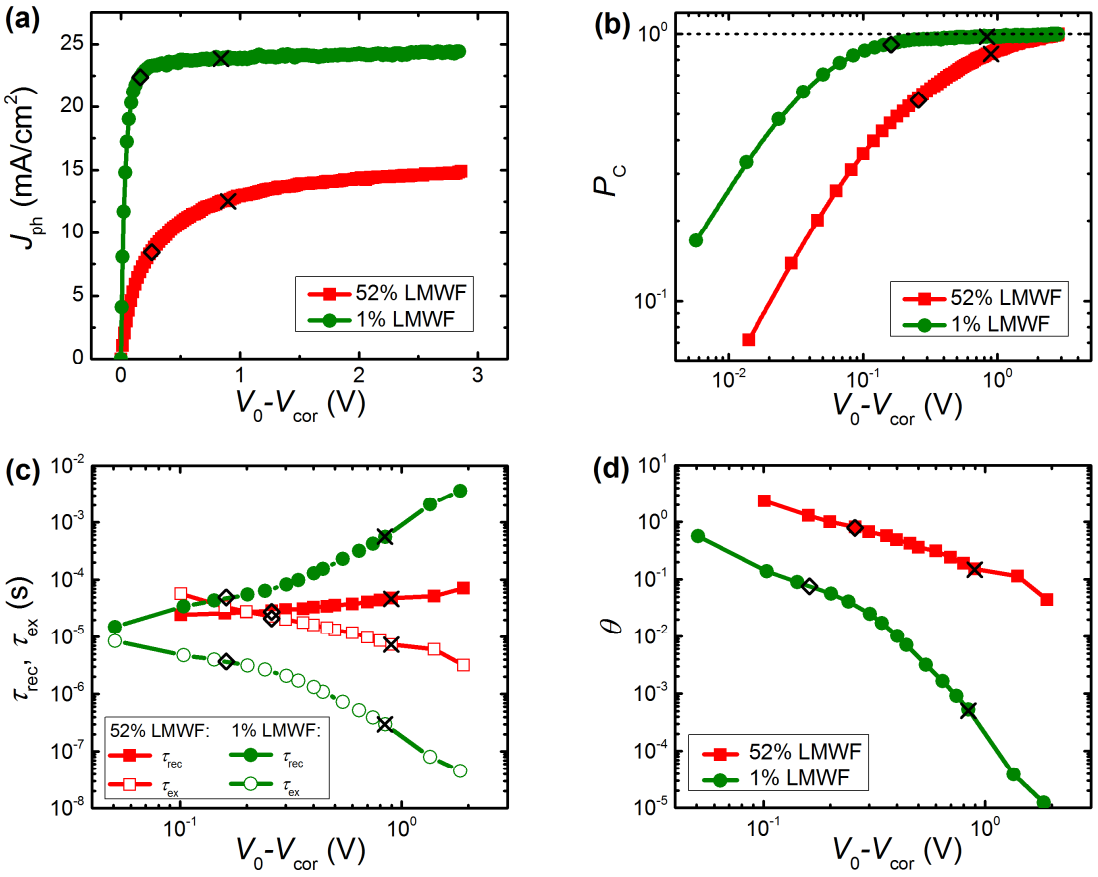

Figure 4.6. (a) Photocurrent J_{ph} and (b) collection probability P_C of the two investigated devices with varying PM6 batches. (c) Average extraction time τ_{ex} and charge carrier lifetime τ_{rec} of the two batches. (d) Comparison of the competition factor $\theta = \tau_{ex}/\tau_{rec}$ of the two types of investigated solar cells. Operation conditions of interest are highlighted (black crosses: short-circuit; black lozenges: max-power).

4.3. Conclusions

In summary, different amounts (1% and 52%) of LMWFs of the PM6 polymer were used as a tool to exert control over the interfacial and bulk morphology in the two PM6:Y6 blends. The use of four morphological characterization techniques from sub-nanometer to sub-micrometer length scales enabled a full characterization of the bulk and interfacial morphology in these two blend systems. The drop in PCEs from over 15% to 5% with the

increased LMWFs was due to a drop in the J_{SC} and *FF* values, caused by compromised charge generation efficiencies, increased bulk trap densities, lower competition factors, and reduced charge transport. The origins for the high device performance in the 1% LMWF blend could be rationalized by the favorable bulk and interfacial morphological features, summarized by two main points. First, the long-range ordering and optimally phase separated D:A regions led to its superior charge transport and extraction. Second, the closer D:A interactions, smaller D and A domains, and increased interfacial area facilitated ultrafast electron and hole transfer at the D:A interface. Therefore, this study is the first to make recommendations on detailed bulk and interfacial morphological features that are critical in achieving high PCEs of over 15% in polymer:NFA OSCs.

4.4. Experimental Section

Materials and synthesis. Different batches of the PM6 polymers and Y6 NFA were synthesized by 1-material inc. Figure C1 below depicts the synthetic pathway to the PM6 donor polymer. All reagents were purchased from commercial sources and were used without further purification unless noted otherwise. $Pd(PPh_3)_4$ was purchased from Strem Chemicals, anhydrous toluene was purchased from Sigma-Aldrich. 1M_IT5259(CAS#1514905-25-9; 1,1'-[4,8-bis[5-(2-ethylhexyl)-4-fluoro-2-thienyl]benzo[1,2-*b*:4,5-*b*']dithiophene-2,6-diyl]bis[1,1,1-trimethylstannane; purity 99+%, NMR shown in Figure. C2) and 1M_IT9780 (CAS#1415929-78-0; 1,3-bis(5-bromo-2-thienyl)-5,7-bis(2-ethylhexyl4*H*,8*H*-Benzo[1,2-*c*:4,5-*c*']dithiophene-4,8-dione); purity 99+%, NMR shown in Figure. C3) are commercially available from 1-Material Inc.

Device Fabrication: Indium tin oxide (ITO) patterned glass substrates were cleaned by scrubbing with soapy water, followed by sonication in soapy water, deionized (DI) water, acetone, and isopropanol for 20 minutes each. The substrates were dried using compressed nitrogen and placed in an oven overnight at 100 °C. The ITO substrates were treated with UV-ozone for 15 minutes and a layer of poly(3,4-ethylenedioxythiophene): poly(styrenesulfonate) (PEDOT:PSS, Clevios P VP Al 8043) was spin-coated at 3000 rpm for 40 s onto the ITO substrates. The substrates were then annealed in air at 150 °C for 20 minutes. 18 mg/mL of PM6:Y6 blend solutions were prepared with a D:A ratio of 1:1.2 in chloroform with 0.5% v/v 1-chloronaphthanene (CN). The active layers were spin-cast inside a nitrogen glovebox at 4000 rpm and annealed inside the glovebox at 110 ^{0}C for 10 minutes. The substrates were left to cool for 5 minutes and 1 mg/mL PDINO solution dissolved in methanol was spin-coated on top of the active layer. The substrates were then pumped down under vacuum (< 10^{-6} torr), and a 100 nm thick Aluminum electrode was deposited on top of the active layer by thermal evaporation. Devices of neat materials (PM6 or Y6) were prepared using similar solid concentrations as that in the blend solution.

Device Testing: Photovoltaic characteristic measurements were carried out inside the glove box using a high-quality optical fiber to guide the light from the solar simulator equipped with a Keithley 2635A source measurement unit. *J-V* curves were measured under AM 1.5G illumination at 100 mW cm^{-2} for devices with an electrode area of 0.22 cm^{2}.

External quantum efficiency (EQEPV) measurements: External quantum efficiency (EQE) for all solar cells was measured using a 75 W Xe light source, monochromator, optical chopper (138 Hz), and a lock-in amplifier. Power-density calibration of the EQE characteristics was achieved using a calibrated silicon photodiode from Newport. For the sub-bandgap EQE,

higher sensitivity settings were used with a longer time delay between measurement points.

Internal quantum efficiency (IQE) measurements: The total reflectance of the solar cell devices with the configuration: glass/ITO/PEDOT:PSS/Active layer/Ba/Al were measured with an integrating sphere to obtain the total absorption, which was corrected for the parasitic absorption simulated with the transfer matrix model.[97] The active layer optical properties were measured with transmittance and reflectance measurements using an integrating sphere. The optical properties of the other layers were determined from ellipsometry with a Woolam M-2000DI Variable Angle Spectroscopic Ellipsometer, with reflectance and transmission measurements, or taken from the literature.[98,99] The IQE spectra of the devices were calculated by subtracting the parasitic absorption from the total device absorption to obtain the active layer absorption and dividing the EQE spectra by the corresponding fraction of active layer absorption. As described in the literature report,[32] since the experimentally measured total absorption is highly accurate, errors in the resulting active layer absorption are only as small as the errors in the parasitic absorptions.

Electroluminescence and EQE_{EL} Measurements: EL measurements were performed using two setups depending on the wavelength range of interest. For measurements under 1050 nm, a home-made EL spectrometer was used. The EL emission from a sample driven by a Keithley source-measure unit (model 2602A) was collected by a lens system and focused on the entrance slit of a spectrograph (Acton Research SP-500) equipped with a Si charge-coupled detector (Princeton Instruments Pixis:400). The spectra collected by the detector were corrected for the instrument response function. The correction factors were determined by measuring the spectrum of a black body-like light source (Ocean Optics LS-1). For EL measurements in the range 900 - 1700 nm, we utilized a Photon Technology International

(PTI) Quantamaster fluorimeter equipped with an Edinburgh Instruments EI-L Ge detector. The excitation monochromator of the fluorimeter was not used, and the EL emission was generated by driving the devices by a Keithley 2602 source-measure unit. An optical chopper (Thorlabs MC2000) was placed in front of the emission monochromator to make use of the fluorimeter's lock-in amplifier-based detection system. The PTI Felix fluorimeter software was used for the data collection and correction of the instrumental artifacts. The efficiency of electroluminescence was obtained by applying a bias from -1 to 2V with a dual-channel Keithley 2602 to the solar cell and placing a silicon or germanium photodiode directly in front of it to collect the emission as a function of applied bias. The current running through the device and the photodiode were simultaneously measured.

Transient Absorption (TA) spectroscopy: TA was performed on either one of two experimental setups. For "visible" region TA (500–950 nm), a Yb amplifier (PHAROS, Light Conversion), operating at 38 kHz and generating 200 fs pulses centred at 1030 nm with an output of 14.5 W was used. The pump pulse was provided by a TOPAS optical parametric amplifier. The probe is provided by a WL supercontinuum generated in a YAG crystal. After passing through the sample, the probe is imaged using a Si photodiode array (Stresing S11490). This setup provided additional flexibility by allowing for broadband spectrum acquisition in one measurement for improved consistency, as well good signal to noise (s/n) in the 750–850 nm region, which is difficult to obtain on the other setups due to large fluctuations in the WL seed around the 800 nm fundamental. The near infrared (NIR) TA was performed on a setup which was powered using a commercially available Ti:sapphire amplifier (Spectra Physics Solstice Ace). The amplifier operates at 1 kHz and generates 100 fs pulses centered at 800 nm with an output of 7 W. For these measurements, a small fraction

of the 800 nm fundamental was used as the pump. The probe was provided by a broadband NIR NOPA. To complement the NIR probe wavelengths available, the probe pulses are collected with an InGaAs dual-line array detector (Hamamatsu G11608-512DA), driven and read out by a custom-built board from Stresing Entwicklungsbüro. The probe beam was split into two identical beams by a 50/50 beamsplitter. This allowed for the use of a second reference beam which also passes through the sample but does not interact with the pump. The role of the reference was to correct for any shot-to-shot fluctuations in the probe that would otherwise greatly increase the structured noise in our experiments. Through this arrangement, very small signals with a $\frac{\Delta T}{T} < 10^{-5}$ could be measured.

Capacitance spectroscopy: Capacitance spectroscopy measurements were performed with an impedance analyzer Solartron 1260A in the dark and under 1 sun AM1.5 illumination inside a nitrogen-filled glovebox. The amplitude of the AC signal was 40 mV to ensure a negligible impact on the measured impedance.

Photo-conductive atomic force microscopy (pc-AFM): Photoconductive atomic force microscopy (pc-AFM) measurements were done with an Asylum Research MFP-3D microscope sitting atop an inverted optical microscopy (Olympus, IX71). All measurements were conducted under inert atmosphere. A white light source with a power of 30 W cm^{-2} was used to generate photocurrent morphology which was recorded by an internal preamplifier (Asylum Research ORCA head model). Electrically conductive Chromium/Platinum-coated silicon probes with a spring constant of 0.2 N m^{-1} and resonant frequency of 13 kHz (Budget Sensors) were used. A light spot with 160 μm diameter was focused on the active layer of the device through an inverted optical microscope (Olympus), and the conductive tip was positioned at the center of the light spot.

Grazing incidence wide angle X-ray Scattering (GIWAXS): This measurement was performed at the Advanced Light Source at Lawrence Berkeley National Lab on the 7.3.3 beamline. The sample was scanned for 40 seconds at an incidence angle of 0.12° and a photon energy of 10 keV (λ = 1.24 Å), while under a helium environment to minimize beam damage and reduce air scattering. The width of the incident X-ray beam is about 1 mm, and silver behenate was used to calibrate the lengths in the reciprocal space. A 2D detector (PILATUS 2 M from Dectris) with a sample-to-detector distance of 276.9 mm was used to collect the images. The Nika software package for Igor (by Wavemetrics) and the Igor script WAXStools were used to process the image.

Resonant-Soft X-ray Scattering (R-SoXs): R-SoXS was performed at the beamline 11.0.1.2[100] Advanced Light Source (ALS), Lawrence Berkeley National Laboratory. Samples for R-SoXS measurements were prepared on a PSS modified ITO substrates under the same conditions as those used for device fabrication, and then transferred by floating in water to a 1.5 × 1.5 mm^2, 100 nm thick Si3N4 membrane supported by a 5 × 5 mm, 200 mm thick Si frame (Norcada Inc.). R-SoXS was performed in a transmission geometry with linearly polarized photons under high vacuum (1×10^{-7} torr) and a cooled (–45 °C) CCD (Princeton PI-MTE) was used to capture the soft X-ray scattering 2D maps and PS300 was used for geometry calibration.

*Solid-State NMR spectroscopy***.** Spin-coated PM6 and Y6 materials and different batches of PM6:Y6 blends were scratched off from the glass substrates, and packed into either 1.3 mm or 3.2 mm (outer diameter) zirconia rotors. All fast magic-angle spinning (MAS = 60 KHz) 1D ^{1}H, ^{19}F, and 2D ^{19}F-^{19}F NMR experiments were carried out on a Bruker Avance Neo (21.1 T, Larmor frequencies of ^{1}H and ^{19}F were 900.2 MHz and 845.9 MHz, respectively)

spectrometer with 1.3 mm H-X probe head. The nutation frequency of ^{1}H was 100 kHz, corresponding to 90° pulse duration of 2.5 μs. Single-pulse ^{1}H MAS NMR experiments were carried out by co-adding 32 transients with a relaxation delay of 4 s (Figure. S8). 1D ^{19}F MAS NMR spectra of neat materials and blends were acquired using 128 co-added transitions. To probe short and long-range through-space ^{19}F-^{19}F proximities, 2D ^{19}F-^{19}F spin diffusion spectra (Figure. S9) were acquired with 100 ms and 1 s of mixing times, respectively. 2D spectra was acquired using 128 t_1 increments, each with 8 co-added transients, with a rotor-synchronized t_1 increment of 16.66 μs, corresponding to a total experimental time of 6 h for each sample. All 1D ^{13}C{^{1}H} cross polarization (CP)-MAS and 2D ^{13}C-^{1}H heteronuclear correlation (HETCOR) NMR experiments of neat materials and blends were carried out on a Bruker Avance II (9.4 T, Larmor frequencies of ^{1}H and ^{13}C were respectively 400.1 MHz and 100.6 MHz) spectrometer with 3.2 mm H-X probe. 1D ^{13}C{^{1}H} CP-MAS and 2D HETCOR spectra were acquired at 12.5 kHz MAS. 1D ^{13}C{^{1}H} CP-MAS spectra (Figure. S10) were acquired with CP contact times of 0.1 and 4 ms, each by co-adding 2048 transients with a ^{1}H relaxation delay of 4s, corresponding to an experimental time of 2.4 h. In 2D ^{1}H-^{13}C HETCOR experiments, the indirect ^{1}H dimension was acquired with 64 t_1 increments, each with 128 co-added transients, corresponding to a total experimental time of 9 h with a recycle delay of 4 s. The high-power homonuclear decoupling was applied during the acquisition of indirect ^{1}H dimension using DUMBO decoupling sequence, and heteronuclear decoupling was applied during the detection of ^{13}C dimension using SPINAL-64 sequence. 2D time domain spectra were processed with FFT (Fourier Transformation) in both vertical ^{1}H and horizontal ^{13}C dimensions (Figure. S11-S12). The vertical ^{1}H dimension spectral width was scaled by 1.6, which corresponds to a DUMBO scaling factor of 0.6. The ^{1}H and ^{13}C experimental shifts

were calibrated with respect to neat TMS using adamantane as an external reference (higher ppm ^{13}C resonance, 35.8 ppm, and the ^{1}H resonance, 1.85 ppm), and ^{19}F chemical shifts were calibrated to the ^{19}F chemical shift of neat $CFCl_3$ (^{19}F, 0 ppm) as an external reference.

Chapter 5

Unifying Energetic Disorder from Charge Transport and Band Bending in Organic Semiconductors

5.1. Introduction

An accurate depiction of the electronic structures of organic semiconducting polymers can have important implications in understanding their performances when incorporated in organic solar cells (OSCs)[171], organic field-effect transistors (OFETs)[172], and organic light-emitting diodes (OLEDs)[173]. Unlike ordered crystalline semiconductors such as silicon, which have clearly defined conduction and valence bands, disordered organic systems such as polymeric semiconductors have a broadened electronic density-of-states (DOS) distribution.[174] This broadening is a result of the different types of intra- and inter-molecular interactions, rotation and kinking of polymer chains, and conformational diversity that gives rise to a morphologically diverse film.[175] The DOS distribution is frequently described by a Gaussian function, where the extent of broadening is determined by the variance sigma (σ). A consequence of a broadened DOS is that low energy tail states extend far into the band gap, which give rise to thermally-activated hopping transport. In fact, different experimental and theoretical studies have characterized these tail states in organic semiconductors, revealing either Gaussian or exponential shaped tails.[176–193] Characterizing energetic disorder accurately is important in understanding the charge-transport properties of organic polymer semiconductors as broader DOS distributions generally give rise to an inferior transport. In

turn, the performance of organic semiconductor devices largely depends on the charge transport properties of the organic semiconductor.[66,194–198] From a morphological standpoint, the relative densities of ordered and disordered regions in thin films are known to affect charge transport properties with crystalline regions enhancing charge transport due to the high degree of π-π stacking of backbone moieties and lamellar structural order of side chains.[199,200] However, to this end, a comparative study between molecular structures showing clearly distinguishable ordered and disordered regions at an atomic-level and its impact on the DOS widths and ultimately the charge transport properties have yet to be established.

Additionally, while there exist several techniques in the literature that give relevant information on the shape or width of the DOS distribution, efforts to try and unify these different techniques are lacking. In this work, we characterize the DOS distribution widths of two structurally unique organic semiconducting polymers using temperature-dependent current density-voltage (*J-V*) measurements, Kelvin probe measurement (KP) of band bending, and energy-resolved electrochemical impedance spectroscopy (ER-EIS). In order to eliminate unexpected changes in morphology due to additional post processing steps, both polymers were dissolved in the same solvent (chlorobenzene), and spin-coated for all characterization techniques. From a comparison of the DOS widths measured using these three techniques to a parallel measurement of charge transport, we establish a quantitative relationship between charge transport and band bending measurements for the first time. For a standardized and comparative study incorporating all three techniques, two conjugated polymers (**Figure 5.1**), poly[4,8-bis(5-(2-ethylhexyl)thiophen-2-yl)benzo[1,2-b;4,5-b']dithiophene-2,6-diyl-alt-(4-(2-ethylhexyl)-3-fluorothieno[3,4-b]thiophene-)-2-carboxylate-2-6-diyl)] (PTB7-Th) and poly[2-methoxy-5-(2-ethylhexyloxy)-1,4-

phenylenevinylene] (MEH-PPV) were selected with clearly distinct charge-transport properties. MEH-PPV is a conjugated polymer commonly used in OLEDs and PTB7-Th is a conjugated polymer commonly used as a donor material in organic bulk heterojunction solar cells.

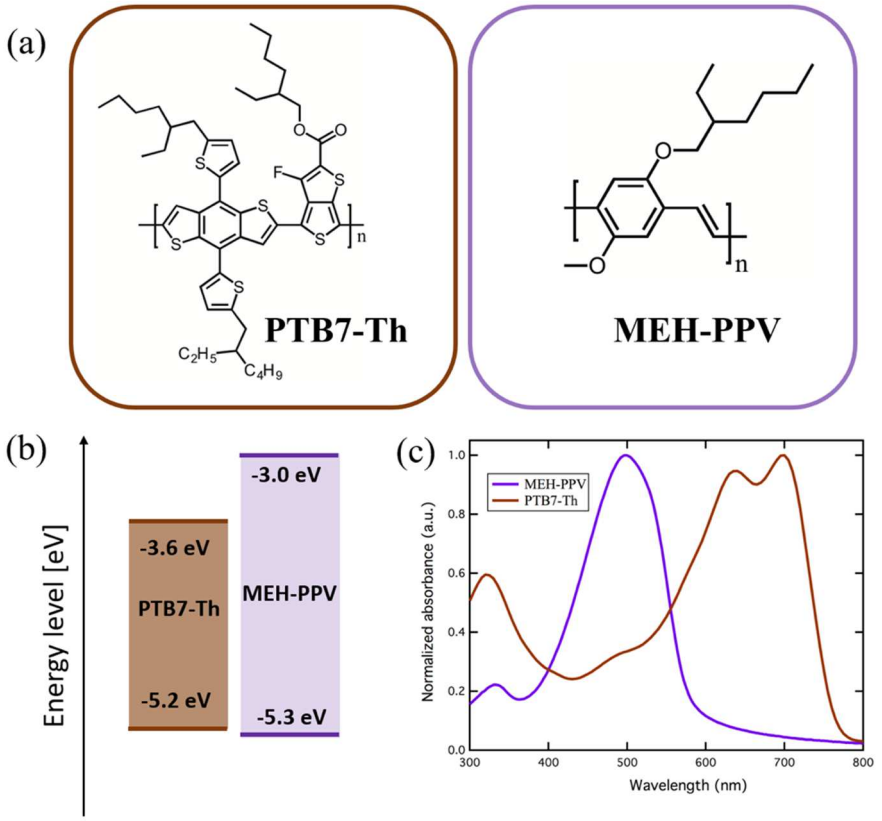

Figure 5.1. a) Chemical structures of PTB7-Th and MEH-PPV. b) Energy levels showing HOMO and LUMO levels of the two polymers. c) Normalized absorption spectra of the polymers.

5.2. Results and Discussion

Temperature Dependent Mobility Measurements for Characterizing Charge Transport and Energetic Disorder

To characterize hole transport and energetic disorder of transport sites in these polymers using *J-V* measurements, symmetric hole-only devices were fabricated. Films of the pristine

polymers were sandwiched between an ITO/PEDOT:PSS (35 nm) bottom contact and a MoO_3 layer (10 nm) capped with Ag (100 nm) top contact. A previous study has shown that the work functions of PEDOT:PSS (~5.2 eV) and MoO_3 (~6.9 eV [201]) are sufficient to act as Ohmic hole-injecting contacts into the MEH-PPV HOMO level of ~ -5.3 eV and produce symmetric *J-V* curves [202]; this is also shown to be the case for the PTB7-Th polymer in this study, which has a HOMO of ~ -5.2 eV (See Figure D1 in Appendix D).[203]

Measurement of space-charge-limited currents (SCLC) is a widely established method to characterize charge transport in conjugated polymers.[204,205] The expression for a SCLC in a diode sandwiched between two metal contacts derived by Mott and Gurney is

$$J = \frac{9\varepsilon_0 \varepsilon_r \mu V^2}{8L^3} \quad (1)$$

where, ε_0 is the vacuum permittivity, ε_r is the relative permittivity of the material, μ is the charge-carrier mobility, and L is the active layer thickness. In order to determine the mobility from experimental data, it should first be verified that the measured currents are indeed limited by space charge.

The experimentally measured *J-V* characteristics of PTB7-Th (**Figure 5.2**a) and MEH-PPV (**Figure 5.2**c) hole-only devices on a double logarithmic scale show Ohmic currents at low voltages and a transition to a quadratic voltage dependence at higher voltages. The quadratic voltage dependence is characteristic of SCLC, with the Ohmic current at low voltage being due to the diffusion contribution to the current, which is neglected in the derivation of Equation 1. As established from Equation 1, a prerequisite for satisfying the criterion for space-charge limited currents in a diode is that the current has a L^{-3} dependence on the thickness of the diodes. As shown in **Figure 2**b and **2**d, when multiplying the current density by L^3 the current densities almost coalesce — now with little deviation between the highest

current density (thinnest) and the lowest current density (thickest) device — confirming that the thickness dependence behavior expected for space-charge-limited currents is indeed satisfied. The thickness dependence is slightly stronger than L^{-3}, which is due to the density dependence of the mobility.[202] Fits to Equation 1 shown by the black dotted lines in Figure 2b and 2d give average mobilities of $2.7 \pm 0.7 \times 10^{-3}$ cm^2/Vs for PTB7-Th and $4.2 \pm 2 \times 10^{-5}$ cm^2/Vs for MEH-PPV for the range of layer thicknesses.

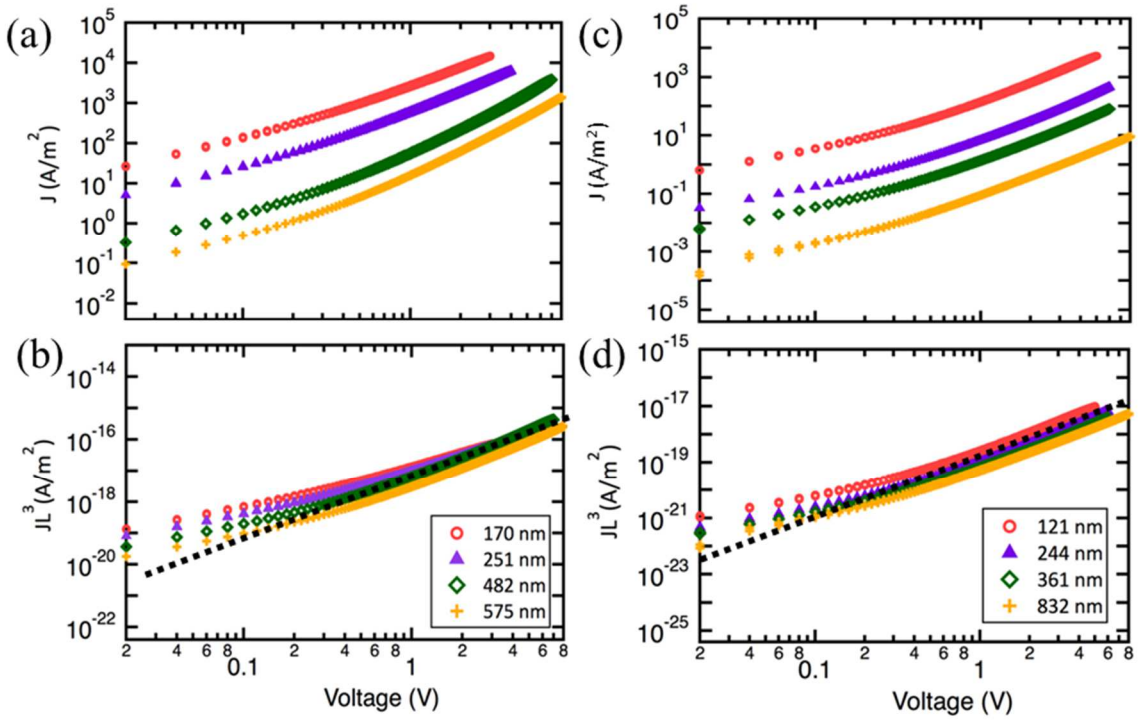

Figure 5.2. *J-V* characteristics of symmetric a) PTB7-Th and c) MEH-PPV diodes of different layer thicknesses at 300 K. The current density is multiplied by L^3 for b) PTB7-Th and d) MEH-PPV to show the layer-thickness dependence of current. The dotted black lines on Figure 2b and 2d represent the average fits to Equation 1 for different thicknesses.

A limitation of using Equation 1 to extract the charge-carrier mobility is that while it describes the experimental data well in low electric field regimes and at room temperature, it fails to describe the current density-voltage characteristics at higher fields — especially at lower temperatures. The reason for this discrepancy is the fact that the mobility is not constant, as assumed in Equation 1 (See Figure D2 in Appendix D).

As a result of energetic disorder of hopping sites, the mobility in organic semiconductors is charge-carrier density, electric-field, and temperature dependent.[206] In 2005, Pasveer et al. developed a model referred to as the extended Gaussian disorder model (EGDM) that describes the density, electric field, and temperature dependence of mobility in a system with localized states having a Gaussian distribution of energy.[207] The parameters describing transport in the EGDM are the width of the density of states distribution (σ), the lattice constant (a), and a mobility pre-factor (μ_∞). The temperature-dependent mobility at zero field and density is given by

$$\mu_0(T) = \mu_\infty c_1 \exp\left[-c_2\left(\frac{\sigma}{kT}\right)^2\right] \quad (2)$$

where, c_1= 1.8 × 10^{-9} and c_2 = 0.42 are constants derived from the EGDM[207], k is the Boltzmann constant, and T is the temperature. The temperature dependence of mobility is exclusively determined by the energetic disorder σ, which enables us to extract the energetic disorder from the temperature dependence of mobility. We have incorporated the EGDM mobility function in a drift-diffusion model[208] to simulate the full current density-voltage characteristics.

Figure 5.3a and **3**b show the experimental temperature-dependent *J-V* curves for PTB7-Th and MEH-PPV in the forward bias along with the simulations (dotted lines) obtained from a numerical drift-diffusion model, which now takes the charge carrier density, electric field, and temperature dependence into account, according to the EGDM. For PTB7-Th, best fits were obtained using σ = 75 meV and a = 4.5 nm. This set of parameters was found to be consistent across devices with different layer thicknesses (See Figure D3 in Appendix D). The fits to the experimental data for three different layer thicknesses gave a mobility of 1.6 ×10^{-3}

cm^2/Vs at vanishing charge carrier densities and electric field at room temperature. This mobility is slightly lower than the mobility obtained from fits to Equation 1 shown in Figure 2b and 2d and relatively high for a bulk value, which is consistent with weak temperature dependence [192] and a small value for the energetic disorder.

It is visually apparent that the MEH-PPV *J-V* curves have a stronger temperature dependence than PTB7-Th, indicating a stronger temperature dependence of the mobility. The *J-V* characteristics were fitted with the drift-diffusion model using σ = 125 meV and a = 2.2 nm. Also, in this case, this set of parameters was found to be consistent across all layer thicknesses (See Figure D5 in Appendix D) and fits to all the experimental data gave a room-temperature mobility of 5.9×10^{-6} cm^2/Vs at vanishing charge-carrier densities and electric field. The lower value of a for MEH-PPV is consistent with its disordered and amorphous nature in comparison to the highly ordered PTB7-Th film. The lower mobilities obtained at vanishing charge-carrier densities and electric field compared to mobilities from the SCLC fits (Figure 2b and 2d) confirm the density and electric-field dependence of mobility — which is more pronounced in the more disordered MEH-PPV polymer. The higher energetic disorder for MEH-PPV is consistent with its lower charge-carrier mobility.

It is worth noting the slightly lower σ and higher μ for MEH-PPV reported in this study from that reported in literature[202,209] is likely due to the difference in the M_w of MEH-PPV used (1,000,000 Da [202,209] vs. 125,000 Da in this study). This discrepancy alludes to the fact that the molecular weight (M_w) of polymers can play a rather significant role in the orientation of polymer chains in a film, thereby giving rise to the observed differences in the energetic disorder term, σ, as well as the charge carrier mobility, μ.[210,211]

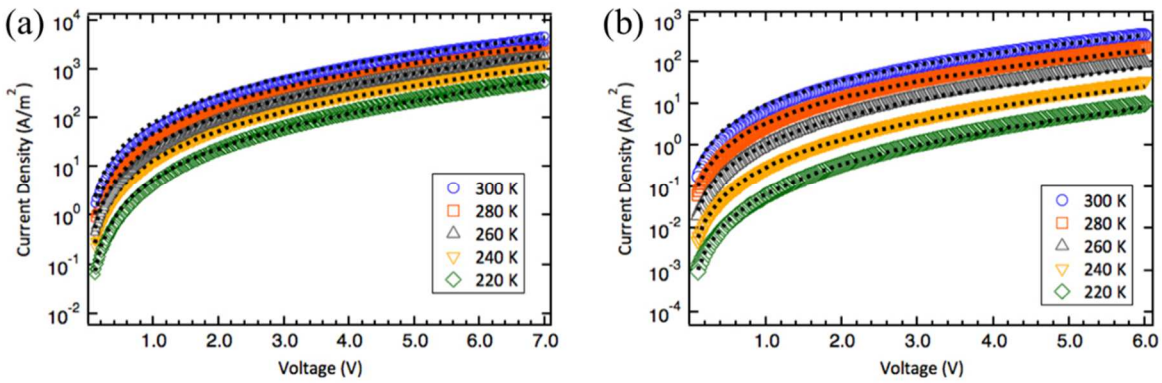

Figure 5.3. Temperature-dependent *J-V* characteristics of a) PTB7-Th and b) MEH-PPV hole-only diodes with a layer thickness of 481 nm and 244 nm, respectively. Dotted lines correspond to calculations obtained from a drift-diffusion model.

Kelvin Probe Method for Characterizing Tail States Disorder

The width of the Gaussian DOS distribution obtained from the charge-transport measurements was determined to be 75 meV for PTB7-Th and 125 meV for MEH-PPV. We now compare these values to the DOS distribution widths obtained by a second technique, where a Kelvin probe is used to measure band bending in the conjugated-polymer films. Kelvin probe is a capacitive, non-contact measurement that measures the contact potential difference between a tip and a semiconductor film of interest, deposited on a conductive substrate. The contact potential difference gives the fermi energy at the surface of the semiconductor with respect to a calibrated tip.[212,213]

One of the first ever studies of band bending of conjugated polymer layers was done by Blakesley and Greenham.[214] When a semiconductor is in contact with an electrode with a high or low work function, such that an Ohmic contact is formed, the semiconductor exhibits band bending in the vicinity of the electrode due to the charge transfer to establish thermodynamic equilibrium across the interface. The high carrier density at the interface results in a gradient

in the electrostatic potential, giving rise to a diffusion of carriers, accompanied by band bending.[214,215] It has been shown that the amount of bending is a function of energetic disorder, with a broader DOS distribution resulting in more band bending. The KP technique can probe this gradient in electrostatic potential, which allows for extraction of the width of the DOS distribution.

An expression for the distribution of charge carriers (*n(x)*) diffusing in from the electrode into the polymer semiconductor and the subsequent change in the electrostatic potential (*V(x)*) in the film can be found by solving an expression for the charge carrier density *(n*) from a certain distance (*x*) of the polymer-electrode interface using a combined expression of the Fermi-Dirac distribution and the DOS of the polymer, as shown in Equation 3 below

$$n(x) = \int_{-\infty}^{\infty} \frac{1}{1+\exp[(E-E_F)/k_BT}\, g[E + eV(x)]dE \quad (3)$$

where *E* is energy, k_B is the Boltzmann constant, *T* is temperature, *g(E)* is the model DOS, and *V(x)* is the electrostatic potential. *V(x)* is obtained by solving the one-dimensional Poisson's equation (4) below

$$\frac{d^2V}{dx^2} = \frac{en(x)}{\varepsilon} \quad (4)$$

with the assumption that the electric field vanishes at the polymer surface, *e* is the elementary charge, and ε is the permittivity of the polymer film.[215] Equation 5 is the Gaussian DOS function that was used to fit the data.

$$g(E) = \frac{N_0}{\sigma\sqrt{2\pi}} \exp\left[-\frac{(E-E_0)^2}{2\sigma^2}\right] \quad (5)$$

Here, N_0 is the integrated state density, σ is the width of the Gaussian DOS, and E_0 is the center of the distribution. The Gaussian DOS model can only be solved numerically by varying E_0 and σ to obtain the best fit to the experimental data. For an exponential DOS distribution, on the other hand, an analytical model was expressed as a function of the film thickness, d.[215,216]

$$d = \sqrt{\frac{2E_t\varepsilon_0\,\varepsilon_r}{q^2\,N}}\exp\left(\frac{|\varphi(d)|}{2E_t}\right)\arccos\left[\exp\left(-\frac{|\varphi(d)|}{2E_t}\right)\right] \quad (6)$$

In Equation 6, d is the film thickness, E_t is the exponential disorder term of the DOS, ε_r is the relative dielectric constant, ε_0 is the vacuum permittivity, N is the DOS maximum, and $\phi(d)$ is the net potential shift at a distance d from the electrode.

Figure 5.4 shows the band bending fits for a Gaussian and exponential DOS distribution to the experimentally measured work function values at different layer thicknesses for the two polymers. Both polymers were spin coated on top of the high work function electrode MoO_3, to ensure diffusion of holes from the electrode into the HOMO of the organic semiconducting polymer, giving rise to band bending. The Gaussian and exponential models describe the DOS function in characteristically different ways with the Gaussian DOS tailing off faster as a function of site energy than the exponential DOS.[217] The band bending method is only sensitive to the tail states and it is not possible to distinguish a preference between the two models from this analysis. Therefore, fits to the experimental band-bending profiles can give estimates for both disorder parameters — σ for the Gaussian model and E_t for the exponential model.

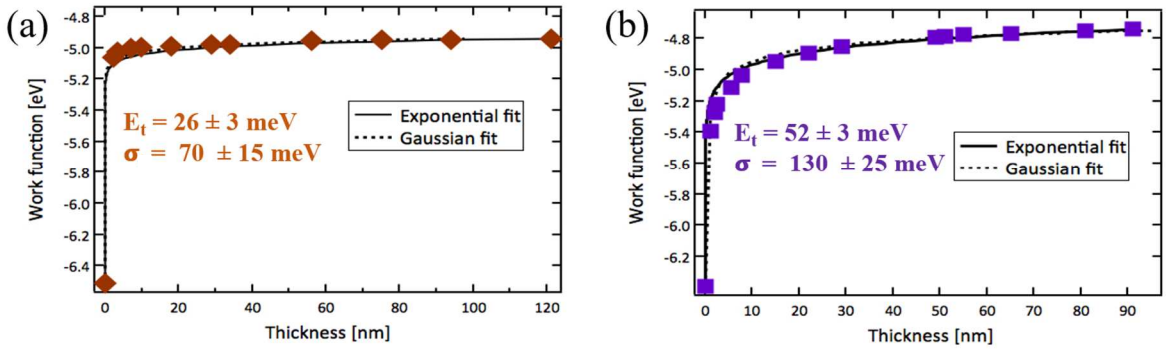

Figure 5.4. Band bending profiles of a) PTB7-Th and b) MEH-PPV films cast on 70 nm thick MoO_3 layer.

As shown in Figure 4a, in the case of PTB7-Th, there is minimal change in the work-function of the film with increasing thickness. This is equivalent to a small degree of band bending. A fit to Equation 6 gives an exponential disorder (E_t) term of 26 meV — which is almost equivalent to kT and is the limit for the application of the exponential DOS model. The disorder width (σ) obtained from the Gaussian DOS model is 70 meV. Furthermore, previous reports have shown that band bending profiles that show a quick, sharp plateau at relatively small (< 10 nm) thicknesses — which is the case for PTB7-Th — is indicative of highly ordered films.[17,215,218] On the other hand, the band bending profile for MEH-PPV (Figure 4b) shows a larger change in the work-function of films with increasing polymer thickness. Both exponential DOS and Gaussian DOS fits to the band bending profiles for this polymer reveal large DOS widths, giving E_t of 52 meV and σ of 130 meV, respectively.

Energy-Resolved Electrochemical Impedance Spectroscopy Method for Characterizing Tail States Disorder

Using the Kelvin probe method, we obtain exponential DOS widths of 52 meV and 26 meV for MEH-PPV and PTB7-Th, respectively. These values are now compared to the

exponential widths of the DOS distributions from a third technique, namely electrochemical impedance spectroscopy (ER-EIS). There has been significant progress in the last few decades on electrochemical impedance spectroscopy (EIS) methods.[219] Recently, a novel energy resolved electrochemical impedance spectroscopy (ER-EIS) method was developed as a way to measure the DOS of organic polymers over wide energy ranges.[51,220] The ER-EIS technique is based on the reduction-oxidation reaction occurring at the interface of a polymer semiconductor film and an electrolyte. In the experimental set-up, an electrochemical cell is placed on a conductive ITO substrate spin-coated with an organic polymer semiconductor film. The DOS of an organic polymer film can be measured by sweeping an externally applied potential (U) of the polymer thin film in order to modify the fermi level. At each applied potential, U, impedance spectroscopy is performed by applying a small perturbing potential at different frequencies. A few assumptions are made in order to derive the DOS from the measured redox current at the semiconductor-electrolyte interface.[220] The charge transfer current density between the electrolyte and the semiconductor surface can be written as

$$j = ek_{et}n_s[A] \tag{7}$$

where e is the elementary charge, k_{et} is the charge transfer coefficient, n_s is the semiconductor surface carrier concentration at the Fermi level, and $[A]$ is the electrolyte concentration.

In order to construct the DOS from the ER-EIS method, it is defined as the number of states at a given energy E in an energy interval dE, such that $g(E) = dn/dE$. With the assumption that the surface electronic structure of the polymers is well represented by that of the bulk, the DOS can now be written in the form below

$$g(E_F = eU) = \frac{dn_s}{d(eU)} \tag{8}$$

Since the application of the perturbing potential varies n_s, the charge transfer resistance can be found experimentally, where $R_{ct} = dU/d(jS)$.

Substituting Equation 7 to Equation 8, and replacing the expression for R_{ct}, the DOS function at the fermi energy, $g(E_F)$, can now be expressed in terms of the charge transfer resistance, R_{ct}, under an applied voltage U, as follows:

$$g\ (E_F = eU) = \frac{1}{e^2\, k_{et}\, [A] S R_{ct}} \tag{9}$$

where, S is the active sample surface area. From Equation 9, the reconstructed DOS, $g(E_F)$, is found to be inversely proportional to the experimentally measured charge-transfer resistance term, R_{ct}.[220]

Figure 5.5 shows the ER-EIS measurements of the electronic structures of the polymers. In contrast to other competing methods[177,178,222–224], information about the DOS parameters can be directly obtained from the measured spectra by using ER-EIS. By fitting the extremities of the HOMO DOS with an exponential dependence, the exponential disorder parameter ΔE_0 can be found, which corresponds to the exponential disorder arising from the tail states of the HOMO DOS distribution. In this analysis, a steeper slope obtained from the exponential fit corresponds to a narrower DOS width. The exponential disorder terms obtained from fitting the DOS extremities using this method is 25 meV for PTB7-Th and 51 meV for MEH-PPV.

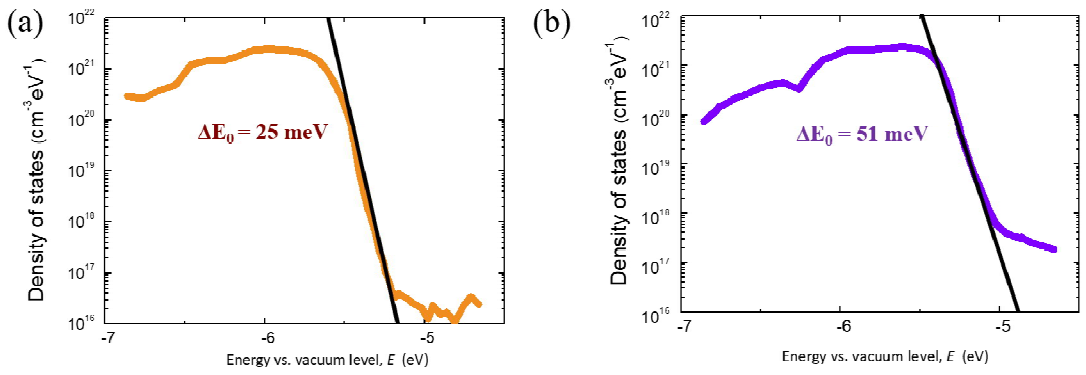

Figure 5.5. HOMO DOS functions of a) PTB7-Th and b) MEH-PPV films measured by the ER-EIS method.

Connecting the DO(T)S: Unification of charge transport and band bending

The energetic disorder terms for the HOMO DOS from the Gaussian and exponential models using different techniques are summarized in **Table 5.1**. A measure of disorder using these different techniques give agreeable estimates of disorder values. A good agreement is found between the Gaussian widths estimated using the KP and temperature-dependent *J-V* measurements — with values for both polymers falling within error of each other. The exponential widths estimated from KP and ER-EIS methods are also in agreement. It is worth noting that the correlation observed between the Gaussian and exponential DOS width values obtained from this work for both polymers is equivalent to the correlation reported in the literature.[206]

Table 5.1. Comparison of Gaussian and Exponential energetic disorder terms obtained from Kelvin probe, temperature-dependent *J-V*s (EGDM), and ER-EIS methods.

Donor Polymer	σ_t (Kelvin Probe) [meV][a)]	σ_o (Temperature-dependent J-V) [meV][a)]	E_t (Kelvin Probe) [meV][a)]	ΔE_0 (ER-EIS) [meV][a)]
MEH-PPV	130 ± 25	125 ± 10	52 ± 3	51
PTB7-Th	70 ± 15	75 ± 10	26 ± 3	25

[a)] Measurements for each technique were repeated three times for reproducibility.

The similar values obtained from the different techniques can be attributed to the common assumptions and conditions in each measurement. Discrepancies in mobility values between hole-only diodes and field-effect transistors have been shown to be due to differences in the values of charge carrier densities at operating conditions (10^{21} -10^{23} m^{-3} for diodes vs. 10^{23} - 10^{25} m^{-3} for FETs).[206] The similar DOS widths obtained from all three techniques in this study can likely be attributed to the similarities in charge carrier densities in all three techniques (10^{21} -10^{23} m^{-3}).[202,218,220]

KP and ER-EIS techniques are both based on the band-bending phenomenon happening at a semiconductor-electrode or semiconductor-electrolyte interface, which is independent of any influence of electric-field or light-intensity. While temperature dependent *J-V* measurements are done under the influence of an applied electric field and at different temperatures, the EGDM model takes the electric-field, charge carrier density, and temperature-dependence into account, thereby bearing out a disorder value that has no influence on such extrinsic effects. While KP and ER-EIS techniques specifically probe only

the tail states of the DOS distribution, EGDM assumes that the whole DOS distribution is described by a single Gaussian. An important assumption in obtaining the DOS width is that charge carriers be under no influence of applied electric-field or light-intensity, and so the assumptions during the measurements (from KP and ER-EIS) and in the analysis for the EGDM (from *J-V* measurements) ensure that in the DOS width being probed, the effect of charges near the tail states of the DOS distribution — where the number of charge carriers are much less than the number of hopping sites — are taken into account.

Quantification of Ordered and Disordered Regions in Thin Films Using GIWAXS and Solid-state NMR

For a better understanding of the origins in the differences of charge transport and DOS widths between these two structurally distinct polymers, we complement the experimentally measured energetic disorder values with a suitable study of the solid-state film morphology. It has long been established that degrees of film ordering play crucial roles in determining the charge transport properties; specifically, ordered films lead to higher charge carrier mobilities.[225–227] Grazing-Incidence Wide-Angle X-Ray Scattering (GIWAXS) is a commonly used technique to probe the relative differences in the long-range order of films. Qualitative comparison of the 100 reflections in the GIWAXS patterns of PTB7-Th and MEH-PPV films (Appendix D, Figure D4) showed MEH-PPV with a broader peak indicative of more features that are randomly oriented in this film in comparison to the narrower reflection pattern of PTB7-Th.[228] Furthermore, the crystalline coherence length (L_c), which is a quantity related to the average crystal size in a film, is larger for PTB7-Th in both the in-plane and out-of-plane directions (Appendix D, Table D1).[228] A drawback to GIWAXS, however, is that it only detects signals coming from the ordered regions in a film and so, accurately quantifying

the absolute amount of crystalline and amorphous regions in a film requires the use of additional complementary techniques.[229]

For the purpose of identifying and quantifying the ordered and disordered backbone regions in the spin-coated PTB7-Th and MEH-PPV thin films, solid-state magic-angle-spinning (MAS) NMR was used to probe the structures of these polymers at a molecular level. Solid-state MAS NMR is sensitive to local (ca. 1 nm) bonding environments and complements scattering analyses that are sensitive to long-range structural order (ca. 100's nm).[80,81,143,153] Specifically, ^{1}H, ^{13}C and ^{19}F isotropic chemical shifts provide information on backbone conformation and inter- or intra-molecular interactions. In this respect, the presence of well-ordered backbone moieties is expected to yield relatively narrow ^{1}H and ^{19}F signals, whereas disordered regions exhibit relatively broad signals that manifest distributions of polymer conformations and structural disorder associated with the backbone moieties. In addition, the ordered and disordered regions of alkyl sidechains can be distinguished on the basis of the γ-gauche effect;[230] for example, when two -CH_2- groups are in a γ-position relative to one another and in *trans*/*trans* (*tt*) configurations, the isotropic ^{13}C chemical shifts are displaced to higher frequencies, compared to the same moieties with *trans*/*gauche* (*tg*) or *gauche*/*gauche* (*gg*) conformations that are displaced to lower frequencies. Analyses of ^{1}H, ^{13}C, and ^{19}F NMR isotropic chemical shifts and integrated signal intensities are therefore expected to provide quantitative information on the relative populations of different polymer moieties in ordered and disordered regions, which is difficult to obtain from X-ray scattering and electron microscopy techniques.

Analyses of one-dimensional (1D) solid-state ^{1}H MAS NMR spectra of PTB7-Th and MEH-PPV enabled numerous ^{1}H signals associated with polymer backbone and sidechain

moieties to be identified and distinguished (Appendix D, Figure D5), but not all, as severely overlapped signals stemming from 17 chemically distinct ^{1}H sites in PTB7-Th and 10 different ^{1}H sites in MEH-PPV hinder the assignment of these ^{1}H signals. The ^{1}H signals from the PTB7-Th sidechains are only partially resolved due to structurally identical sidechains substituted on the thiophene and thienothiophene moieties in comparison to the analogous ^{1}H signals from the MEH-PPV sidechains. Nevertheless, the high intrinsic sensitivity, high natural abundance (100%), and substantial chemical shift range associated with ^{19}F MAS NMR permitted ^{19}F signals to be resolved and assigned to specific fluorine atom moieties, on which the quantitative description of ordered and disordered backbone regions in PTB7-Th is based. The 1D ^{19}F MAS NMR spectrum of PTB7-Th powdered thin films acquired at 30 kHz MAS (**Figure 5.6**a) showed a narrow signal at -110 ppm that corresponds to ^{19}F sites in ordered PTB7-Th backbone moieties, along with broad weak signals in the ranges -125 ppm to -135 ppm and -155 ppm to -170 ppm, which were attributed to fluorine atoms in disordered PTB7-Th backbone moieties. Integration of the ^{19}F signal intensities indicates that the vast majority (99±1%) of the ^{19}F atoms are in locally ordered PTB7-Th backbone environments (-110 ppm), with a very small percentage (<1%) in disordered backbones.

To distinguish between ordered and disordered regions in MEH-PPV thin films, a single-pulse ^{13}C MAS NMR spectrum was acquired and analyzed (**Figure 5.6b**). On the basis of isotropic ^{13}C chemical shifts of MEH-PPV reported in the literature[231] and subsequent line shape analyses, the ^{13}C signals in the aromatic region could be assigned to the backbone moieties, as follows: 151 ppm to carbon atoms *C1* and *C4*, 126 ppm to *C3* and *C6*, 120 ppm to *C7* and *C8*, and the range 107-120 ppm to *C2* and *C5*. Similarly, in the alkyl region of the spectrum, the ^{13}C signals are assigned to the alkyl sidechains, as follows: 71 ppm to carbon

atom *Ca* , 55 ppm to *Ci*, 40 ppm *Cb*, 30 ppm to *Cc* and *Cd*, 23 to *Ce* and *Cg*, 14 to *Cf*, and 11 ppm to *Cg*. In particular, the ^{13}C chemical shifts of carbon atoms C2 and C5 are expected to be sensitive to conformational differences across the C5-C6-C7-C8 dihedral angle that bisects the phenylene and vinylene moieties: the narrow ^{13}C signal at 107 ppm is attributed to C2 and C5 atoms in ordered MEH-PPV backbones and the broad ^{13}C intensity centered at 112 ppm is attributed to C2 and C5 atoms in disordered MEH-PPV backbones. Line shape analyses of partially resolved signals were deconvoluted to estimate the relative fractions of ordered and disordered regions of MEH-PPV backbones. The average of integrals of the deconvoluted ^{13}C signals associated with the C1-C8 moieties indicate that the MEH-PPV film consisted of 43±5% ordered and 57±5% disordered backbone moieties, respectively. Thus, quantitative solid-state ^{19}F and ^{13}C NMR analyses suggest that PTB7-Th films have relatively higher fraction of ordered conjugated backbone regions, compared to the backbone moieties in the MEH-PPV films, which is consistent with the measured differences in the DOS widths and with their distinct charge-carrier properties.

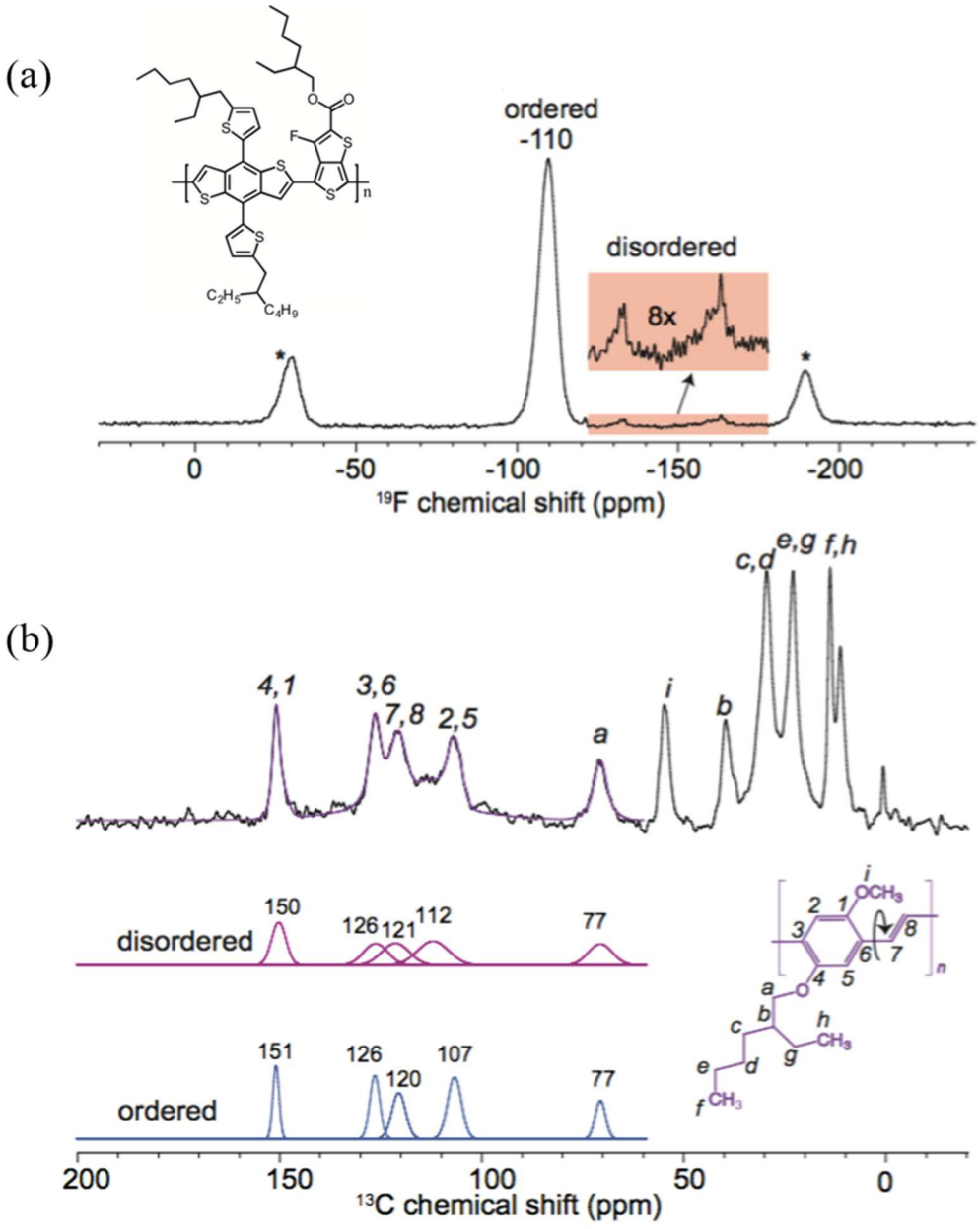

Figure 5.6. a) Solid-state 1D ^{19}F MAS NMR spectrum acquired at 9.4 T, 298 K, and 30 kHz MAS for powdered PTB7-Th films; b) Solid-state 1D ^{13}C MAS NMR spectrum of powdered MEH-PPV films acquired at 9.4 T, 298 K, and 15 kHz MAS.

5.3. Conclusion

To summarize, here for the first time by using three different techniques, a quantitative correlation between energetic disorder from band bending measurements and charge transport is established. This work provides direct experimental evidence that charge carrier mobility is compromised due to the relaxation of carriers into the tail states of the DOS. An amorphous and disordered polymer, MEH-PPV, with a low charge carrier mobility and a crystalline and ordered polymer, PTB7-Th, with a high charge carrier mobility both show trap-free hole transport and reveal distinctly different energetic disorder values as a result of different film morphologies. By combining quantitative solid-state film morphology studies of organic semiconducting polymers at an atomic level to energetic disorder and in turn charge transport, this work presents useful guidelines to characterize organic semiconducting polymers for applications in pertinent devices.

5.4. Experimental Section

Materials: Poly[4,8-bis(5-(2-ethylhexyl)thiophen-2-yl)benzo[1,2-b;4,5-b']dithiophene-2,6-diyl-alt-(4-(2-ethylhexyl)-3-fluorothieno[3,4-b]thiophene-)-2-carboxylate-2-6-diyl)] (PTB7-Th) of M_w 145,000 Da and Poly[2-methoxy-5-(2-ethylhexyloxy)-1,4-phenylenevinylene] (MEH-PPV) of M_w 120,000 Da were purchased from 1-material and used as-received.

Hole only diode fabrication: Diodes were prepared on Corning glass substrates patterned with 140 nm of indium tin oxide (ITO) and scrubbed with detergent followed by sonication in soapy water, deionized water, acetone, and isopropanol. Substrates were then treated with O_2 plasma for 30 mins and spin-coated with a ~35 nm thick PEDOT:PSS (Clevios P VP Al 8043) layer and annealed in air for 20 mins at 140 ^{0}C. Pristine polymer solutions in chlorobenzene

were prepared inside the glovebox and left stirring on a hot-plate overnight before spin-coating the films onto the layer of PEDOT:PSS films inside a nitrogen-filled glovebox. In order to ensure an unchanged morphology for polymer films made with different thicknesses, the polymer solution concentrations were varied while keeping the spin-speeds constant at 1500 rpm. The devices were finished with a deposition of a 10 nm MoO_3 layer followed by a 100 nm Ag capping layer with a thermal evaporator at a pressure of less than 1×10^{-6} torr.

Electrical measurements: Temperature-dependent *J-V* curves of diodes were measured using a liquid nitrogen cryostat with a Keithley 2602A system source-meter and a Lakeshore 321 temperature controller at a pressure of less than 1×10^{-6} torr. Film thicknesses were measured using an Ambios XP-100 profilometer.

Kelvin Probe measurements: Films of PTB7-Th and MEH-PPV were cast on ITO substrates with a 70 nm evaporated MoO_3 layer. The concentration of films cast on substrates were varied to obtain a range of layer thicknesses. All polymer films were spin cast at 1500 rpm to avoid any morphological changes. Contact potential difference (CPD) values were measured using a SKP 5050 (KP technology, UK) Kelvin probe with a stainless-steel tip of 2 mm diameter. The probe work function was calibrated against freshly cleaved HOPG, with its work function assumed to be 4.6 eV. [232,233] All measurements were done inside an inert nitrogen-filled glovebox.

Energy-resolved Electrochemical Impedance spectroscopy: Electrochemical microcells were formed on ITO substrates with deposited polymer thin films. All polymer films were spin cast at 1500 rpm to avoid any morphological changes. The solution of 0.1 M TBAPF6 in anhydrous acetonitrile was used as the supporting electrolyte. The dissociation of this electrolyte in the inert atmosphere occurred at an overpotential of 63.5 V. The active polymer electrode area

was 12 mm^2. The potential of the working electrode with respect to the reference Ag/AgCl electrode was controlled via a potentiostat. Pt wire was used as the counter electrode. The potential recorded with respect to the reference Ag/AgCl electrode was recalculated to the local vacuum level assuming the Ag/AgCl energy vs. vacuum value of 4.66 eV. An Impedance/ gain-phase analyzer, Solartron analytical, model 1260 (Ametek, Berwyn, USA), was used. The AC harmonic voltage signal frequency was 0.5Hz, its amplitude was 100mV, and the sweep rate of the DC voltage ramp was 10 mV/s. Bode and Cole-Cole diagrams in the frequency range of 0.01–1 MHz were used as a preliminary ER-EIS method adjustment. The sensitive nature of the experimental method requires the experiment to be conducted in an inert atmosphere, yielding reproducible measured DOS spectra.

Solid-state NMR: Spin-coated thin films of PTB7-Th and MEH-PPV were scratched off by using a scraper blade and the extracted powdered films were packed into 1.3 mm and 2.5 mm (outer diameter) zirconia rotors fitted with Vespel® caps. Single-pulse ^1H MAS NMR spectra of PTB7-Th and MEH-PPV were acquired at 11.7 T, 298 K, and 58 kHz MAS on a Bruker AVANCE-II NMR spectrometer operating at a ^1H frequency of 500.2 MHz and equipped with Bruker 1.3 mm H-X MAS probehead; 32 coadded transients were signal-averaged using a recycle delay of 3 s, corresponding to a total experimental time of 2 min for each spectrum. 1D ^{19}F and ^{13}C MAS NMR spectra were acquired at 9.4 T and 298 K on a Bruker AVANCE-III NMR spectrometer operating at a ^{19}F frequency of 376.5 MHz and a ^{13}C frequency of 100.6 MHz equipped with a 2.5 mm H-F-X MAS probehead. A 1D single-pulse ^{19}F MAS spectrum of PTB7-Th was acquired at 30 kHz MAS with 512 co-added transients and a recycle delay of 15 s, corresponding to a total experimental time of 2 h. A 1D single-pulse ^{13}C MAS spectrum of MEH-PPV was acquired at 15 kHz MAS with 7568 co-added transients and

recycle delay of 10 s, corresponding to a total experimental time of 21 h. Heteronuclear decoupling was applied during acquisition using the SPINAL64 pulse sequence.[234]

GIWAXS: GIWAXS measurements were performed at beamline 7.3.3 at the Advanced Light Source with an X-ray wavelength of 1.2398 Å at a 300 mm sample detector distance. The measurements were calibrated using a AgB standard. Samples were scanned in a He environment at an incident angle of 0.14^{o}.

Appendices

Appendix A:

Appendix to Chapter 2

Average power conversion efficiencies (*PCE*s) of PTB7-Th:IOTIC-4F, PTB7-Th:IOTIC-2F$_a$, and PTB7-Th:IOTIC solar cells

Table A1. Average *PCE*s obtained at 1 sun illumination (100 mWcm^{-2}, AM 1.5) from 30 devices for each blend system.

Blend system	V_{OC} [V]	J_{SC} [mA cm^{-2}]	Integrated J_{SC} from EQE [mA cm^{-2}]	FF	PCE_{max} (PCE_{avg}) [%]
PTB7-Th:IOTIC-4F	0.72 ± 0.002	20.5 ± 0.5	19.7	0.68 ± 0.02	10.2 (10.1 ± 0.2)
PTB7-Th:IOTIC-2F$_a$	0.79 ± 0.003	14.8 ± 0.7	14.5	0.60 ± 0.02	7.2 (7.0 ± 0.2)
PTB7-Th:IOTIC	0.88 ± 0.003	10.7 ± 0.5	10.3	0.60 ± 0.01	6.0 (5.7 ± 0.3)

Qualitative determination of the dominant recombination process in the blends from 300 K to 200 K

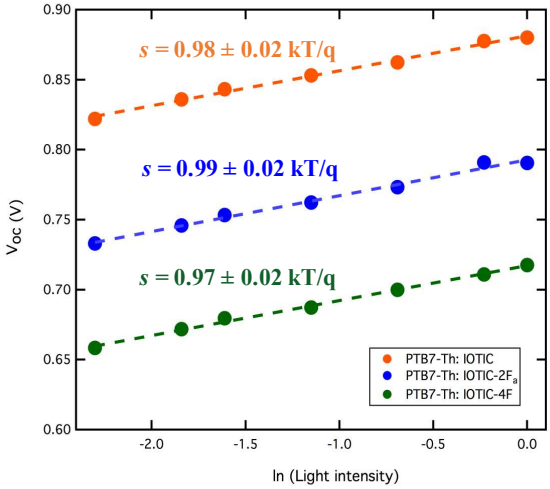

Figure A1. V_{OC} vs. ln (light intensity) plots for the three studied blend systems.

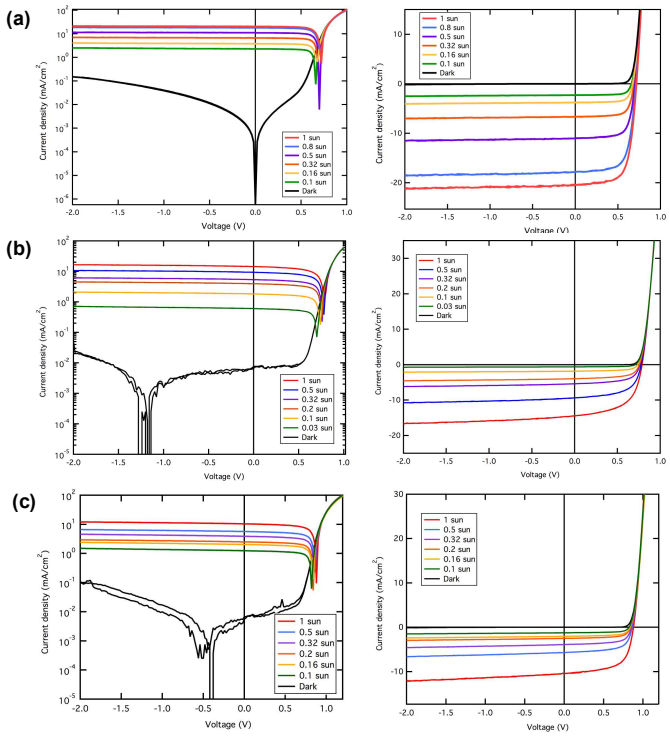

Figure A2. *J-V* curves of the three blend systems plotted at varying light intensities on semi-log and linear scale for (a) PTB7-Th:IOTIC-4F, (b) PTB7-Th:IOTIC-2Fa, and (c) PTB7-Th:IOTIC blends to assess the effect of leakage currents on the slopes of V_{OC} vs. ln (I) plots.

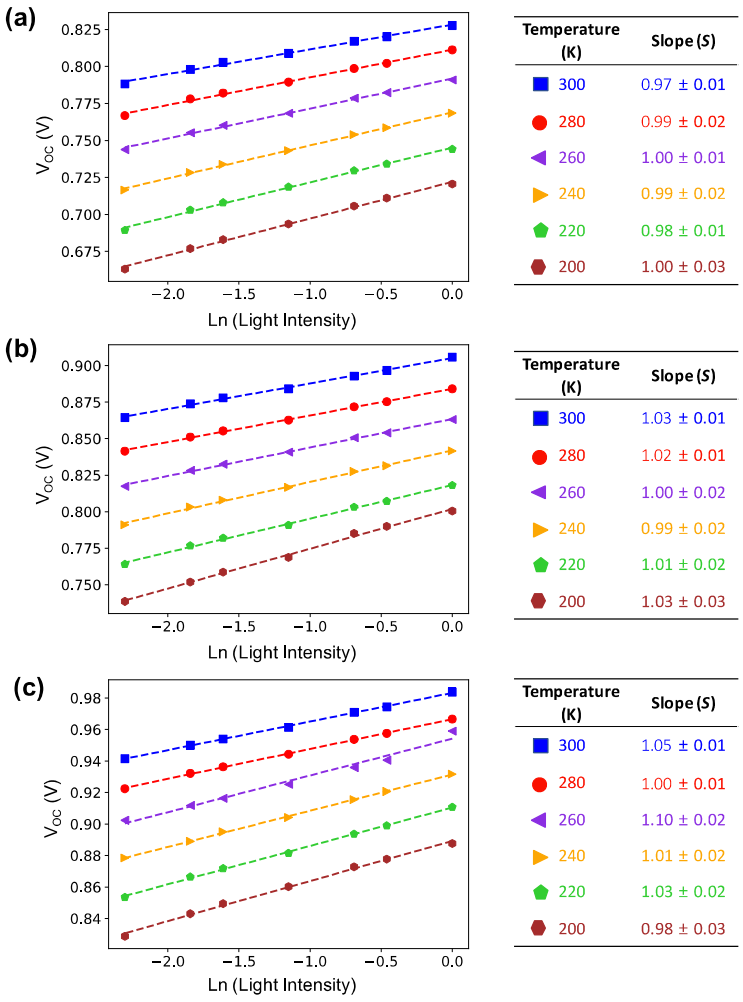

Figure A3. V_{OC} vs. ln (light intensity) plots and the determined slopes s for (a) PTB7-Th:IOTIC-4F, (b) PTB7-Th:IOTIC-2F$_a$, and (c) PTB7-Th:IOTIC blend systems at temperatures of 200 - 300 K.

Determination of S_1 by the EQE and EL intersection of the lower bandgap acceptors (IOTIC, IOTIC-2F$_a$, and IOTIC-4F)

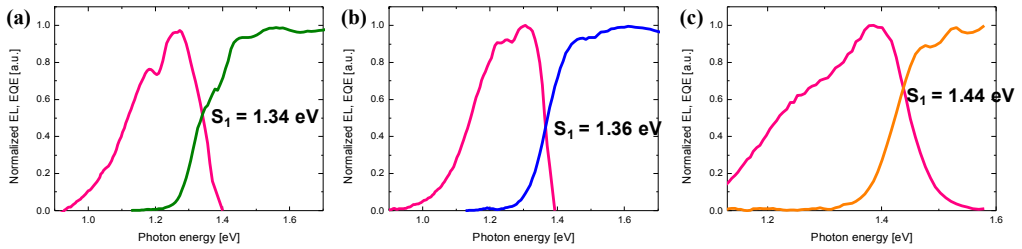

Figure A4. Determination of S_1 by the intersection of EQE and EL of acceptor only devices: (a) IOTIC-4F, (b) IOTIC-2Fa, and (c) IOTIC.

Quantifying the contribution to voltage losses from S_1 to V_{OC}

a. Equations used to obtain the CT energy:

$$EQE_{PV,CT}(E) = \frac{f}{E\sqrt{4\pi\lambda k_B T}} \exp\left(\frac{-(E_{CT}+\lambda-E)^2}{4\lambda k_B T}\right) \quad \text{(S1)}$$

$$EQE_{EL,CT}(E) = E\frac{f}{\sqrt{4\pi\lambda k_B T}} \exp\left(\frac{-(E_{CT}-\lambda-E)^2}{4\lambda k_B T}\right)$$

(S2)

$$EQE_{PV}(E) \propto EL(E)E^{-2} \exp\left(\frac{E}{k_B T}\right)$$

(S3)

Here, k_B is Boltzmann's constant, E is the photon energy, and T is the absolute temperature. The fit parameters are E_{CT}, which is the energy at the point of intersection between CT absorption and emission, λ, which is the reorganization energy, and f, which is a measure of the strength of the donor-acceptor coupling.

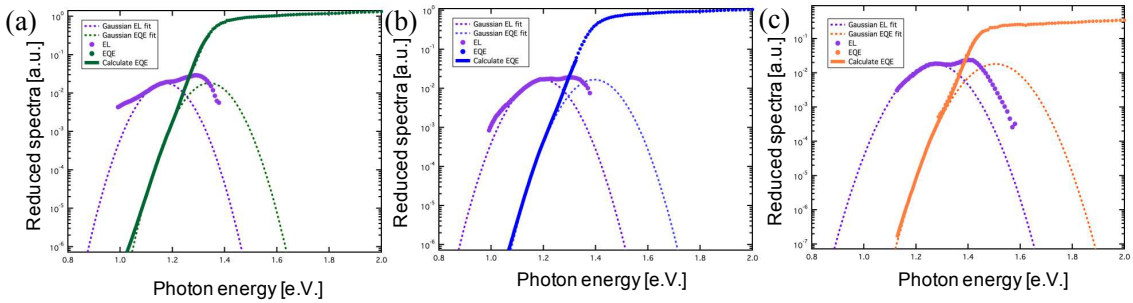

Figure A5. Reduced emission and absorption spectra for the three blend systems with the Marcus Theory fits. The dotted lines are fits to the reduced spectra, calculated from Equations S1 and S2. The reciprocity relationship in Equation S3 has been used to fit the Gaussian to the EQE$_{PV}$ spectra. The following fit parameters were used for (a) PTB7-Th:IOTIC-4F: λ =

0.085 eV, E_{CT} = 1.26 eV, f = 3.5E-3 eV^2, (b) PTB7-Th:IOTIC-2Fa: λ = 0.1 eV, E_{CT} = 1.295 eV, f = 3.5E-3 eV^2, and (c) PTB7-Th:IOTIC: λ = 0.117 eV, E_{CT} = 1.39 eV, f = 3.5E-3 eV^2 blend systems.

Extrapolation of temperature dependent V_{OC} at different light intensities to obtain the E_{CT} at 0 K

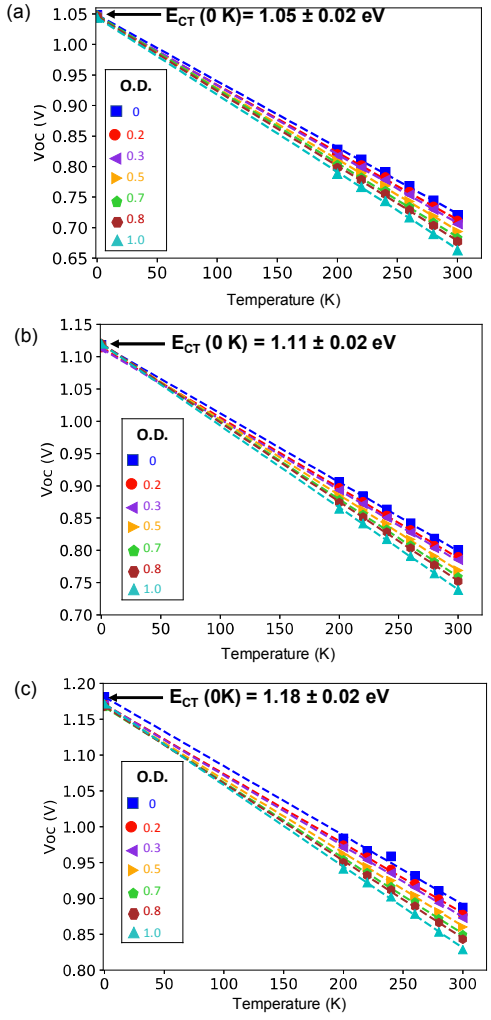

Figure A6. Temperature-dependent V_{OC} for (a) PTB7-Th:IOTIC-4F, (b) PTB7-Th:IOTIC-2F$_a$, and (c) PTB7-Th:IOTIC blend systems measured at seven different light intensities (0, 0.2, 0.3, 0.5, 0.7, 0.8, and 1 OD) extrapolated to 0 K for an estimate of the E_{CT} at 0 K.

Table A2. Comparison of the E_{CT} values at 0 K (obtained from the extrapolation of temperature dependent V_{OC} measurements) and at 295 K (obtained from Marcus fitting).

	PTB7-Th:IOTIC-4F	**PTB7-Th:IOTIC-2F$_a$**	**PTB7-Th:IOTIC**	**Δ E_{CT}**
E_{CT} at 295 K [eV]	1.26 ± 0.01	1.295 ± 0.01	1.39 ± 0.01	0.13 ± 0.02
E_{CT} at 0 K [eV]	1.05 ± 0.01	1.11± 0.01	1.18 ± 0.01	0.13 ± 0.02

Equations used to calculate the radiative and non-radiative recombination:

$$V_{OC} = \frac{E_{CT}}{q} - \Delta V_{rad}(T) - \Delta V_{nonrad}(T)$$

(S4)

$$\Delta V_{rad}(T) = -\frac{kT}{q} ln(\frac{J_{SC} h^3 c^2}{f q 2\pi (E_{CT} - \lambda)})$$

(S5)

$$\Delta V_{nonrad}(T) = -\frac{kT}{q} ln(EQE_{EL})$$

(S6)

Using the fit parameters: f, λ, and E_{CT} obtained from **Equations S1** and **S2**, the losses due to radiative recombination in the PTB7-Th:IOTIC, PTB7-Th:IOTIC-2F$_a$, and PTB7-Th:IOTIC-4F blend systems are calculated from **Equation S5.** Non-radiative recombination losses can be calculated using **Equation S4,** where the calculated radiative recombination obtained from **Equation S5** is used.

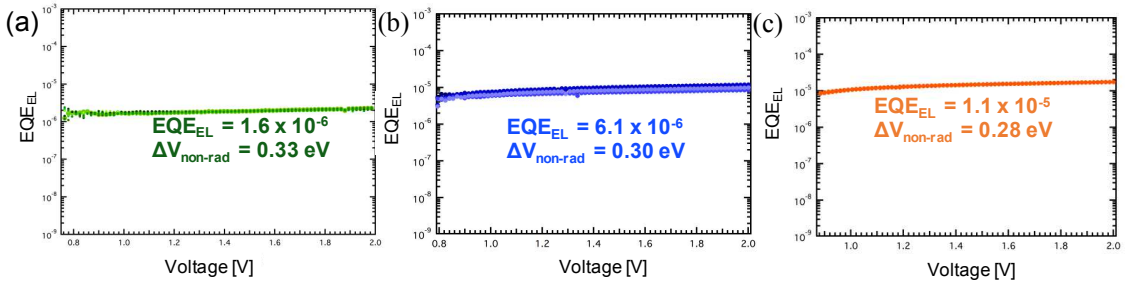

Figure A7. Measured EQE$_{EL}$ values for (a) PTB7-Th:IOTIC-4F, (b) PTB7-Th:IOTIC-2F$_a$, and (c) PTB7-Th:IOTIC over applied bias for five devices, where the EQE$_{EL}$ values were

extracted from the voltage at which the injected current is equal to the J_{SC} of the devices under 1 sun illumination.

Table A3. Summarizing energy losses from S_1 to V_{OC} for all three blends. S_1 is determined from the intersection of the EL and EQE of the narrower bandgap components (acceptors) in the blends, E_{CT} is obtained via simultaneous fitting to the reduced emission and absorption spectrum using Marcus theory and the trends in E_{CT} are confirmed with temperature dependent V_{OC} method, ΔV_{rad} is obtained from **Equation S5**, the calculated $\Delta V_{non\text{-}rad}$ is obtained from **Equation S4 and S5**, and the experimental $\Delta V_{non\text{-}rad}$ is obtained from EQE_{EL} measurements (**Equation S6**).

Blend system	S_1 **[eV]**	E_{CT} **[eV]**	ΔV_{rad} **[eV]**	$\Delta V_{non\text{-}rad,\ calc}$ **[eV]**	$\Delta V_{non\text{-}rad,\ exp}$ **[eV]**	V_{OC} **[V]**
PTB7-Th:IOTIC	1.44	1.39	0.227	0.283	0.284	0.88
PTB7-Th:IOTIC-2F$_a$	1.36	1.295	0.212	0.298	0.300	0.792
PTB7-Th:IOTIC-4F	1.34	1.26	0.203	0.337	0.330	0.716

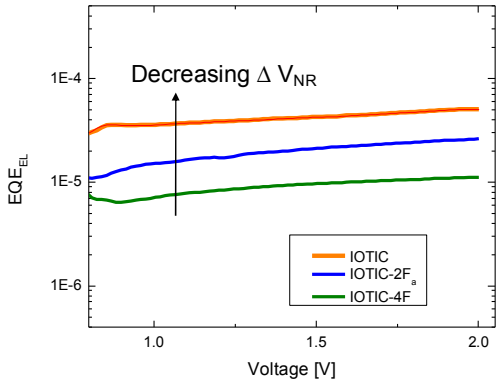

Figure A8. EQE_{EL} of neat acceptor only devices.

Comparing losses due to energetic disorder between the three blend systems

i. Energy-Resolved Electrochemical Impedance Spectroscopy (ER-EIS):

The ER-EIS technique is based on the reduction-oxidation reaction occurring at the interface of a polymer semiconductor film and an electrolyte. In the experimental set-up, an

electrochemical cell is placed on a conductive ITO substrate spin-coated with an organic polymer semiconductor film. The DOS of an organic polymer film can be measured by sweeping an externally applied potential (U) of the polymer thin film in order to modify the fermi level. At each applied potential, U, impedance spectroscopy is performed by applying a small perturbing potential at different frequencies. A few assumptions are made in order to derive the DOS from the measured redox current at the semiconductor-electrolyte interface.[220] The charge transfer current density between the electrolyte and the semiconductor surface can be written as

$$j = ek_{et}n_s[A] \quad \text{(S7)}$$

where e is the elementary charge, k_{et} is the charge transfer coefficient, n_s is the semiconductor surface carrier concentration at the Fermi level, and $[A]$ is the electrolyte concentration.

In order to construct the DOS from the ER-EIS method, it is defined as the number of states at a given energy E in an energy interval dE, such that $g(E) = dn/dE$. With the assumption that the surface electronic structure of the polymers is well represented by that of the bulk, the DOS can now be written in the form below

$$g(E_F = eU) = \frac{dn_s}{d(eU)} \quad \text{(S8)}$$

Since the application of the perturbing potential varies n_s, the charge transfer resistance can be found experimentally, where $R_{ct} = dU/d(jS)$.

Substituting **Equation S7** to **Equation S8**, and replacing the expression for R_{ct}, the DOS function at the fermi energy, $g(E_F)$, can now be expressed in terms of the charge transfer resistance, R_{ct}, under an applied voltage U, as follows:

$$g\,(E_F = eU) = \frac{1}{e^2\,k_{et}\,[A]SR_{ct}} \quad \text{(S9)}$$

where, S is the active sample surface area. From **Equation S9**, the reconstructed DOS, $g(E_F)$, is found to be inversely proportional to the experimentally measured charge-transfer resistance term, R_{ct}.[220]

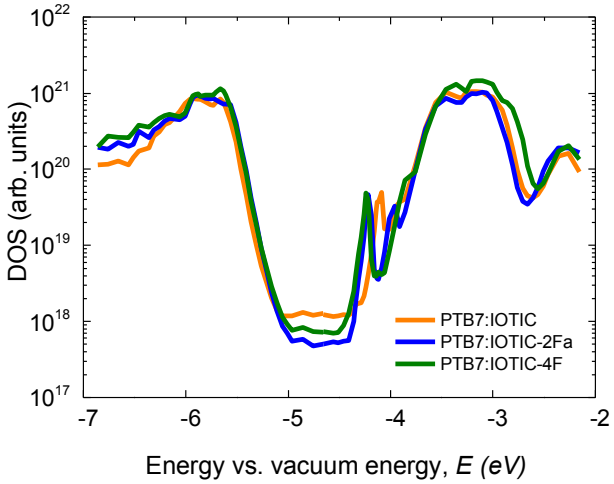

Figure A9. DOS spectra of PTB7-Th:IOTIC, PTB7-Th:IOTIC-2F$_a$, and PTB7-Th:IOTIC-4F thin films as measured by the ER-EIS method. The LUMO I blend peaks at ~ -4.10-4.24 eV in all three spectra are near the energy of the CT states in the blends which is further useful for confirming that the differences in the E_{CT} values of the three blends are minimal (~ 0.13 eV) and similar to that reported of the other two techniques in **Table S2**.[235]

ii. Urbach energy as a measure of the disorder in the tail states

The Urbach rule[236] includes a fit parameter called the Urbach energy (E_U), which in the case of disordered semiconductors has been shown to be related to the tails of the density-of-states (DOS) distribution.[55,237] The E_U can therefore be extracted from the dependence of the absorption on photon energies below the band-edge of a semiconductor as measured by photothermal deflection spectroscopy[55,237] or EQE techniques[17,44,238]. The relationship between E_U and absorption is shown in **Equation S10** below:

$$\alpha(E) = \alpha_0 e^{\frac{(E-E_0)}{E_U}} \quad \text{(S10)}$$

where α_0 and E_0 are constants and E is the photon energy.

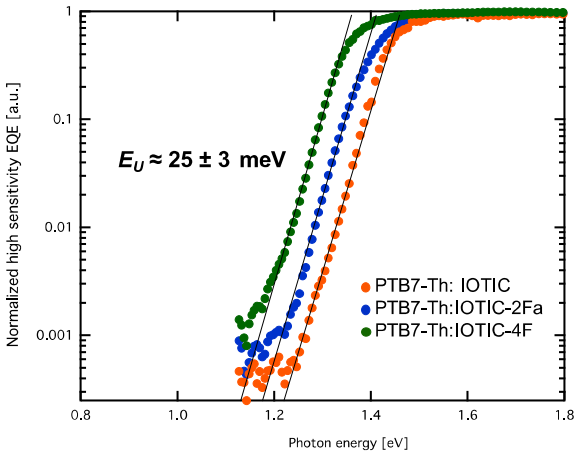

Figure A10. Black line shows a fit to the tail of the highly sensitive EQE spectra using **Equation S10** showing an Urbach energy of $E_U \approx 25 \pm 3$ meV.

Probing charge generation dynamics in the three blend systems

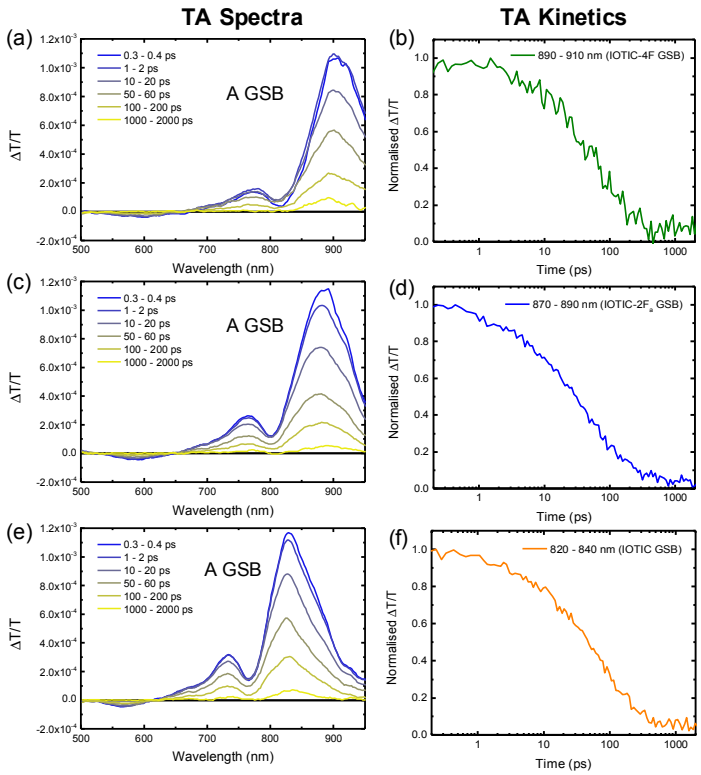

Figure A11. TA spectra and fitted kinetics showing the ground state bleach of **(**a,b) PS:IOTIC-4F (pump: 925 nm and fluence: 0.96 μJ cm^{-2}) (c,d) PS:IOTIC-2F$_a$ (pump: 900 nm and fluence: 0.65 μJ cm^{-2}), and (e,f) PS:IOTIC (pump: 860 nm and fluence: 0.74 μJ cm^{-2}).

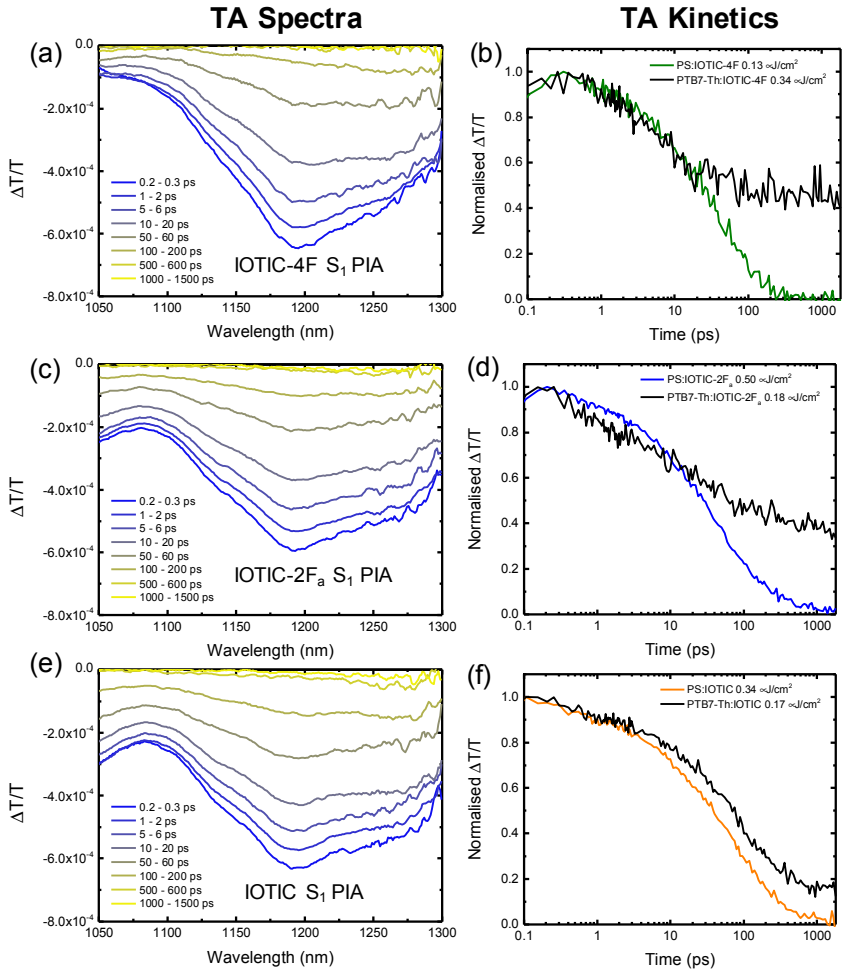

Figure A12. TA spectra showing the photo-induced absorption (PIA) band of the first singlet excited state centered at around 1200 nm and fitted kinetics of (a,b) PS:IOTIC-4F (pump: 800 nm and fluence: 0.13 μJ cm^{-2}) (c,d) PS:IOTIC-2F_a (pump: 800 nm and fluence: 0.5 μJ cm^{-2}), and (e,f) PS:IOTIC (pump: 800 nm and fluence: 0.34 μJ cm^{-2}). Also included are the fitted kinetics of (b) PTB7-Th:IOTIC-4F (pump: 800 nm and fluence: 0.34 μJ cm^{-2}) (d) PTB7-Th:IOTIC-2F_a (pump: 800 nm and fluence: 0.18 μJ cm^{-2}), and (f) PTB7-Th:IOTIC (pump: 800 nm and fluence: 0.17 μJ cm^{-2}).

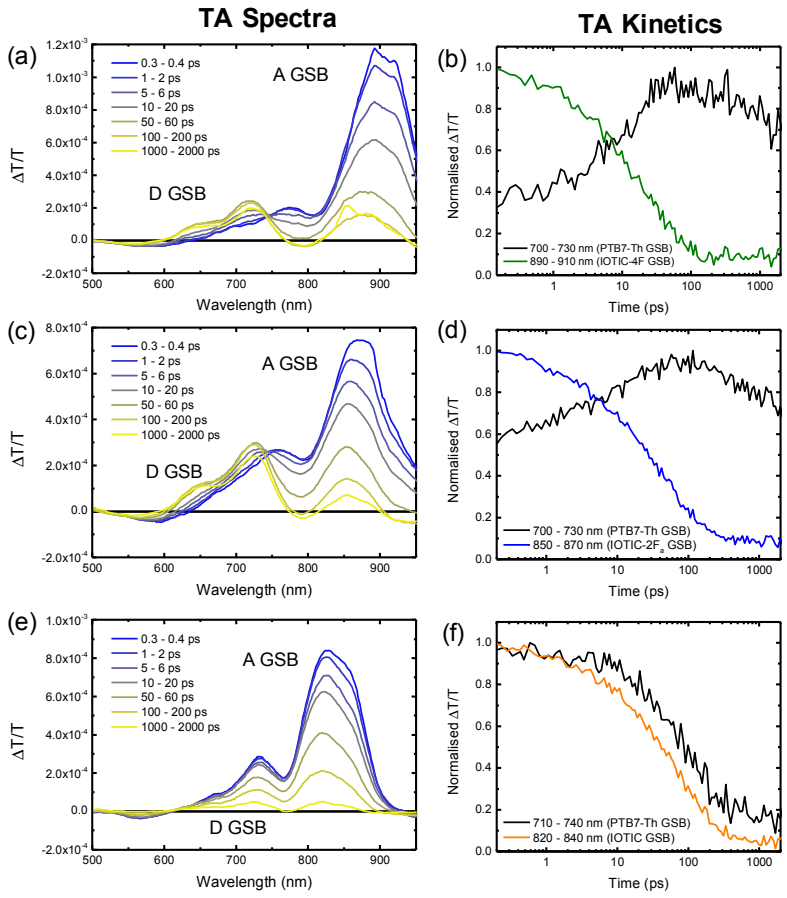

Figure A13. Visible region TA of (a,b) PTB7-Th:IOTIC-4F film (pump: 925 nm and fluence: 0.51 μJ cm^{-2}) (c,d) PTB7-Th:IOTIC-2F$_a$ (pump: 900 nm and fluence: 0.87 μJ cm^{-2}), and (e,f) PTB7-Th:IOTIC (pump: 860 nm and fluence: 0.5 μJ cm^{-2}).

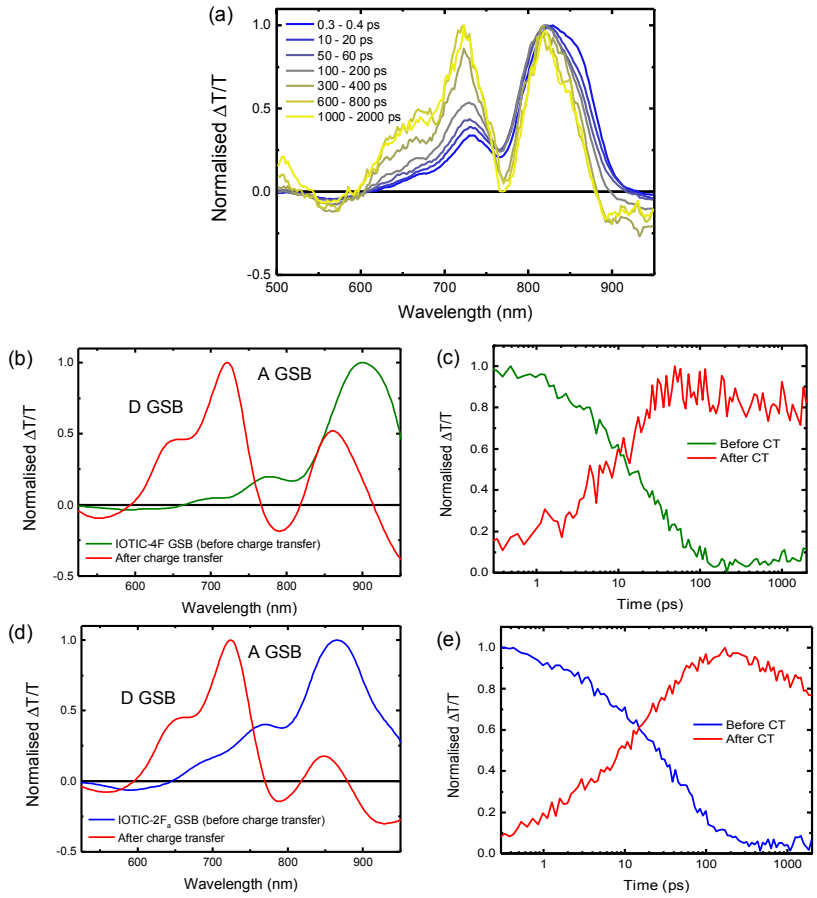

Figure A14. (a) Normalized TA spectra of the PTB7-Th:IOTIC blend. TA spectra and fitted kinetics before and after charge transfer of (b,c) PTB7-Th:IOTIC-4F film (pump: 925 nm and fluence: 0.51 μJ cm^{-2}) (d,e) PTB7-Th:IOTIC-2F$_a$ (pump: 900 nm and fluence: 0.87 μJ cm^{-2}).

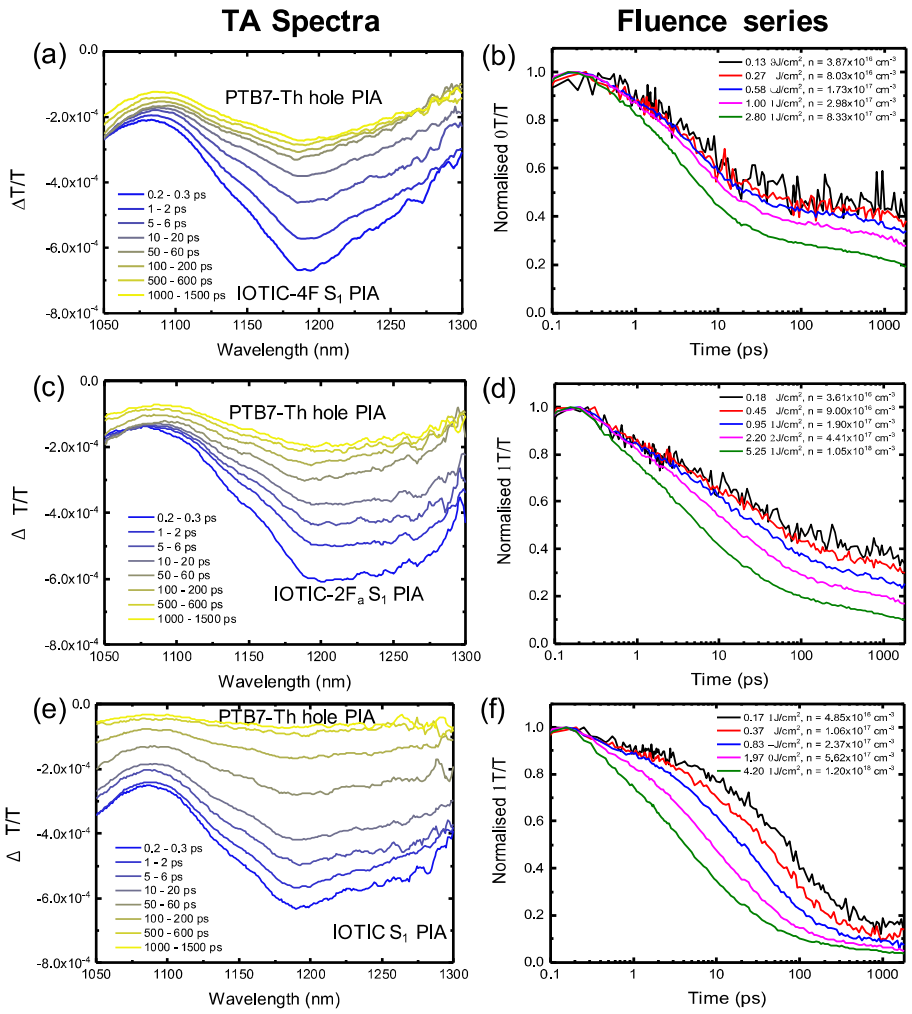

Figure A15. TA and fluence series of films excited with a pump wavelength of 800 nm for (a,b) PTB7-Th:IOTIC-4F film (fluence: 0.27 μJ cm^{-2}) (c,d) PTB7-Th:IOTIC-2F_a (0.45 μJ cm^{-2}), and (e,f) PTB7-Th:IOTIC (fluence: 0.37 μJ cm^{-2}).

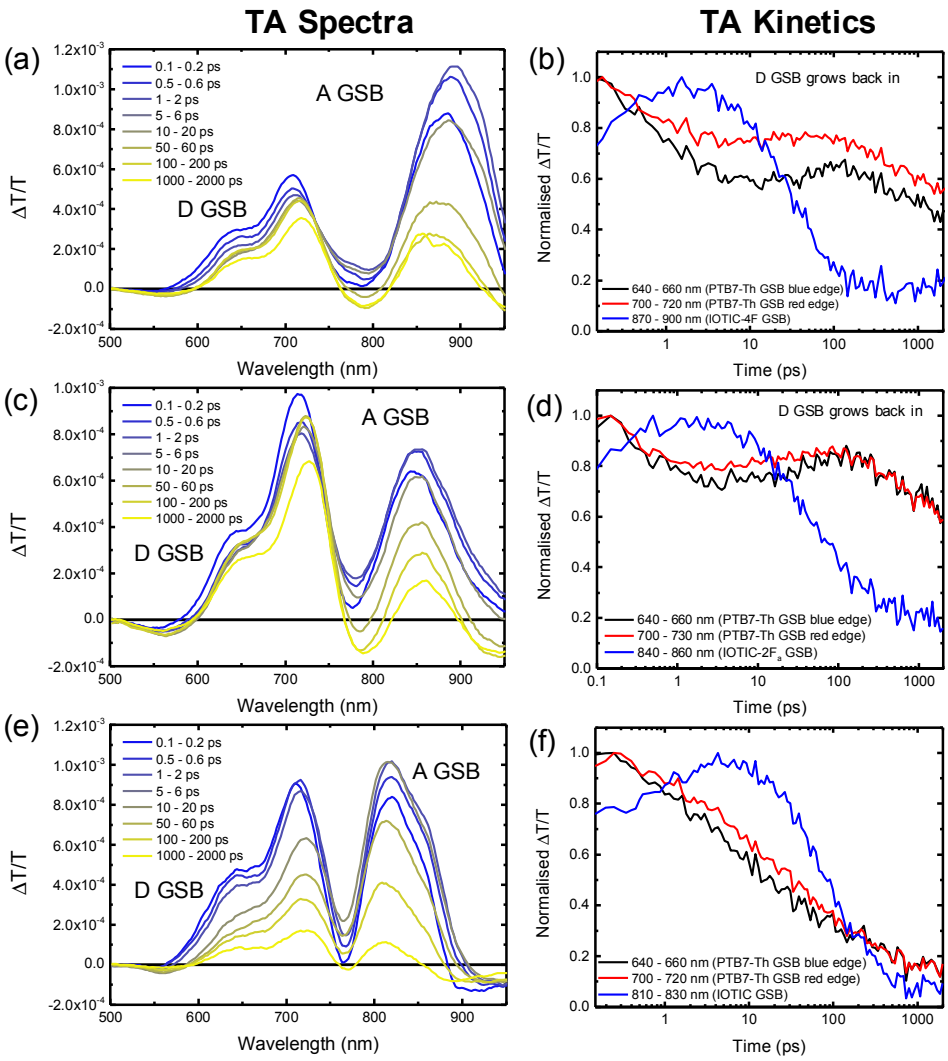

Figure A16. Visible TA and kinetics of films excited with a pump wavelength of 600 nm (mainly excitation of the PTB7-Th donor) of (a,b) PTB7-Th:IOTIC-4F film (fluence: 0.54 μJ cm^{-2}) (c,d) PTB7-Th:IOTIC-2F$_a$ (0.77 μJ cm^{-2}), and (e,f) PTB7-Th:IOTIC (fluence: 0.81 μJ cm^{-2}).

Determining the non-geminate charge recombination and extraction dynamics

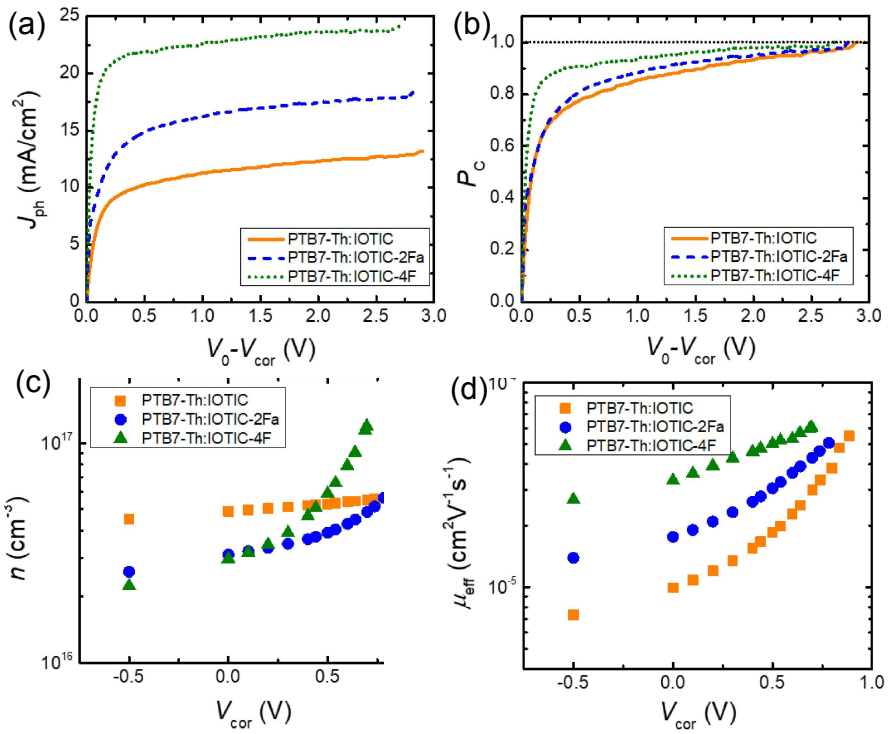

Figure A17. (a) Photocurrent density J_{ph}, (b) collection probability *Pc* over collected bias. (c) charge carrier density *n,* and (d) effective mobility μ_{eff} over corrected voltages of the studied solar cell devices.

b. Determining charge carrier densities from capacitance spectroscopy

The dielectric constants (ε_r) of the three blend systems measured by capacitance spectroscopy at a reverse bias of -3 V and in the dark (**Figure A18**) were found to be similar (PTB7-Th:IOTIC-4F = 2.52 ± 0.2, PTB7-Th:IOTIC-2Fa = 2.35 ± 0.2, PTB7-Th:IOTIC = 2.61 ± 0.2). At this DC bias, there should be no frequency dependence of the capacitance. Then, the assumption is that the capacitance of the blend (C_b) measured under these conditions is equal to the geometric capacitance (C_g), which would allow employing the following equation to calculate the dielectric constant ε_r:

$$\varepsilon_r = \frac{C_g L}{\varepsilon_0 A}, \quad \text{(S11)}$$

where L is the thickness of the active layer and A is the area of the device. To begin a quantitative analysis of the recombination dynamics, it is necessary to obtain values for the charge carrier density n. It is known that capacitance spectroscopy can be employed to determine the density of charge carriers in organic solar cells under illumination. Capacitance

spectroscopy was performed to yield the charge carrier density n, *via* integration of the chemical capacitance ($C_{chem} = C_b[\omega = 50\ kHz] - C_g$) using the following equations:

$$n(V_{cor}) = n_{sat} + \frac{1}{qAL}\int_{V_{sat}}^{V_{cor}} C_{chem} dV_{cor}, \tag{S12}$$

$$n_{sat} = \frac{1}{qAL} C_{sat}(V_0 - V_{sat}), \tag{S13}$$

where A is the area of the solar cell, L is the thickness, V_{sat} is the reverse bias at which the photocurrent saturates, n_{sat} is the charge carrier density at the saturation voltage V_{sat}, and C_{sat} is the difference in capacitance of the BHJ layer C_b under illumination and in the dark at V_{sat} and an angular frequency $\omega = 50$ kHz. V_0 is the forward bias at which the photocurrent is equal to zero.

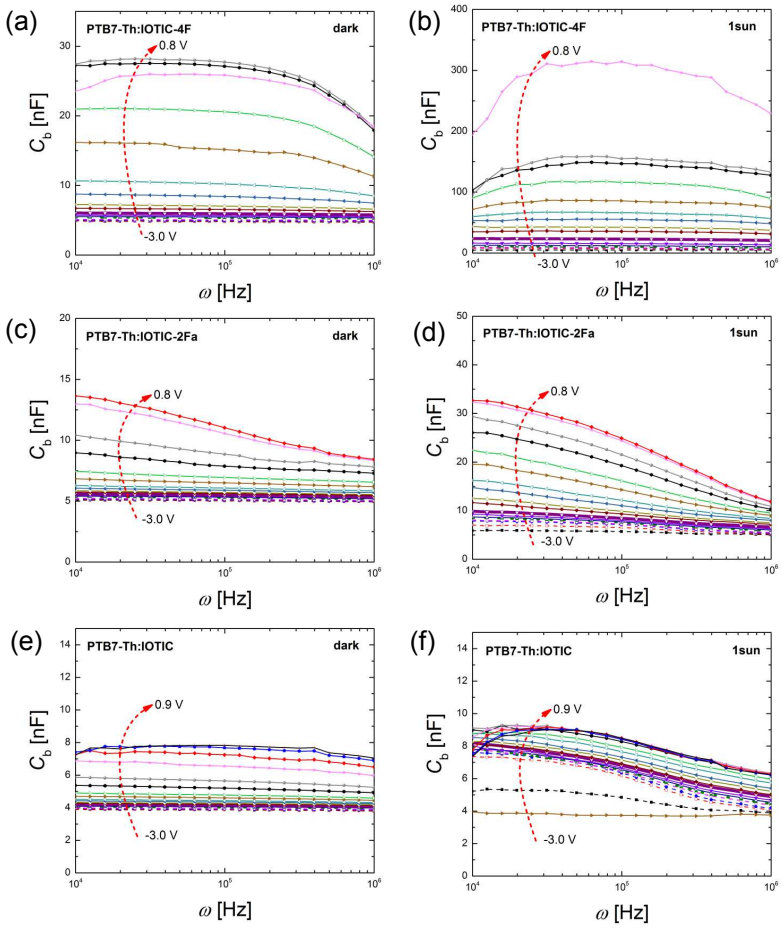

Figure A18. Frequency and DC bias dependent corrected capacitance C_b of the tested solar cells in the (a,c,e) dark and (b,d,f) under 1-sun illumination for the three studied blend systems. C_b at an angular frequency $\omega = 50$ kHz was used to determine the chemical capacitance C_{chem}.

c. Determining the effective mobilities (μ_{eff}) under operating conditions

The calculation of a field and charge carrier dependent, effective mobility $\mu_{eff}(n,V)$ has been introduced by Albrecht *et. al.* as an alternative to the hole/electron mobility $\mu_{p/n}$ determined *via* the Mott-Gurney relationship of space-charge limited currents (SCLC) in single carrier devices.[68] It has been shown that mobilities determined *via* SCLC measurements may be unreliable due to deviation from the expected thickness dependent behavior, the variation of electrode materials that may have an impact on the morphology, charge carrier densities and electric-fields that are larger in the SCLC regime in comparison to the normal operating conditions of a solar cell (ultimately leading to overestimated mobilities), inconsistencies in determining the built-in fields, and finally the fact that the motion of injected carriers is measured in contrast to photogenerated carriers.[53,68,239–241] The use of such an effective mobility μ_{eff} is especially encouraged, if a strong dependence of the mobility on either the applied bias V, the charge carrier density n, or both can be expected. Here, μ_{eff} can be calculated by employing the following equation:

$$\mu_{eff}(n,V_{cor}) = \frac{J(V_{cor}) \cdot L}{2qn(V_{cor}) \cdot [V_{cor} - V_0]},$$

(S14)

where J is the current density, V_{cor} is the corrected voltage, V_0 is the voltage at which the photocurrent is equal to zero, L is the device thickness, q is the elementary charge, and n is the charge carrier density obtained from capacitance spectroscopy.

d. A full quantitative approach for determination of the non-geminate recombination dynamics

The following relationship has to be considered as a starting point for the full quantitative analysis of the non-geminate recombination dynamics, where it is assumed that the recombination current density ($J_{rec} = J_{ph,sat} - J_{ph}$) is a superposition of the three aforementioned recombination mechanisms, namely bimolecular, bulk trap-assisted, and surface trap-assisted recombination:

$$J_{rec} = J_{bm} + J_{tb} + J_{ts} = qL\left(\frac{n}{\tau_{bm}} + \frac{n}{\tau_{tb}} + \frac{n}{\tau_{ts}}\right) = qL(k_{bm}n^2 + k_{tb}n + k_{ts}n).$$

(S15)

Here L is the active layer thickness, τ is the charge carrier lifetime, and k is the recombination coefficient of the three different recombination mechanisms (bm: bimolecular; tb: bulk trap-

assisted; ts: surface trap-assisted). It should be noted that the recombination coefficient describing surface recombination, k_{ts}, depends on the voltage.

The bimolecular component $J_{rec,bm}$ can be described by the following equation:

$$J_{rec,bm} = qLk_{bm}n^2 = \frac{q^2L}{\varepsilon_0\varepsilon_r}\xi(\mu_n+\mu_p)n^2 \quad , \tag{S16}$$

where k_{bm} is the bimolecular recombination coefficient, ξ is the reduction factor (also known as Langevin prefactor), n is the charge carrier density, and $\mu_{n,p}$ are the electron and hole mobility, respectively. The effective mobility μ_{eff} was used to replace $\mu_{n,p}$. The following expression describes the bulk trap-assisted contribution $J_{rec,bulk}$:

$$J_{rec,bulk} = qLk_{t,b}n = \frac{q^2L}{\varepsilon_0\varepsilon_r}\mu_n N_{t,b}n \, , \tag{S17}$$

where $N_{t,b}$ is the density of deep traps in the bulk, and $k_{t,b}$ is the bulk-trap assisted recombination coefficient. Again, the effective mobility μ_{eff} was used. The surface trap-assisted component $J_{rec,surf}$ can be described in a similar way as $J_{rec,bulk}$, with the addition of a field-dependent term:

$$J_{rec,surf} = qLk_{t,s}(V_{cor})n = \frac{q^2}{\varepsilon_0\varepsilon_r}\frac{\mu_p N_{t,s}n}{\exp\left\{\frac{q(V_{bi}-V_{cor})}{kT}\right\}} \, , \tag{S18}$$

where $N_{t,s}$ is the density of surface traps, V_{bi} is the built-in voltage, V_{cor} is the corrected voltage, $k_{t,s}(V_{cor})$ is the surface-trap assisted recombination coefficient, and μ_p is replaced by the effective mobility. A detailed description and derivation of this analytical model can be found in Ref. 3.[3] The reconstruction of the recombination current density ($J_{rec,sum}$) is optimized by determining the highest adjusted R^2 value with the reduction factor (ξ), bulk trap density ($N_{t,b}$), and surface trap density ($N_{t,s}$) selected as fitting parameters. The quality of the fit can be assessed by an adjusted R^2. Indeed, it can be confirmed from the fits in **Figure A19** that in accordance to the qualitative results of the V_{OC} vs. ln(I) plots, bimolecular recombination is the dominant non-geminate recombination mechanism for the three blend systems. Bulk trap-assisted recombination is negligible for all blends and surface trap-assisted recombination has only a very limited, unavoidable contribution at high forward biases.[120]

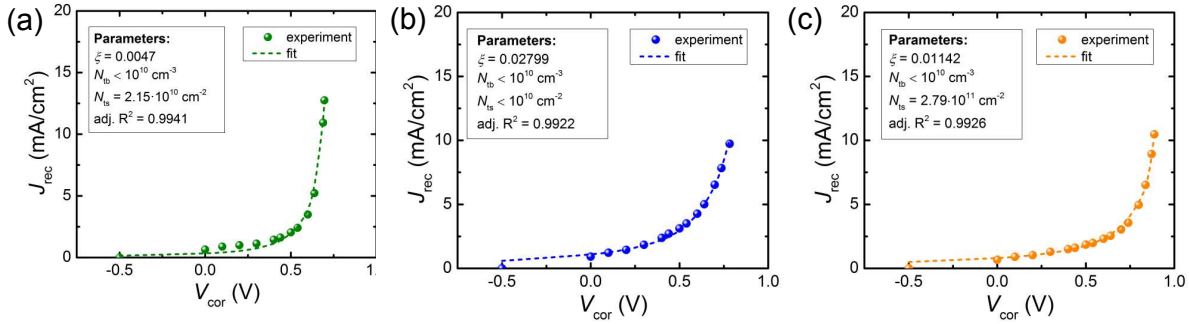

Figure A19. Experimental and fitted recombination current density J_{rec} for (a) PTB7-Th:IOTIC-4F, (b) PTB7-Th:IOTIC-2F$_a$, and (c) PTB7-Th:IOTIC devices.

e. Comparison of recombination and extraction lifetimes across corrected voltages

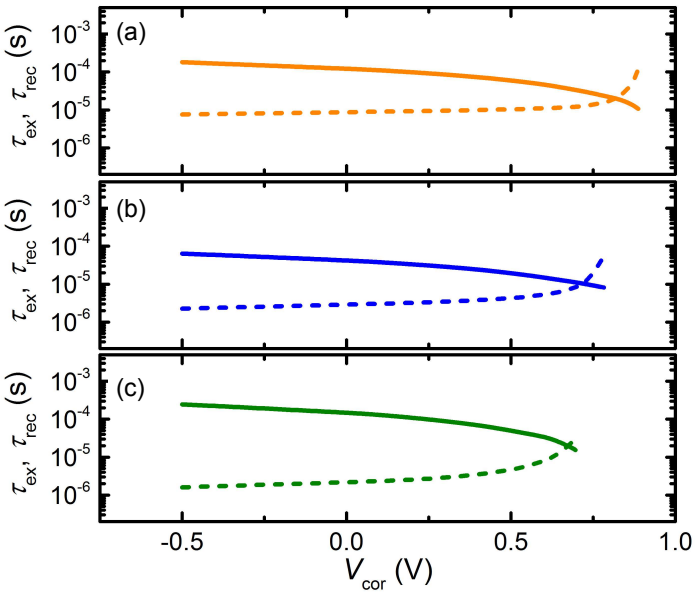

Figure A20. Comparison of charge carrier and extraction lifetimes across the corrected voltages of (a) PTB7-Th:IOTIC, (b) PTB7-Th:IOTIC-2F$_a$, (c) PTB7-Th:IOTIC-4F devices.

Analysis of photoconductive atomic force microscopy (pc-AFM)

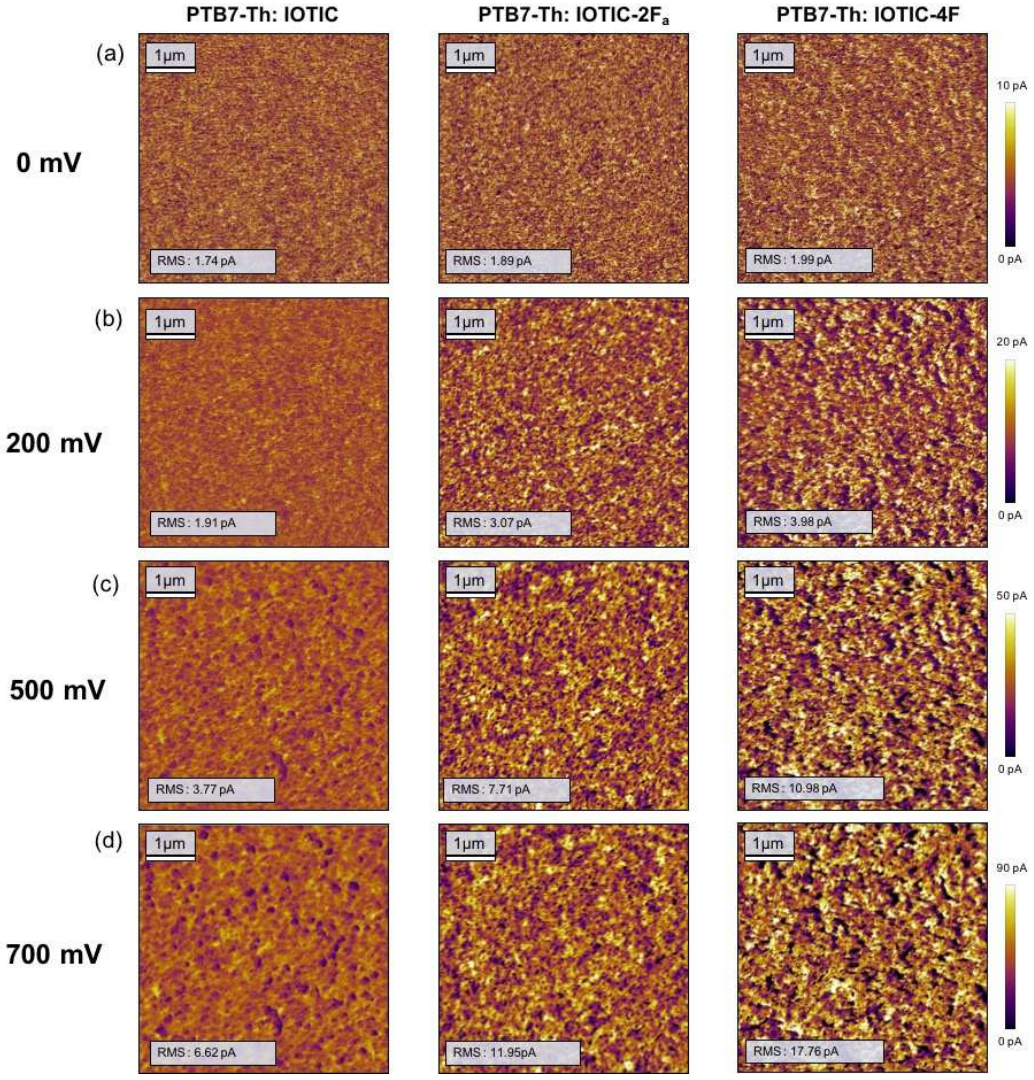

Figure A21. Photocurrent images normalized to the device with the highest photocurrent (PTB7-Th: IOTIC-4F) obtained under white light illumination and at (a) 0 V, (b) 200 mV, (c) 500 mV, and (d) 700 mV biases.

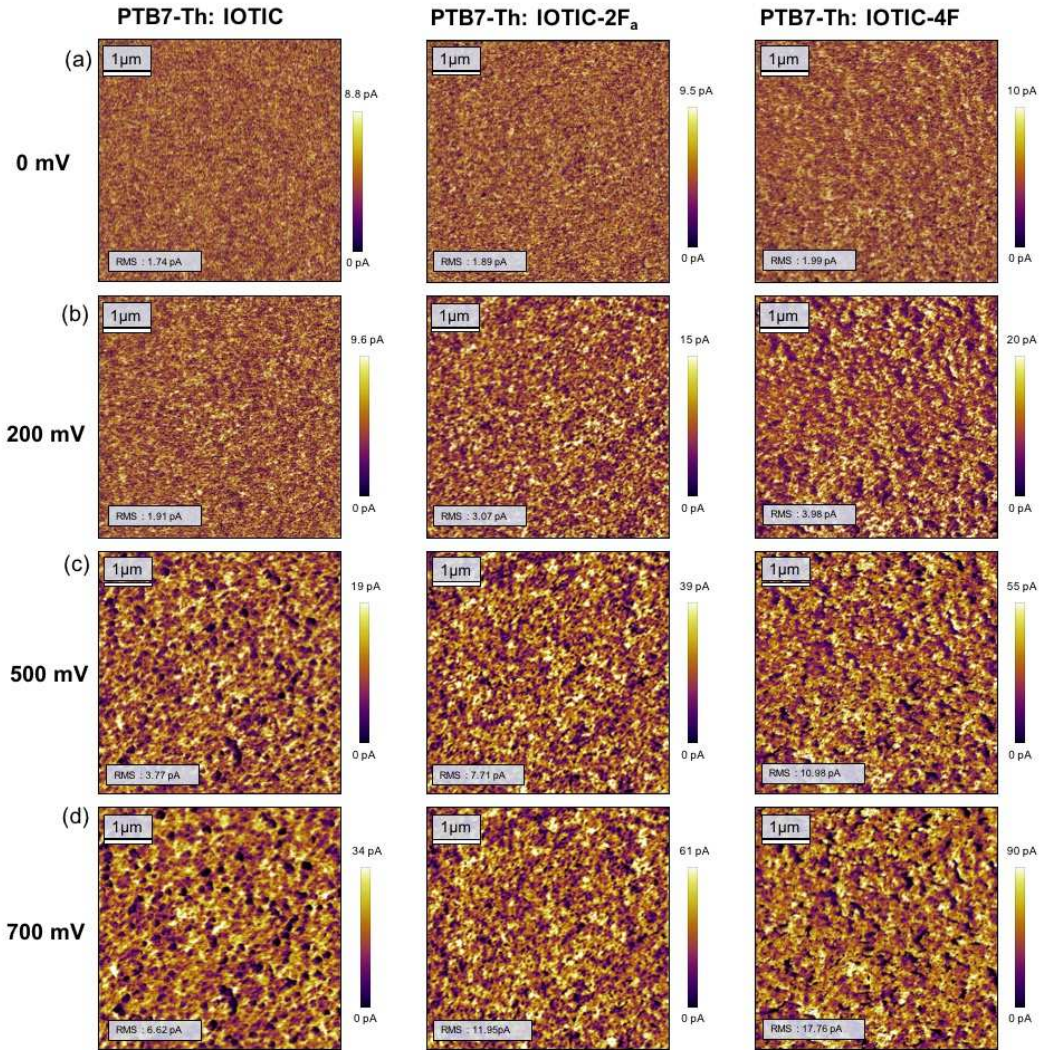

Figure A22. Photocurrent images of the three studied devices under white light illumination obtained at (a) 0 V, (b) 200 mV, (c) 500 mV, and (d) 700 mV.

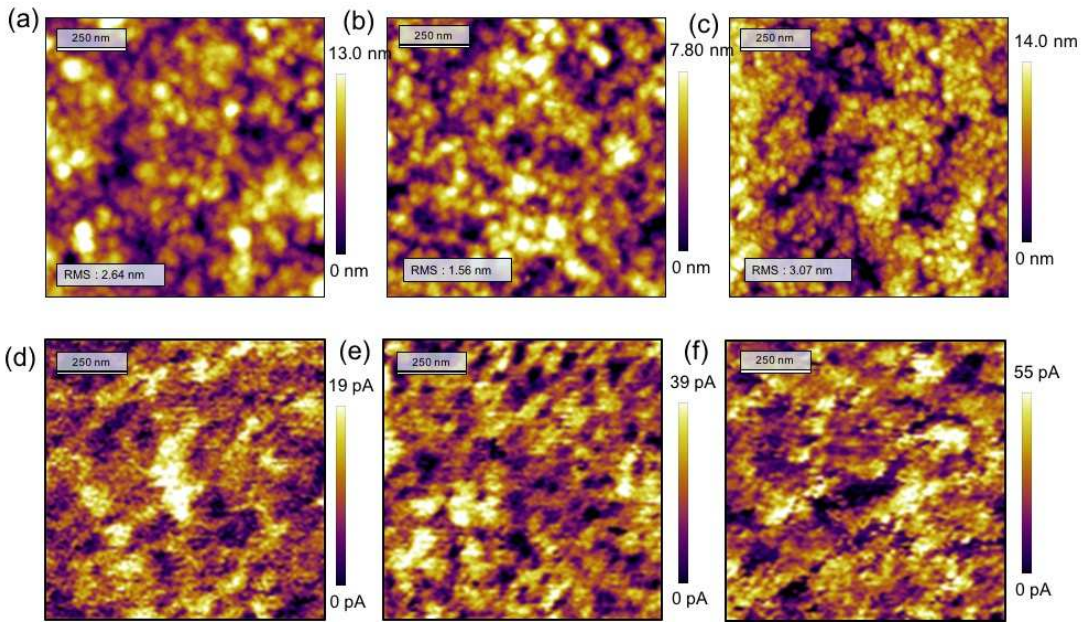

Figure A23. High resolution (1 x 1 μm^2) height images of the (a) PTB7-Th: IOTIC, (b) PTB7-Th: IOTIC-$2F_a$, and (c) PTB7-Th: IOTIC-4F blends and the corresponding photocurrent images: (d) PTB7-Th: IOTIC, (e) PTB7-Th: IOTIC-$2F_a$, and (f) PTB7-Th: IOTIC-4F.

GIWAXS analyses of neat and blend films

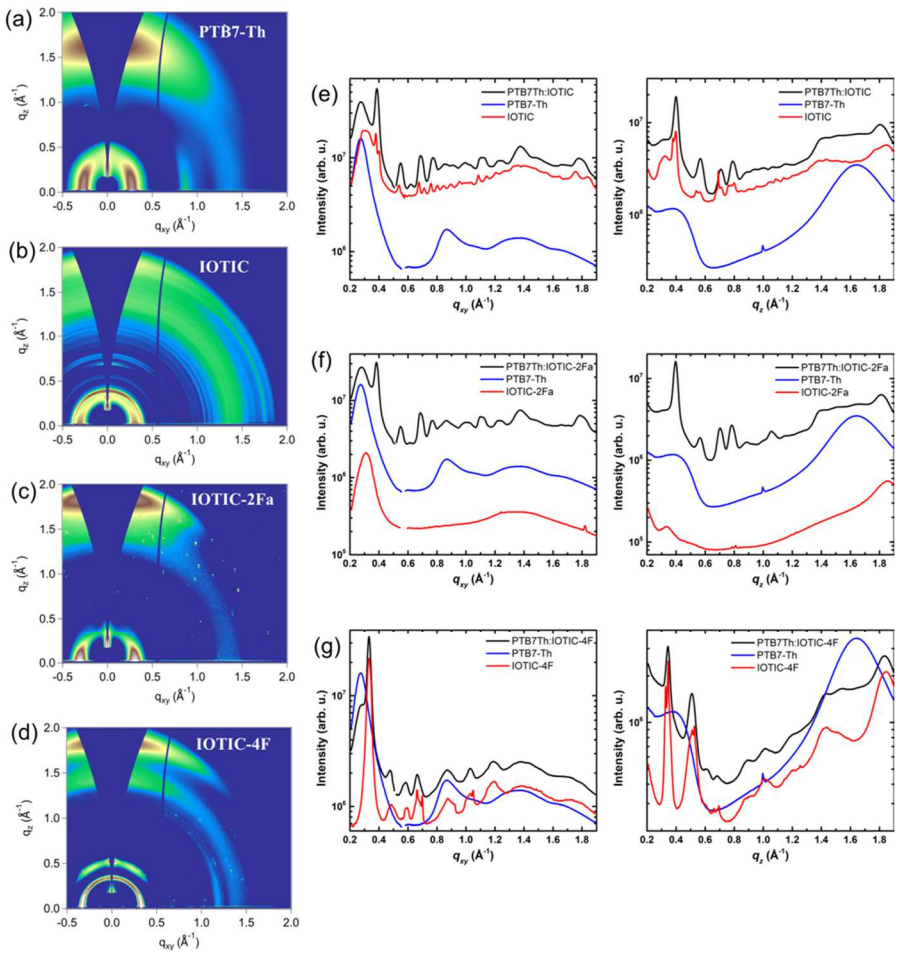

Figure A24. 2-D GIWAXS images of (a) PTB7-Th, (b) IOTIC, (c) IOTIC-2F$_a$, and (d) IOTIC-4F neat films. Corresponding in-plane and out-of-plane line cuts of (e) PTB7-Th:IOTIC, (f) PTB7-Th:IOTIC-2F$_a$, and (g) PTB7-Th:IOTIC-4F neat and blend films.

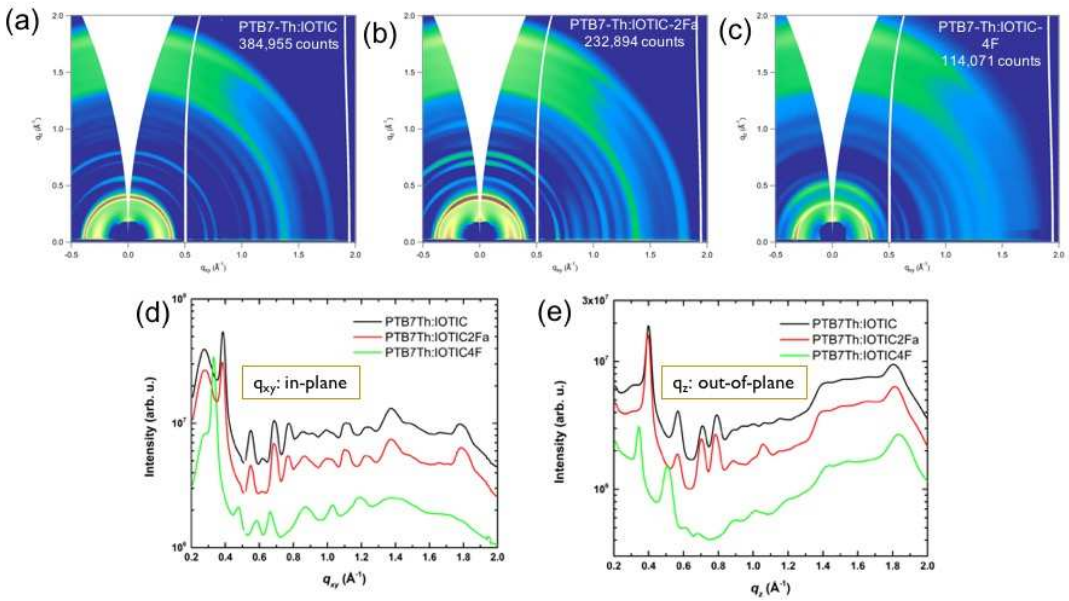

Figure A25. 2D GIWAXS images of (a) PTB7-Th:IOTIC, (b) PTB7-Th:IOTIC-2F$_a$, and (c) PTB7-Th:IOTIC-4F blend systems. (d) In-plane and (e) out-of-plane line cuts of the three blend films.

Table A4. Summarizing the d-spacings and crystalline coherence lengths of the three blend and neat films in the in-plane (q_{xy}) and out-of-plane (q_z) directions.

PTB7-Th:IOTIC						PTB7-Th:IOTIC-2Fa						PTB7-Th:IOTIC-4F					
Q_{xy} (Å^{-1})	d (nm)	L_c (nm)	Q_z (Å^{-1})	d (nm)	L_c (nm)	Q_{xy} (Å^{-1})	d (nm)	L_c (nm)	Q_z (Å^{-1})	d (nm)	L_c (nm)	Q_{xy} (Å^{-1})	d (nm)	L_c (nm)	Q_z (Å^{-1})	d (nm)	L_c (nm)
0.28	2.27	4.21	0.40	1.57	16.90	0.28	2.24	3.99	0.40	1.58	15.90	0.28	2.22	4.37	0.34	1.83	19.13
0.39	1.63	13.34	0.57	1.11	7.59	0.38	1.64	12.80	0.56	1.11	6.43	0.33	1.90	19.57	0.51	1.24	10.54
0.55	1.14	10.62	0.71	0.89	9.44	0.55	1.14	10.66	0.70	0.89	8.11	0.59	1.06	16.82	0.68	0.92	10.46
0.68	0.93	18.33	0.79	0.79	7.26	0.68	0.92	22.36	0.79	0.80	6.98	0.48	1.32	15.48	1.84	0.34	2.57
0.70	0.90	10.96	1.80	0.35	2.73	0.70	0.90	13.38	1.06	0.59	5.72	0.66	0.94	13.49			
0.76	0.82	16.20				0.76	0.83	17.63	1.81	0.35	2.87	0.57	1.10	11.48			
0.78	0.81	7.54				0.78	0.81	8.37				1.03	0.61	9.39			
1.37	0.46	5.24				1.37	0.46	6.05				1.19	0.53	4.56			
1.42	0.44	2.36				1.41	0.45	3.67				0.87	0.72	3.29			
1.82	0.35	7.38				1.78	0.35	6.83				1.38	0.46	1.99			
1.77	0.35	5.14				1.82	0.34	8.87									

PTB7-Th						IOTIC						IOTIC-2F$_a$						IOTIC-4F					
Q_{xy} (Å^{-1})	d (nm)	L_c (nm)	Q_z (Å^{-1})	d (nm)	L_c (nm)	Q_{xy} (Å^{-1})	d (nm)	L_c (nm)	Q_z (Å^{-1})	d (nm)	L_c (nm)	Q_{xy} (Å^{-1})	d (nm)	L_c (nm)	Q_z (Å^{-1})	d (nm)	L_c (nm)	Q_{xy} (Å^{-1})	d (nm)	L_c (nm)	Q_z (Å^{-1})	d (nm)	L_c (nm)
0.27	2.29	5.75	0.38	1.66	0.58	0.31	2.04	1.95	0.32	1.94	5.14	0.31	2.02	3.38	1.86	0.34	3.41	0.33	1.90	13.44	0.33	1.92	80.34
0.87	0.72	2.83	1.64	0.38	1.38	0.38	1.66	25.20	0.38	1.66	18.40							0.49	1.30	6.66	0.35	1.82	61.00
						0.40	1.57	10.76	0.40	1.58	21.13										0.51	1.23	7.52
									0.69	0.91	86.43										1.43	0.44	2.46
									1.76	0.36	5.37										1.85	0.34	2.52
									1.85	0.34	3.66												

Summary of GIWAXS findings:

The PTB7-Th neat film orients face-on relative to the substrate, meaning the π-conjugated backbone lies flat against the substrate and forms π-π stacks extending in the direction normal to the substrate. In this film, the π-π stacking produces scattering at 1.64 q_z, indicating a stacking distance of 0.38 nm and L_c value of 1.38 nm; lamellar stacking appears at 0.27 q_{xy} (d: 2.29 nm, L_c: 5.75 nm) with a higher order reflection at 0.87 q_{xy}. This face-on molecular orientation has been shown to be favorable for vertical charge transport between the electrodes in photovoltaic devices.[242] The small molecule acceptor IOTIC has larger crystalline coherence length (L_c) values than the other two NFAs, but notably does not display a preferential face-or edge-on orientation relative to the substrate. The stacking features in this material are more isotropically distributed as indicated by the broad angular distribution of scattering in the 2D image. The intense isotropic low q scattering from IOTIC results in a similar feature in the PTB7-Th:IOTIC blend film near 0.4 $Å^{-1}$. The broader blend peak near 0.28 q_{xy} is assigned to PTB7-Th as this material displays lamellar stacking near this distance.[242–244] PTB7-Th π-π stacking and higher order reflections from the 0.27 q_{xy} peak are not clearly identifiable in the PTB7-Th:IOTIC blend film. Further, the contribution from the IOTIC feature near 0.31 q_{xy} may be obscured due to scattering from the two features with very similar stacking distances. The multiple relatively low intensity scattering peaks are likely coming from the isotropic IOTIC neat film.

On the other hand, the neat IOTIC-2F_a film can more readily be identified as exhibiting face-on orientation with a π-π stacking peak at 1.86 q_z (d: 0.34 nm; L_c: 3.41 nm) and lamellar stacking at 0.31 q_{xy} (d: 2.02 nm; L_c 3.38 nm). However, the PTB7-Th:IOTIC-2F_a film also displays isotropic scattering. In this case, the blend film peak at 0.28 q_{xy} is likely to result from the donor, while the slightly narrower (real-space) stacking of the acceptor material may be obscured by the donor lamellar scattering as well as a sharp blend film peak near 0.4 $Å^{-1}$. In this case, however, the high intensity isotropic peak producing the 0.4 $Å^{-1}$ scattering cannot be identified in either of the neat films. While the blend peak at 1.81 q_z can be correlated with that of the neat IOTIC at 1.86 q_z,, several smaller intensity scattering peaks at intermediate q-spacings are not identifiable in the neat materials.

The neat IOTIC-4F film displays face-on character in addition to significant contributions from isotropic scattering. Scattering from π-π stacking appears at 1.85 q_z (d: 0.34 nm; L_c: 2.52 nm) and lamellar stacking appears at 0.33 q_{xy} (d: 1.90 nm; L_c: 13.44 nm). The isotropic distribution of this peak can be seen in the 2-D images. This isotropic IOTIC-4F feature can also be identified in the blend along with the 0.51 $Å^{-1}$ feature and π-π stacking from the NFA. The lamellar stacking of the donor and its higher order reflection can also be identified in the blend although the π-π stacking peak cannot be identified.

Resonant soft X-ray Scattering (RSoXS) analyses of blend films

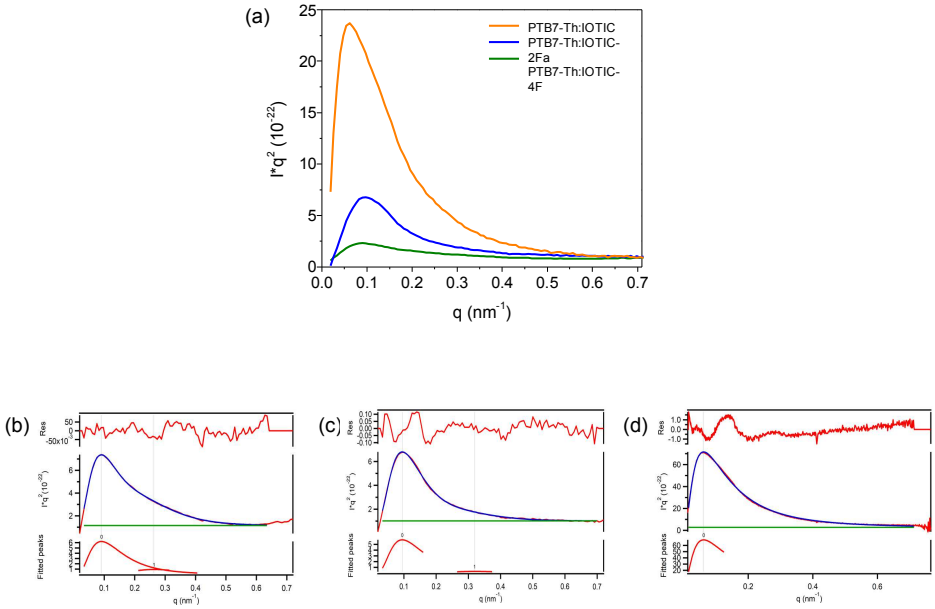

Figure A26. (a) Lorentz corrected and circularly averaged RSoXS profiles of the three studied blend films. Peak fittings with two lognormal peaks in the case of (b) PTB7-Th:IOTIC-4F and (c) PTB7-Th:IOTIC-2Fa, and (d) PTB7-Th:IOTIC.

Table A5. Parameters obtained from fitting the RSoXS profiles.

Blend system	Low-*q* Peak position [nm^{-1}]	Long period for low-*q* peak [nm]	Relative volume fraction of low-*q* peak [%]	High-*q* Peak position [nm^{-1}]	Long period for high-*q* peak [nm]	Relative volume fraction of high-*q* peak [%]	Root-mean-square (RMS) composition variation
PTB7-Th:IOTIC-4F	0.093	68	83	0.26	24	17	0.44

PTB7-Th:IOTIC-2F$_a$	0.094	67	93	0.32	20	7	0.60
PTB7-Th:IOTIC	0.065	97	-	-	-	-	1

Solid-state NMR analyses

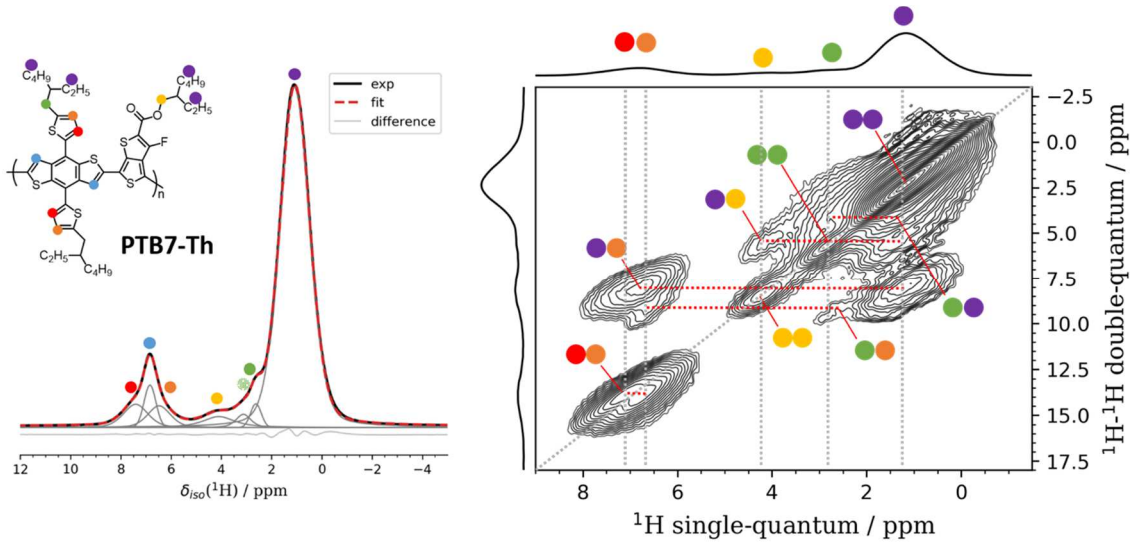

Figure A27. Left: 1D ^{1}H MAS NMR spectrum of PTB7-Th, including spectral deconvolution and signal assignment. Right: 2D ^{1}H-^{1}H DQ-SQ correlation acquired at 18.8 T (800 MHz), 28.490 kHz MAS, using the Back-to-Back excitation scheme (2 rotor periods), signal assignment is the same as on the left. Cross-correlations are marked by red dashed lines.

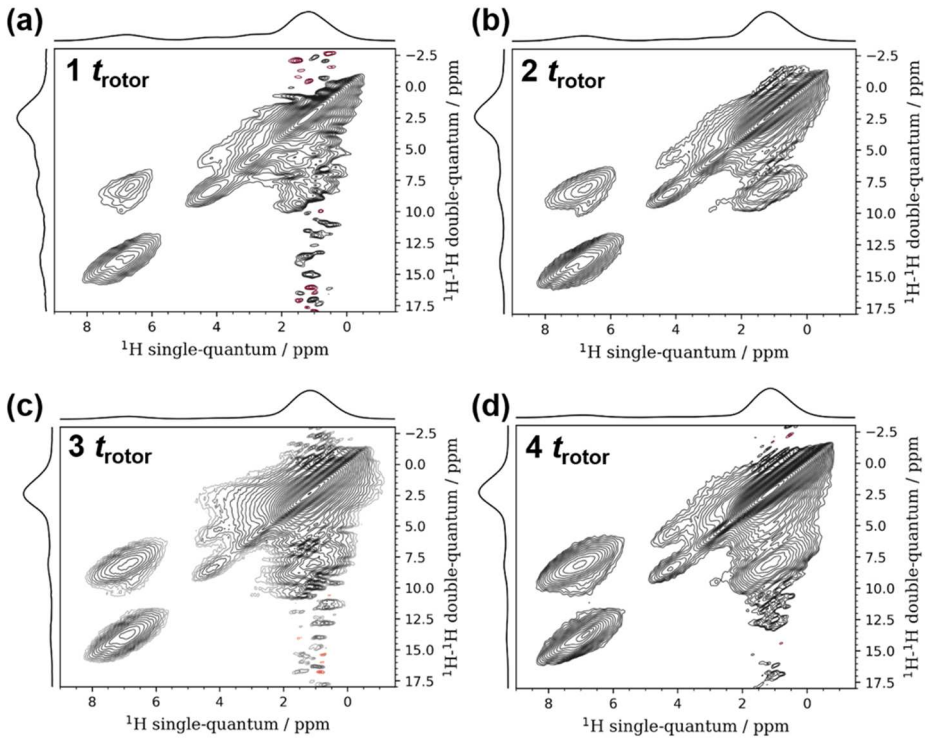

Figure A28. 2D ^{1}H-^{1}H double-quantum single-quantum correlation spectra of PTB7-Th, acquired at 18.8 T (800 MHz), 28.490 kHz MAS, using (a) 1 $\tau_{Rotor,}$ (b) 2 τ_{Rotor}, (c) 3 τ_{Rotor}, and (d) 4 τ_{Rotor} for the double-quantum excitation.

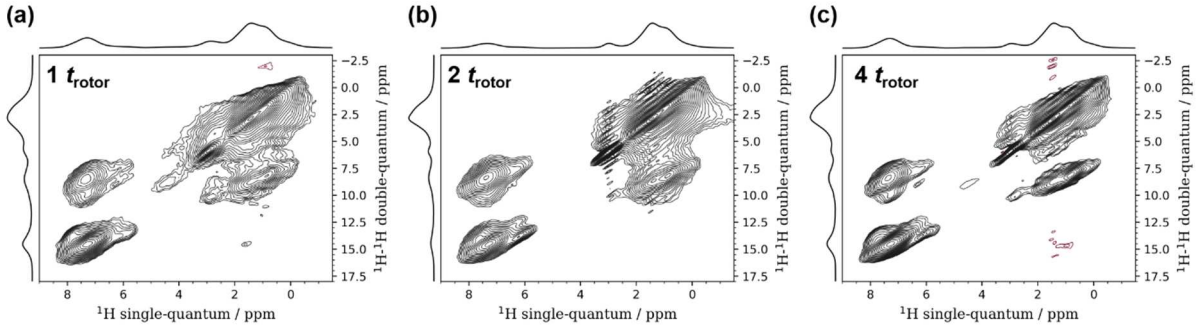

Figure A29. 2D ^{1}H-^{1}H double-quantum single-quantum correlation spectra of PTB7-Th: IOTIC-4F, acquired at 18.8 T (800 MHz), 28.490 kHz MAS, using (a) 1 $\tau_{Rotor,}$ (b) 2 τ_{Rotor}, (c) 4 τ_{Rotor} for the double-quantum excitation.

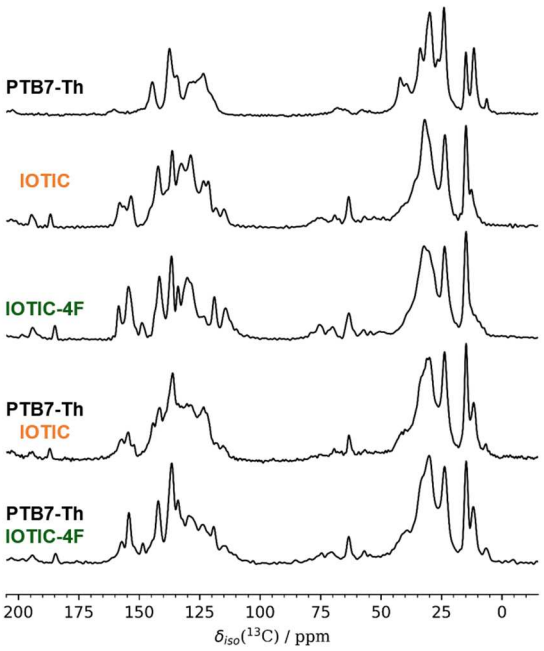

Figure A30. 1D $^{13}C\{^{1}H\}$ CP/MAS spectra of PTB7-Th, IOTIC, IOTIC-4F, and their respective blends, acquired at 11.7 T (125 MHz/500 MHz) and 10 kHz MAS, using a CP contact time of 2ms.

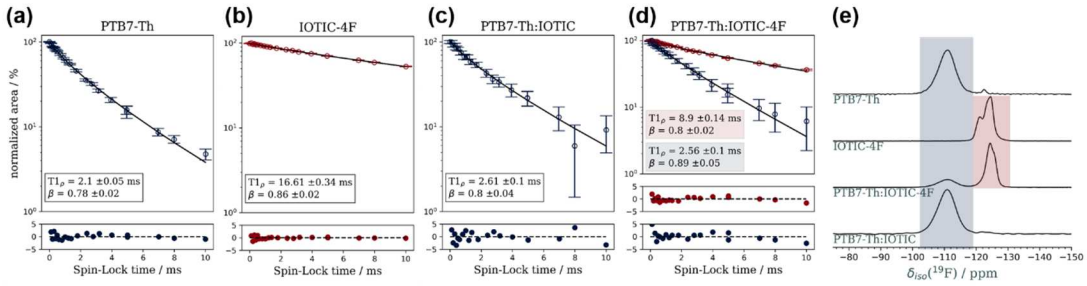

Figure A31. ^{19}F Spin-Lock results. Intensities correspond to the signals indicated in panel (e), normalized to 100% of the highest value, plots use log scaling of the y-axes, except for the residual plots which are linear. Error bars were calculated based on the baseline noise RMS. A stretched exponential with a stretch-factor beta was used for fitting.

To probe the molecular motion of the polymer backbone we measured the ^{19}F spin-lattice relaxation rate in the rotating frame ($T_{1\rho}$) for the two blends by using a ^{19}F spin-lock experiment. Similar to the spin-lattice relaxation in the laboratory frame, $T_{1\rho}$-measurements are particularly sensitive to motion on the same timescale as the nutation frequency of the applied field, in this case the transverse B_1 field with a nutation frequency of 100 kHz. Differences in molecular motion on this timescale result in variations of the $T1_\rho$ relaxation

rate, as can be seen by comparing $T1_\rho$ of the ^{19}F nuclei in the IOTIC-4F neat film (16.61 ms), compared to the same nuclei but in the blend (8.9 ms). Similarly, this technique is often used to distinguish the rigid crystalline from the more mobile amorphous domains in fluoropolymers such as PVDF or PTFE.[245–247] The results of the ^{19}F spin-lock experiments are shown in **Figure A29**, with blue data points indicating the fluorine atoms of the polymer backbone and red data points indicating the fluorine atoms of the IOTIC-4F NFA. Apart from the aforementioned difference of the NFA fluorine moieties, only slight differences between the polymer backbone in the neat film and the two blends are observed, with differences between the two blends being on the edge of the confidence interval (one sigma).

Blending of the polymer with the different NFA molecules could lead to changes in segmental mobility of the polymer backbone, potentially affecting charge transport and charge-carrier lifetime. In polymers, this type of motion is usually associated with frequencies in the range of several kHz, which can be probed by ^{19}F spin-lattice relaxation measurements in the rotating frame ($T_{1\rho}$).[245,248] Measurements of the ^{19}F $T_{1\rho}$ relaxation times showed no significant differences between the two blends, thus indicating the two blends exhibit similar segmental mobility of the polymer.

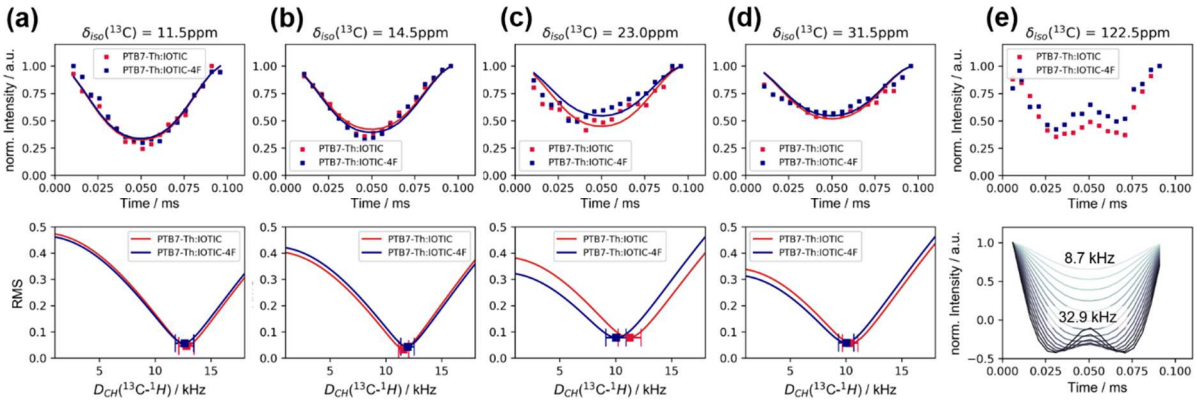

Figure A32. Top row: ^{13}C-^{1}H DIPSHIFT curves of both PTB7-Th:IOTIC (red squares) and PTB7-Th:IOTIC-4F (blue squares) for the peaks at (a) 11 ppm, (b) 14.5 ppm, (c) 23 ppm, 31.5 ppm, and (e) 122.5 ppm. The solid lines represent the best fits obtained by the analytical expression from Hackel et al.[107] Bottom row: RMS deviation (y-axis) of various curves calculated for different dipolar couplings (x-axis) for a CH spin system, the minimum is the best fit and the error bars represent the error based on the corresponding RMS value. Due to signal overlap direct fitting of the data set in (e) was not feasible as the curve is displaced from the expected baseline; instead various calculated profiles are shown below highlighting the similarity of both curves with analytical curves corresponding to strong (30 kHz) dipolar coupling strength.

Figure A32 shows the ^{1}H-^{13}C DIPSHIFT results for selected peaks in the aliphatic region (a-d), along with the fit results using a simple CH spin-system. Due to the strong overlap of

the numerous ^{13}C signals of both the polymer and NFA (compare **Figure A30**), especially in the aromatic region above 100 ppm, extracting DIPSHIFT curves for all signals was not feasible. **Figure A32e** shows the DIPSHIFT curves the ^{13}C signal at 122.5 ppm, which is actually the superposition of a directly bonded CH pair, and several non-bonded ^{13}C signals. The effect is a displaced baseline, which precludes automated fitting, though both curves show similar oscillations which indicates that they experience similar dipolar interactions. In summary, the DIPSHIFT data shows no evidence for significant differences in molecular motion in the sample, though our data are mostly from the aliphatic sidechains and not the polymer backbone.

Absorbance of neat and blend thin films

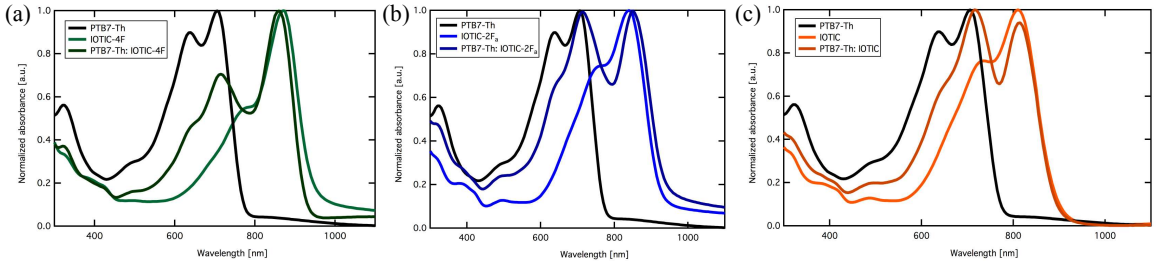

Figure A33. Normalized absorbance spectra of neat and blend films of (a) PTB7-Th: IOTIC-4F, (b) PTB7-Th: IOTIC-2F_a, and (c) PTB7-Th: IOTIC.

Appendix B:

Appendix to Chapter 3

J-V curves and EQE spectra

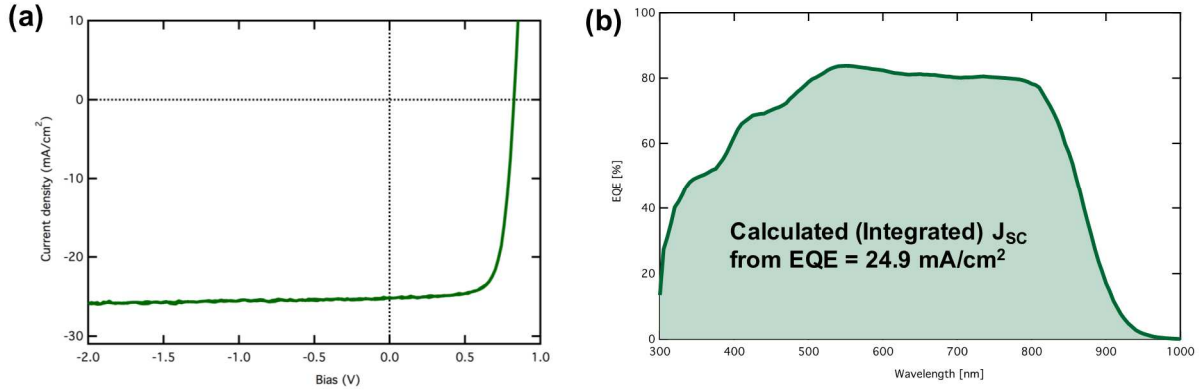

Figure B1. (a) *J-V* characteristics of a PM6:Y6 BHJ device at 1 sun illumination (100 mW cm^{-2} AM 1.5) and (b) EQE spectra of the PM6:Y6 BHJ device.

Average power conversion efficiencies of PM6:Y6 BHJ solar cells

Table B1. Average PCE from 20 devices.

Solvent	Annealing	V_{OC} (V)	J_{SC} (mA cm^{-2})	FF	Average PCE (Max) [%]
CF with 0.5% CN	10 min at 110 ^{0}C	0.825 ± 0.003	25.5± 0.7	0.72 ± 0.02	15.0 ± 0.4 (15.35)

Determination of the S1 of Y6, EL and EQE_{PV} of neat Y6 and PM6:Y6 BHJ blend devices, EQE_{EL} of Y6 devices

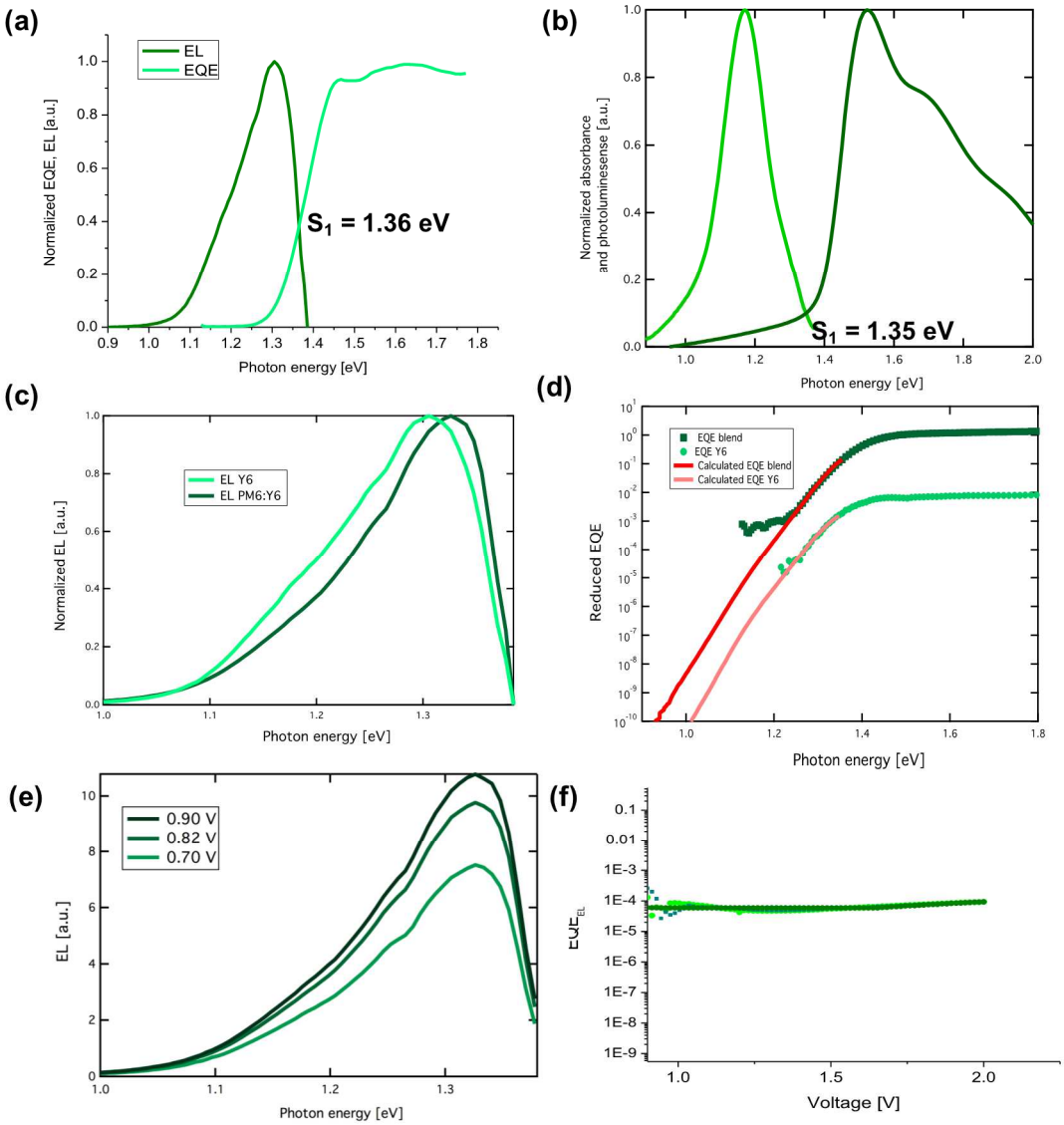

Figure B2. Determination of the S1 in the blend from the intersection of (a) the EL and EQE spectra of Y6 devices and from (b) the absorbance and PL spectra of Y6 films. **(**c) Normalized EL spectra of neat and blend devices, (d) EQE_{PV} – measured (in green) and calculated (in red) by Equation S4 of the blend and neat devices. (e) Bias-dependent EL of PM6:Y6 devices. (f) EQE_{EL} of Y6 devices showing a lower $\Delta V_{non\text{-}rad}$ = 0.242 ± 5 eV in the acceptor compared to that of the blend $\Delta V_{non\text{-}rad}$ = 0.286 ± 3 eV eV.

Deconvoluting contributions to voltage losses from S_1 to V_{OC}

Equations used to obtain the CT energy:

$$EQE_{PV,CT}(E) = \frac{f}{E\sqrt{4\pi\lambda k_B T}} \exp\left(\frac{-(E_{CT}+\lambda-E)^2}{4\lambda k_B T}\right) \quad \text{(S1)}$$

$$EQE_{EL,CT}(E) = E\frac{f}{\sqrt{4\pi\lambda k_B T}} \exp\left(\frac{-(E_{CT}-\lambda-E)^2}{4\lambda k_B T}\right) \quad \text{(S2)}$$

$$EQE_{PV}(E) \propto EL(E)E^{-2} \exp\left(\frac{E}{k_B T}\right) \quad \text{(S3)}$$

Here, k_B is Boltzmann's constant, E is the photon energy, and T is the absolute temperature. The fit parameters are E_{CT}, which is the energy at the point of intersection between CT absorption and emission, λ, which is the reorganization energy, and f, which is a measure of the strength of the donor-acceptor coupling. The solid red line in **Figure 2**a shows the calculated blend EQE_{PV} from the EL spectra using **Equation S4** at lower energies, confirming the good match between the measured and experimental EQE_{PV} data.

Radiative and non-radiative recombination analysis:

Non-radiative recombination losses can be calculated using **Equation S5,** where the calculated radiative recombination obtained from **Equation S6** is used and measured using the EL quantum efficiency (EQE_{EL}), which is defined as the photons emitted normalized by electrons injected into the device.

$$V_{OC} = \frac{E_{CT}}{q} - \Delta V_{rad}(T) - \Delta V_{nonrad}(T) \quad \text{(S4)}$$

$$\Delta V_{rad}(T) = -\frac{kT}{q} ln(\frac{J_{SC} h^3 c^2}{f q 2\pi (E_{CT}-\lambda)}) \quad \text{(S5)}$$

$$\Delta V_{nonrad}(T) = -\frac{kT}{q} ln(EQE_{EL}) \quad \text{(S6)}$$

Table B2. Table summarizing the voltage losses from E_g^{opt} to E_{CT}.

E_g^{opt} (V)	E_{CT} (eV)	ΔV_{rad} (meV)	$\Delta V_{non\text{-}rad,\ calc}$ (meV)	$\Delta V_{non\text{-}rad,\ exp}$ (meV)	V_{oc} (V)
1.36	1.31± 0.002	199 ± 3	287 ± 3	286 ± 3	0.825 ± 0.003

Calculating the recombination and extraction dynamics in the blend

Qualitative analysis of recombination dynamics

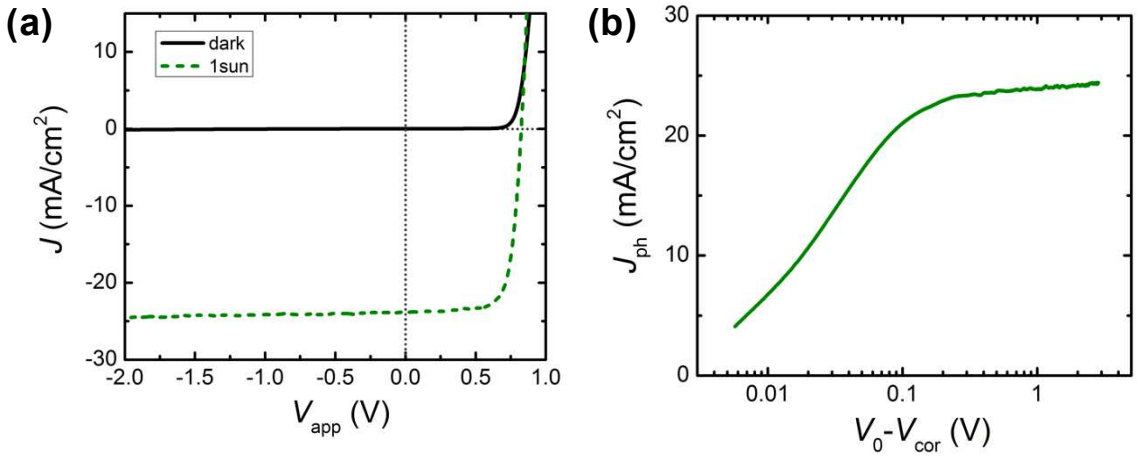

Figure B3. (a) *J*-*V*-characteristics of the tested devices in the dark (black line) and under 1 sun (green dashes), (b) photocurrent density J_{ph} vs. effective voltage.

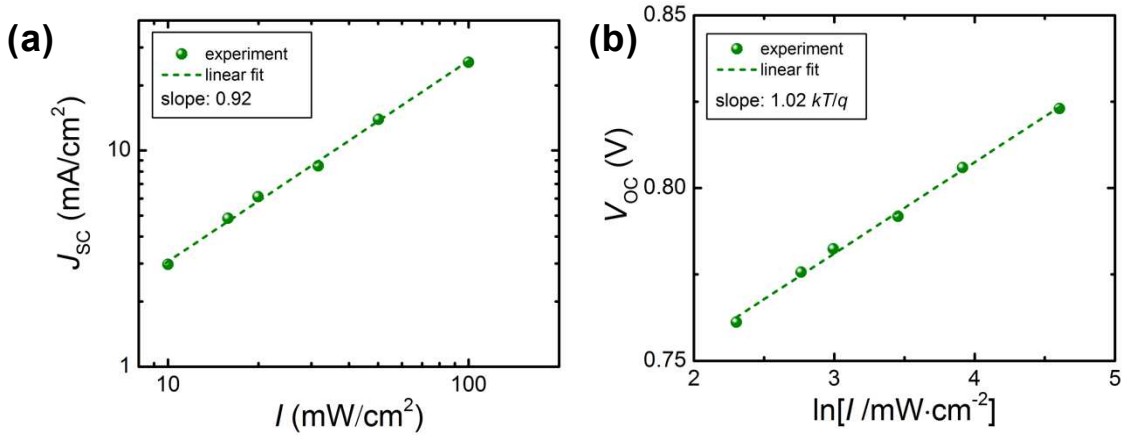

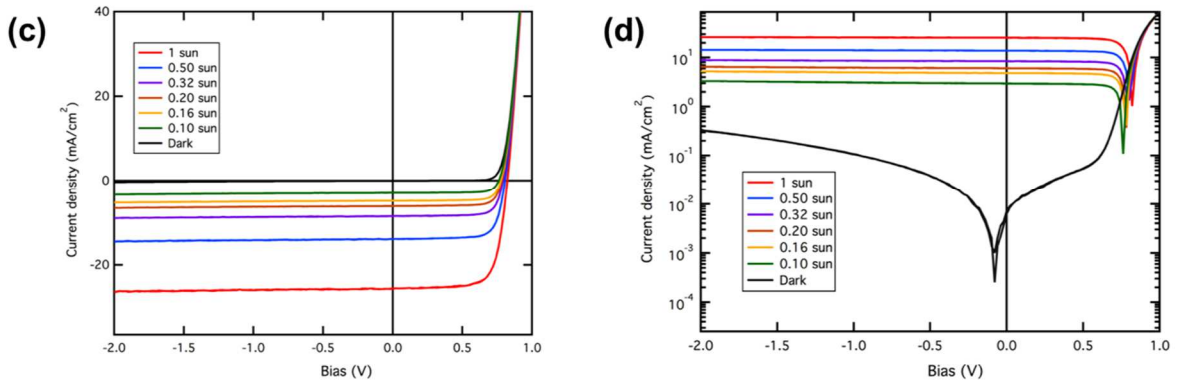

Figure B4. Light intensity dependent (a) short-circuit current density J_{SC} and (b) open-circuit voltage V_{OC}. *J-V* curves at different light intensities in the (c) linear scale and (d) log scale.

The dielectric constant ($\varepsilon_r = 2.2$) of the blend was measured by capacitance spectroscopy at a reverse bias of -3 V and in the dark (**Figure B5**). For this DC bias, there should be no frequency dependence of the capacitance. Then, the assumption is that the capacitance of the blend C_b measured under these conditions is equal to the geometric capacitance C_g, which would allow employing the following equation to calculate the dielectric constant ε_r:

$$\varepsilon_r = \frac{C_g L}{\varepsilon_0 A}, \tag{S7}$$

where L is the thickness of the active layer and A is the area of the device. Four devices with thicknesses of 75 nm, 80 nm, 89 nm, and 90 nm were investigated for capacitance spectroscopy measurements and for the analysis of the recombination and extraction dynamics. To begin a quantitative analysis of the recombination dynamics, it is necessary to obtain values for the charge carrier density n. It is known that capacitance spectroscopy can be employed to determine the density of charge carriers in organic solar cells under illumination. Capacitance spectroscopy was performed to yield the charge carrier density n, *via* integration of the chemical capacitance ($C_{chem} = C_b[\omega = 50\ \text{kHz}] - C_g$) using the following equations:

$$n(V_{cor}) = n_{sat} + \frac{1}{qAL}\int_{V_{sat}}^{V_{cor}} C_{chem} dV_{cor}, \tag{S8}$$

$$n_{sat} = \frac{1}{qAL} C_{sat}(V_0 - V_{sat}), \tag{S9}$$

where A is the area of the solar cell, L is the thickness, V_{sat} is the reverse bias at which the photocurrent saturates, n_{sat} is the charge carrier density at the saturation voltage V_{sat}, and C_{sat}

is the difference in capacitance of the BHJ layer C_b under illumination and in the dark at V_{sat} and an angular frequency ω = 50 kHz. V_0 is the forward bias at which the photocurrent is equal to zero.

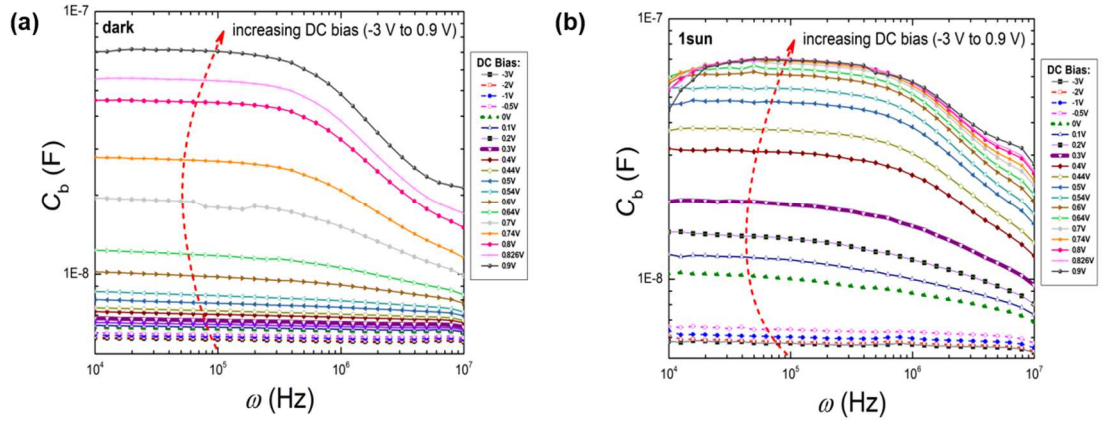

Figure B5. Frequency and DC bias dependent corrected capacitance C_b of the tested solar cells in the (a) dark and (b) under 1-sun illumination. C_b at an angular frequency ω = 50 kHz was used to determine the chemical capacitance C_{chem}.

Calculating μ_{eff}

The calculation of a field and charge carrier dependent, effective mobility $\mu_{eff}(n,V)$ has been introduced by Albrecht *et. al.* as an alternative to the hole/electron mobility $\mu_{p/n}$ determined *via* the Mott-Gurney relationship of space-charge limited currents (SCLC) in single carrier devices.[68] It was argued that mobilities determined *via* SCLC measurements may be unreliable due to deviation from the expected thickness dependent behavior, the variation of electrode materials that may have an impact on the morphology, charge carrier densities and electric-fields that are larger in the SCLC regime in comparison to the normal operating conditions of a solar cell (ultimately leading to overestimated mobilities), and finally the fact that the motion of injected carriers is measured in contrast to photogenerated carriers. The use of such an effective mobility μ_{eff} is especially encouraged, if a strong dependence of the mobility on either the applied bias V, the charge carrier density n, or both can be expected. The effective mobility μ_{eff} can be calculated by employing the following equation:

$$\mu_{eff}(n,V_{cor}) = \frac{J(V_{cor}) \cdot L}{2qn(V_{cor}) \cdot [V_{cor} - V_0]}, \quad \text{(S10)}$$

where J is the current density, V_{cor} is the corrected voltage, V_0 is the voltage at which the

photocurrent is equal to zero, L is the device thickness (L = 75 nm) , q is the elementary charge, and n is the charge carrier density obtained from capacitance spectroscopy. The effective mobility μ_{eff} ideally relates to the two different types of mobility μ_{n} and μ_{p} *via* the following equation:

$$\mu_{eff} = \frac{2\mu_n\mu_p}{\mu_n + \mu_p}. \tag{S11}$$

Determining $\mu_{\text{h/e}}$ *via* the Mott-Gurney relationship of space-charge limited currents (SCLC) in single carrier devices

We have performed SCLC measurements to confirm whether the Mott Gurney analysis for SCLC is valid in this case – especially given that a lot of reports in the literature use this limited analysis to derive largely erroneous (and often, overestimated) mobility values. In order to determine the mobility values from the experimental data, it was important to verify that the measured currents were indeed limited by space charge. From the Mott-Gurney expression of SCLC, a pre-requisite for satisfying the criterion for SCLCs in a diode is that the current has an L^{-3} dependence on the thickness of the diodes. In the case of the hole only diodes, the thickness dependent behavior was found to be valid when normalizing by the thicknesses of the measured diodes (See **Figure B6** a and b). Additionally, as expected, the hole mobilities decrease slightly with increasing thicknesses and yield mobility values of 1.5 (± 0.4) × 10^{-4} cm^2 Vs^{-1} (similar to previously reported values in the literature[111]. When plotting the thickness dependence of electron mobilities, we find that the thickness-dependence of current expected in utilizing the SCLC equation no longer holds (See **Figure B6**c and d). This is further confirmed with the reported electron mobility values in the previous report[111], where an increase in mobility of up to 2 × 10^{-3} cm^2 Vs^{-1} is seen with increasing thicknesses, which is counter intuitive. **Figures B6**e and f show a comparison of the SCLC fitting for electron and hole mobilities. While the J-V plots for the hole mobility values show reasonable fits with deviations from a slope of 2 really only seen at higher voltages (as expected), the electron mobility J-V plots show a fast-increasing slope above ~ 0.6 V. This is most likely indicative of a field-dependent mobility (seen as a fast-upward deviation of the data from the SCLC fits at higher biases). A field dependent mobility would render mobility values that are over-estimated by the limited analysis of the Mott-Gurney equation; in the previous report[111] the SCLC fitting has been done at high voltages (3-7 V) where the field

dependence on electron mobility is seemingly very pronounced in the blend. While the mobility of organic semiconductors is well established to be both charge carrier density- and electric field- dependent[206], unfortunately, many reports still inaccurately describe this more complicated J-V behavior of diodes at higher voltages by neglecting the pronounced field and density dependence of mobilities by using the SCLC equation unfittingly – where the mobility is simply assumed to be constant. Therefore, we would like to highlight that while the SCLC measurements provide a quick and easy way to extract mobilities, a tendency to over-interpret erroneous mobility values have become common and should be approached with caution.

An increase in the effective mobility values at large reverse bias could then be attributed to a pronounced field dependent mobility[66,240,249], which can explain the minimum value observed at 0.6 V.

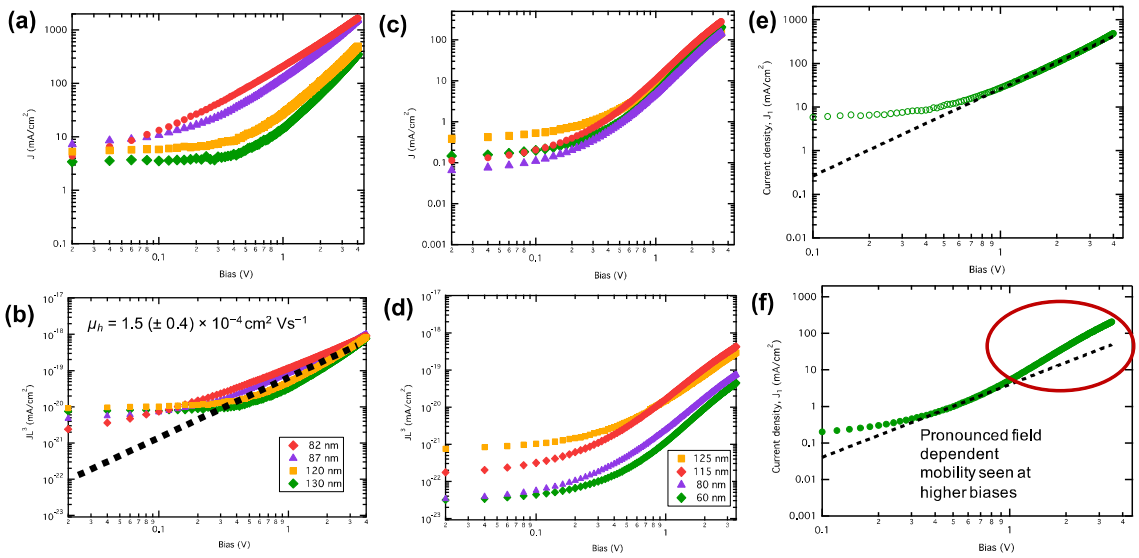

Figure B6. J-V characteristics of (a) hole-only and (c) electron-only diodes of different thicknesses measured in the dark. The current density is multiplied by L^3 for (b) hole-only and (d) electron only diodes, showing that the thickness dependence is only valid in the case of hole-only diodes. Examples of SCLC fitting for (e) hole only and (f) electron-only diode show that the field dependence of mobility is pronounced in the case of electron only diodes.

Reconstruction of the current density $J_{rec,sum}$

The recombination current density $J_{rec,sum}$ obtained from the *J-V*-curves can be reconstructed by using the following equation:

$$J_{rec,sum} = J_{rec,bm} + J_{rec,bulk} + J_{rec,surf}. \quad \text{(S12)}$$

The bimolecular component $J_{\mathrm{rec,bm}}$ can be described by the following equation:

$$J_{rec,bm} = qLk_{bm}n^2 = \frac{q^2 L}{\varepsilon_0 \varepsilon_r}\xi(\mu_n + \mu_p)n^2, \quad \text{(S13)}$$

where k_{bm} is the bimolecular recombination coefficient, ξ is the reduction factor (also known as Langevin prefactor), n is the charge carrier density, and $\mu_{\mathrm{n,p}}$ are the electron and hole mobility, respectively. The effective mobility μ_{eff} was used to replace $\mu_{\mathrm{n,p}}$. The following expression describes the bulk trap-assisted contribution $J_{\mathrm{rec,bulk}}$:

$$J_{rec,bulk} = qLk_{t,b}n = \frac{q^2 L}{\varepsilon_0 \varepsilon_r}\mu_n N_{t,b} n, \quad \text{(S14)}$$

where $N_{\mathrm{t,b}}$ is the density of deep traps in the bulk, and $k_{\mathrm{t,b}}$ is the bulk-trap assisted recombination coefficient. Again, the effective mobility μ_{eff} was used. The surface trap-assisted component $J_{\mathrm{rec,surf}}$ can be described in a similar way as $J_{\mathrm{rec,bulk}}$, with the addition of a field-dependent term:

$$J_{rec,surf} = qLk_{t,s}(V_{cor})n = \frac{q^2}{\varepsilon_0 \varepsilon_r}\frac{\mu_p N_{t,s} n}{\exp\left\{\frac{q(V_{bi} - V_{cor})}{kT}\right\}}, \quad \text{(S15)}$$

where $N_{\mathrm{t,s}}$ is the density of surface traps, V_{bi} is the built-in voltage, V_{cor} is the corrected voltage, and $k_{\mathrm{t,s}}(V_{\mathrm{cor}})$ is the surface-trap assisted recombination coefficient. Again, the effective mobility μ_{eff} was used. A detailed description and derivation of this analytical model can be found in Ref. 3.[3] The reconstruction of the recombination current density $J_{\mathrm{rec,sum}}$ is successful, if a reduction factor $\xi = 0.00332$, a bulk trap density of $N_{\mathrm{t,b}} = 0$ cm^{-3}, and a surface trap density $N_{\mathrm{t,s}} = 2.78 \cdot 10^{10}$ cm^{-2} are selected as fitting parameters. The quality of the fit can be described by an adjusted $R^2 = 0.9888$. Subsequently, it is possible to determine the voltage dependent bimolecular recombination coefficient k_{bm} by re-arranging equation (S13) (**Figure B7).**

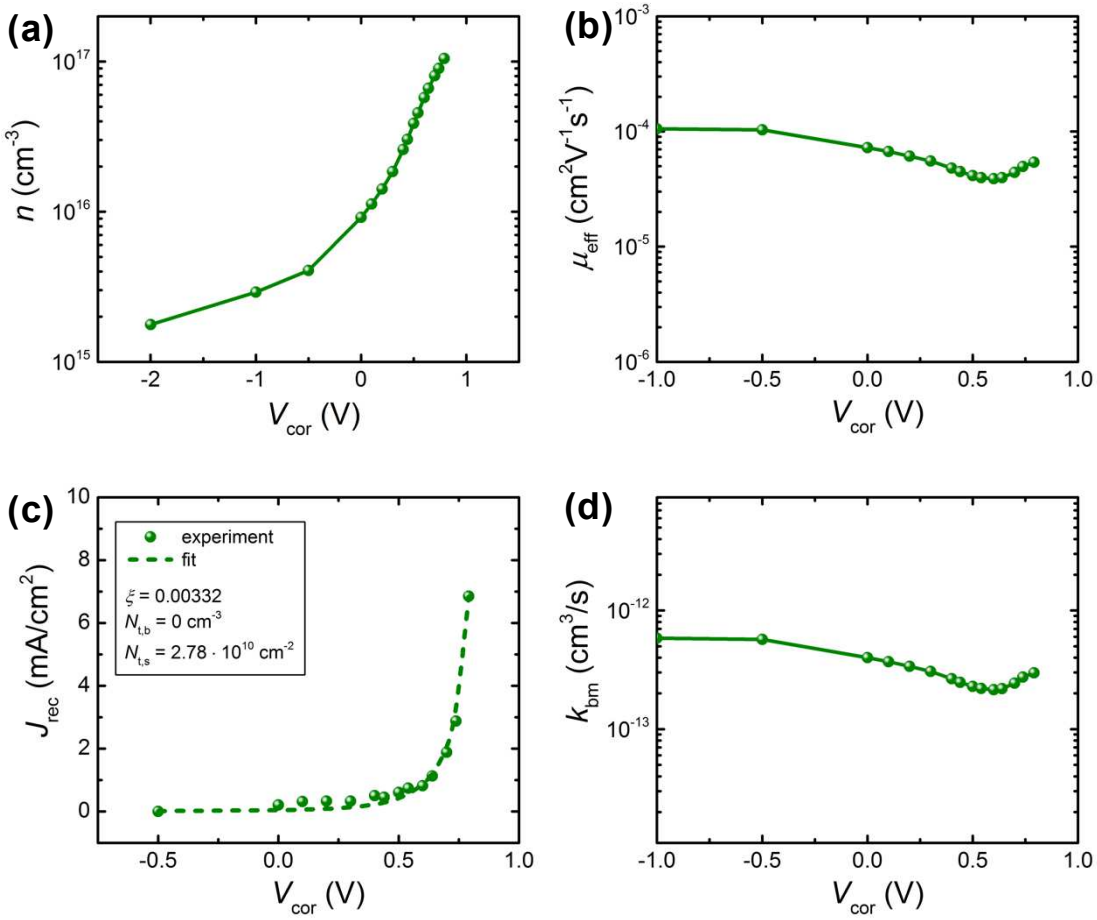

Figure B7. (a) Charge carrier density n, (b) effective mobility μ_{eff}, (c) experimental and fitted recombination current density J_{rec}, and (d) bimolecular recombination coefficient k_{bm} of the tested solar cells plotted as a function of corrected voltage.

i. Open-circuit voltage decay measurements and analysis

As a second technique, V_{OC}-decay measurements (also known as transient photovoltage decay) were performed to obtain the charge carrier lifetime τ, the transient charge carrier density n_{OC} and ultimately values for the bimolecular recombination coefficient k_{bm} and the trap-assisted recombination coefficient k_t. It should be noted that this technique does not allow to distinguish the different types of trap-assisted recombination (i.e. surface traps vs. bulk traps). These key parameters can be derived from the following equation describing the net recombination rate $R_{eff}(n)$ once the light excitation ends:

$$R_{eff}(n) = -\frac{dn}{dt} = -\frac{n}{\tau} = k_{eff}\, n^{\beta} \qquad \text{(S16)}$$

where n is the charge carrier density, t is the time, τ is the charge carrier lifetime, and k_{eff} is the effective recombination coefficient.[118] The value of β depends on the ratio of recombination mechanisms, ideally with $\beta = 1$ for trap-assisted recombination ($R_t = k_t n$), and $\beta = 2$ for bimolecular recombination ($R_{bm} = k_{bm} n^2$).[250] When Equation S16 is rearranged, the charge carrier lifetime τ can be described as follows:

$$\tau = \frac{n}{R_{eff}(n)} = \frac{1}{k_{eff} n^{(\beta-1)}} \tag{S17}$$

For values of $\beta > 1$, τ becomes dependent on the charge carrier density n, and therefore on time t.[124,251] This means that τ is an instantaneous charge carrier lifetime that evolves continuously over time. Under the assumption that $n \propto \exp\{qV_{OC}/kT\}$, τ can be expressed as:

$$\tau = -\frac{kT}{q}\left(\frac{dV_{OC}}{dt}\right)^{-1} \tag{S18}$$

where V_{OC} in this case is the continuously decreasing open-circuit voltage of the tested solar cell once the light source is turned off. The measurement of this time-dependent, transient V_{OC} opens up the possibility to obtain the charge carrier lifetime τ as shown in Equation S17.[124,251]

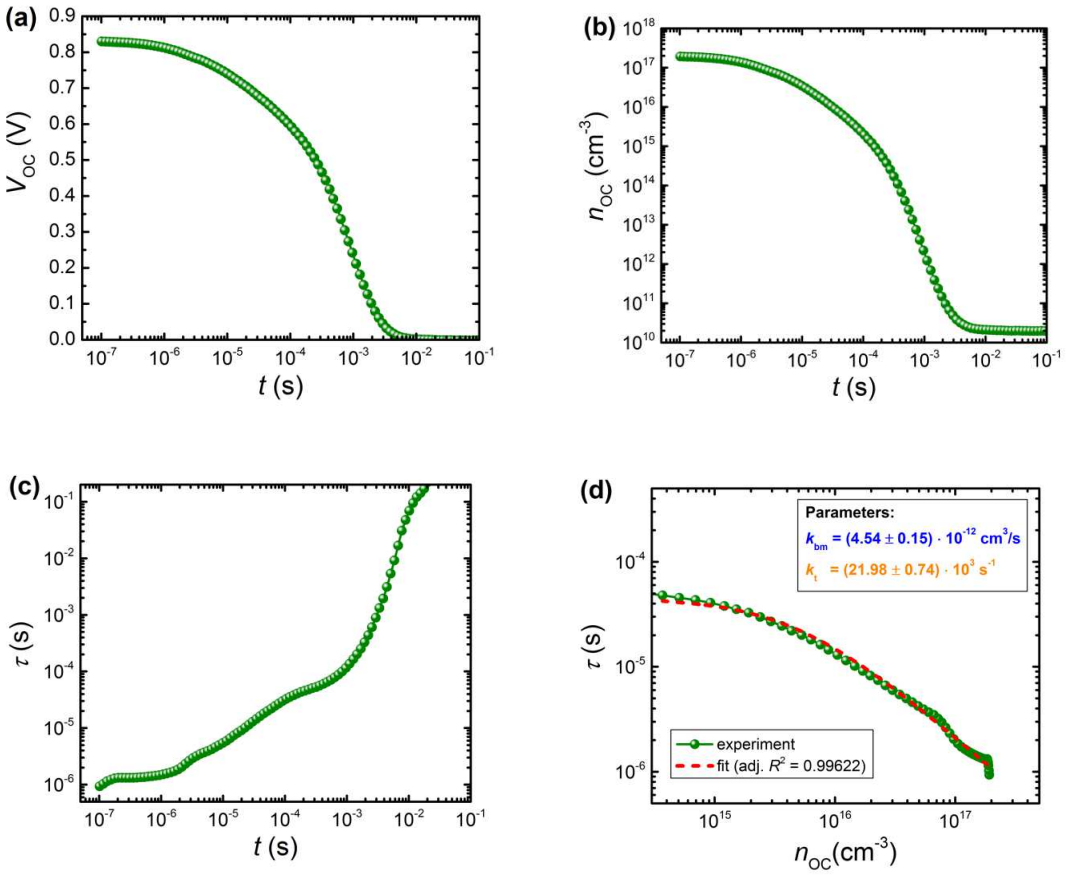

Figure B8. (a) Transient V_{OC}-decay, (b) transient charge carrier decay n_{OC}, (c) relationship of the lifetime τ on time t, and (d) lifetime τ in relationship to the charge carrier density n_{OC} determined *via* experiment and fitted according to Equation S18.

To further quantify the recombination dynamics, it is necessary to calculate the transient charge carrier density n_{OC} from the measured transient V_{OC} by applying the fundamental equation listed below:

$$n_{OC} = \sqrt{n_i^2 \cdot \exp\left\{\frac{qV_{OC}}{kT}\right\}}, \tag{S19}$$

where n_i is the intrinsic charge carrier density.[250] The initial charge carrier density n_{OC} at t = 0 s can be set equal to the charge carrier density under open-circuit conditions determined *via* capacitance spectroscopy ($n = 1.92 \cdot 10^{17}$ cm^{-3}). This yields the intrinsic charge carrier density ($n_i = 2.05 \cdot 10^{10}$ cm^{-3}). Once the relationship between the charge carrier lifetime τ and the charge carrier density n_{OC} is established, it is possible to quantify the recombination

coefficients k_{bm} and k_t. Similar to the approach for the capacitance spectroscopy analysis, the assumption is that the measured recombination rate $R_{eff}(n)$ can be described as a superposition of the contributions from bimolecular recombination $R_{bm}(n)$ and trap-assisted recombination $R_t(n)$:

$$R_{eff}(n) = R_{bm}(n) + R_t(n) = -\left(\frac{n}{\tau_{bm}} + \frac{n}{\tau_t}\right) = k_{bm}n^2 + k_t n\,. \tag{S20}$$

The bimolecular recombination coefficient ($k_{bm} = (4.54 \pm 0.15) \cdot 10^{-12}$ cm^3/s) could be determined by fitting the charge carrier lifetime τ during the relevant timescale of $t < 5 \cdot 10^{-4}$ s (Figure B8d). On longer timescales ($t > 5 \cdot 10^{-4}$ s), effects outside of the scope of the proposed model need to be considered, such as low excitation leakage. The coefficient for trap-assisted recombination ($k_t = (21.98 \pm 0.74) \cdot 10^3$ cm^3/s) indicates the presence of reasonably low amounts of trap-assisted recombination, although it should be stressed that this analysis is limited in its capability to distinguish between the exact types of trap-assisted mechanism (i.e. surface vs. bulk traps).[118] The results determined for the bimolecular recombination coefficients by the open-circuit voltage decay (OCVD) technique are higher compared to the results determined by capacitance spectroscopy (CS; $k_{bm,OCVD} = (4.54 \pm 0.15) \cdot 10^{-12}$ cm^3/s vs. $k_{bm,CS} = 3.0 - 5.8 \cdot 10^{-13}$ cm^3/s). Such differences in the results (i.e. $k_{bm,OCVD} > k_{bm,CS}$) between the two techniques have been reported in prior studies for fullerene and NFA solar cells.[28,118] All in all, this transient technique also yields important parameters related to the recombination dynamics. However, it is limited to open-circuit conditions and it is not possible to separate the different contributions from bulk and surface trap-assisted recombination.

The effective extraction τ_{ex} can be derived under the assumptions that a charge carrier will on average have to traverse half of the active layer thickness and that the active layer is assumed to be an effective medium. Then, the following two equations describing the drift velocity v_D have to be considered:

$$v_D = \mu\left|\vec{E}\right| = \mu\frac{V}{d}, \tag{S21}$$

$$v_D = \frac{d}{\tau_{ex}}, \tag{S22}$$

where μ is the charge carrier mobility, E is the electric field, V is the voltage, d is the distance, and τ_{ex} is the effective extraction time. By setting equations (S21) and (S22) equal and by solving for τ_{ex}, we obtain the following relationship:

$$\tau_{ex} = \frac{d^2}{\mu V} = \frac{L^2}{2\mu V} = \frac{L^2}{2\mu_{eff}[V_0 - V_{cor}]} = \frac{qLn}{J}, \quad \text{(S23)}$$

where the distance d was replaced by half the active layer thickness L, the mobility μ_{eff} was replaced by the effective mobility ($\mu_{eff} = JL/(2qn[V_0\text{-}V_{cor}])$) and the voltage was replaced by the effective voltage $V_{eff} = V_0\text{-}V_{cor}$.

Photoconductive AFM (pc-AFM) of PM6:Y6 BHJ photoactive layers

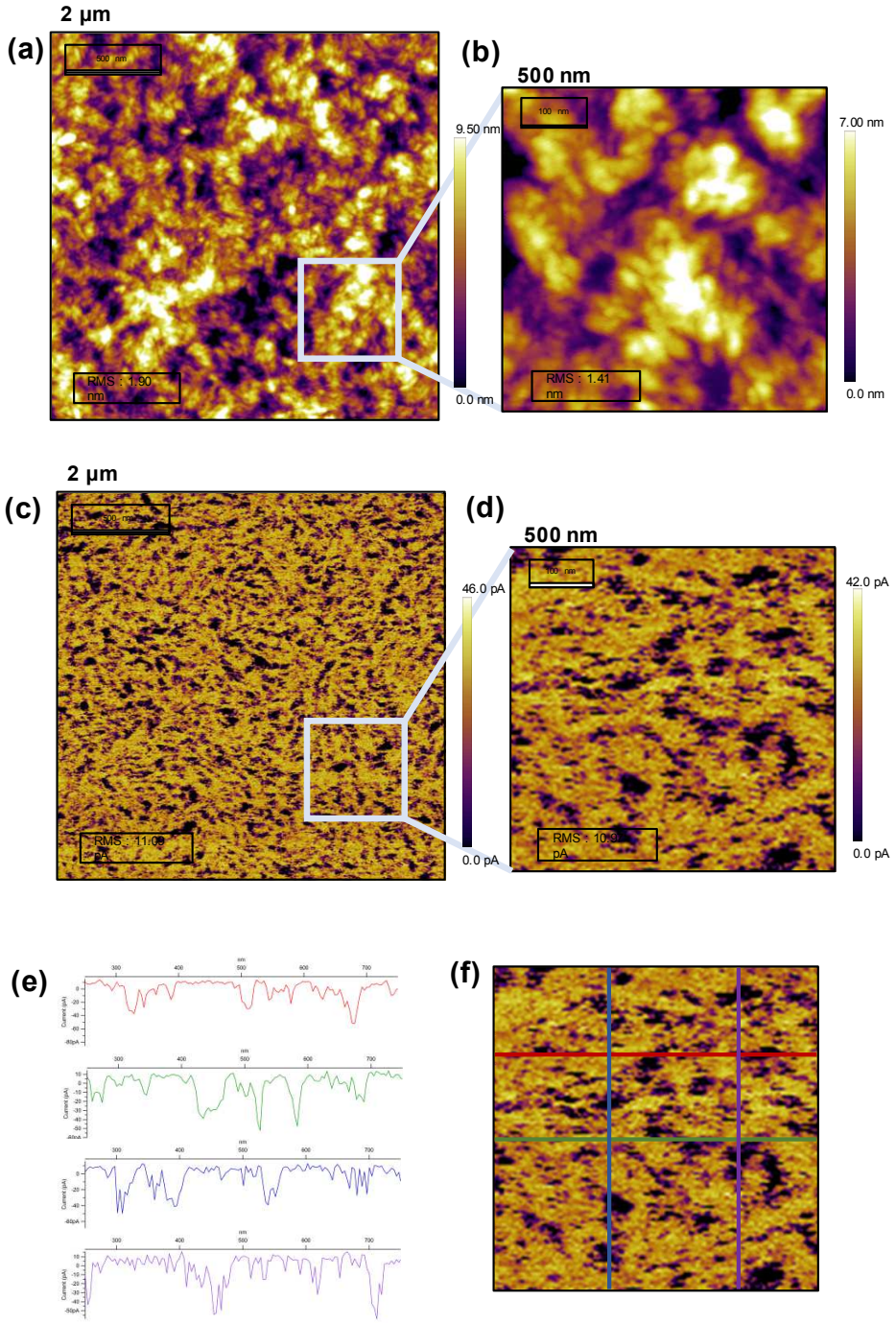

Figure B9. High resolution tapping mode a) 2 x 2 μm and b) 500 x 500 nm images of the surface topography and c) 2 x 2 μm and D) 500 x 500 nm photocurrent images collected at 0 V. Section cuts on (f) high resolution (500 x 500 nm) photocurrent image used to extract the domain sizes on the film surface, where the domain sizes are obtained from lateral section cuts (e) from several different locations on the film surface.

***GIWAXS* analysis of PM6:Y6 BHJ blend**

The coherence lengths (L_c) were estimated through the Scherrer equation.[252] Peaks from π-π stacking are located at 1.75 $Å^{-1}$ q_z and may be too broad and close to the each other to definitively say if they are coming from PM6 or Y6 as was reported in previous literature.[111] The highest intensity lamellar stacking peaks are at 0.29 $Å^{-1}$ q_{xy} (d = 2.14 nm, L_c = 10.60 nm) and 0.31 $Å^{-1}$ q_{xy} (d = 2.03 nm, L_c = 7.68 nm).[111] Lamellar stacking in neat Y6 has previously been observed at 0.285 $Å^{-1}$ q_{xy} (d = 2.19 nm).[111] This is closest to the peak at 0.29 $Å^{-1}$ observed for the blend prepared in this work. Bimodal lamellar stacking has been observed previously for neat PM6 at 0.300 $Å^{-1}$ q (d = 2.09 nm).[111] This is closest to the 0.31 $Å^{-1}$ peak observed here. Notably, this peak does not appear to have a bimodal distribution, suggesting a more uniformly ordered lamellar stacking. Additional lamellar stacking peaks can be seen in-plane at 0.22 $Å^{-1}$ (d = 2.85 nm, L_c = 26.30 nm) and 0.43 $Å^{-1}$ (d = 1.46 nm, L_c = 5.91 nm). The peak at 0.43 $Å^{-1}$ may be assigned to Y6.[111] Unassigned scattering peaks differ in stacking distances from those previously observed in the neat materials as a result of altered solid-state morphology in the blend (**Table S3**). Tight π-π stacking distances of approximately 1.8 $Å^{-1}$ have also been reported in other high performing (PCE > 9%) blend films using non-fullerene acceptors.[109,121,253] The reported coherence lengths for π-π stacking features in high performance blends appears to vary around 10 nm which is significantly larger than the value seen here.[121,253]

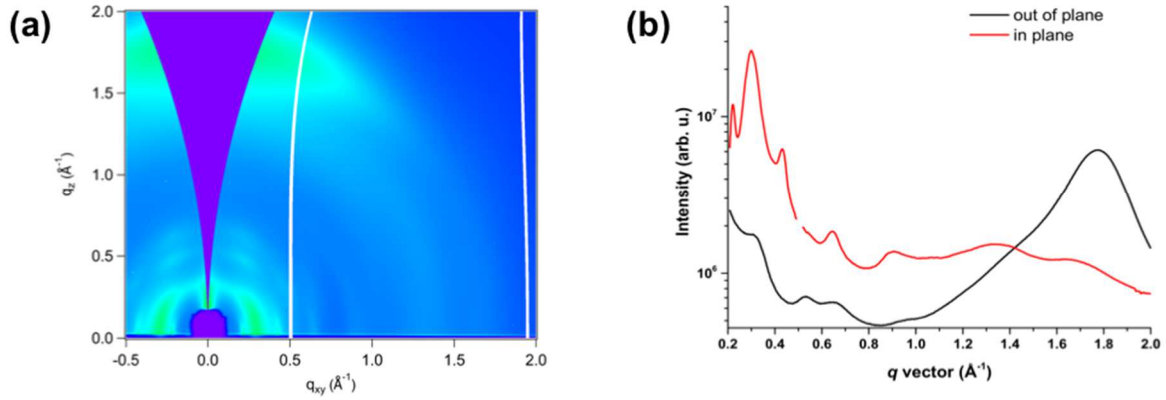

Figure B10. (a) 2-D GIWAXS image of the PM6:Y6 BHJ blend, (b) Line-cuts in the in-plane and out-of-plane direction.

Table B3. Summarizing the d-spacings and crystalline coherence lengths obtained from GIWAXS measurements of the PM6:Y6 BHJ blend.

Q_{xy} (Å^{-1})	d (nm)	L_c (nm)	Q_z (Å^{-1})	d (nm)	L_c (nm)
0.22	2.85	26.30	1.75	0.36	2.31
0.29	2.14	10.60	1.81	0.35	3.89
0.31	2.03	7.68	$Q_{off\text{-}axis}$ (Å^{-1})	d (nm)	L_c (nm)
0.43	1.46	5.91	0.52	1.21	4.71

2D solid-state ^{19}F MAS NMR spectroscopy

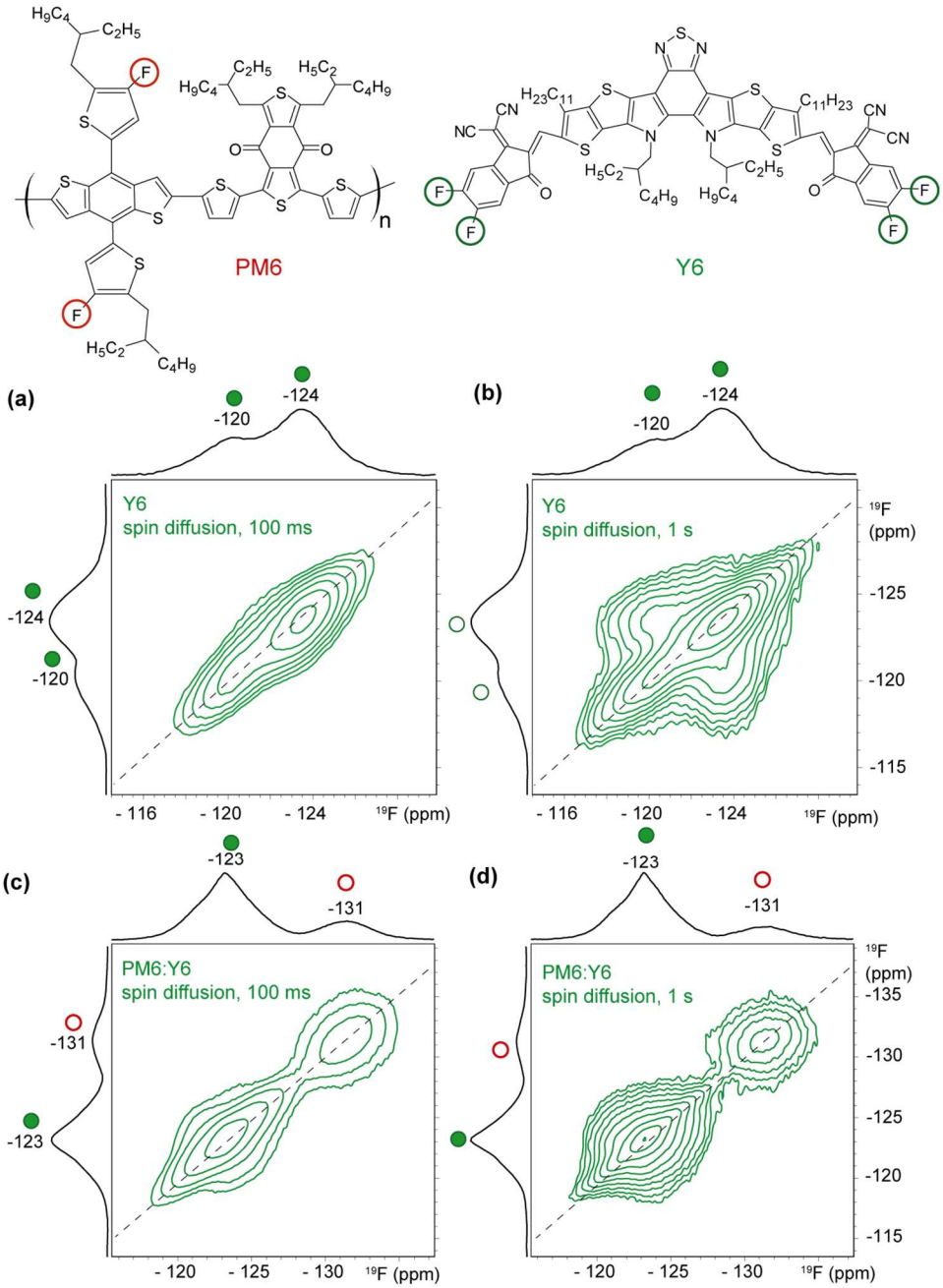

Figure B11. Two-dimensional ^{19}F{^{19}F} spin-diffusion solid-state MAS NMR spectra of Y6 acquired by using (a) 100 ms and (b) 1 s, and PM6:Y6 blend at (c) 100 ms and (d) 1 s of mixing times, respectively. Off-diagonal intensities between -120 and -124 ppm in (b) indicate spatially proximate ^{19}F sites in different Y6 backbone structures. The absence of such correlation intensities between -123 and -131 ppm for the spectrum recorded under identical experimental conditions (c-d) confirm that the ^{19}F sites in Y6 and PM6 backbone moieties are segregated into different structural regimes in the PM6:Y6 films, and suggest that intermixing is likely to occur in the sidechain regions.

Absorbance spectra of films

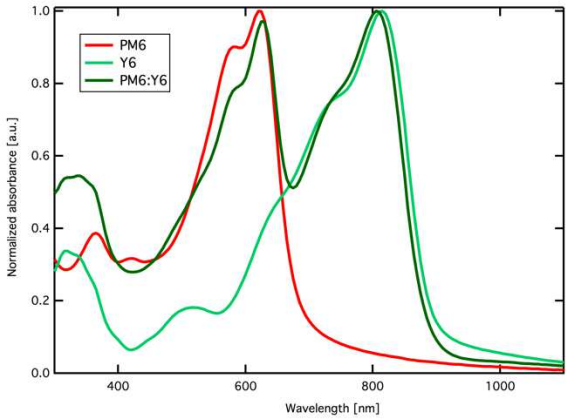

Figure B12. Normalized absorbance spectra of PM6, Y6, and PM6:Y6.

Appendix C:

Appendix to Chapter 4

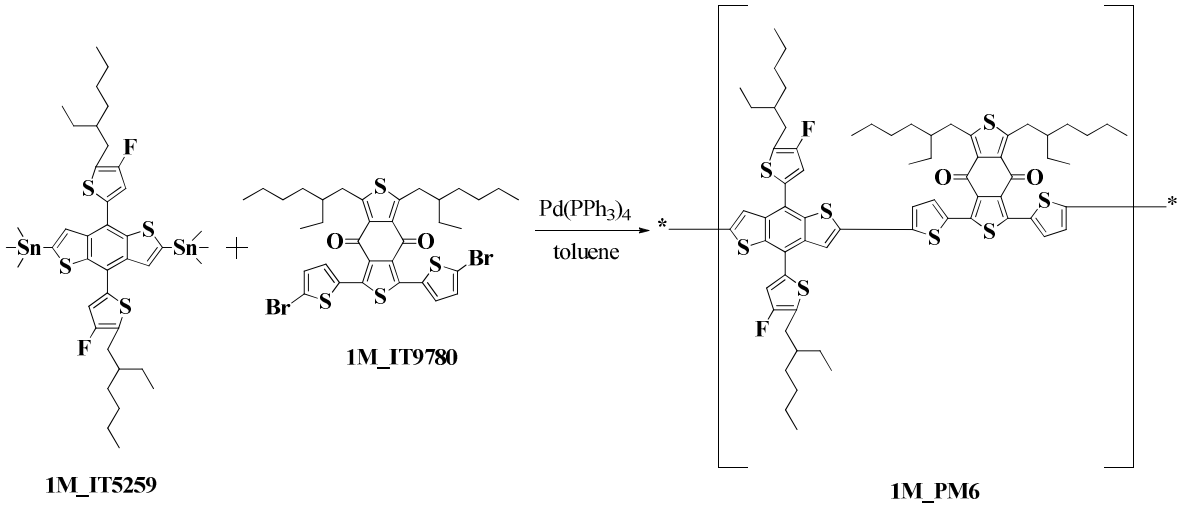

Figure C1. Schematic of synthesis pathway to PM6 polymer

A four-necked 250 ml flask equipped with a mechanic stirrer, an argon inlet, a condenser caped with an argon outlet, and a thermometer, was thoroughly dried by a torch and cooled to room temperature under continuous flow of argon. Into this reaction flask, 60 ml of anhydrous toluene, 2.82 g of 1M_IT5259 (3.0 mmol), 2.30 g of 1M_IT9780 (3.0 mmol), 151 mg of $Pd(PPh_3)_4$ (0.13 mmol) were added. The reaction mixture was heated using a heating mantel and stirred at 110 °C for 24 h, and subsequentially quenched by 2-(tributylstannyl)thiophene and bromobenzene. Then, the quenched reaction mixture was cooled to room temperature. While vigorously stirring, the cooled polymer solution was dripped into a solvent mixture containing 600 ml of methanol and 600 ml of acetone. The polymer product was collected by

filtration and dried naturally overnight to yield a dark solid, which is referred as the crude polymer PM6 (CAS# 1802013-83-7; Poly[[4,8-bis[5-(2-ethylhexyl)-4-fluoro-2-thienyl]benzo[1,2-*b*:4,5-*b*']dithiophene-2,6-diyl]-2,5-thiophenediyl[5,7-bis(2-ethylhexyl)-4,8-dioxo-4*H*,8*H*-benzo[1,2-*c*:4,5-*c*']dithiophene-1,3-diyl]-2,5-thiophenediyl]).

PM6 samples tested here are from different polymerization batches and from different after-treatments. A crude polymer of Lot# YY13208 was transferred to a Soxhlet extractor and was subsequentially extracted by acetone (4 h), hexane (17 h) and chloroform (24 h). The chloroform extracted fraction was concentrated and precipitated in acetone to yield the PM6 sample of YY13208CH. Another crude polymer of Lot#YY15258 was extracted by a Soxhlet extractor following the same procedure of YY13208 to give YY15258CH. However, we found the chloroform solution of YY15258CH was gradually becoming reddish, and we suspected some probable degradation. Thus, we took YY1528CH for further after-treatments to yield SX8055A, SX8055B and SX8055C85, as follows. First, we re-labelled the original YY15258CH as SX8055A for comparing with other SX8055 series. Second, we scavenged SX8055A following our patented procedure described in US Patent 6,894,145 to obtained PM6 sample SX8055B. Thirdly, we used a Soxhlet extractor to extract SX8055A again in a solvent sequence of methanol, acetone, a mixture of 85% chloroform and 15% methanol (referred as C85 herein), and finally chloroform. The fraction extracted by C85 was concentrated and precipitated in acetone, filtered and naturally dried to give sample of SX8055C85.

Gel Permeation Chromatography (GPC). Molecular weight of the PM6 polymers was estimated by GPC method; two peaks were observed for most of batches in GPC profiles. One peak was associated with a low molecular weight fraction with an estimated Mn of 2200-2800 g/mol and another peak was associated with a high molecular weight fraction with an estimated Mn of 30000-50000 g/mol. The polydispersity index (PDI) of all polymers were determined to be the same of around 2.2 to ensure a systematic comparison of the samples. The relative fractions of two peaks obtained from the area integrates associated with different peaks are summarized below in **Table C1**.

Table C1. Summary of GPC fractions of the different PM6 batches.

Sample	Peak-1 (low Mw fraction)		Peak-2 (high Mw fraction)	
	Peak area (%)	Estimated Mn (Da)	Peak area (%)	Estimated Mn (Da)
YY13208CH	1	2400	99	43700
SX8055B	7	2600	93	42500
SX8055A	9	2600	91	42100
SX8055C85	52	2200	48	38900

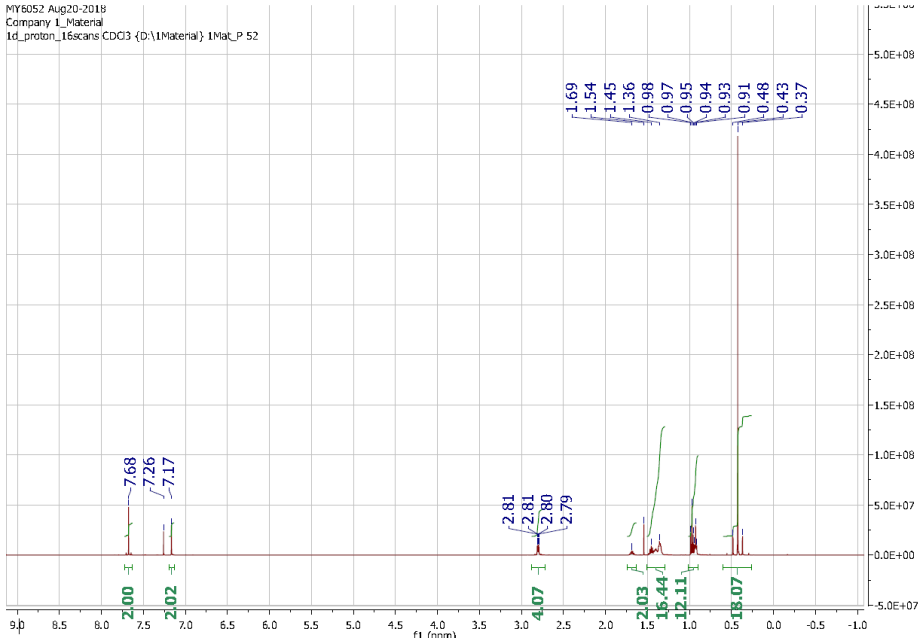

Figure C2. Solution-state 1D ^{1}H NMR spectrum of 1M_IT5259 in $CDCl_3$.

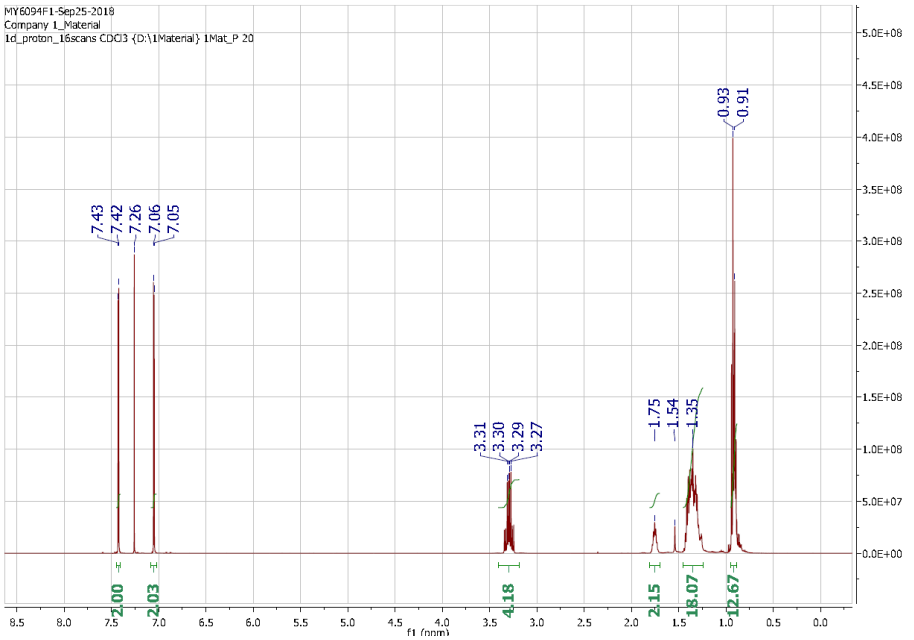

Figure C3. Solution-state 1D ^{1}H NMR spectrum of 1M_IT9780 in $CDCl_3$.

Power conversion efficiency (PCE) averages

Table C2. Power conversion efficiency averages for at least 20 devices for the four different batches of PM6 polymer with the Y6 NFA. The solvent (CF, 0.5% CN) and processing conditions (annealing at 110 °C for 10 min) were kept the same to ensure a systematic comparison of the blend systems.

PM6 batch number	**V_{OC} (V)**	**J_{SC} (mA cm^{-2})**	**FF**	**Average PCE (Max) [%]**
YY13208CH (1% LMWF)	0.825 ± 0.003	25.5 ± 0.7	0.712 ± 0.02	15.04 ± 0.4 (**15.35**)
SX8055A (6% LMWF)	0.846 ± 0.003	20.6 ± 1.2	0.681 ± 0.02	11.8 ± 0.6 (**12.9**)
SX8055B (9% LMWF)	0.843 ± 0.005	20.4 ± 1	0.646 ± 0.02	11.1 ± 0.5 (**12.3**)
SX8055C85 (51.7% LWMF)	0.85 ± 0.006	12.0 ± 0.7	0.51 ± 0.02	5.2 ± 0.5 (**5.7**)

On accurately quantifying the voltage losses in these blend systems.

The contributions to the V_{OC} losses in the two blend systems were determined to understand the slight increase in the V_{OC} upon going from the 1% LMWF blend to the 52% LMWF blend. It should be noted that the determination of the CT state energies in these two blends are prone to error, as discussed in some earlier publications[19,20], due to the inability to distinguish the S_1 and CT states unambiguously. Nonetheless, as an estimate, we can confirm that the slight red-shift in the EQE spectra of the low performing blend suggests that the E_{CT} value would be higher for the lower performing blends causing the S_1-CT offset in this blend to be much lower (< 0.1 eV) than the higher performing blend (S_1-CT offset ~0.05 eV). Additionally, we find the experimentally measured EQE_{EL} values to be very similar in the two blends indicating that the non-radiative recombination losses in the blends would be similar. Therefore, the reduced voltage losses in the low performing blend leading to the slight increase in the V_{OC} is due to a reduction in losses due to the decreased S_1-CT offset. Furthermore, due to the presence of additional bulk traps in the lower performing PM6:Y6 blend system, a systematic comparison between the two blend systems to identify the origins of the non-radiative recombination losses may not be possible within the design rules formulated in the paper to identify origins of non-radiative recombination losses.[15,168] The presence of trap-assisted recombination in the low performing blend will likely further contribute to additional non-radiative recombination losses, as depicted in the simplified Jablonski diagram. (**Figure. S4**)

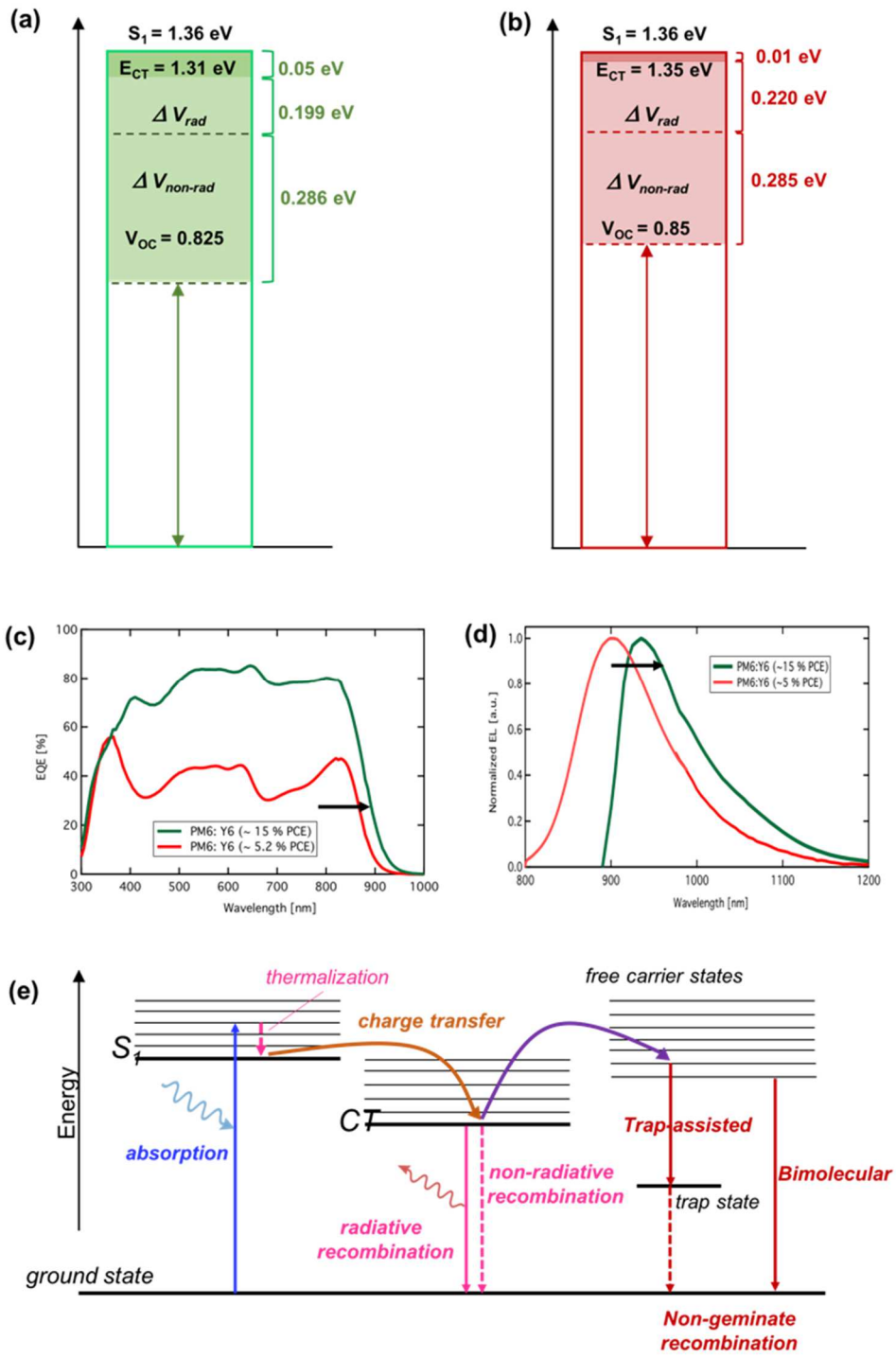

Figure C4. Voltage loss contributions obtained via methods described in a previous report[20] for (a) 1% LMWF and (b) 52% LMWF blends. (c) EQE and (d) EL spectra of the two blend systems. (e) A simplified Jablonski diagram summarizing the pathways for recombination losses.

High resolution AFM and Photoconductive AFM (pc-AFM) of blend films

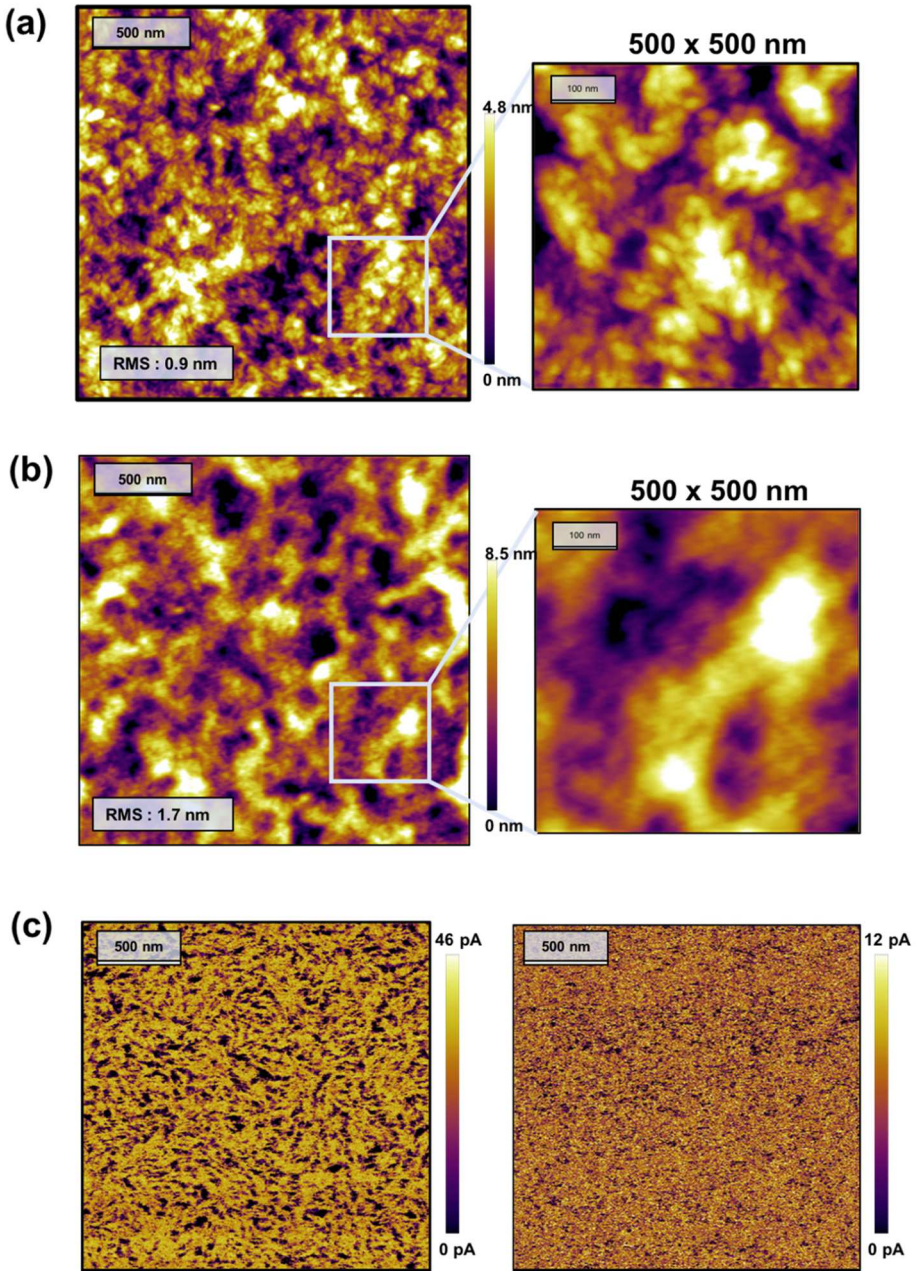

Figure C5. High resolution AFM images of (a) 1% LMWF and (b) 52% LMWF PM6:Y6 blends. (c) Photoconductive AFM images taken at 0 V bias and under white light illumination of 1% LMWF and 52% LMWF PM6:Y6 blends.

GIWAXS analyses of neat compounds and BHJ blend films

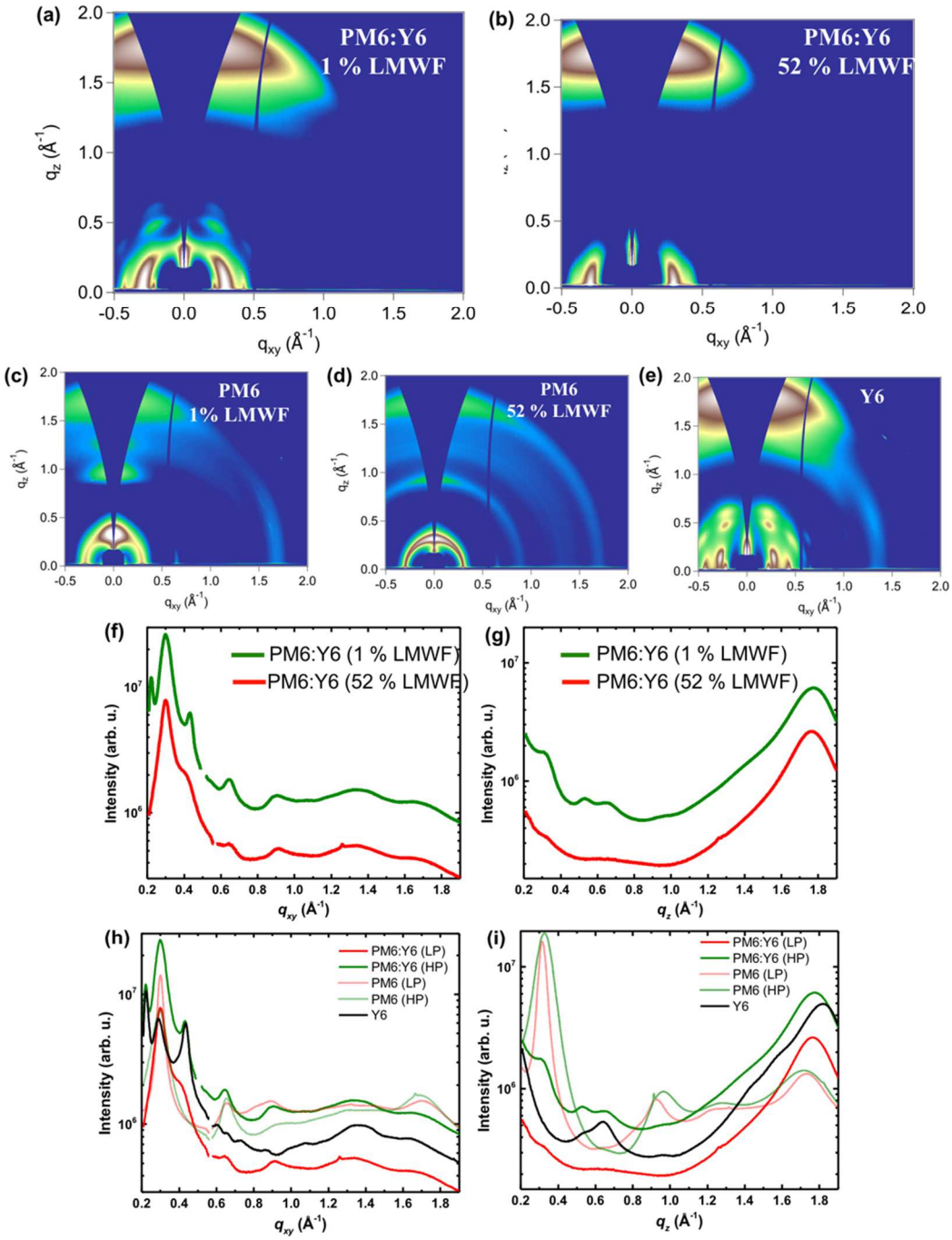

Figure C6. 2D GIWAXS spectra of (a) 1% LMWF PM6:Y6 blend, (c) 52% LMWF PM6:Y6 blend, (c) neat PM6 1% LMWF (d) neat PM6 52% LMWF, and (e) Y6. (f-i) Corresponding in-plane and out-of-plane line cuts of neat and blend films.

Table C3. GIWAXS parameters including in-plane and out-of-plane d-spacing, π-π and lamellae stacking distances obtained from the analyses GIWAXS patterns.

PM6:Y6 1% LMWF blend

Q_{xy} (Å^{-1})	d (nm)	L_c (nm)	Q_z (Å^{-1})	d (nm)	L_c (nm)
0.22	2.85	26.30	1.75	0.36	2.31
0.29	2.14	10.60	1.81	0.35	3.89
0.31	2.03	7.68	$Q_{off\text{-}axis}$ (Å^{-1})	d (nm)	L_c (nm)
0.43	1.46	5.91	0.518	1.21	4.71

PM6:Y6 52% LMWF blend

Q_{xy} (Å^{-1})	d (nm)	L_c (nm)	Q_z (Å^{-1})	d (nm)	L_c (nm)
0.29	2.16	18.30	1.76	0.36	2.32
0.30	2.07	12.16			
0.38	1.66	2.12			

PM6 1% LMWF

Q_{xy} (Å^{-1})	d (nm)	L_c (nm)	Q_z (Å^{-1})	d (nm)	L_c (nm)
0.30	2.12	5.48	0.33	1.92	5.19
0.66	0.96	5.19	0.97	0.65	2.56
1.69	0.37	1.92	1.29	0.49	1.23
			1.71	0.37	1.47

PM6 52% LMWF:

Q_{xy} (Å^{-1})	d (nm)	L_c (nm)	Q_z (Å^{-1})	d (nm)	L_c (nm)
0.30	2.09	11.59	0.32	1.99	9.98
0.66	0.96	3.76	0.93	0.68	3.79
0.86	0.71	4.26	1.73	0.36	2.18
1.70	0.37	1.73			

Y6:

Q_{xy} (Å^{-1})	d (nm)	L_c (nm)	Q_z (Å^{-1})	d (nm)	L_c (nm)
0.22	2.82	24.47	1.82	0.35	2.24
0.29	2.17	10.06			
0.43	1.45	13.99			
1.36	0.46	1.36			

GIWAXS measurements were performed on both the PM6:Y6 blend film and its neat components to provide insight into the molecular ordering within these films. The 2-D GIWAXS 1D linecuts corresponding to the in-plane (q_{xy}) and out-of-plane (q_z) scattered intensities are shown. The coherence lengths (L_c) represent the distance over which each scattering feature is maintained within their respective directions. These values are calculated through the Scherrer equation.

Neat films: The neat film of Y6 orients face-on with π-π stacking at 1.82 q_z (d: 0.35 nm, L_c: 2.24 nm), and lamellar stacking at 0.22 q_{xy} (d: 2.82 nm, L_c: 24.47 nm) which produces higher order reflections at 0.43 and 1.36 q_{xy}. The face-on orientation implies the long π-conjugated backbones are lying flat along the substrate with stacks of similarly oriented molecules extending in the direction normal to the substrate. This orientation favors transport in the direction normal to the substrate. Ordered features aligned neither in-plane nor out-of-plane produce off-axis scattering centered at 0.31 q (61.1 °X) and 0.53 q (27.3 and 22.3 °X). Because this feature is close to the substrate surface, it appears in the in-plane line cut near 0.29 q_{xy}.

Both the 1% and 52% PM6 neat films display weak scattering from π-π stacking near 1.7 q_z and intense bimodal scattering at the low q value of 0.3 $Å^{-1}$ (d: 2.1 nm) with higher order diffraction peaks near 0.66 q_{xy} and 0.93 q_z. This suggests that the donor material does not orient strictly face-on. The weak scattering observed near 1.7 q_{xy} further supports the more isotropic nature of this material as this is due to π-π stacks which are lying in the plane of the substrate. The most notable difference between the two batches of donor material is that the long-distance (real-space) isotropic stacking in the low performance PM6 extends for a distance roughly twice as long as that in the high performance PM6 as indicated by the L_c values. Long-distance real-space stacking typically corresponds to lamellar end-to-end stacks which do not transport charges as efficiently as the closely spaced π-π stacks. Isotropic orientation in this feature may hinder anisotropic charge transport between electrodes. The longer these features are, the more dominant isotropic charge transport may become, possibly contributing to some of the decrease in performance for the low molecular weight PM6.

Blend films: It is notable that in the 52% LMWF PM6:Y6 blend, π-π stacking is only observed for the PM6 donor at 1.76 q_z (d: 0.36 nm, L_c: 2.32 nm). In a previous study, this blend peak was near 1.75 q_z and assigned to Y6 in light of literature reports for Y6 π-π stacking at a similar value.[20,111] The presence of two π-π stacking peaks in the high performance blend and the additional measurements of the neat materials provide reasons to assign the PM6 π-π stacking to those peaks near 1.75 q_z in both blends. The π-π stacking from Y6 should be re-assigned as that present at 1.81 q_z (d: 0.35, L_c: 3.89 nm) in the 1% LMWF PM6:Y6 blend. The inability to resolve a scattering peak in the 52% LMWF blend corresponding to Y6 π-π stacking suggests that this feature is either not present or is present in a relatively small volume so that its resulting scattering is at an insufficient intensity to be identified separately.

The in-plane stacking peaks observed in the 52% LMWF PM6:Y6 blend are at 0.3 q_{xy} (d: 2.09 nm, L_c: 8.80 nm) which may result from features in both blends, and 0.38 q_{xy} (d: 1.66 nm, L_c: 2.12 nm) resulting from Y6. PM6 is able to contribute to the 0.3 q_{xy} peak due to its lamellar scattering; however, scattering at this distance from Y6 is due to off-axis scattering. Both of these stacking features are maintained for slightly longer distances within the 52% LMWF PM6:Y6 blend as evidenced by the L_c values. However, the 1% LMWF PM6:Y6 blend contains additional lamellar scattering from the acceptor at 0.22 q_{xy} (d: 2.85 nm, L_c: 26.30 nm) and 0.43 q_{xy} (d: 1.46 nm, L_c: 5.91 nm) in addition to the off axis acceptor scattering near 30° X from the substrate normal. This information provides evidence that the acceptor ordering is better maintained in the 1% LMWF PM6:Y6 blend.

RSoXS analysis of blend systems

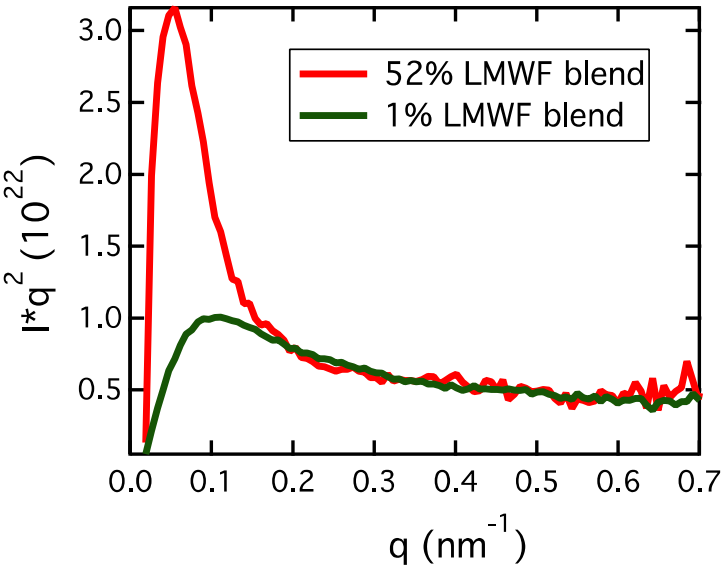

Figure C7. Lorentz corrected and circularly averaged RSoXS profiles of the 1% LMWF and 52% LMWF PM6:Y6 blend systems.

Table C4. RSoXS parameters obtained from fitting the RSoXS profiles.

Sample	Peak position (nm^{-1})	Long period (nm)	Root-mean-square (RMS) composition variation
1 % LMWF	0.112	56	0.84
52 % LMWF	0.050	126	1

Solid state 1D and 2D NMR spectra of neat compounds and blends

A comparison of 1D ^{1}H MAS NMR spectra of the neat Y6 acceptor, the two different batches of PM6 (1% and 52% LMWF) donor, and their respective blends is given in Figure C8. Although ^{1}H signals corresponding to aliphatic and aromatic moieties are clearly resolved in the ^{1}H MAS spectra of neat PM6 and Y6 compounds, the ^{1}H MAS spectra of BHJ blends exhibited severely overlapped signals that hindered accurate assignments of the ^{1}H sites in PM6 and Y6.

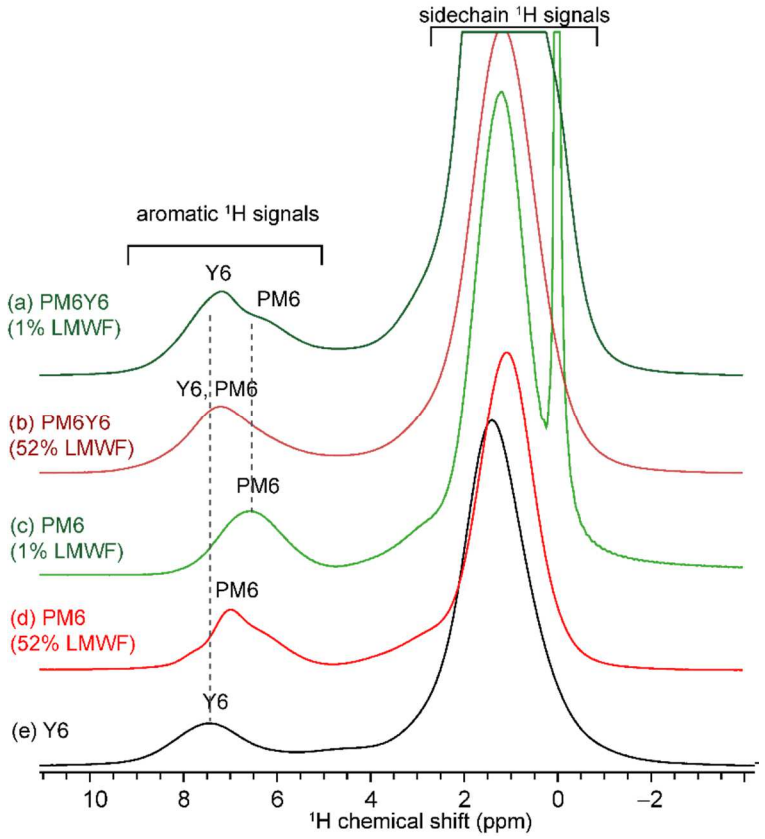

Figure C8. Comparison of solid-state 1D ^{1}H NMR spectra of different batches of PM6 donor polymers, Y6 acceptor and their blends acquired at 21.1 T (60 kHz MAS). (a) PM6:Y6 blend with 1% LMWF, (b) PM6:Y6 blend with 52% LMWF, (c) PM6 with 1% LMWF, (d) PM6 52% LMWF, and (e) Y6 acceptor.

Figure C9 compares the 1D ^{19}F MAS NMR spectra obtained for PM6:Y6 blends consisting of 1% and 52% LMWF PM6 donor polymers. Intrinsically high sensitivity and spectral resolution associated with ^{19}F MAS NMR enable different distributions of ^{19}F sites associated with Y6 and PM6 moieties to be detected and identified in the PM6:Y6 blends.[20] In PM6:Y6 blends with different LMFWs, the ^{19}F signals at −131 ppm were attributed to the ^{19}F sites in fluorinated thiophene groups of the PM6 donor polymer. The broad distributions

of ^{19}F signals centered at −124 ppm were ascribed to the local environments of ^{19}F sites in the difluorophenyl groups of the Y6 acceptor molecules. It is noteworthy the ^{19}F MAS NMR spectrum of neat Y6 exhibited partially resolved signals at −120 ppm and −124 ppm, suggesting different distributions of ^{19}F chemical shifts,[20] which could be correlated to the different structural orders observed by GIWAXS measurements and analysis.[20,111] However, in both PM6:Y6 blends, the Y6 moieties showed a ^{19}F signal at −124 ppm, instead of two different ^{19}F signals as described above, indicating the improved Y6 molecular order in the BHJ blends compared to the neat Y6 molecules. In addition, the ^{19}F chemical shift of fluorinated thiophene groups in the PM6 polymer at −131 ppm reveals identical local bonding environments in both PM6:Y6 blends, which is consistent with the ^{19}F chemical shift (−131 ppm) of fluorinated thiophene groups in the neat PM6 polymer.[20] These results are further corroborated by 2D ^{19}F-^{19}F spin-diffusion (SD) measurements and analyses (Figure C9c,d).

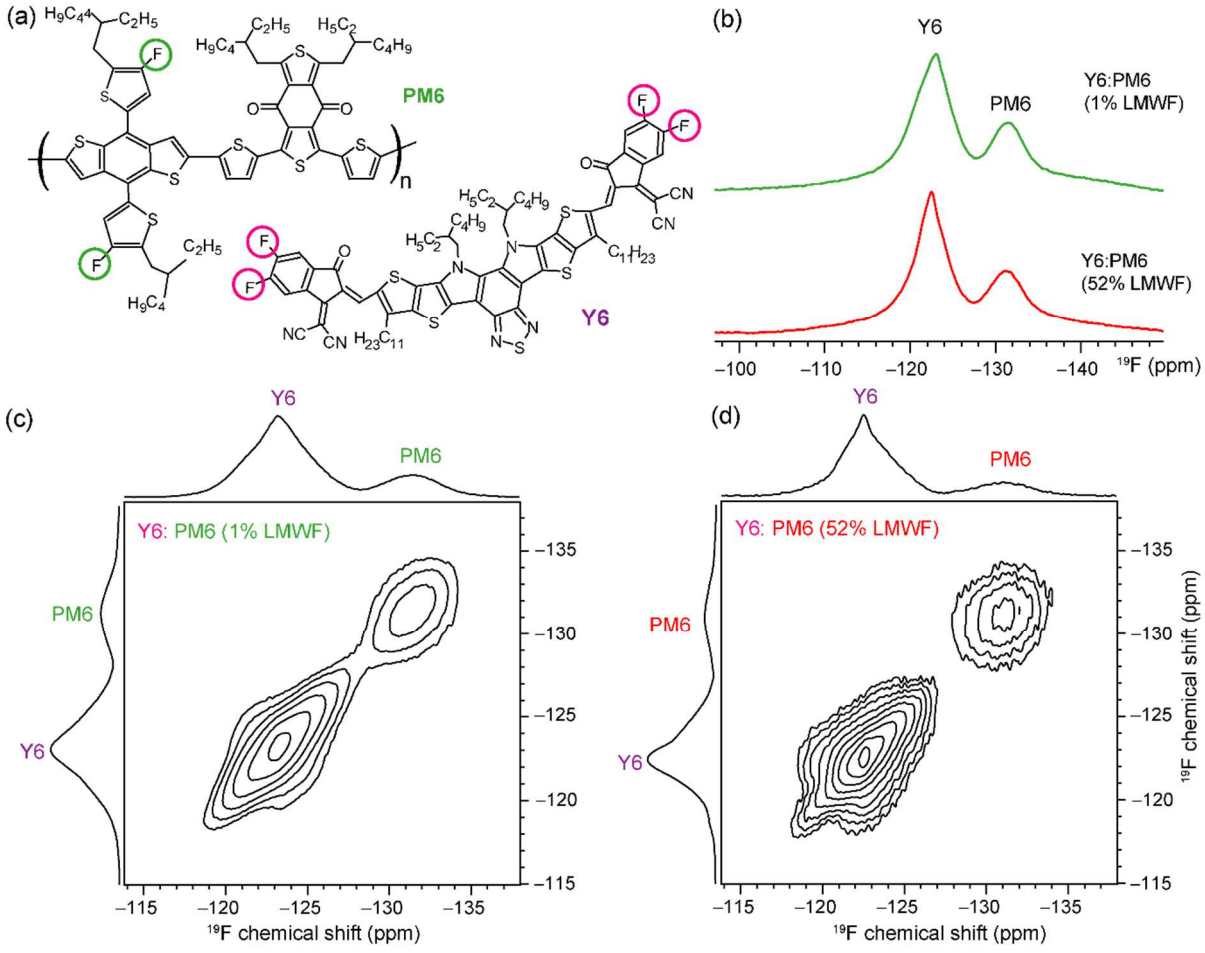

Figure C9. Comparison of solid-state 1D ^{19}F NMR spectra, and 2D ^{19}F-^{19}F correlation spectra of different batches of PM6:Y6 blends acquired at 21.1 T (60 kHz MAS); (a) schematic structures of PM6 and Y6, (b) 1D ^{19}F MAS NMR spectra of PM6:Y6 blend with 52% and 1% LMWFs, (c) 2D ^{19}F-^{19}F correlation of PM6:Y6 blend with 1% LMWF of PM6, and (d) 2D

^{19}F-^{19}F correlation of PM6:Y6 blend with 52% LMWF of PM6.

In a 2D ^{19}F-^{19}F spin-diffusion experiment, the ^{19}F magnetization exchange between spatially proximate ^{19}F sites is probed as a function of mixing time, also referred to as spin-diffusion time. This leads to on-diagonal self-correlation and off-diagonal cross-correlation intensities, whereby the off-diagonal peaks imply the magnetization exchange between different ^{19}F chemical shifts. 2D ^{19}F-^{19}F spectra of both the 1% LMWF and 52% LMWF blends exhibited self-correlation intensities along the diagonal corresponding to fluorine sites in PM6 (−131 ppm) and Y6 (−124 ppm) moieties, whereas no cross-correlation intensities between them were observed even when a long mixing time of 1 s was used. This confirms there is no magnetization exchange between the ^{19}F sites in PM6 and Y6 molecules in both high and low performing blends, suggesting that the effective spatial distance between fluorine atoms in the PM6 and Y6 molecules is greater than a nm, which would have shown a cross peak when they are closer to each other within 1 nm distance. This result rules out the possibility of intercalation of Y6 molecules in between PM6 polymer chains, which is corroborated by the GIWAXS patterns that showed π–π stacked PM6 polymers (Figure C6). While the information acquired from the ^{19}F spectra alone is not sufficient to reveal differences in the more detailed D:A inter- and intramolecular interactions of the two blends, complementary insights into D:A contacts can be attained by analyzing 1D ^{13}C{^{1}H} cross-polarization (CP) MAS and 2D ^{13}C-^{1}H correlation NMR spectra of neat compounds and blends, as will be discussed in the subsequent sections.

A comparison of 1D ^{13}C{^{1}H} CP-MAS NMR spectra of neat Y6, PM6 (1% and 52% LMWF) and their blends is given in Figure C10, which allows the signals corresponding to different carbon sites in the PM6 and Y6 molecules to be distinguished and identified. In a CP experiment, ^{1}H and ^{13}C nuclei are simultaneously excited and ^{1}H→^{13}C polarization transfer is achieved in order to enhance the signal intensities of these latter. For neat Y6 and different batches of PM6 polymers consisting of 1% and 52% LMWFs, ^{13}C signals in the aliphatic regions at 12, 13 and 15 ppm are assigned to terminal methyl groups, and partially resolved signals in the range of 23-35 ppm and 42 ppm are attributed to methylene groups in the branched sidechains. In the aromatic region of the ^{13}C{^{1}H} CP-MAS spectra of different PM6 polymer batches, signals associated with the protonated and quaternary carbon atoms in thiophene, benzodithiophene and benzodithiophenedione moieties (120-142 ppm), fluorinated carbon sites in thiophene moieties (153 ppm), and carbonyl groups of benzodithiophenedione (178 ppm) are distinguished and identified. In comparison, the aromatic ^{13}C signals in the ^{13}C{^{1}H} CP-MAS spectrum of Y6 molecules, 115-120 ppm, 127-134 ppm, and 146-147 ppm are attributed to different aromatic carbon atoms. The signals at 153-154 ppm are attributed to fluorinated carbon sites in difluorophenyl end groups and the signal at 178 ppm is attributed to carbonyl groups of the Y6 molecule. Even though the ^{13}C{^{1}H} CP-MAS spectra of the two PM6:Y6 blends mostly consist of severely overlapped frequencies originating from PM6 and Y6, signals corresponding to a few specific ^{13}C sites, e.g. carbonyl groups, can still be

identified and distinguished.

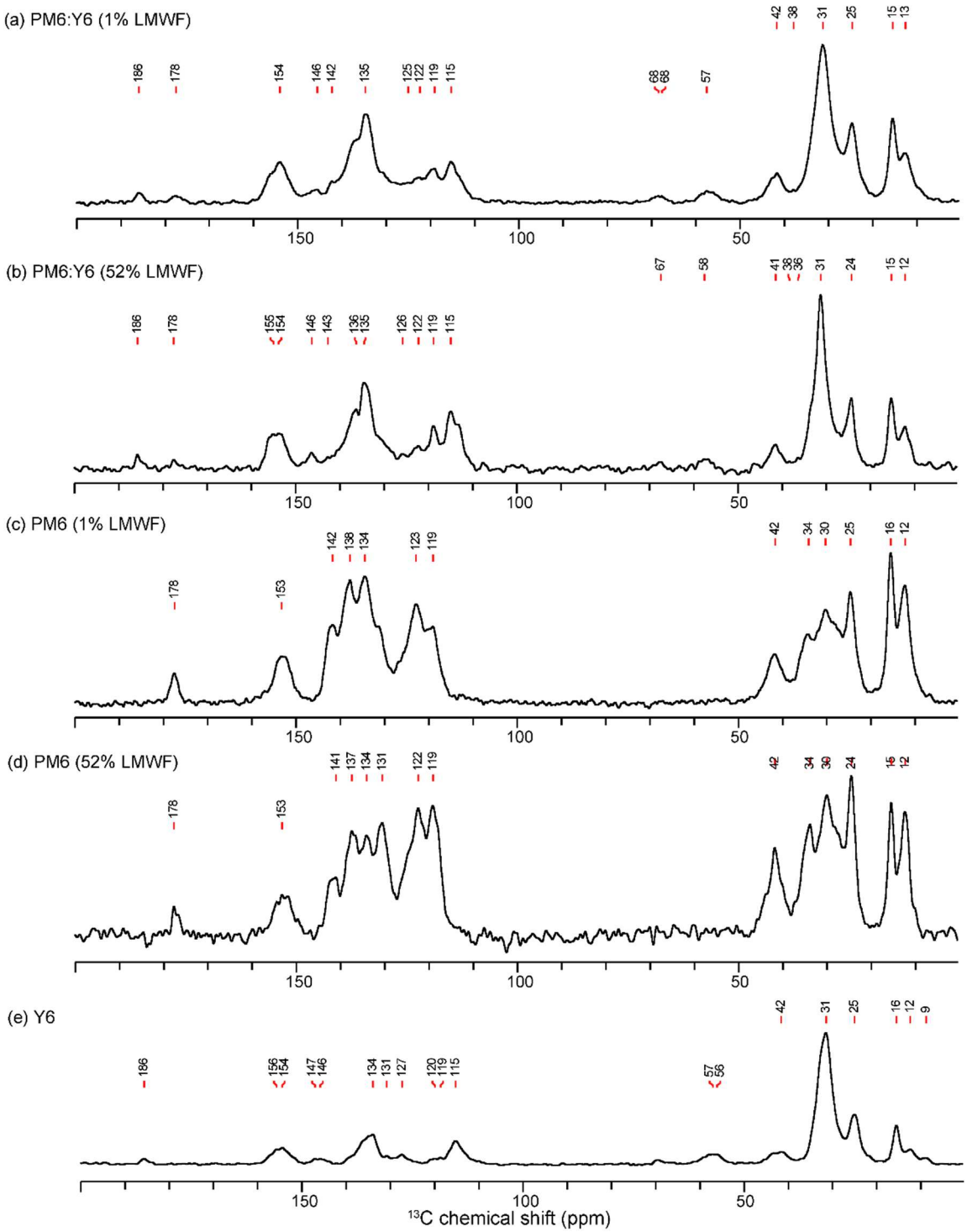

Figure C10. Comparison of solid-state 1D $^{13}C\{^{1}H\}$ CP-MAS spectra of different batches of PM6 donor polymers and their blends acquired at 9.4 T (12.5 kHz MAS); (a) PM6:Y6 blend

with 1% LMWF, (b) PM6:Y6 blend with 52% LMWF, (c) PM6 1% LMWF, (d) PM6 52% LMWF and (e) Y6 acceptor, acquired with 4 ms of CP contact time.

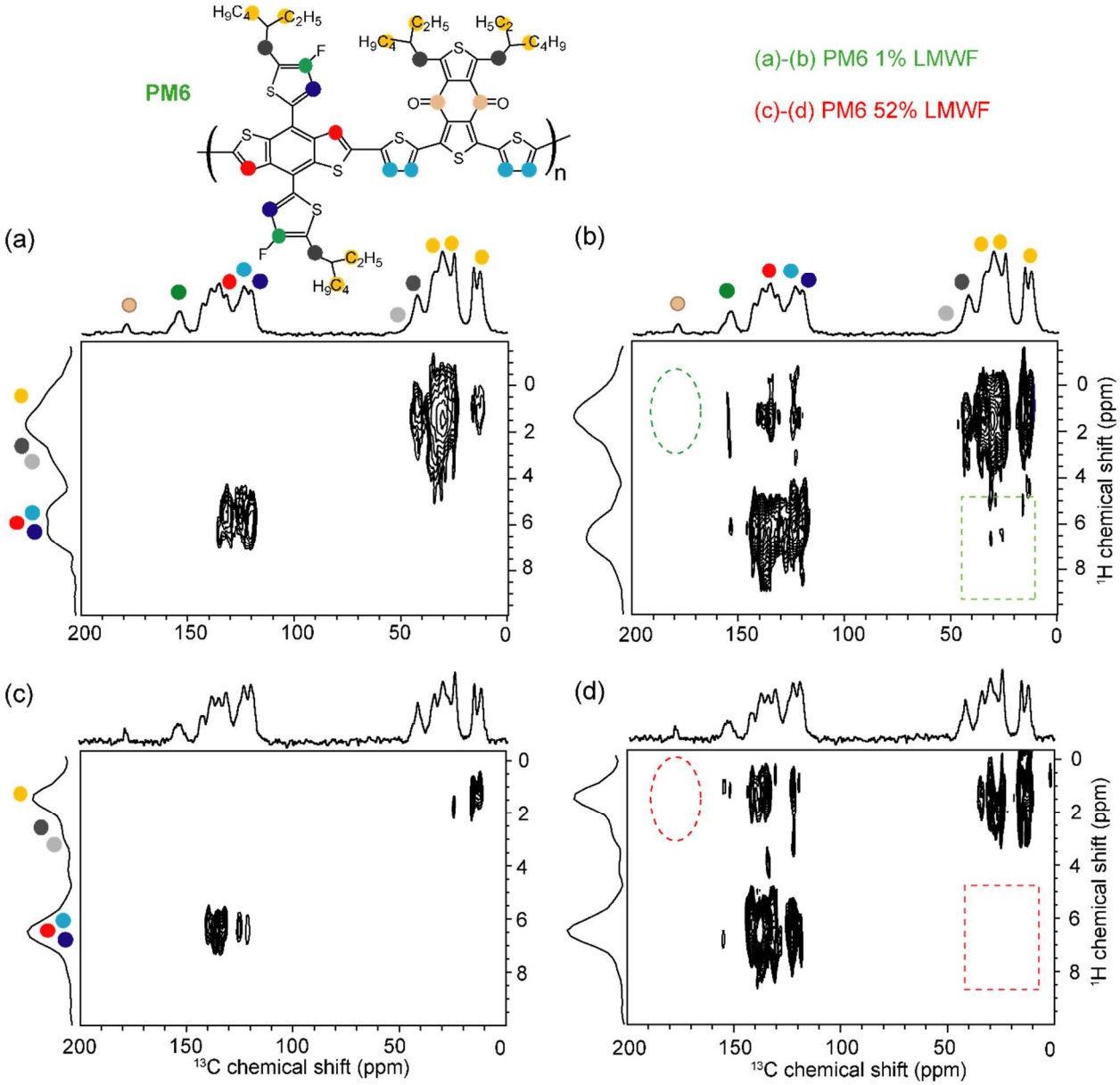

Figure C11. Comparison of solid-state 2D ^{13}C-^{1}H HETCOR spectra of different batches of PM6 donor polymer acquired at 9.4 T (12.5 kHz MAS) with 1% LMWF using (a) 0.1 ms and (b) 4 ms, and with 52% LMWF using (c) 0.1 ms and (d) 4 ms of CP contact times.

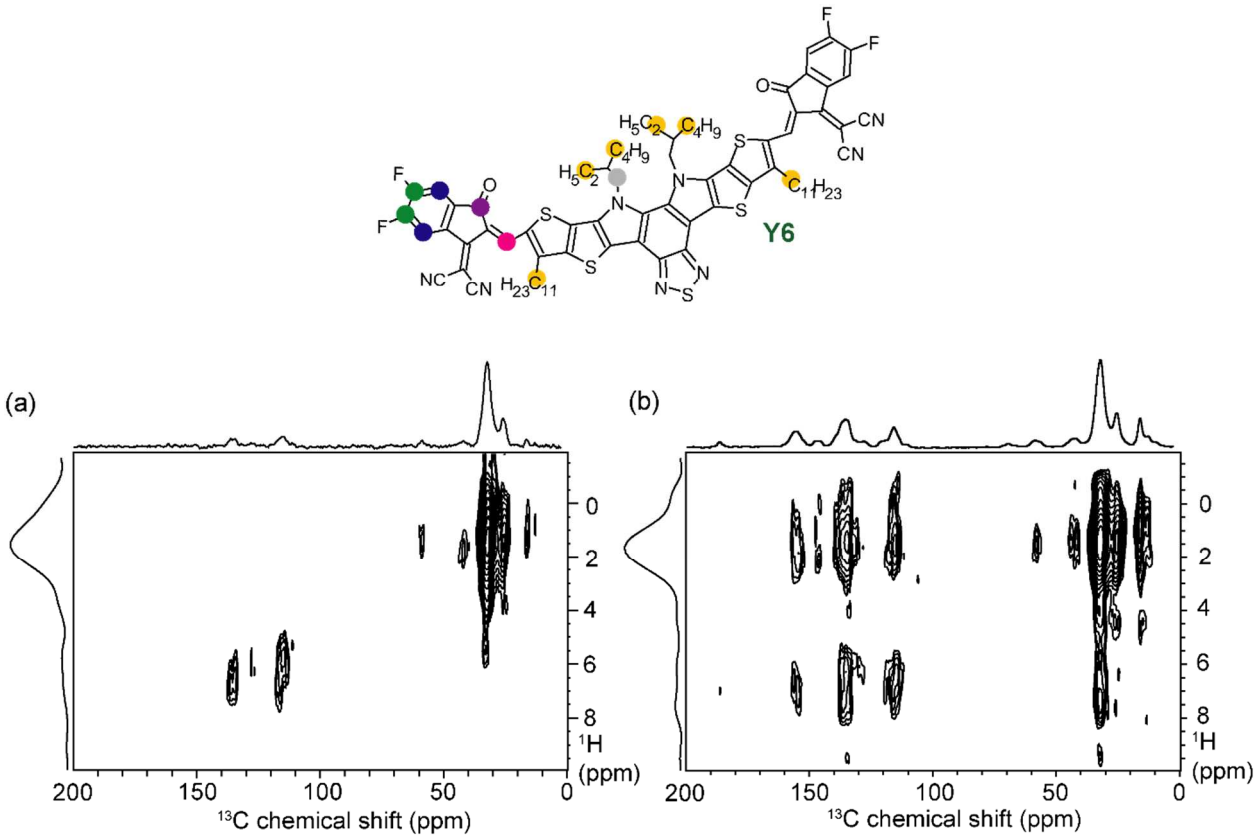

Figure C12. Comparison of solid-state 2D ^{13}C-^{1}H HETCOR NMR spectra of neat Y6 material acquired at 9.4 T (12.5 kHz MAS) using (a) 0.1 ms and (b) 4 ms CP contact times.

Probing Charge Generation Dynamics

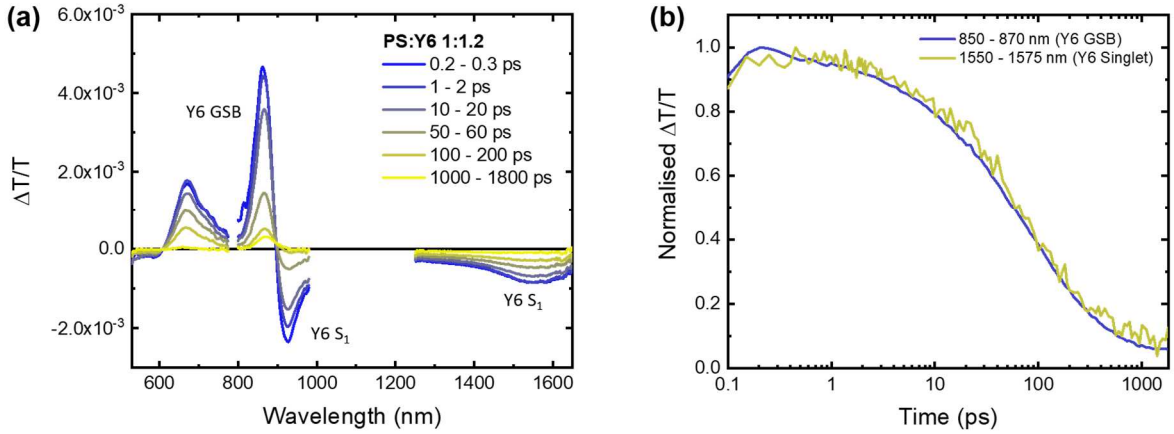

Fig. C13 (a) TA spectra and (b) fitted kinetics of Polystyrene:Y6 (pump: 800 nm and fluence: 1.8 μJ cm^{-2}).

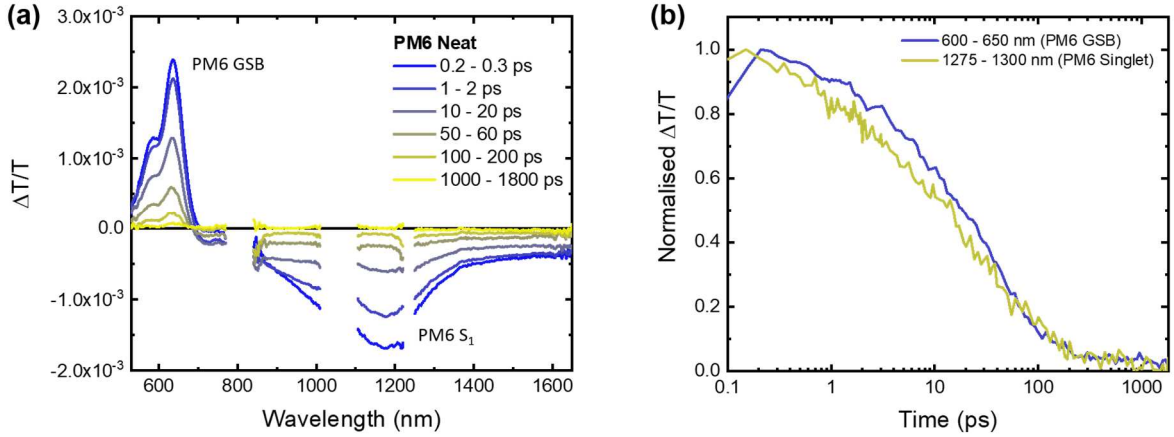

Figure C14. (a) TA spectra and (b) fitted kinetics of 1% LMWF (pump: 532 nm and fluence: 3.1 μJ cm^{-2}).

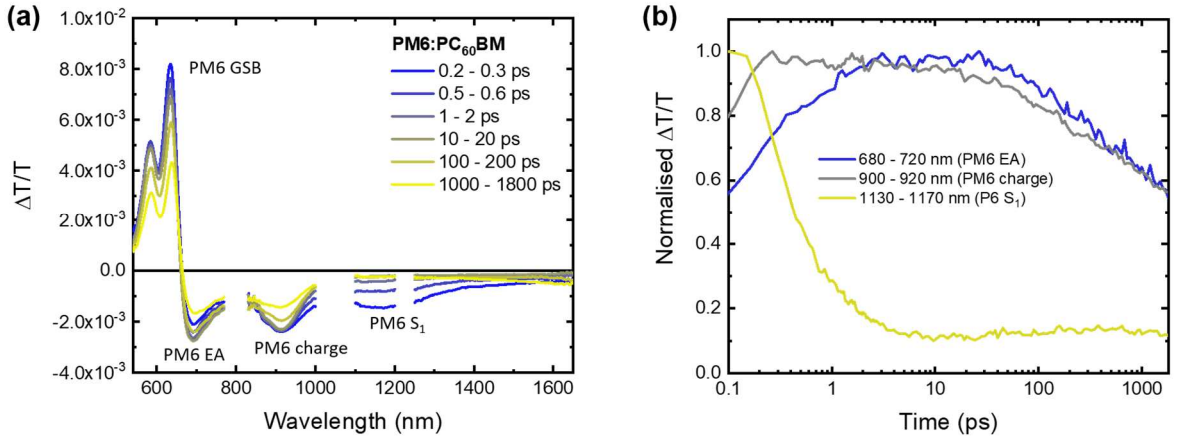

Figure C15. (a) TA spectra and (b) fitted kinetics of PM6:PCBM (pump: 532 nm and fluence: 5.1 μJ cm^{-2}).

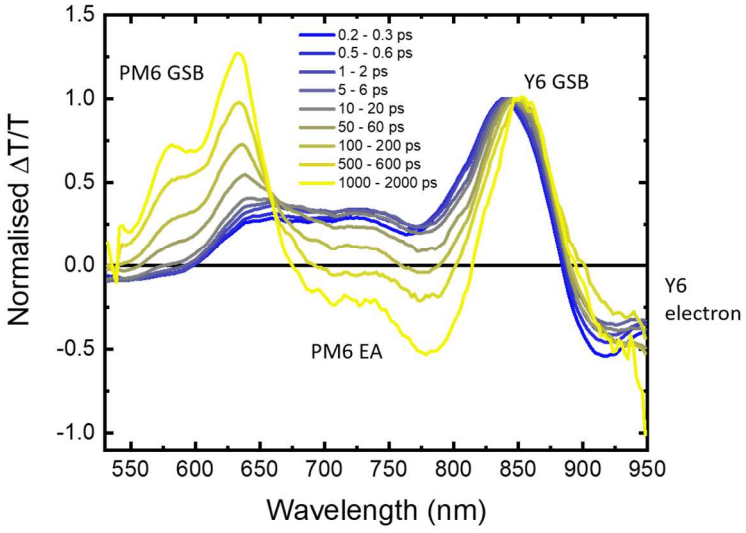

Figure C16. (a) TA spectra and of PM6:Y6 52% LMWF (pump: 800 nm and fluence: 0.5 μJ cm^{-2}).

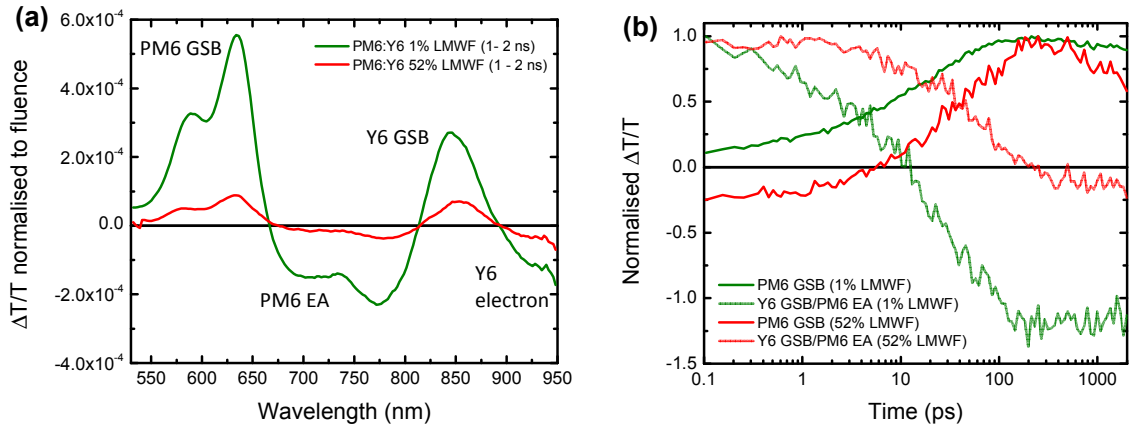

Figure C17. Comparison of the PM6:Y6 1% and 52% LMWF blends (a) TA spectra at 1-2 ns normalized to fluence to account for the greater total number of excitons created in the 1% LMWF blend (due to the higher fluence) and (b) fitted kinetics.

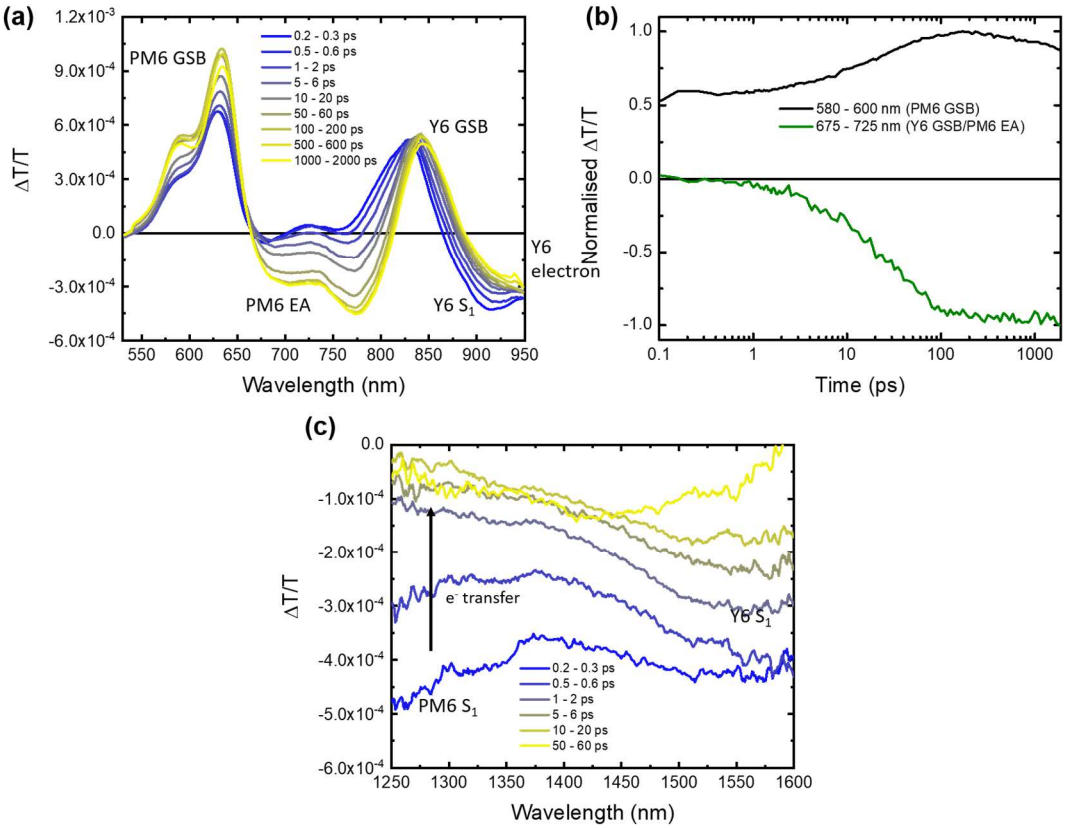

Figure C18. (a) Visible region TA spectra, (b) fitted kinetics of PM6:Y6 1% LMWF blend (pump: 580 nm and fluence: 0.67 μJ cm^{-2}), and (c) Near IR TA spectra (fluence: 2.38 μJ cm^{-2}).

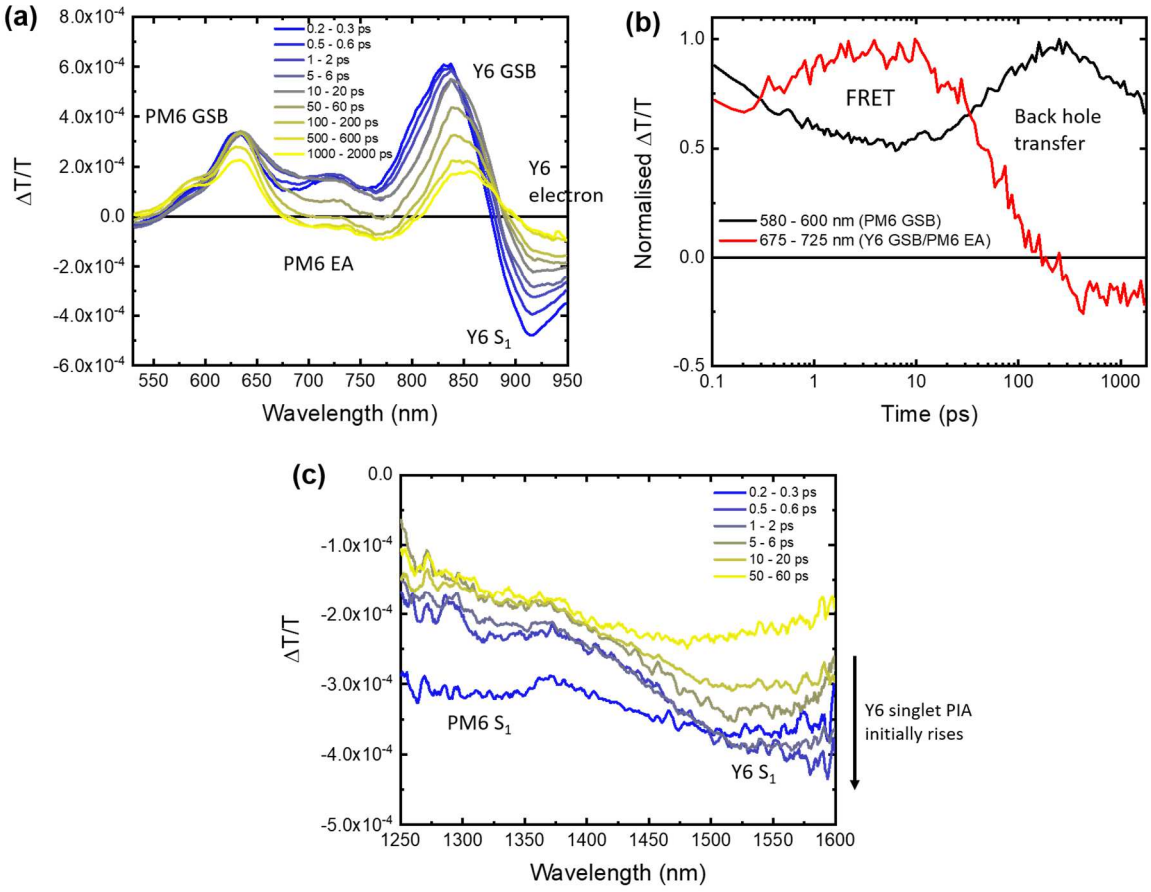

Figure C19. (a) Visible region TA spectra, (b) fitted kinetics of PM6:Y6 52% LMWF blend (pump: 580 nm and fluence: 0.95 μJ cm^{-2}), and (c) Near IR TA spectra (fluence: 3.50 μJ cm^{-2}).

Non-geminate recombination and extraction dynamics

a. V_{OC} vs. ln (intensity) for a qualitative determination the dominant recombination mechanism

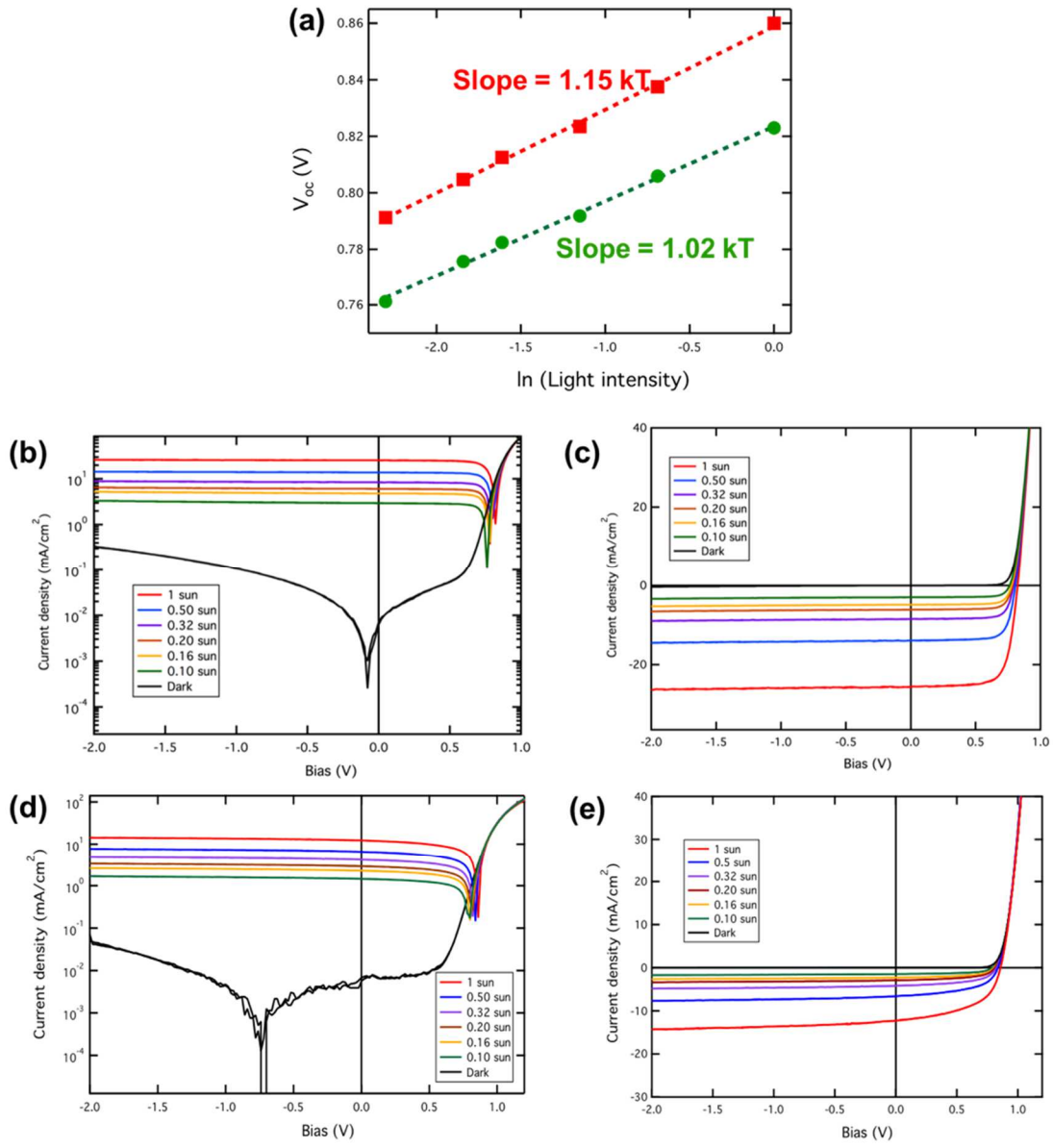

Figure C20. (a) V_{OC} vs. ln(light intensity) plots for the 1% LMWF and 52% LMWF blend systems. *J-V* curves of the two blend systems plotted at varying light intensities on semi-log and linear scale for (a) 1% LMWF and (b) 52% LMWF PM6:Y6 blend systems.

b. Capacitance spectroscopy for determining charge carrier densities

The dielectric constants of the two blends were measured by capacitance spectroscopy at a reverse bias of -3 V and in the dark (**Figure C21**). For this DC bias, there should be no frequency dependence of the capacitance. Then, the assumption is that the capacitance of the blend C_b measured under these conditions is equal to the geometric capacitance C_g, which would allow employing the following equation to calculate the dielectric constant ε_r:

$$\varepsilon_r = \frac{C_g L}{\varepsilon_0 A}, \tag{S1}$$

where L is the thickness of the active layer and A is the area of the device. To begin a quantitative analysis of the recombination dynamics, it is necessary to obtain values for the charge carrier density n. It is known that capacitance spectroscopy can be employed to determine the density of charge carriers in organic solar cells under illumination. Capacitance spectroscopy was performed to yield the charge carrier density n, *via* integration of the chemical capacitance using the following equations:

$$C_{chem} = C_b^{1sun} - C_b^{dark}, \tag{S2}$$

$$n(V_{cor}) = \frac{1}{qAL}\int_{V_{sat}}^{V_{cor}} C_{chem}\, dV_{cor}, \tag{S3}$$

where A is the area of the solar cell, L is the thickness, V_{sat} is the reverse bias at which the photocurrent saturates, and V_0 is the forward bias at which the photocurrent is equal to zero. In this analysis the capacitance in the bulk-heterojunction C_b at the plateau at frequencies of $\omega = 10$ kHz and $\omega = 50$ kHz for the low and high performing devices was chosen. It is assumed that the difference of C_b under illumination and in the dark is related to the density of photogenerated charge carriers (**Figure C21**). Therefore, this difference equates to the chemical capacitance C_{chem}, as described in **Equation S2**.[170] This approach to determine the charge carrier density n does not require the addition of the saturated charge carrier density n_{sat}, in contrast to other approaches commonly used. The charge carrier density n then becomes available once the chemical capacitance is integrated over the voltage (**Figure C22a**).

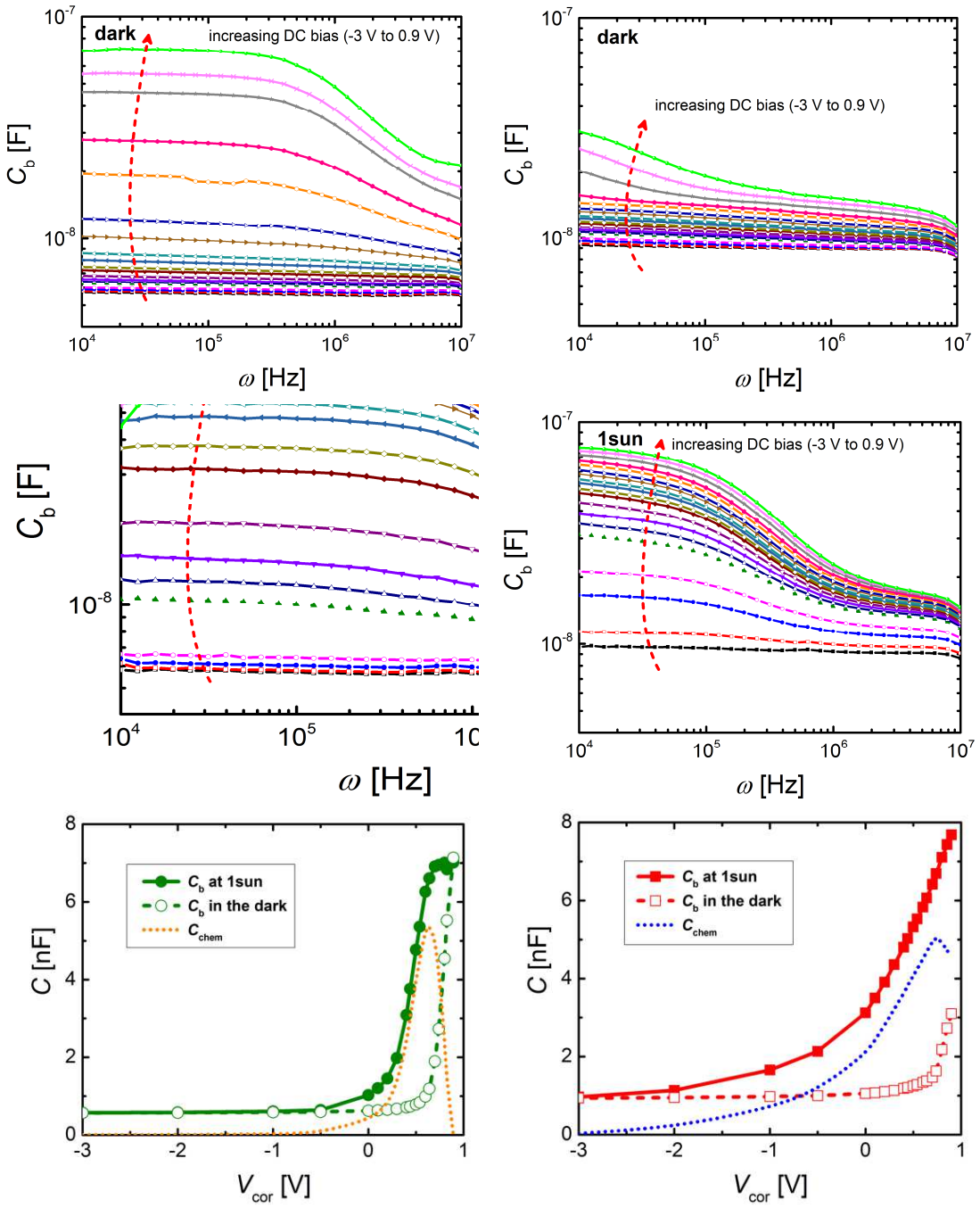

Figure C21. Frequency dependent capacitance in the bulk-heterojunction C_b in the dark and under 1 sun illumination of the solar cells employing the high (LMWF = 1%; left column) and low (LMWF = 52%; right column) performing PM6 batches. The difference between the capacitance C_b at 1 sun illumination and in the dark at a specific frequency (LMWF = 1%: ω = 50 kHz; LMWF = 52%: ω = 10 kHz) is used to calculate the chemical capacitance C_{chem} (orange and blue dots) that is attributed to the photogenerated charge carriers within the bulk-heterojunction.

c. Determining effective mobilities under operating conditions

The calculation of a field and charge carrier dependent, effective mobility $\mu_{eff}(n,V)$ has been introduced by Albrecht *et. al.* as an alternative to the hole/electron mobility $\mu_{p/n}$ determined *via* the Mott-Gurney relationship of space-charge limited currents (SCLC) in single carrier devices.[68] It was argued that mobilities determined *via* SCLC measurements may be unreliable due to deviation from the expected thickness dependent behavior, the variation of electrode materials that may have an impact on the morphology, charge carrier densities and electric-fields that are larger in the SCLC regime in comparison to the normal operating conditions of a solar cell (ultimately leading to overestimated mobilities), and finally the fact that the motion of injected carriers is measured in contrast to photogenerated carriers. The use of such an effective mobility μ_{eff} is especially encouraged, if a strong dependence of the mobility on either the applied bias V, the charge carrier density n, or both can be expected. The effective mobility μ_{eff} can be calculated by employing the following equation:

$$\mu_{eff}(n,V_{cor}) = \frac{J(V_{cor}) \cdot L}{2qn(V_{cor}) \cdot [V_{cor} - V_0]}, \tag{S4}$$

where J is the current density, V_{cor} is the corrected voltage, V_0 is the voltage at which the photocurrent is equal to zero, L is the device thickness, q is the elementary charge, and n is the charge carrier density obtained from capacitance spectroscopy. The effective mobility μ_{eff} ideally relates to the two different types of mobility μ_n and μ_p *via* the following equation:

$$\mu_{eff} = \frac{2\mu_n\mu_p}{\mu_n + \mu_p}. \tag{S5}$$

The effective mobility of the low performing devices is more or less constant over the entire voltage range, as can be seen in **Figure C22b**. In contrast, the high performing devices show a wider variability in the effective mobility values. In the subsequent analysis, the average mean of the determined effective mobility is used.

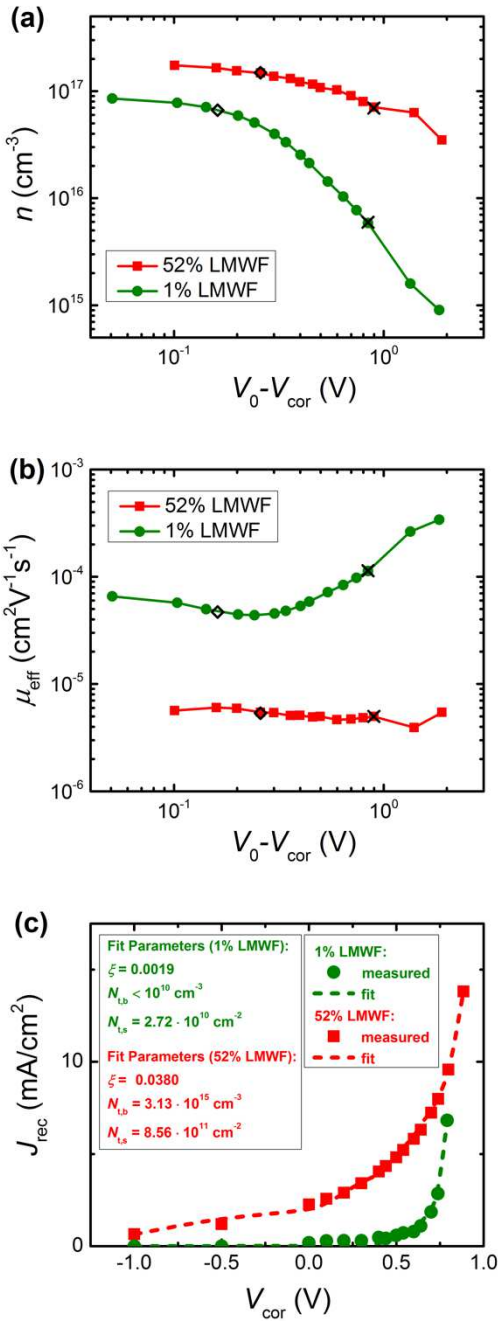

Figure C22. (a) Charge carrier density n and (b) effective mobility μ_{eff} of the solar cells employing the high (LMWF = 1%; left column) and low (LMWF = 52%; right column) performing PM6 batches. Operating conditions of interest are highlighted (black crosses: short-circuit; black logenzes: max-power). (c) Experimentally determined recombination current density J_{rec} (squares and circles) and reconstructed recombination current J_{rec} employing the analytical approach (dotted lines). The required fitting parameters are listed in the inset.

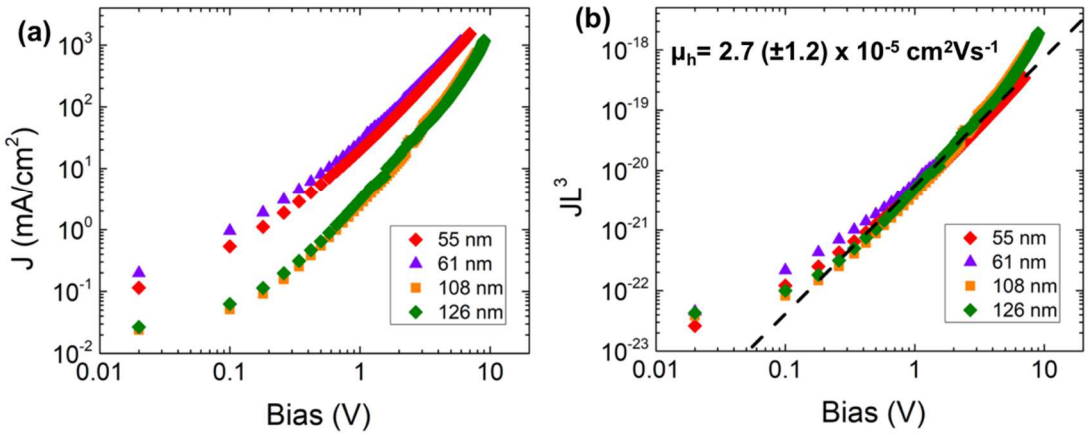

Figure C23. (a) *J-V* curves of hole-only diodes of the 52% LMWF PM6:Y6 blend at different thicknesses measured in the dark. The current density is multiplied by L^3 showing that the thickness dependence requirement for utilizing the SCLC question is satisfied. The hole-only diodes of the 1% LMWF PM6:Y6 blend is reported in previous literature[20] and found to be an order of magnitude higher than the 52% LMWF blend (μ_h = 1.5 (± 0.4) × 10^{-4} cm^2 Vs^{-1}). It should be noted that when plotting the thickness dependence of electron mobilities in the 1% LMWF as discussed in the previous report[20], we found that the thickness-dependence of current expected in utilizing the SCLC equation no longer holds and therefore we will stay away from making comparisons of the electron mobilities in these blends using this technique.

d. Non-geminate Recombination Dynamics

The recombination current density $J_{rec,sum}$ obtained from the *J-V*-curves can be reconstructed by using the following equation:

$$J_{rec,sum} = J_{rec,bm} + J_{rec,bulk} + J_{rec,surf} \quad \text{(S6)}$$

The bimolecular component $J_{rec,bm}$ can be described by the following equation:

$$J_{rec,bm} = qLk_{bm}n^2 = \frac{q^2L}{\varepsilon_0\varepsilon_r}\xi(\mu_n + \mu_p)n^2 \quad \text{(S7)}$$

where k_{bm} is the bimolecular recombination coefficient, ξ is the reduction factor (also known as Langevin prefactor), n is the charge carrier density, and $\mu_{n,p}$ are the electron and hole mobility, respectively. The effective mobility μ_{eff} was used to replace $\mu_{n/p}$. The following expression describes the bulk trap-assisted contribution $J_{rec,bulk}$:

$$J_{rec,bulk} = qLk_{t,b}n = \frac{q^2L}{\varepsilon_0\varepsilon_r}\mu_n N_{t,b} n, \quad \text{(S8)}$$

where $N_{t,b}$ is the density of deep traps in the bulk, and $k_{t,b}$ is the bulk-trap assisted recombination coefficient. Again, the effective mobility μ_{eff} was used. The surface trap-assisted component $J_{rec,surf}$ can be described in a similar way as $J_{rec,bulk}$, with the addition of a field-dependent term:

$$J_{rec,surf} = qLk_{t,s}(V_{cor})n = \frac{q^2}{\varepsilon_0\varepsilon_r} \frac{\mu_p N_{t,s} n}{\exp\left\{\frac{q(V_{bi}-V_{cor})}{kT}\right\}}, \quad \text{(S9)}$$

where $N_{t,s}$ is the density of surface traps, V_{bi} is the built-in voltage, V_{cor} is the corrected voltage, and $k_{t,s}(V_{cor})$ is the surface-trap assisted recombination coefficient. Again, the effective mobility μ_{eff} was used. A detailed description and derivation of this analytical model can be found in Ref 13.[67] Subsequently, it is possible to determine the recombination coefficients as well. All necessary constant parameters, fitting parameters and subsequently determined values are summarized in **Table C5**.

Table C5. Overview and values of constants and variables used in the capacitance spectroscopy analysis and the subsequent investigation of the recombination dynamics.

	PM6:Y6 (1% LMWF)	**PM6:Y6 (52% LMWF)**
A/cm^2	0.22	0.22
L/nm	75	81
ε_r	2.17	3.86
ω/kHz	50	10
V_{bi}/V	0.8417	0.954
V_0/V	0.8415	0.899
V_{sat}/V	-3	-3
μ_{eff}/(cm^{2}V^{-1}s^{-1})	$9.57\cdot10^{-5}$	$5.18\cdot10^{-6}$
ξ	0.0019	0.0380
$N_{t,b}$/(cm^{-3})	$< 1\cdot10^{10}$	$3.13\cdot10^{15}$
$N_{t,s}$/(cm^{-2})	$2.72\cdot10^{10}$	$8.56\cdot10^{11}$
Adj. R^2	0.98805	0.99448
k_{bm}/(cm^{3}s^{-1})	$3.05\cdot10^{-13}$	$1.85\cdot10^{-13}$
$k_{t,b}$/(s^{-1})	0.08	7598.97

Appendix D:

Appendix to Chapter 5

Symmetric J-V curves for different film thicknesses

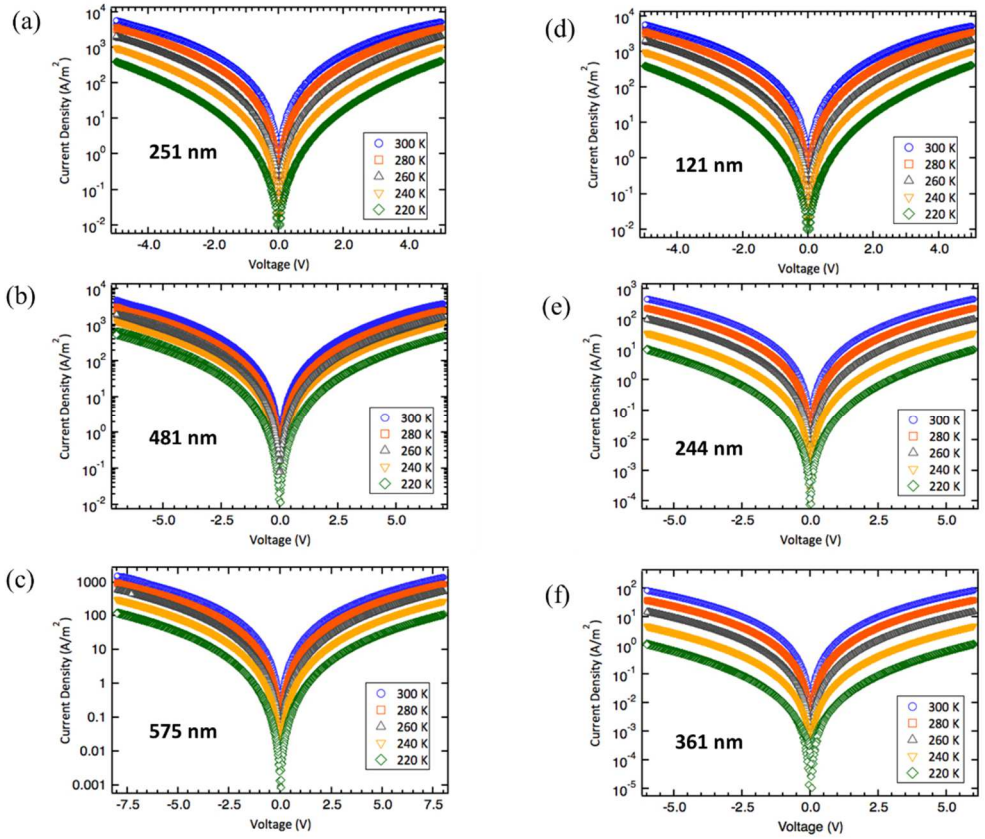

Figure D1. J-V curves of symmetric hole-only diodes for PTB7-Th films of a) 251 nm, b) 481 nm, and c) 575 nm thicknesses and MEH-PPV films of a) 121 nm, b) 244 nm, and c) 361 nm thicknesses with the following device configuration: PEDOT:PSS (35 nm) / Active layer/ MoO_3 (10 nm) /Ag (100 nm).

Temperature-dependent J-V curves and SCLC fits to the current density

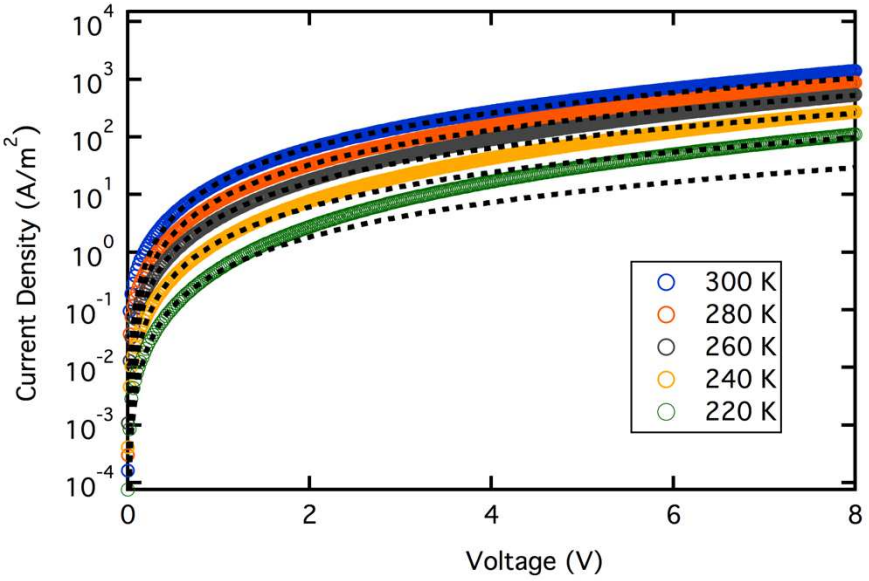

Figure D2. Temperature-dependent J-V curves (solid lines) and fits to the SCLC equation (dotted lines) for a PTB7-Th hole-only diode of 481 nm. The underestimation of current density at higher electric fields and lower temperatures is evident.

Temperature-dependent J-V curves and drift-diffusion calculations for current density for different thickness devices

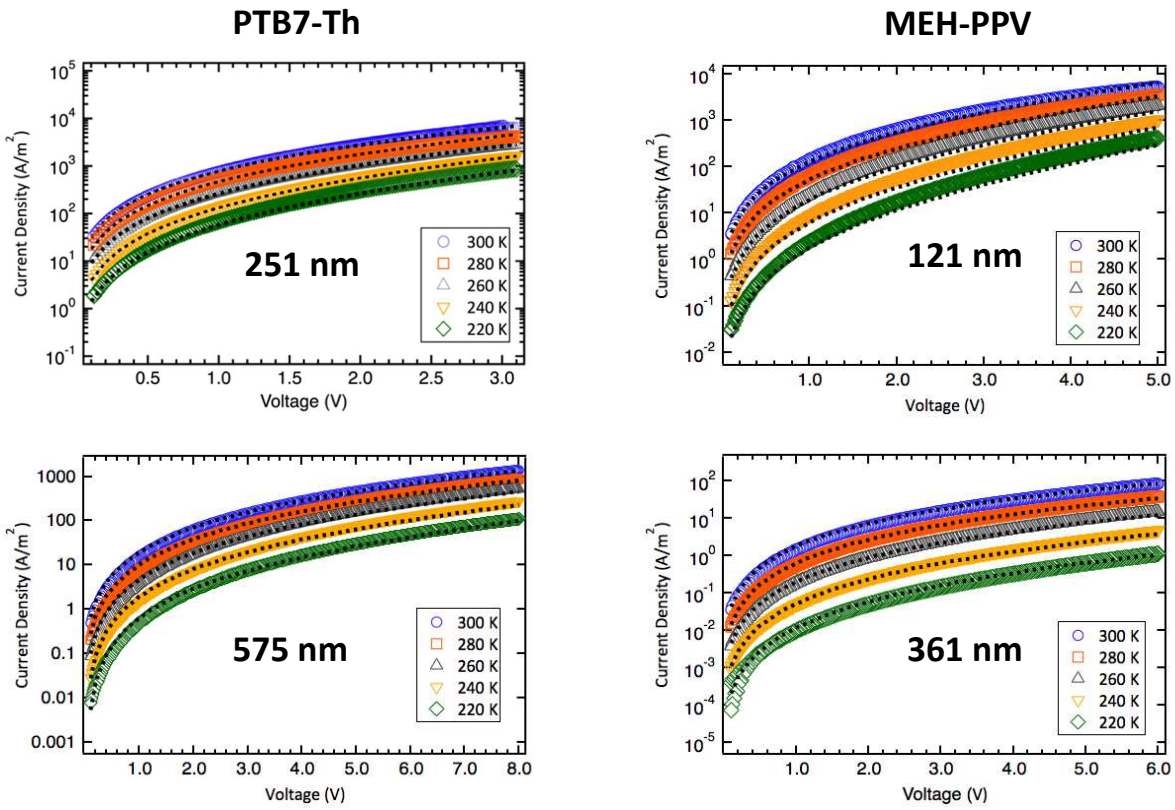

Figure D3. Temperature-dependent J-V curves of PTB7-Th hole-only diodes of thicknesses a) 251 nm and c) 575 nm and MEH-PPV hole-only diodes of thicknesses b) 121 nm and d) 361 nm. The dotted lines are the drift-diffusion calculations for the current densities.

Probing differences in crystallinity by GIWAXS of PTB7-Th and MEH-PPV

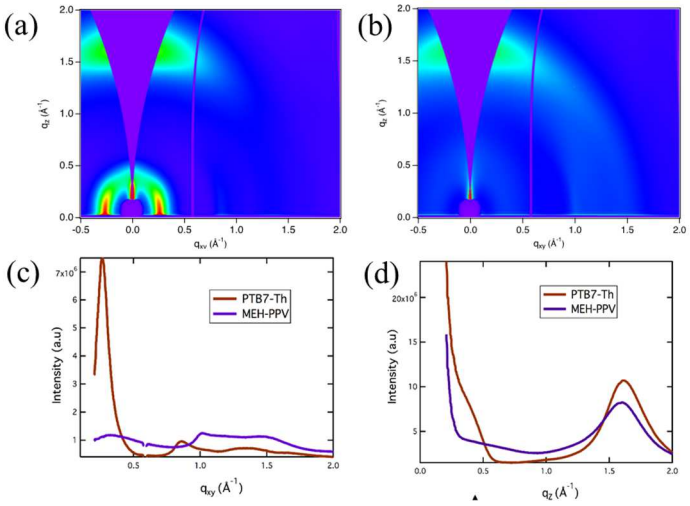

Figure D4. GIWAXS spectra of a) PTB7-Th and b) MEH-PPV films of 100 ± 5 nm thicknesses. Line-cut profiles of GIWAXS measurements of PTB7-Th and MEH-PPV films in the c) in-plane and d) out-of-plane direction.

Table D1. GIWAXS parameters for PTB7-Th and MEH-PPV in the in-plane and out-of plane direction obtained from line-cuts.

Material	Lamellar spacing			π-π stack		
	q_{XY} (Å^{-1})	d-spacing (Å)	L_C(Å)	q_Z (Å^{-1})	d-spacing (Å)	L_C(Å)
PTB7-Th	0.26	23.6	59.4	1.62	3.88	13.8
MEH-PPV	0.33	18.7	26.0	1.59	3.94	12.9

Solid-state NMR analyses of PTB7-Th and MEH-PPV

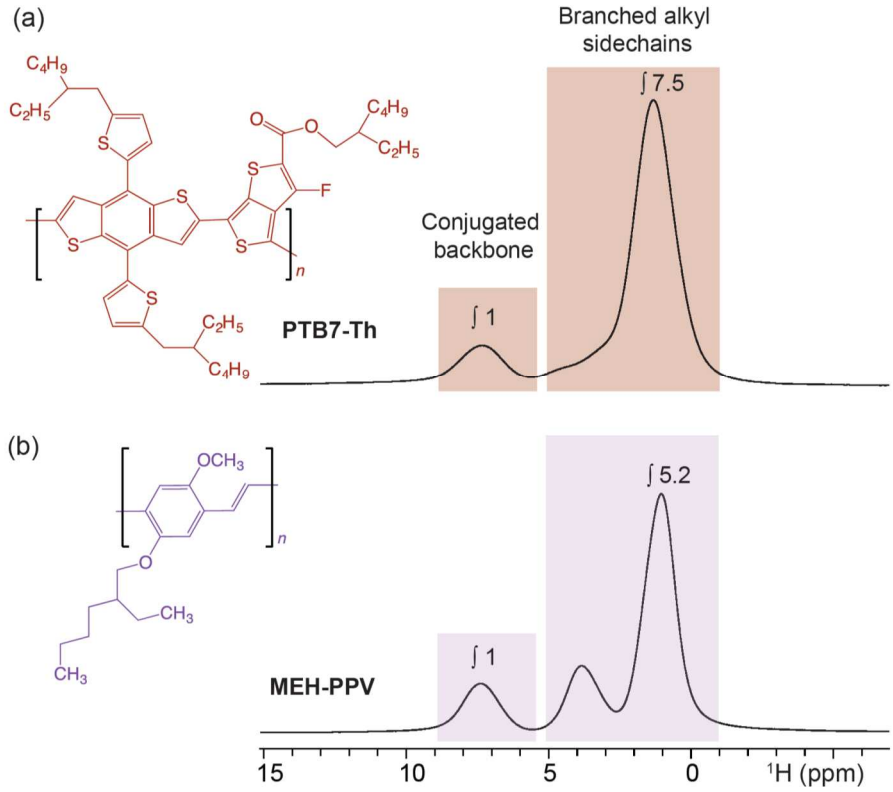

Figure D5. Solid-state ^{1}H MAS NMR spectra of (a) PTB7-Th and (b) MEH-PPV acquired at 11.7 T and at room temperature under 58 kHz MAS depicting the ^{1}H signals of branched alkyl sidechains (0-5 ppm) and aromatic backbone moieties (6-9 ppm).

References:

1. U.S. energy facts explained - consumption and production - U.S. Energy Information Administration (EIA). https://www.eia.gov/energyexplained/us-energy-facts/.
2. US EPA, O. Overview of Greenhouse Gases. *US EPA* https://www.epa.gov/ghgemissions/overview-greenhouse-gases (2015).
3. US EPA, O. Climate Change Indicators: Climate Forcing. *US EPA* https://www.epa.gov/climate-indicators/climate-change-indicators-climate-forcing (2016).
4. USGCRP. Fourth National Climate Assessment. https://nca2018.globalchange.gov (2018).
5. Semi-transparent solar cells could make greenhouses self-sufficient. *New Atlas* https://newatlas.com/energy/semi-transparent-solar-cells-greenhouses-self-sufficient/ (2020).
6. Organic photovoltaic window device generates electricity and blocks heat. *Chemical & Engineering News* https://cen.acs.org/energy/solar-power/Organic-photovoltaic-window-device-generates/96/i28.
7. Wide-gap non-fullerene acceptor enabling high-performance organic photovoltaic cells for indoor applications | Nature Energy. https://www.nature.com/articles/s41560-019-0448-5.
8. Cui, Y. *et al.* Over 16% efficiency organic photovoltaic cells enabled by a chlorinated acceptor with increased open-circuit voltages. *Nature Communications* **10**, 2515 (2019).
9. Fan, B. *et al.* Achieving over 16% efficiency for single-junction organic solar cells. *Science China Chemistry* (2019) doi:10.1007/s11426-019-9457-5.

10. Rau, U. Reciprocity relation between photovoltaic quantum efficiency and electroluminescent emission of solar cells. *Phys. Rev. B* **76**, 085303 (2007).
11. Cui, Y. *et al.* Single-Junction Organic Photovoltaic Cells with Approaching 18% Efficiency. *Advanced Materials* **n/a**, 1908205.
12. Chen, S. *et al.* Efficient Nonfullerene Organic Solar Cells with Small Driving Forces for Both Hole and Electron Transfer. *Adv. Mater. Weinheim* **30**, e1804215 (2018).
13. Liu, J. *et al.* Fast charge separation in a non-fullerene organic solar cell with a small driving force. *Nature Energy* **1**, 16089 (2016).
14. Hou, J., Inganäs, O., Friend, R. H. & Gao, F. Organic solar cells based on non-fullerene acceptors. *Nature Materials* **17**, 119–128 (2018).
15. Qian, D. *et al.* Design rules for minimizing voltage losses in high-efficiency organic solar cells. *Nature Materials* **17**, 703 (2018).
16. Ran, N. A. *et al.* Charge Generation and Recombination in an Organic Solar Cell with Low Energetic Offsets. *Advanced Energy Materials* **8**, 1701073 (2018).
17. Ran, N. A. *et al.* Harvesting the Full Potential of Photons with Organic Solar Cells. *Advanced Materials* **28**, 1482–1488 (2016).
18. Kawashima, K., Tamai, Y., Ohkita, H., Osaka, I. & Takimiya, K. High-efficiency polymer solar cells with small photon energy loss. *Nature Communications* **6**, (2015).
19. Eisner, F. D. *et al.* Hybridization of Local Exciton and Charge-Transfer States Reduces Nonradiative Voltage Losses in Organic Solar Cells. *J. Am. Chem. Soc.* **141**, 6362–6374 (2019).

20. Karki, A. *et al.* Understanding the High Performance of over 15% Efficiency in Single-Junction Bulk Heterojunction Organic Solar Cells. *Advanced Materials* **31**, 1903868 (2019).

21. Baran, D. *et al.* Reduced voltage losses yield 10% efficient fullerene free organic solar cells with >1 V open circuit voltages. *Energy Environ. Sci.* **9**, 3783–3793 (2016).

22. Zhao, W. *et al.* Fullerene-Free Polymer Solar Cells with over 11% Efficiency and Excellent Thermal Stability. *Adv. Mater. Weinheim* **28**, 4734–4739 (2016).

23. Baran, D. *et al.* Robust nonfullerene solar cells approaching unity external quantum efficiency enabled by suppression of geminate recombination. *Nature Communications* **9**, 1–9 (2018).

24. Tan, C.-H. *et al.* Barbiturate end-capped non-fullerene acceptors for organic solar cells: tuning acceptor energetics to suppress geminate recombination losses. *Chemical Communications* **54**, 2966–2969 (2018).

25. Perdigón□Toro, L. *et al.* Barrierless Free Charge Generation in the High-Performance PM6:Y6 Bulk Heterojunction Non-Fullerene Solar Cell. *Advanced Materials* **32**, 1906763 (2020).

26. Göhler, C., Wagenpfahl, A. & Deibel, C. Nongeminate Recombination in Organic Solar Cells. *Advanced Electronic Materials* **4**, 1700505 (2018).

27. Cha, H. *et al.* Influence of Blend Morphology and Energetics on Charge Separation and Recombination Dynamics in Organic Solar Cells Incorporating a Nonfullerene Acceptor. *Advanced Functional Materials* **28**, 1704389 (2018).

28. Heiber, M. C. *et al.* Measuring the competition between bimolecular charge recombination and charge transport in organic solar cells under operating conditions. *Energy Environ. Sci.* **11**, 3019–3032 (2018).

29. Bartesaghi, D. *et al.* Competition between recombination and extraction of free charges determines the fill factor of organic solar cells. *Nature Communications* **6**, 7083 (2015).

30. Selter, P. & Hansen, M. R. Chapter 16:Molecular Chain Packing and Conformation in π-Conjugated Polymers from Solid-state NMR. in *NMR Methods for Characterization of Synthetic and Natural Polymers* 363–386 (2019). doi:10.1039/9781788016483-00363.

31. Ye, L. *et al.* Quantitative relations between interaction parameter, miscibility and function in organic solar cells. *Nature Materials* **17**, 253 (2018).

32. Burkhard, G. F., Hoke, E. T. & McGehee, M. D. Accounting for Interference, Scattering, and Electrode Absorption to Make Accurate Internal Quantum Efficiency Measurements in Organic and Other Thin Solar Cells. *Advanced Materials* **22**, 3293–3297 (2010).

33. Koster, L. J. A., Mihailetchi, V. D., Ramaker, R. & Blom, P. W. M. Light intensity dependence of open-circuit voltage of polymer:fullerene solar cells. *Appl. Phys. Lett.* **86**, 123509 (2005).

34. Proctor, C. M., Kuik, M. & Nguyen, T.-Q. Charge carrier recombination in organic solar cells. *Progress in Polymer Science* **38**, 1941–1960 (2013).

35. Proctor, C. M. & Nguyen, T.-Q. Effect of leakage current and shunt resistance on the light intensity dependence of organic solar cells. *Appl. Phys. Lett.* **106**, 083301 (2015).

36. Vandewal, K., Benduhn, J. & C. Nikolis, V. How to determine optical gaps and voltage losses in organic photovoltaic materials. *Sustainable Energy & Fuels* **2**, 538–544 (2018).

37. Vandewal, K., Tvingstedt, K., Gadisa, A., Inganäs, O. & Manca, J. V. Relating the open-circuit voltage to interface molecular properties of donor:acceptor bulk heterojunction solar cells. *Phys. Rev. B* **81**, 125204 (2010).

38. Menke, S. M. *et al.* Limits for Recombination in a Low Energy Loss Organic Heterojunction. *ACS Nano* **10**, 10736–10744 (2016).

39. Ran, N. A. *et al.* Impact of interfacial molecular orientation on radiative recombination and charge generation efficiency. *Nature Communications* **8**, 79 (2017).

40. Tuladhar, S. M. *et al.* Low Open-Circuit Voltage Loss in Solution-Processed Small-Molecule Organic Solar Cells. *ACS Energy Lett.* **1**, 302–308 (2016).

41. Rosenthal, K. D. *et al.* Quantifying and Understanding Voltage Losses Due to Nonradiative Recombination in Bulk Heterojunction Organic Solar Cells with Low Energetic Offsets. *Advanced Energy Materials* **9**, 1901077 (2019).

42. Babics, M. *et al.* Negligible Energy Loss During Charge Generation in Small-Molecule/Fullerene Bulk-Heterojunction Solar Cells Leads to Open-Circuit Voltage over 1.10 V. *ACS Appl. Energy Mater.* **2**, 2717–2722 (2019).

43. Burke, T. M., Sweetnam, S., Vandewal, K. & McGehee, M. D. Beyond Langevin Recombination: How Equilibrium Between Free Carriers and Charge Transfer States Determines the Open-Circuit Voltage of Organic Solar Cells. *Advanced Energy Materials* **5**, 1500123 (2015).

44. Nikolis, V. C. *et al.* Strong light-matter coupling for reduced photon energy losses in organic photovoltaics. *Nat Commun* **10**, 1–8 (2019).

45. Shockley, W. & Queisser, H. J. Detailed Balance Limit of Efficiency of p-n Junction Solar Cells. *Journal of Applied Physics* **32**, 510–519 (1961).

46. Benduhn, J. *et al.* Intrinsic non-radiative voltage losses in fullerene-based organic solar cells. *Nature Energy* **2**, 17053 (2017).

47. Ullbrich, S. *et al.* Emissive and charge-generating donor–acceptor interfaces for organic optoelectronics with low voltage losses. *Nature Materials* **18**, 459 (2019).

48. Chen, X.-K., Ravva, M. K., Li, H., Ryno, S. M. & Brédas, J.-L. Effect of Molecular Packing and Charge Delocalization on the Nonradiative Recombination of Charge-Transfer States in Organic Solar Cells. *Advanced Energy Materials* **6**, 1601325 (2016).

49. Vandewal, K., Tvingstedt, K. & Inganäs, O. Polarization anisotropy of charge transfer absorption and emission of aligned polymer:fullerene blend films. *Phys. Rev. B* **86**, 035212 (2012).

50. Bixon, M., Jortner, J. & Verhoeven, J. W. Lifetimes for Radiative Charge Recombination in Donor-Acceptor Molecules. *J. Am. Chem. Soc.* **116**, 7349–7355 (1994).

51. Nádaždy, V., Schauer, F. & Gmucová, K. Energy resolved electrochemical impedance spectroscopy for electronic structure mapping in organic semiconductors. *Appl. Phys. Lett.* **105**, 142109 (2014).

52. Schauer, F. *et al.* Electronic structure of UV degradation defects in polysilanes studied by Energy Resolved – Electrochemical Impedance Spectroscopy. *Polymer Degradation and Stability* **126**, 204–208 (2016).

53. Karki, A. *et al.* Unifying Energetic Disorder from Charge Transport and Band Bending in Organic Semiconductors. *Advanced Functional Materials* **29**, 1901109 (2019).

54. Collins, S. D., Proctor, C. M., Ran, N. A. & Nguyen, T.-Q. Understanding Open-Circuit Voltage Loss through the Density of States in Organic Bulk Heterojunction Solar Cells. *Advanced Energy Materials* **6**, 1501721 (2016).

55. Venkateshvaran, D. *et al.* Approaching disorder-free transport in high-mobility conjugated polymers. *Nature* **515**, 384–388 (2014).

56. Hood, S., Zarrabi, N., Meredith, P., Kassal, I. & Armin, A. Measuring Energetic Disorder in Organic Semiconductors Using the Photogenerated Charge-Separation Efficiency. *J. Phys. Chem. Lett.* **10**, 3863–3870 (2019).

57. Englman, R. & Jortner, J. The energy gap law for radiationless transitions in large molecules. *Molecular Physics* **18**, 145–164 (1970).

58. Ziffer, M. E. *et al.* Long-Lived, Non-Geminate, Radiative Recombination of Photogenerated Charges in a Polymer/Small-Molecule Acceptor Photovoltaic Blend. *J. Am. Chem. Soc.* **140**, 9996–10008 (2018).

59. Zhong, Y. *et al.* Molecular helices as electron acceptors in high-performance bulk heterojunction solar cells. *Nat Commun* **6**, 1–8 (2015).

60. Tamai, Y. *et al.* Ultrafast Long-Range Charge Separation in Nonfullerene Organic Solar Cells. *ACS Nano* **11**, 12473–12481 (2017).

61. Gélinas, S. *et al.* Ultrafast long-range charge separation in organic semiconductor photovoltaic diodes. *Science* **343**, 512–516 (2014).

62. Gautam, B. R., Younts, R., Carpenter, J., Ade, H. & Gundogdu, K. The Role of FRET in Non-Fullerene Organic Solar Cells: Implications for Molecular Design. *J. Phys. Chem. A* **122**, 3764–3771 (2018).

63. Kyaw, A. K. K. *et al.* Improved Light Harvesting and Improved Efficiency by Insertion of an Optical Spacer (ZnO) in Solution-Processed Small-Molecule Solar Cells. *Nano Lett.* **13**, 3796–3801 (2013).

64. Brus, V. V. Light dependent open-circuit voltage of organic bulk heterojunction solar cells in the presence of surface recombination. *Organic Electronics* **29**, 1–6 (2016).

65. Brus, V. V., Proctor, C. M., Ran, N. A. & Nguyen, T.-Q. Capacitance Spectroscopy for Quantifying Recombination Losses in Nonfullerene Small-Molecule Bulk Heterojunction Solar Cells. *Advanced Energy Materials* **6**, 1502250 (2016).

66. Proctor, C. M., Kim, C., Neher, D. & Nguyen, T.-Q. Nongeminate Recombination and Charge Transport Limitations in Diketopyrrolopyrrole-Based Solution-Processed Small Molecule Solar Cells. *Advanced Functional Materials* **23**, 3584–3594 (2013).

67. Vollbrecht, J. *et al.* Quantifying the Nongeminate Recombination Dynamics in Nonfullerene Bulk Heterojunction Organic Solar Cells. *Advanced Energy Materials* **9**, 1901438 (2019).

68. Albrecht, S. *et al.* Quantifying Charge Extraction in Organic Solar Cells: The Case of Fluorinated PCPDTBT. *J. Phys. Chem. Lett.* **5**, 1131–1138 (2014).

69. Rand, B. P. *et al.* The Impact of Molecular Orientation on the Photovoltaic Properties of a Phthalocyanine/Fullerene Heterojunction. *Advanced Functional Materials* **22**, 2987–2995 (2012).

70. Mukherjee, S., Proctor, C. M., Bazan, G. C., Nguyen, T.-Q. & Ade, H. Significance of Average Domain Purity and Mixed Domains on the Photovoltaic Performance of High-Efficiency Solution-Processed Small-Molecule BHJ Solar Cells. *Advanced Energy Materials* **5**, 1500877 (2015).

71. Burke, T. M. & McGehee, M. D. How High Local Charge Carrier Mobility and an Energy Cascade in a Three-Phase Bulk Heterojunction Enable >90% Quantum Efficiency. *Advanced Materials* **26**, 1923–1928 (2014).

72. Yi, Y., Coropceanu, V. & Brédas, J.-L. Exciton-Dissociation and Charge-Recombination Processes in Pentacene/C60 Solar Cells: Theoretical Insight into the Impact of Interface Geometry. *J. Am. Chem. Soc.* **131**, 15777–15783 (2009).

73. Liu, Y. *et al.* Aggregation and morphology control enables multiple cases of high-efficiency polymer solar cells. *Nat Commun* **5**, 1–8 (2014).

74. Collins, B. A. *et al.* Absolute Measurement of Domain Composition and Nanoscale Size Distribution Explains Performance in PTB7:PC71BM Solar Cells. *Advanced Energy Materials* **3**, 65–74 (2013).

75. Ye, L. *et al.* Quenching to the Percolation Threshold in Organic Solar Cells. *Joule* **3**, 443–458 (2019).

76. Alla, M. & Lippmaa, E. Resolution limits in magic-angle rotation NMR spectra of polycrystalline solids. *Chemical Physics Letters* **87**, 30–33 (1982).

77. Robbins, A. J. *et al.* Combining insights from solid-state NMR and first principles calculation: applications to the 19F NMR of octafluoronaphthalene. *Phys. Chem. Chem. Phys.* **9**, 2389–2396 (2007).

78. Hanrahan, M. P. *et al.* Enhancing the resolution of 1H and 13C solid-state NMR spectra by reduction of anisotropic bulk magnetic susceptibility broadening. *Phys. Chem. Chem. Phys.* **19**, 28153–28162 (2017).

79. Barich, D. H., Davis, J. M., Schieber, L. J., Zell, M. T. & Munson, E. J. Investigation of solid-state NMR line widths of ibuprofen in drug formulations. *Journal of Pharmaceutical Sciences* **95**, 1586–1594 (2006).

80. Melnyk, A. *et al.* Macroscopic Structural Compositions of π-Conjugated Polymers: Combined Insights from Solid-State NMR and Molecular Dynamics Simulations. *J. Phys. Chem. Lett.* **8**, 4155–4160 (2017).

81. Hansen, M. R., Graf, R. & Spiess, H. W. Interplay of Structure and Dynamics in Functional Macromolecular and Supramolecular Systems As Revealed by Magnetic Resonance Spectroscopy. *Chem. Rev.* **116**, 1272–1308 (2016).

82. Chaudhari, S. R. *et al.* Donor–acceptor stacking arrangements in bulk and thin-film high-mobility conjugated polymers characterized using molecular modelling and MAS and surface-enhanced solid-state NMR spectroscopy. *Chem. Sci.* **8**, 3126–3136 (2017).

83. Saalwächter, K. & Spiess, H. W. Solid-State NMR of Polymers. *Polymer Science: A Comprehensive Reference* 185–219 (2012).

84. Dudenko, D. *et al.* A strategy for revealing the packing in semicrystalline π-conjugated polymers: crystal structure of bulk poly-3-hexyl-thiophene (P3HT). *Angew. Chem. Int. Ed. Engl.* **51**, 11068–11072 (2012).

85. Schnell, I. & Spiess, H. W. High-resolution 1H NMR spectroscopy in the solid state: very fast sample rotation and multiple-quantum coherences. *J. Magn. Reson.* **151**, 153–227 (2001).

86. Feike, M. *et al.* Broadband Multiple-Quantum NMR Spectroscopy. *Journal of Magnetic Resonance, Series A* **122**, 214–221 (1996).

87. Hansen, M. R., Graf, R. & Spiess, H. W. Solid-State NMR in Macromolecular Systems: Insights on How Molecular Entities Move. *Acc. Chem. Res.* **46**, 1996–2007 (2013).

88. Nieuwendaal, R. C., Snyder, C. R. & DeLongchamp, D. M. Measuring Order in Regioregular Poly(3-hexylthiophene) with Solid-State 13C CPMAS NMR. *ACS Macro Lett.* **3**, 130–135 (2014).

89. Nieuwendaal, R. Chapter 15:Solid-state NMR of Organic Electronics. in *NMR Methods for Characterization of Synthetic and Natural Polymers* 325–362 (2019). doi:10.1039/9781788016483-00325.

90. Ivanir□Dabora, H., Nimerovsky, E., Madhu, P. K. & Goldbourt, A. Site-Resolved Backbone and Side-Chain Intermediate Dynamics in a Carbohydrate-Binding Module Protein Studied by Magic-Angle Spinning NMR Spectroscopy. *Chemistry – A European Journal* **21**, 10778–10785 (2015).

91. deAzevedo, E. R. *et al.* Intermediate motions as studied by solid-state separated local field NMR experiments. *J Chem Phys* **128**, 104505 (2008).

92. Schäler, K., Achilles, A., Bärenwald, R., Hackel, C. & Saalwächter, K. Dynamics in Crystallites of Poly(ε-caprolactone) As Investigated by Solid-State NMR. *Macromolecules* **46**, 7818–7825 (2013).

93. Straasø, L. A., Saleem, Q. & Hansen, M. R. Chapter Six - A Toolbox of Solid-State NMR Experiments for the Characterization of Soft Organic Nanomaterials. in *Annual Reports on NMR Spectroscopy* (ed. Webb, G. A.) vol. 88 307–383 (Academic Press, 2016).

94. Lee, J. *et al.* Design of Nonfullerene Acceptors with Near□Infrared Light Absorption Capabilities. *Advanced Energy Materials* **8**, 1801209 (2018).

95. Yao, H. *et al.* Design and Synthesis of a Low Bandgap Small Molecule Acceptor for Efficient Polymer Solar Cells. *Advanced Materials* **28**, 8283–8287 (2016).

96. Yao, H. *et al.* Design, Synthesis, and Photovoltaic Characterization of a Small Molecular Acceptor with an Ultra-Narrow Band Gap. *Angewandte Chemie International Edition* **56**, 3045–3049 (2017).

97. Pettersson, L. A. A., Roman, L. S. & Inganäs, O. Modeling photocurrent action spectra of photovoltaic devices based on organic thin films. *Journal of Applied Physics* **86**, 487–496 (1999).

98. Chen, C.-W. *et al.* Optical properties of organometal halide perovskite thin films and general device structure design rules for perovskite single and tandem solar cells. *J. Mater. Chem. A* **3**, 9152–9159 (2015).

99. Rakić, A. D. Algorithm for the determination of intrinsic optical constants of metal films: application to aluminum. *Appl. Opt., AO* **34**, 4755–4767 (1995).

100. Gann, E. *et al.* Soft x-ray scattering facility at the Advanced Light Source with real-time data processing and analysis. *Review of Scientific Instruments* **83**, 045110 (2012).

101. Apperley, D., Harris, R. & Hodgkinson, P. *Solid-State NMR: Basic Principles & Practice*. (Momentum Press, 2012). doi:10.5643/9781606503522.

102. Harris, R. K. *et al.* Further Conventions for NMR shielding and chemical shifts (IUPAC recommendations 2008). *Magnetic Resonance in Chemistry* **46**, 582–598 (2008).

103. Feike, M. *et al.* Broadband multiple-quantum NMR spectroscopy. *Journal of Magnetic Resonance - Series A* **122**, 214–221 (1996).

104. Schnell, I. & Spiess, W. H. High-resolution1H NMR spectroscopy in the solid state: Very fast sample rotation and multiple-quantum coherences. *Journal of Magnetic Resonance* **151**, 153–227 (2001).

105. Saalwächter, K., Lange, F., Matyjaszewski, K., Huang, C. F. & Graf, R. BaBa-xy16: Robust and broadband homonuclear DQ recoupling for applications in rigid and soft solids up to the highest MAS frequencies. *Journal of Magnetic Resonance* **212**, 204–215 (2011).

106. Ivanir-Dabora, H., Nimerovsky, E., Madhu, P. K. & Goldbourt, A. Site-Resolved Backbone and Side-Chain Intermediate Dynamics in a Carbohydrate-Binding Module Protein Studied by Magic-Angle Spinning NMR Spectroscopy. *Chemistry - A European Journal* **21**, 10778–10785 (2015).

107. Hackel, C. *et al.* The trehalose coating effect on the internal protein dynamics. *Physical Chemistry Chemical Physics* **14**, 2727–2734 (2012).

108. Baran, D. *et al.* Reduced voltage losses yield 10% efficient fullerene free organic solar cells with >1 V open circuit voltages. *Energy Environ. Sci.* **9**, 3783–3793 (2016).

109. Sun, C. *et al.* A low cost and high performance polymer donor material for polymer solar cells. *Nat Commun* **9**, 743 (2018).

110. Han, G. & Yi, Y. Local Excitation/Charge-Transfer Hybridization Simultaneously Promotes Charge Generation and Reduces Nonradiative Voltage Loss in Nonfullerene Organic Solar Cells. *J. Phys. Chem. Lett.* 2911–2918 (2019) doi:10.1021/acs.jpclett.9b00928.

111. Yuan, J. *et al.* Single-Junction Organic Solar Cell with over 15% Efficiency Using Fused-Ring Acceptor with Electron-Deficient Core. *Joule* **3**, 1140–1151 (2019).

112. Rosenthal, K. D. *et al.* Quantifying and Understanding Voltage Losses Due to Nonradiative Recombination in Bulk Heterojunction Organic Solar Cells with Low Energetic Offsets. *Advanced Energy Materials* **0**, 1901077.

113. Vandewal, K., Tvingstedt, K., Gadisa, A., Inganäs, O. & Manca, J. V. On the origin of the open-circuit voltage of polymer-fullerene solar cells. *Nat Mater* **8**, 904–909 (2009).

114. Rau, U., Paetzold, U. W. & Kirchartz, T. Thermodynamics of light management in photovoltaic devices. *Phys. Rev. B* **90**, 035211 (2014).

115. Vollbrecht, J., Wiebeler, C., Bock, H., Schumacher, S. & Kitzerow, H.-S. Curved Polar Dibenzocoronene Esters and Imides versus Their Planar Centrosymmetric Homologs: Photophysical and Optoelectronic Analysis. *J. Phys. Chem. C* **123**, 4483–4492 (2019).

116. Koster, L. J. A., Mihailetchi, V. D., Xie, H. & Blom, P. W. M. Origin of the light intensity dependence of the short-circuit current of polymer/fullerene solar cells. *Appl. Phys. Lett.* **87**, 203502 (2005).

117. Cowan, S. R., Banerji, N., Leong, W. L. & Heeger, A. J. Charge Formation, Recombination, and Sweep-Out Dynamics in Organic Solar Cells. *Advanced Functional Materials* **22**, 1116–1128 (2012).

118. Vollbrecht, J. *et al.* Quantifying the Nongeminate Recombination Dynamics in Nonfullerene Bulk Heterojunction Organic Solar Cells. *Advanced Energy Materials* **0**, 1901438.

119. Brus, V. V. *et al.* Solution-Processed Semitransparent Organic Photovoltaics: From Molecular Design to Device Performance. *Advanced Materials* **0**, 1900904.

120. Poindexter, E. H., Caplan, P. J., Deal, B. E. & Razouk, R. R. Interface states and electron spin resonance centers in thermally oxidized (111) and (100) silicon wafers. *Journal of Applied Physics* **52**, 879–884 (1981).

121. Baran, D. *et al.* Reduced voltage losses yield 10% efficient fullerene free organic solar cells with >1 V open circuit voltages. *Energy & Environmental Science* **9**, 3783–3793 (2016).

122. Liang, R.-Z. *et al.* Higher Mobility and Carrier Lifetimes in Solution-Processable Small-Molecule Ternary Solar Cells with 11% Efficiency. *Advanced Energy Materials* **9**, 1802836 (2019).

123. Armin, A. *et al.* Reduced Recombination in High Efficiency Molecular Nematic Liquid Crystalline: Fullerene Solar Cells. *Advanced Energy Materials* **6**, 1600939 (2016).

124. Zaban, A., Greenshtein, M. & Bisquert, J. Determination of the Electron Lifetime in Nanocrystalline Dye Solar Cells by Open-Circuit Voltage Decay Measurements. *ChemPhysChem* **4**, 859–864 (2003).

125. Love, J. A. *et al.* Film Morphology of High Efficiency Solution-Processed Small-Molecule Solar Cells. *Advanced Functional Materials* **23**, 5019–5026 (2013).

126. Love, J. A. *et al.* Silaindacenodithiophene-Based Molecular Donor: Morphological Features and Use in the Fabrication of Compositionally Tolerant, High-Efficiency Bulk Heterojunction Solar Cells. *J. Am. Chem. Soc.* **136**, 3597–3606 (2014).

127. Dang, X.-D. *et al.* Nanostructure and Optoelectronic Characterization of Small Molecule Bulk Heterojunction Solar Cells by Photoconductive Atomic Force Microscopy. *Advanced Functional Materials* **20**, 3314–3321 (2010).

128. Xu, X. *et al.* Thermally stable, highly efficient, ultraflexible organic photovoltaics. *PNAS* 201801187 (2018) doi:10.1073/pnas.1801187115.

129. Guide, M., Dang, X.-D. & Nguyen, T.-Q. Nanoscale characterization of tetrabenzoporphyrin and fullerene-based solar cells by photoconductive atomic force microscopy. *Adv. Mater. Weinheim* **23**, 2313–2319 (2011).

130. Lee, J. *et al.* Bandgap Narrowing in Non-Fullerene Acceptors: Single Atom Substitution Leads to High Optoelectronic Response Beyond 1000 nm. *Advanced Energy Materials* **0**, 1801212.

131. Proctor, C. M., Albrecht, S., Kuik, M., Neher, D. & Nguyen, T.-Q. Overcoming Geminate Recombination and Enhancing Extraction in Solution-Processed Small Molecule Solar Cells. *Advanced Energy Materials* **4**, 1400230 (2014).

132. Walker, B. *et al.* Nanoscale Phase Separation and High Photovoltaic Efficiency in Solution-Processed, Small-Molecule Bulk Heterojunction Solar Cells. *Advanced Functional Materials* **19**, 3063–3069 (2009).

133. Miller, N. C. *et al.* Use of X-Ray Diffraction, Molecular Simulations, and Spectroscopy to Determine the Molecular Packing in a Polymer-Fullerene Bimolecular Crystal. *Advanced Materials* **24**, 6071–6079 (2012).

134. Vohra, V. *et al.* Efficient inverted polymer solar cells employing favourable molecular orientation. *Nature Photonics* **9**, 403–408 (2015).

135. Tumbleston, J. R. *et al.* The influence of molecular orientation on organic bulk heterojunction solar cells. *Nature Photonics* **8**, 385–391 (2014).

136. Yang, B. *et al.* Impact of Electron Delocalization on the Nature of the Charge-Transfer States in Model Pentacene/C60 Interfaces: A Density Functional Theory Study. *J. Phys. Chem. C* **118**, 27648–27656 (2014).

137. Nieuwendaal, R. C. *et al.* Characterization of Interfacial Structure in Polymer-Fullerene Bulk Heterojunctions via $^{13}\mathrm{C}$ ${^{2}\mathrm{H}}$ Rotational Echo Double Resonance NMR. *Phys. Rev. Lett.* **121**, 026101 (2018).

138. Karki, A. *et al.* Unifying Energetic Disorder from Charge Transport and Band Bending in Organic Semiconductors. *Advanced Functional Materials* **0**, 1901109.

139. Seifrid, M. T., Reddy, G. N. M., Zhou, C., Chmelka, B. F. & Bazan, G. C. Direct Observation of the Relationship between Molecular Topology and Bulk Morphology for a π-Conjugated Material. *J. Am. Chem. Soc.* **141**, 5078–5082 (2019).

140. Graham, K. R. *et al.* Importance of the Donor:Fullerene Intermolecular Arrangement for High-Efficiency Organic Photovoltaics. *J. Am. Chem. Soc.* **136**, 9608–9618 (2014).

141. Elena, B., Pintacuda, G., Mifsud, N. & Emsley, L. Molecular Structure Determination in Powders by NMR Crystallography from Proton Spin Diffusion. *J. Am. Chem. Soc.* **128**, 9555–9560 (2006).

142. Reddy, G. N. M., Kumar, M. V. V., Row, T. N. G. & Suryaprakash, N. N–H···F hydrogen bonds in fluorinated benzanilides: NMR and DFT study. *Phys. Chem. Chem. Phys.* **12**, 13232–13237 (2010).

143. Reddy, G. N. M. *et al.* Co-existence of Distinct Supramolecular Assemblies in Solution and in the Solid State. *Chemistry* **23**, 2315–2322 (2017).

144. Liu, Q. *et al.* 18% Efficiency organic solar cells. *Science Bulletin* **65**, 272–275 (2020).

145. Wadsworth, A. *et al.* Progress in Poly (3-Hexylthiophene) Organic Solar Cells and the Influence of Its Molecular Weight on Device Performance. *Advanced Energy Materials* **8**, 1801001 (2018).

146. F. Hoefler, S. *et al.* The effect of polymer molecular weight on the performance of PTB7-Th:O-IDTBR non-fullerene organic solar cells. *Journal of Materials Chemistry A* **6**, 9506–9516 (2018).

147. Li, S., Li, C.-Z., Shi, M. & Chen, H. New Phase for Organic Solar Cell Research: Emergence of Y-Series Electron Acceptors and Their Perspectives. *ACS Energy Lett.* 1554–1567 (2020) doi:10.1021/acsenergylett.0c00537.

148. Zhu, L. *et al.* Efficient Organic Solar Cell with 16.88% Efficiency Enabled by Refined Acceptor Crystallization and Morphology with Improved Charge Transfer and Transport Properties. *Advanced Energy Materials* **n/a**, 1904234.

149. Collins, S. D., Ran, N. A., Heiber, M. C. & Nguyen, T.-Q. Small is Powerful: Recent Progress in Solution-Processed Small Molecule Solar Cells. *Adv. Energy Mater.* **7**, n/a-n/a (2017).

150. Zalar, P., Kuik, M., Ran, N. A., Love, J. A. & Nguyen, T.-Q. Effects of Processing Conditions on the Recombination Reduction in Small Molecule Bulk Heterojunction Solar Cells. *Advanced Energy Materials* **4**, 1400438 (2014).

151. Oberhofer, H. & Blumberger, J. Electronic coupling matrix elements from charge constrained density functional theory calculations using a plane wave basis set. *J. Chem. Phys.* **133**, 244105 (2010).

152. Tsao, H. N. *et al.* Ultrahigh Mobility in Polymer Field-Effect Transistors by Design. *J. Am. Chem. Soc.* **133**, 2605–2612 (2011).

153. Lo, C. K. *et al.* Every Atom Counts: Elucidating the Fundamental Impact of Structural Change in Conjugated Polymers for Organic Photovoltaics. *Chem. Mater.* **30**, 2995–3009 (2018).

154. Yurash, B. *et al.* Atomic-Level Insight into the Postsynthesis Band Gap Engineering of a Lewis Base Polymer Using Lewis Acid Tris(pentafluorophenyl)borane. *Chem. Mater.* **31**, 6715–6725 (2019).

155. Reddy, G. N. M., Marsh, A., Davis, J. T., Masiero, S. & Brown, S. P. Interplay of Noncovalent Interactions in Ribbon-like Guanosine Self-Assembly: An NMR Crystallography Study. *Crystal Growth & Design* **15**, 5945–5954 (2015).

156. Luzio, A. *et al.* Microstructural control suppresses thermal activation of electron transport at room temperature in polymer transistors. *Nature Communications* **10**, 1–13 (2019).

157. Reddy G. N, M., Ballesteros□Garrido, R., Lacour, J. & Caldarelli, S. Determination of Labile Chiral Supramolecular Ion Pairs by Chromatographic NMR Spectroscopy. *Angewandte Chemie International Edition* **52**, 3255–3258 (2013).

158. Elena, B., de Paëpe, G. & Emsley, L. Direct spectral optimisation of proton–proton homonuclear dipolar decoupling in solid-state NMR. *Chemical Physics Letters* **398**, 532–538 (2004).

159. Sakellariou, D., Lesage, A., Hodgkinson, P. & Emsley, L. Homonuclear dipolar decoupling in solid-state NMR using continuous phase modulation. *Chemical Physics Letters* **319**, 253–260 (2000).

160. Jakowetz, A. C. *et al.* Visualizing excitations at buried heterojunctions in organic semiconductor blends. *Nat Mater* **16**, 551–557 (2017).

161. Scarongella, M. *et al.* A Close Look at Charge Generation in Polymer:Fullerene Blends with Microstructure Control. *J. Am. Chem. Soc.* **137**, 2908–2918 (2015).

162. Menke, S. M. *et al.* Order enables efficient electron-hole separation at an organic heterojunction with a small energy loss. *Nature Communications* **9**, 277 (2018).

163. Wróbel, D. & Graja, A. Photoinduced electron transfer processes in fullerene–organic chromophore systems. *Coordination Chemistry Reviews* **255**, 2555–2577 (2011).

164. Scully, S. R., Armstrong, P. B., Edder, C., Fréchet, J. M. J. & McGehee, M. D. Long-Range Resonant Energy Transfer for Enhanced Exciton Harvesting for Organic Solar Cells. *Advanced Materials* **19**, 2961–2966 (2007).

165. Sun, C. *et al.* High Efficiency Polymer Solar Cells with Efficient Hole Transfer at Zero Highest Occupied Molecular Orbital Offset between Methylated Polymer Donor and Brominated Acceptor. *J. Am. Chem. Soc.* **142**, 1465–1474 (2020).

166. Xue, L. *et al.* Side Chain Engineering on Medium Bandgap Copolymers to Suppress Triplet Formation for High-Efficiency Polymer Solar Cells. *Adv. Mater. Weinheim* **29**, (2017).

167. Liu, Y., Zuo, L., Shi, X., Jen, A. K.-Y. & Ginger, D. S. Unexpectedly Slow Yet Efficient Picosecond to Nanosecond Photoinduced Hole-Transfer Occurs in a Polymer/Nonfullerene Acceptor Organic Photovoltaic Blend. *ACS Energy Lett.* **3**, 2396–2403 (2018).

168. Karki, A. *et al.* Unifying Charge Generation, Recombination, and Extraction in Low-offset Non-fullerene Acceptor Organic Solar Cells. *Advanced Energy Materials*.

169. Mandoc, M. M., Kooistra, F. B., Hummelen, J. C., de Boer, B. & Blom, P. W. M. Effect of traps on the performance of bulk heterojunction organic solar cells. *Appl. Phys. Lett.* **91**, 263505 (2007).

170. Zonno, I., Zayani, H., Grzeslo, M., Krogmeier, B. & Kirchartz, T. Extracting Recombination Parameters from Impedance Measurements on Organic Solar Cells. *Phys. Rev. Applied* **11**, 054024 (2019).

171. Günes, S., Neugebauer, H. & Sariciftci, N. S. Conjugated polymer-based organic solar cells. *Chem. Rev.* **107**, 1324–1338 (2007).

172. Horowitz, G. Organic Field-Effect Transistors. *Advanced Materials* **10**, 365–377 (1998).

173. Vaeth, K. M. OLED-Display Technology. *INFORMATION DISPLAY* **19**, 12–17 (2003).

174. Bässler, H. Charge Transport in Disordered Organic Photoconductors a Monte Carlo Simulation Study. *physica status solidi (b)* **175**, 15–56 (1993).

175. Blakesley, J. C. & Neher, D. Relationship between energetic disorder and open-circuit voltage in bulk heterojunction organic solar cells. *Phys. Rev. B* **84**, 075210 (2011).

176. Celebi, K., Jadhav, P. J., Milaninia, K. M., Bora, M. & Baldo, M. A. The density of states in thin film copper phthalocyanine measured by Kelvin probe force microscopy. *Appl. Phys. Lett.* **93**, 083308 (2008).

177. Hulea, I. N. *et al.* Wide Energy-Window View on the Density of States and Hole Mobility in Poly(p-Phenylene Vinylene). *Phys. Rev. Lett.* **93**, 166601 (2004).

178. Tal, O. *et al.* Direct Determination of the Hole Density of States in Undoped and Doped Amorphous Organic Films with High Lateral Resolution. *Phys. Rev. Lett.* **95**, 256405 (2005).

179. Sueyoshi, T., Fukagawa, H., Ono, M., Kera, S. & Ueno, N. Low-density band-gap states in pentacene thin films probed with ultrahigh-sensitivity ultraviolet photoelectron spectroscopy. *Appl. Phys. Lett.* **95**, 183303 (2009).

180. Garcia-Belmonte, G., Boix, P. P., Bisquert, J., Sessolo, M. & Bolink, H. J. Simultaneous determination of carrier lifetime and electron density-of-states in P3HT:PCBM organic solar cells under illumination by impedance spectroscopy. *Solar Energy Materials and Solar Cells* **94**, 366–375 (2010).

181. Tachiya, M. & Seki, K. Theory of bulk electron-hole recombination in a medium with energetic disorder. *Phys. Rev. B* **82**, 085201 (2010).

182. Morphology□Dependent Trap Formation in High Performance Polymer Bulk Heterojunction Solar Cells - Beiley - 2011 - Advanced Energy Materials - Wiley Online Library. https://onlinelibrary.wiley.com/doi/abs/10.1002/aenm.201100204.

183. MacKenzie, R. C. I., Kirchartz, T., Dibb, G. F. A. & Nelson, J. Modeling Nongeminate Recombination in P3HT:PCBM Solar Cells. *J. Phys. Chem. C* **115**, 9806–9813 (2011).

184. Gong, W. *et al.* Influence of energetic disorder on electroluminescence emission in polymer:fullerene solar cells. *Phys. Rev. B* **86**, 024201 (2012).

185. MacKenzie, R. C. I., Shuttle, C. G., Chabinyc, M. L. & Nelson, J. Extracting Microscopic Device Parameters from Transient Photocurrent Measurements of P3HT:PCBM Solar Cells. *Advanced Energy Materials* **2**, 662–669 (2012).

186. Shuttle, C. G., Treat, N. D., Douglas, J. D., Fréchet, J. M. J. & Chabinyc, M. L. Deep Energetic Trap States in Organic Photovoltaic Devices. *Advanced Energy Materials* **2**, 111–119 (2012).

187. Oelerich, J. O., Huemmer, D. & Baranovskii, S. D. How to Find Out the Density of States in Disordered Organic Semiconductors. *Phys. Rev. Lett.* **108**, 226403 (2012).

188. Pingel, P. & Neher, D. Comprehensive picture of p-type doping of P3HT with the molecular acceptor F${}_{4}$TCNQ. *Phys. Rev. B* **87**, 115209 (2013).

189. Fishchuk, I. I. *et al.* Temperature dependence of the charge carrier mobility in disordered organic semiconductors at large carrier concentrations. *Phys. Rev. B* **81**, 045202 (2010).

190. Torricelli, F., Kovács-Vajna, Zs. M. & Colalongo, L. The role of the density of states on the hole mobility of disordered organic semiconductors. *Organic Electronics* **10**, 1037–1040 (2009).

191. Oehzelt, M., Koch, N. & Heimel, G. Organic semiconductor density of states controls the energy level alignment at electrode interfaces. *Nat Commun* **5**, 4174 (2014).

192. Craciun, N. I., Wildeman, J. & Blom, P. W. M. Universal Arrhenius Temperature Activated Charge Transport in Diodes from Disordered Organic Semiconductors. *Phys. Rev. Lett.* **100**, 056601 (2008).

193. Kuik, M. *et al.* 25th Anniversary Article: Charge Transport and Recombination in Polymer Light-Emitting Diodes. *Adv. Mater.* **26**, 512–531 (2014).

194. Yan, H. *et al.* A high-mobility electron-transporting polymer for printed transistors. *Nature* **457**, 679–686 (2009).

195. Tseng, H.-R. *et al.* High-mobility field-effect transistors fabricated with macroscopic aligned semiconducting polymers. *Adv. Mater. Weinheim* **26**, 2993–2998 (2014).

196. Chen, H. *et al.* Highly π-extended copolymers with diketopyrrolopyrrole moieties for high-performance field-effect transistors. *Adv. Mater. Weinheim* **24**, 4618–4622 (2012).

197. McCulloch, I. *et al.* Liquid-crystalline semiconducting polymers with high charge-carrier mobility. *Nat Mater* **5**, 328–333 (2006).

198. Proctor, C. M., Love, J. A. & Nguyen, T.-Q. Mobility guidelines for high fill factor solution-processed small molecule solar cells. *Adv. Mater. Weinheim* **26**, 5957–5961 (2014).

199. Hamadani, B. H., Gundlach, D. J., McCulloch, I. & Heeney, M. Undoped polythiophene field-effect transistors with mobility of 1cm2V−1s−1. *Appl. Phys. Lett.* **91**, 243512 (2007).

200. Chabinyc, M. L., Toney, M. F., Kline, R. J., McCulloch, I. & Heeney, M. X-ray scattering study of thin films of poly(2,5-bis(3-alkylthiophen-2-yl)thieno[3,2-b]thiophene). *J. Am. Chem. Soc.* **129**, 3226–3237 (2007).

201. Kröger, M. *et al.* Role of the deep-lying electronic states of MoO3 in the enhancement of hole-injection in organic thin films. *Appl. Phys. Lett.* **95**, 123301 (2009).

202. Wetzelaer, G. A. H. & Blom, P. W. M. Ohmic current in organic metal-insulator-metal diodes revisited. *Phys. Rev. B* **89**, 241201 (2014).

203. Liao, S.-H., Jhuo, H.-J., Cheng, Y.-S. & Chen, S.-A. Fullerene Derivative-Doped Zinc Oxide Nanofilm as the Cathode of Inverted Polymer Solar Cells with Low-Bandgap Polymer (PTB7-Th) for High Performance. *Advanced Materials* **25**, 4766–4771 (2013).

204. Pauling, L. Electronic Processes in Ionic Crystals. By N. F. Mott and R. W. Gurney. *J. Phys. Chem.* **45**, 1142–1142 (1941).

205. Blom, P. W. M., de Jong, M. J. M. & Vleggaar, J. J. M. Electron and hole transport in poly(p□phenylene vinylene) devices. *Appl. Phys. Lett.* **68**, 3308–3310 (1996).

206. Tanase, C., Meijer, E. J., Blom, P. W. M. & de Leeuw, D. M. Unification of the Hole Transport in Polymeric Field-Effect Transistors and Light-Emitting Diodes. *Phys. Rev. Lett.* **91**, 216601 (2003).

207. Pasveer, W. F. *et al.* Unified Description of Charge-Carrier Mobilities in Disordered Semiconducting Polymers. *Phys. Rev. Lett.* **94**, 206601 (2005).

208. Koster, L. J. A., Smits, E. C. P., Mihailetchi, V. D. & Blom, P. W. M. Device model for the operation of polymer/fullerene bulk heterojunction solar cells. *Phys. Rev. B* **72**, 085205 (2005).

209. Wetzelaer, G. a. H. Analytical description of the current-voltage relationship in organic-semiconductor diodes. *AIP Advances* **8**, 035320 (2018).

210. Koynov, K. *et al.* Molecular Weight Dependence of Chain Orientation and Optical Constants of Thin Films of the Conjugated Polymer MEH-PPV. *Macromolecules* **39**, 8692–8698 (2006).

211. Kline, R. J. *et al.* Dependence of Regioregular Poly(3-hexylthiophene) Film Morphology and Field-Effect Mobility on Molecular Weight. *Macromolecules* **38**, 3312–3319 (2005).

212. Nonnenmacher, M., O'Boyle, M. P. & Wickramasinghe, H. K. Kelvin probe force microscopy. *Appl. Phys. Lett.* **58**, 2921–2923 (1991).

213. V. Contact electricity of metals: The London, Edinburgh, and Dublin Philosophical Magazine and Journal of Science: Vol 46, No 278. https://www.tandfonline.com/doi/abs/10.1080/14786449808621172.

214. Blakesley, J. C. & Greenham, N. C. Charge transfer at polymer-electrode interfaces: The effect of energetic disorder and thermal injection on band bending and open-circuit voltage. *Journal of Applied Physics* **106**, 034507 (2009).

215. Lange, I. *et al.* Band bending in conjugated polymer layers. *Phys. Rev. Lett.* **106**, 216402 (2011).

216. Ottinger, O. M., Melzer, C. & Seggern, H. von. Pitfalls in Kelvin probe measurements. *Journal of Applied Physics* **106**, 023704 (2009).

217. Electronic and Optical Processes of Organic Semiconductors. in *Electronic Processes in Organic Semiconductors* 193–305 (Wiley-Blackwell, 2015). doi:10.1002/9783527685172.ch3.

218. Collins, S. D., Proctor, C. M., Ran, N. A. & Nguyen, T.-Q. Understanding Open-Circuit Voltage Loss through the Density of States in Organic Bulk Heterojunction Solar Cells. *Advanced Energy Materials* **6**, 1501721 (2016).

219. Marcus, R. A. On the Theory of Oxidation□Reduction Reactions Involving Electron Transfer. I. *The Journal of Chemical Physics* **24**, 966–978 (1956).

220. Schauer, F., Nádaždy, V. & Gmucová, K. Electrochemical impedance spectroscopy for study of electronic structure in disordered organic semiconductors—Possibilities and limitations. *Journal of Applied Physics* **123**, 161590 (2018).

221. Lewis, N. S. Progress in Understanding Electron-Transfer Reactions at Semiconductor/Liquid Interfaces. *J. Phys. Chem. B* **102**, 4843–4855 (1998).

222. Garcia-Belmonte, G., Bisquert, J. & Popkirov, G. S. Determination of the electronic conductivity of polybithiophene films at different doping levels using in situ electrochemical impedance measurements. *Appl. Phys. Lett.* **83**, 2178–2180 (2003).

223. Bisquert, J., Garcia-Belmonte, G. & García-Cañadas, J. Effects of the Gaussian energy dispersion on the statistics of polarons and bipolarons in conducting polymers. *J Chem Phys* **120**, 6726–6733 (2004).

224. Pomerantz, Z. *et al.* Capacitance, spectroelectrochemistry and conductivity of polarons and bipolarons in a polydicarbazole based conducting polymer. *Journal of Electroanalytical Chemistry* **614**, 49–60 (2008).

225. Coropceanu, V. *et al.* Charge Transport in Organic Semiconductors. *Chem. Rev.* **107**, 926–952 (2007).

226. Noriega, R. *et al.* A general relationship between disorder, aggregation and charge transport in conjugated polymers. *Nature Materials* **12**, 1038–1044 (2013).

227. Sirringhaus, H. *et al.* Two-dimensional charge transport in self-organized, high-mobility conjugated polymers. *Nature* **401**, 685–688 (1999).

228. Rivnay, J., Mannsfeld, S. C. B., Miller, C. E., Salleo, A. & Toney, M. F. Quantitative Determination of Organic Semiconductor Microstructure from the Molecular to Device Scale. *Chem. Rev.* **112**, 5488–5519 (2012).

229. Ro, H. W. *et al.* Morphology changes upon scaling a high-efficiency, solution-processed solar cell. *Energy Environ. Sci.* **9**, 2835–2846 (2016).

230. Kraffert, F. *et al.* Transport-related triplet states and hyperfine couplings in organic tandem solar cells probed by pulsed electrically detected magnetic resonance spectroscopy. *Journal of Magnetic Resonance* **282**, 10–17 (2017).

231. Jing, C., Chen, L., Shi, Y. & Jin, X. Synthesis and characterization of exfoliated MEH-PPV/clay nanocomposites by in situ polymerization. *European Polymer Journal* **41**, 2388–2394 (2005).

232. Cui, X., Freitag, M., Martel, R., Brus, L. & Avouris, P. Controlling Energy-Level Alignments at Carbon Nanotube/Au Contacts. *Nano Lett.* **3**, 783–787 (2003).

233. Suzuki, S., Bower, C., Watanabe, Y. & Zhou, O. Work functions and valence band states of pristine and Cs-intercalated single-walled carbon nanotube bundles. *Appl. Phys. Lett.* **76**, 4007–4009 (2000).

234. Fung, B. M., Khitrin, A. K. & Ermolaev, K. An improved broadband decoupling sequence for liquid crystals and solids. *J. Magn. Reson.* **142**, 97–101 (2000).

235. Athanasopoulos, S. *et al.* What is the Binding Energy of a Charge Transfer State in an Organic Solar Cell? *Advanced Energy Materials* **9**, 1900814 (2019).

236. Kurik, M. V. Urbach rule. *physica status solidi (a)* **8**, 9–45 (1971).

237. Weinberger, B. R., Roxlo, C. B., Etemad, S., Baker, G. L. & Orenstein, J. Optical Absorption in Polyacetylene: A Direct Measurement Using Photothermal Deflection Spectroscopy. *Phys. Rev. Lett.* **53**, 86–89 (1984).

238. De Wolf, S. *et al.* Organometallic Halide Perovskites: Sharp Optical Absorption Edge and Its Relation to Photovoltaic Performance. *J. Phys. Chem. Lett.* **5**, 1035–1039 (2014).

239. Abbaszadeh, D. *et al.* Electron trapping in conjugated polymers. *Chem. Mater.* (2019) doi:10.1021/acs.chemmater.9b01211.

240. Nicolai, H. T. *et al.* Unification of trap-limited electron transport in semiconducting polymers. *Nature Materials* **11**, 882–887 (2012).

241. Wetzelaer, G.-J. A. H. *et al.* Asymmetric electron and hole transport in a high-mobility n-type conjugated polymer. *Phys. Rev. B* **86**, 165203 (2012).

242. Wang, T., J. Pearson, A. & G. Lidzey, D. Correlating molecular morphology with optoelectronic function in solar cells based on low band-gap copolymer:fullerene blends. *Journal of Materials Chemistry C* **1**, 7266–7293 (2013).

243. Gasparini, N. *et al.* Favorable Mixing Thermodynamics in Ternary Polymer Blends for Realizing High Efficiency Plastic Solar Cells. *Advanced Energy Materials* **9**, 1803394 (2019).

244. Xie, S. *et al.* Vinylene- and ethynylene-bridged perylene diimide dimers as nonfullerene acceptors for polymer solar cells. *Dyes and Pigments* **146**, 143–150 (2017).

245. Kiersnowski, A. *et al.* Formation of Oriented Polar Crystals in Bulk Poly(vinylidene fluoride)/High-Aspect-Ratio Organoclay Nanocomposites. *Langmuir* acs.langmuir.8b02412 (2018) doi:10.1021/acs.langmuir.8b02412.

246. Vega, A. J. & English, A. D. Multiple-Pulse Nuclear Magnetic Resonance of Solid Polymers. Polymer Motions in Crystalline and Amorphous Poly(tetrafluoroethylene). *Macromolecules* **13**, 1635–1647 (1980).

247. Holstein, P., Scheler, U. & Harris, R. K. Semicrystallinity and polymorphism in PVDF: A solid-state19F n.m.r. investigation. *Polymer* **39**, 4937–4941 (1998).

248. Ando, S., Harris, R. K. & Reinsberg, S. A. Solid-state 1 H → 19 F/ 19 F → 1 H CP/MAS NMR study of poly(vinylidene fluoride). *MAGNETIC RESONANCE IN CHEMISTRY Magn. Reson. Chem* **40**, 97–106 (2002).

249. Murgatroyd, P. N. Theory of space-charge-limited current enhanced by Frenkel effect. *J. Phys. D: Appl. Phys.* **3**, 151–156 (1970).

250. Sze, S. M. & Ng, K. K. *Physics of Semiconductor Devices*. (John Wiley & Sons, Inc., 2006).

251. Brus, V. V. *et al.* Defect Dynamics in Proton Irradiated CH3NH3PbI3 Perovskite Solar Cells. *Advanced Electronic Materials* **3**, 1600438 (2017).

252. Smilgies, D.-M. Scherrer grain-size analysis adapted to grazing-incidence scattering with area detectors. *J Appl Cryst* **42**, 1030–1034 (2009).

253. Li, Y. *et al.* High Efficiency Near-Infrared and Semitransparent Non-Fullerene Acceptor Organic Photovoltaic Cells. *J. Am. Chem. Soc.* **139**, 17114–17119 (2017).